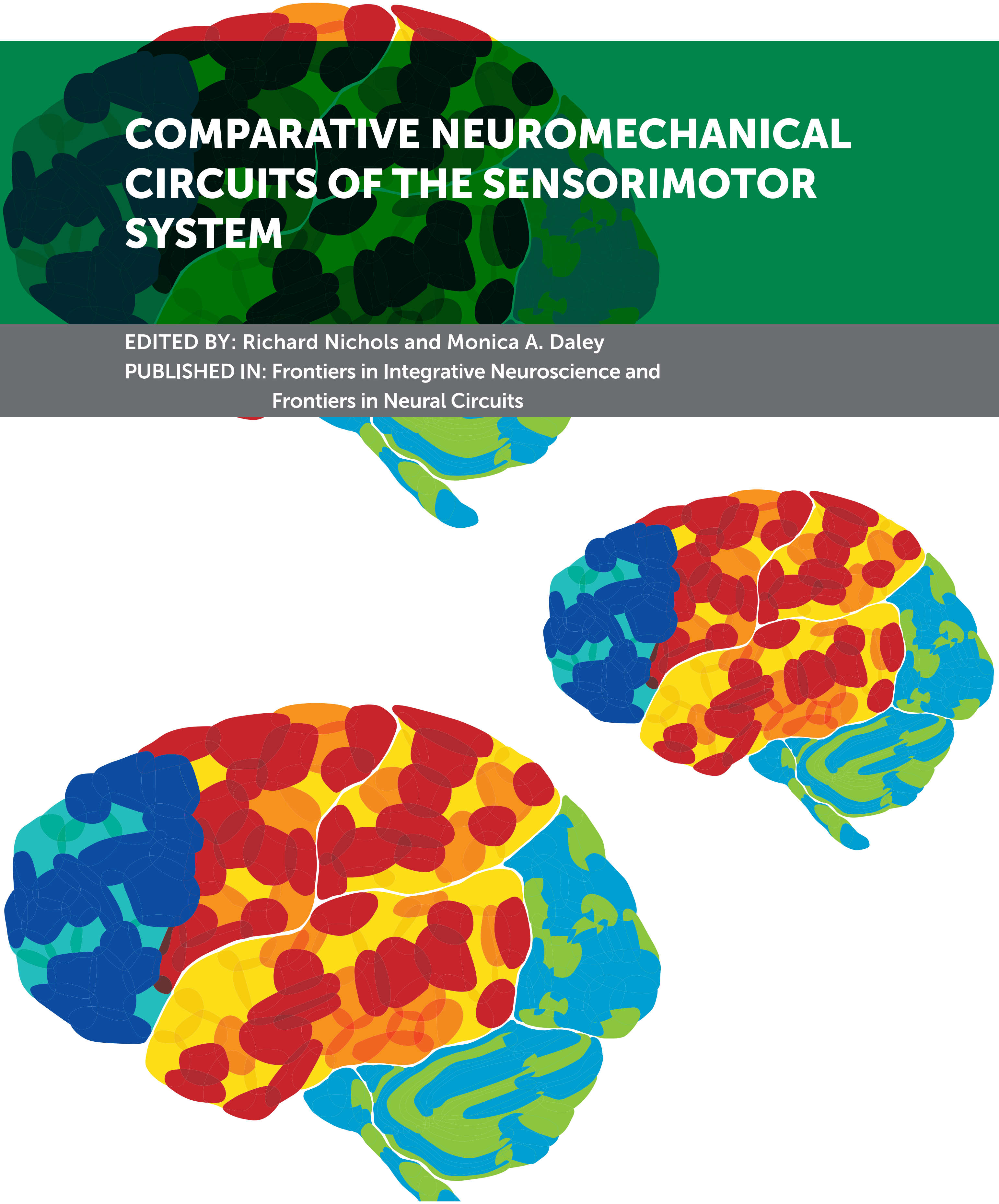

COMPARATIVE NEUROMECHANICAL CIRCUITS OF THE SENSORIMOTOR SYSTEM

EDITED BY: Richard Nichols and Monica A. Daley

PUBLISHED IN: Frontiers in Integrative Neuroscience and
Frontiers in Neural Circuits

frontiers Research Topics

ISSN 1664-8714
ISBN 978-2-8897-6549-2
DOI 10.3389/978-2-8897-6549-2

About Frontiers

Frontiers is more than just an open-access publisher of scholarly articles: it is a pioneering approach to the world of academia, radically improving the way scholarly research is managed. The grand vision of Frontiers is a world where all people have an equal opportunity to seek, share and generate knowledge. Frontiers provides immediate and permanent online open access to all its publications, but this alone is not enough to realize our grand goals.

Frontiers Journal Series

The Frontiers Journal Series is a multi-tier and interdisciplinary set of open-access, online journals, promising a paradigm shift from the current review, selection and dissemination processes in academic publishing. All Frontiers journals are driven by researchers for researchers; therefore, they constitute a service to the scholarly community. At the same time, the Frontiers Journal Series operates on a revolutionary invention, the tiered publishing system, initially addressing specific communities of scholars, and gradually climbing up to broader public understanding, thus serving the interests of the lay society, too.

Dedication to Quality

Each Frontiers article is a landmark of the highest quality, thanks to genuinely collaborative interactions between authors and review editors, who include some of the world's best academicians. Research must be certified by peers before entering a stream of knowledge that may eventually reach the public - and shape society; therefore, Frontiers only applies the most rigorous and unbiased reviews.
Frontiers revolutionizes research publishing by freely delivering the most outstanding research, evaluated with no bias from both the academic and social point of view.
By applying the most advanced information technologies, Frontiers is catapulting scholarly publishing into a new generation.

What are Frontiers Research Topics?

Frontiers Research Topics are very popular trademarks of the Frontiers Journals Series: they are collections of at least ten articles, all centered on a particular subject. With their unique mix of varied contributions from Original Research to Review Articles, Frontiers Research Topics unify the most influential researchers, the latest key findings and historical advances in a hot research area! Find out more on how to host your own Frontiers Research Topic or contribute to one as an author by contacting the Frontiers Editorial Office: frontiersin.org/about/contact

COMPARATIVE NEUROMECHANICAL CIRCUITS OF THE SENSORIMOTOR SYSTEM

Topic Editors:
Richard Nichols, Georgia Institute of Technology, United States
Monica A. Daley, University of California, Irvine, United States

Citation: Nichols, R., Daley, M. A., eds. (2023). Comparative Neuromechanical Circuits of the Sensorimotor System. Lausanne: Frontiers Media SA.
doi: 10.3389/978-2-8897-6549-2

Table of Contents

frontiers | Frontiers in Integrative Neuroscience

TYPE Editorial
PUBLISHED 18 July 2022
DOI 10.3389/fnint.2022.975948

OPEN ACCESS

EDITED AND REVIEWED BY
Elizabeth B. Torres,
Rutgers, The State University of New Jersey, United States

*CORRESPONDENCE
T. Richard Nichols
trn@gatech.edu

RECEIVED 22 June 2022
ACCEPTED 24 June 2022
PUBLISHED 18 July 2022

CITATION
Nichols TR and Daley MA (2022) Editorial: Comparative neuromechanical circuits of the sensorimotor system. *Front. Integr. Neurosci.* 16:975948. doi: 10.3389/fnint.2022.975948

Editorial: Comparative neuromechanical circuits of the sensorimotor system

T. Richard Nichols[1]* and Monica A. Daley[2]

[1]School of Biological Sciences, Georgia Institute of Technology, Atlanta, GA, United States,
[2]Department of Ecology and Evolutionary Biology, School of Biological Sciences, University of California, Irvine, Irvine, CA, United States

KEYWORDS

sensorimotor integration, musculoskeletal system, computational model, comparative motor control, central pattern generator (CPG) control, inertial coupling

Editorial on the Research Topic
Comparative Neuromechanical Circuits of the Sensorimotor System

The musculoskeletal and nervous systems have evolved together to mediate stable and coordinated posture and movement. Although considerable information is available about the structure and function of both systems independently through the research areas of biomechanics and neurophysiology, progress in understanding the mechanisms of motor control has been accelerated by the study of these two systems together, resulting in the emerging area of neuromechanics. This Research Topic includes papers representing this integrated approach to the study of motor function. These contributions also feature a comparative approach, seeking insights from the study of diverse organisms, from coordination in multi-segmented invertebrates to interneuron connectivity in cats, to multi-sensory convergence in human motor control. A wide range of contemporary modeling and experimental approaches are featured, including computer simulations, recording of single motor units and interneurons by micro-electrode arrays, functional imaging, and the use of robotics to control interactions between body and environment. We have grouped the articles into three subtopics, focusing first on the interplay between musculoskeletal mechanics and neural control, then on stretch reflexes and sensorimotor integration in the spinal cord, and finally on the way in which limb mechanics are represented in the human brain and on descending control of spinal pathways.

The first group of articles directly addressed the importance of body and limb mechanics in understanding mechanisms of motor coordination. The first three articles discussed computational models that represent integrated neural and musculoskeletal pathways for repetitive movements. In the first (Ambe et al.), the authors developed a neuromechanical model for multi-legged locomotion. The mechanical model consisted of a number of segments represented by masses interconnected by damped springs. Each segment also included an oscillator with phase-resetting sensory feedback. The authors showed that multiple, naturally observed gait patterns for coordinating multi-legged locomotion emerged from this simple decentralized motor control system. In the second paper (Okamoto et al.), the authors used a simplified neuromechanical model of human walking to investigate the phenomenon of statistical persistence of stride intervals. The model consisted of a simple compass type biomechanical walking model coupled to a Central Pattern Generator (CPG) based controller. The control model included a phase oscillator to generate feedforward motor commands, coupled to phase resetting sensory feedback. The authors found statistical persistence in the model with phase resetting feedback, which is lost in the model without phase resetting feedback. In the third paper (Prilutsky et al.), the authors integrated experimental evidence with a model of the feline hindlimb and spinal cord to understand the paw shake response, a behavioral characterized by high velocities and accelerations. The model consisted of central pattern generating circuits, sensory feedback and a multi-segmented limb with realistic inertial properties of the limb segments. Combining all three components successfully reproduced the whip-like dynamics that are experimentally observed in the paw shake. In the final article in this group (Ludvig et al.), experiments with human participants were used to explore tasks that either used or opposed the natural impedances of the ankle joints. The latter tasks required subjects to modulate muscular activation patterns more than for the former task and were perceived to be more difficult by the subjects. These findings illustrate the importance of leveraging joint impedances to effectively perform natural movements.

The second group of articles addressed structural and functional aspects of sensorimotor integration. Classical studies of feedback from muscles onto motoneurons had shown that motor units concerned with posture and stabilization tend to receive higher densities of input from muscle spindles than those concerned with more dynamic tasks. In an experimental study using human participants (Nicolozakes et al.), the authors showed that the rotator cuff muscles, muscles that are primary stabilizers of the shoulder, exhibit stronger stretch reflexes than the larger prime movers of the shoulder. These results are consistent with the role of stretch reflex to regulate joint stiffness to stabilize the shoulder against disturbances. Investigating functional connectivity within the spinal cord is also critical to understanding sensorimotor integration, because most inputs to spinal motoneurons come from interneurons that integrate sensory and descending inputs, rather than directly from the periphery. In the second study in this group (Zaback et al.), the authors introduced a new method to map the functional connectivity between cutaneous sources and motoneurons. Microelectrode arrays were employed to record single motor units and interneurons in the spinal cord, and connectivity was inferred from correlations between these two sources. The method was validated using pathways that are known to have more or less direct connections to these interneurons. In the third study (Thompson et al.), a comparative approach was used to understand the differences in firing patterns of motor units in response to tendon vibration in cat and man. New, multi-unit recordings of single motor units from muscles were used in both species. The authors found that motor units tend to fire in integral multiples of the vibration frequency in cat but not man. These different firing patterns might be explained by greater temporal dispersion from longer conduction distances in humans, resulting in a smoothed and more uniform synaptic input.

The third group of articles focused on brain and nervous system-wide mechanisms of motor coordination and the convergence of different sensory sources for motor control, continuing the themes of stabilization and impedance control. In a review article (Jayasinghe et al.), the task of stopping a movement is used to introduce a hybrid model of motor control. Continuing the theme of stabilization and impedance control introduced above, the authors argue that there are two independent aspects of motor control, on the one hand, the control of movement trajectory and compensation for inertial coupling between limb segments, and on the other hand, stopping and stabilization of movement. The authors further argued that stabilization is most readily explained by impedance control. Continuing the theme of stabilization, the authors of the second article in this group (Suminski et al.) addressed the contributions of visual and proprioceptive feedback to joint stabilization in response to torque perturbations. When both sources of feedback were congruent, they both contributed; however, when visual information was unreliable, it was apparently ignored. This finding led the authors to reject a long-standing model of multi-sensory convergence. These studies were carried out with a robotic and virtual reality system, as well as fMRI imaging to assess the involvement of principle brain areas. The results of brain imaging provided insights into the neural substrate of the observed interactions between the two sensory sources. Closing the loop on spinal cord and brain mechanisms of motor coordination, the final article (Xu et al.) addressed the influence of brain areas on spinal circuitry by conditioning a measure of the stretch reflex (H- reflex) with transcranial magnetic stimulation (TMS). The cortex influences the spinal cord through both rapid, direct and slower, indirect pathways. By recognizing this, the authors were able to assess the influence of cranial stimulation on the direct and indirect pathways by altering the intervals between cranial and peripheral nerve stimulation. This approach provides a method and normative reference values for investigating these two pathways in health and disease.

Author contributions

All authors listed have made a substantial, direct, and intellectual contribution to the work and approved it for publication.

Conflict of Interest

The authors declare that the research was conducted in the absence of any commercial or financial relationships that could be construed as a potential conflict of interest.

Publisher's note

frontiers
in Neural Circuits

ORIGINAL RESEARCH
published: 06 September 2021
doi: 10.3389/fncir.2021.706064

Generation of Direct-, Retrograde-, and Source-Wave Gaits in Multi-Legged Locomotion in a Decentralized Manner via Embodied Sensorimotor Interaction

Yuichi Ambe[1]*, *Shinya Aoi*[2], *Kazuo Tsuchiya*[2] *and Fumitoshi Matsuno*[3]

[1] Tough Cyberphysical AI Research Center, Tohoku University, Sendai, Japan, [2] Department of Aeronautics and Astronautics, Kyoto University, Kyoto, Japan, [3] Department of Mechanical Engineering and Science, Kyoto University, Kyoto, Japan

Multi-legged animals show several types of ipsilateral interlimb coordination. Millipedes use a direct-wave gait, in which the swing leg movements propagate from posterior to anterior. In contrast, centipedes use a retrograde-wave gait, in which the swing leg movements propagate from anterior to posterior. Interestingly, when millipedes walk in a specific way, both direct and retrograde waves of the swing leg movements appear with the waves' source, which we call the source-wave gait. However, the gait generation mechanism is still unclear because of the complex nature of the interaction between neural control and dynamic body systems. The present study used a simple model to understand the mechanism better, primarily how local sensory feedback affects multi-legged locomotion. The model comprises a multi-legged body and its locomotion control system using biologically inspired oscillators with local sensory feedback, phase resetting. Each oscillator controls each leg independently. Our simulation produced the above three types of animal gaits. These gaits are not predesigned but emerge through the interaction between the neural control and dynamic body systems through sensory feedback (embodied sensorimotor interaction) in a decentralized manner. The analytical description of these gaits' solution and stability clarifies the embodied sensorimotor interaction's functional roles in the interlimb coordination.

Keywords: interlimb coordination, multi-legged locomotion, millipede, metachronal waves, local sensory feedback, embodied sensorimotor interaction

Edited by:
Richard Nichols,
Georgia Institute of Technology,
United States

Reviewed by:
Rhanor Gillette,
University of Illinois at
Urbana-Champaign, United States
Ansgar Buschges,
University of Cologne, Germany

Correspondence:
Yuichi Ambe
ambe@rm.is.tohoku.ac.jp

Received: *06 May 2021*
Accepted: *02 August 2021*
Published: *06 September 2021*

Citation:
Ambe Y, Aoi S, Tsuchiya K and Matsuno F (2021) Generation of Direct-, Retrograde-, and Source-Wave Gaits in Multi-Legged Locomotion in a Decentralized Manner via Embodied Sensorimotor Interaction.
Front. Neural Circuits 15:706064.
doi: 10.3389/fncir.2021.706064

1. INTRODUCTION

Multi-legged animals, even those with a large number of legs, use several types of ipsilateral interlimb coordination according to the species and situations. Centipedes use a retrograde-wave gait in which the swing leg movements propagate from the anterior to posterior (Full, 1997; Kuroda et al., 2014). In contrast, millipedes generally use a direct-wave gait, in which the swing leg movements propagate from the posterior to anterior (Full, 1997; Kuroda et al., 2014). More interestingly, it is reported that when millipedes walk with the body axis bent like a U shape, both direct and retrograde waves of the swing leg movements appear at the source of the waves (Tamura et al., 2016), which we call the source-wave gait. However, it remains unclear what mechanisms generate these different types of interlimb coordination in multi-legged locomotion.

Regarding the locomotion of insects and mammals that use a direct-wave gait, where the swing leg movements propagate from the posterior to anterior, physiological studies have suggested that central pattern generators (CPGs) and sensory feedback play important roles in the interlimb coordination (Delcomyn, 2004; Büschges et al., 2008; Ijspeert, 2008). The CPGs generate rhythmic outputs, which are modulated by sensory feedback. The sensory feedback is critical especially during slow walking, as seen in stick insects (Delcomyn, 2004; Büschges et al., 2008).

However, the mechanism of the interlimb coordination has not been fully understood only from physiological studies because the locomotion is generated through complex interactions between motor control and body dynamics through sensory feedback (embodied sensorimotor interaction). Thus, many mathematical models and robots have been developed to clarify the functional roles of these interactions in the interlimb coordination (Steingrube et al., 2010; Owaki et al., 2012; Aoi et al., 2013; Schilling et al., 2013; Ambe et al., 2015).

Recently, mathematical models and robots for multi-legged locomotion have reproduced many aspects of the gaits of multi-legged animals by focusing on the embodied sensorimotor interaction. Tamura et al. (2016) showed that sensory feedback of load information generates a millipede-like gait. Yasui et al. (2017) and Kano et al. (2017) proposed distributed control schemes with sensory feedback of load information to reproduce the multi-legged locomotion observed when a part of the terrain is removed. They also investigated the transition between swimming and walking of centipedes based on the interplay of brain, CPG, and sensory feedback (Yasui et al., 2019). However, the mechanism for generating various interlimb coordination in multi-legged locomotion is still not fully understood.

The purpose of this study was to use a simple model to demonstrate that local sensory feedback generates the various interlimb coordination observed in multi-legged animals via embodied sensory-motor interactions. For that purpose, we constructed a mechanical model that imitates the flexible body of multi-legged animals and a control model that uses phase oscillators inspired by CPGs and phase resetting as local sensory feedback. The simulation results show that although the oscillators do not interact directly, three types of gaits (direct-, retrograde-, and source-wave gaits) emerge through the embodied sensorimotor interaction. Furthermore, we derive these analytical solutions and stabilities under some assumptions, which produce the three types of gaits regardless of the number of legs and clarify how the local sensory feedback generates these gaits through the embodied sensorimotor interaction.

2. SIMULATION

2.1. Mechanical Model

Skeletal structure and muscle arrangement have large effects on animal locomotion (Ting and Chiel, 2017), and appropriate models need to be created depending on the motion of interest. In particular, in fast locomotion where inertial effects are larger than viscous ones, body elasticity mainly determines the motion. For example, a spring-loaded inverted pendulum (SLIP) model has been widely used to investigate the characteristics of running in mammals (Full and Koditschek, 1999; Tanase et al., 2015; Adachi et al., 2020; Kamimura et al., 2021) and in cockroaches (Seipel et al., 2004; Spence et al., 2010). Detailed musculoskeletal models have been also used (Proctor and Holmes, 2018). Conversely, in slow locomotion, viscosity plays a dominant role. In stick insects, soon after swing muscle activity stops, swing leg movement ceases (Hooper et al., 2009). The effects of sensory feedback are dominant for slow-walking insects (Daun-Gruhn and Büschges, 2011).

In this study, we focus on relatively slow locomotion to investigate the functional roles of sensory feedback in multi-legged locomotion. We construct a simple mechanical model with flexible body and legs. Specifically, the mechanical model is composed of $(N+1)$ mass points, whose mass is m_i and whose height is x_i $(i = 1, \ldots, N+1)$, as shown in **Figure 1**. The mass points move only vertically and are connected by springs and dampers (all the spring constants are κ and the damper constants are σ). The neutral length of the spring is 0. Each mass point has a massless leg (Leg i), which also moves vertically and whose length is l_i. The ground is modeled as a spring and damper (with spring constant K and damper constant D). The ground is much stiffer than the body spring ($K \gg \kappa$) and the damper coefficient is set to provide overdamping. We used $m_i = m$ for $i = 2, \ldots, N$ and $m_1 = m_{N+1} = m_{\mathrm{B}}$ for the edges, where $m/2 < m_{\mathrm{B}} < m$. The gravitational acceleration is g.

For $N \geq 3$, the equations of motion are given by

$$m_i\ddot{x}_i = \begin{cases} -\kappa\left(x_1 - x_2\right) - \sigma\left(\dot{x}_1 - \dot{x}_2\right) - m_1 g \\ \quad -p_1\left\{K\left(x_1 - l_1\right) + D(\dot{x}_1 - \dot{l}_1)\right\} & i = 1 \\ -\kappa\left(2x_i - x_{i+1} - x_{i-1}\right) - \sigma\left(2\dot{x}_i - \dot{x}_{i+1} - \dot{x}_{i-1}\right) - m_i g \\ \quad -p_i\left\{K\left(x_i - l_i\right) + D(\dot{x}_i - \dot{l}_i)\right\} & i = 2, \ldots, N \\ -\kappa\left(x_{N+1} - x_N\right) - \sigma\left(\dot{x}_{N+1} - \dot{x}_N\right) - m_{N+1} g \\ \quad -p_{N+1}\left\{K\left(x_{N+1} - l_{N+1}\right) + D(\dot{x}_{N+1} - \dot{l}_{N+1})\right\} & i = N+1 \end{cases} \tag{1}$$

where p_i $(i = 1, \ldots, N+1)$ represents whether Leg i is in contact with the ground and is defined by,

$$p_i = \begin{cases} 0 & l_i < x_i \\ 1 & \text{otherwise.} \end{cases} \tag{2}$$

2.2. Control Model

To understand the mechanism that generates rhythmic leg movement, central pattern generators (CPGs) have been well studied (Ijspeert, 2008; Daun-Gruhn and Büschges, 2011) and many modeling approaches are available for CPGs, such as relatively detailed biophysical models based on Hodgkin-Huxley-type neuron models (Rybak et al., 2006; Daun et al., 2009), connectionist models composed of simplified neuron models (e.g., leaky-integrator neurons) (Ijspeert, 2001; Pasemann et al., 2003) and abstract models using van der Pol and Matsuoka oscillators (van der Pol, 1926; Matsuoka, 1987). In contrast, some studies proposed reflex chains in place of CPGs to generate rhythmic leg movement, such as Walknet (Cruse et al., 1998), and others proposed heteroclinic oscillator models to represent intermediate behavior between the CPGs and reflex chains (Shaw et al., 2015).

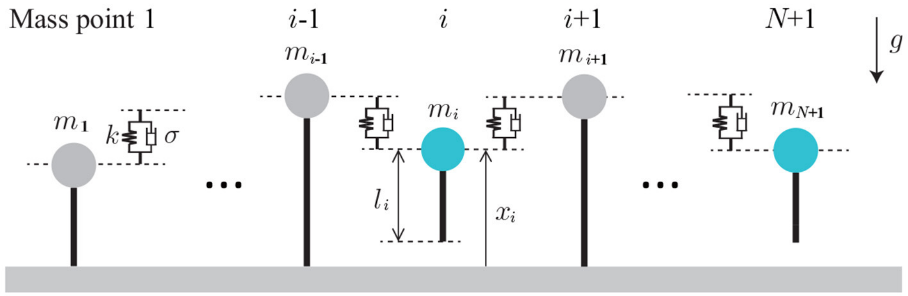

FIGURE 1 | Mechanical model composed of (N+1) mass points. The mass points move only vertically and are connected via springs and dampers. Dotted lines represent the vertical positions of the mass points.

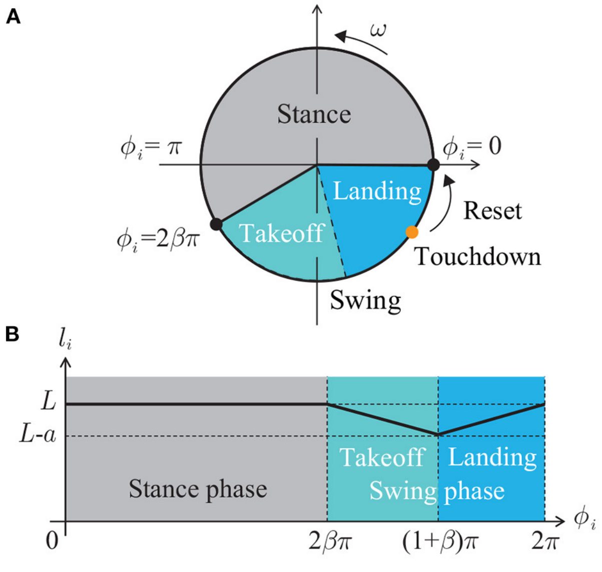

FIGURE 2 | (A) Phase oscillator model. **(B)** Leg length l_i depending on phase ϕ_i.

These models are nonlinear, interact with sensory feedback, and show remarkable adaptation to the environment and prominent replication of animal movement, such as entrainment to limit cycle and extending the timing of the state transition. However, these models are complicated to understand the functional role of embodied sensorimotor interaction for interlimb coordination. We use a simple phase oscillator model developed in our previous studies (Aoi et al., 2017; Ambe et al., 2018) for better understanding of the functional role through the analytical description. Specifically, each leg has a phase oscillator whose phase is $\phi_i \in [0, 2\pi) \pmod{2\pi}$ $(i = 1, \ldots, N+1)$. The leg length l_i is determined by ϕ_i as follows (**Figure 2**):

$$l_i = l(\phi_i) = \begin{cases} L & 0 \le \phi_i \le 2\beta\pi \\ L - a\dfrac{\phi_i - 2\beta\pi}{(1-\beta)\pi} & 2\beta\pi < \phi_i < (1+\beta)\pi \\ L - a\dfrac{2\pi - \phi_i}{(1-\beta)\pi} & (1+\beta)\pi \le \phi_i < 2\pi \end{cases} \quad (3)$$

where L, $a\,(< L)$, and $\beta \in (0.5, 1)$ are the maximum length, the amplitude of the swing leg movement, and the duty factor (ratio between the stance phase and step cycle durations), respectively. We defined the leg length by a piecewise-linear function and used $mg/\kappa < a$ so that the leg is in the air in the swing phase ($\phi_i \in (2\beta\pi, 2\pi)$). While the length is L in the stance phase ($\phi_i \in [0, 2\beta\pi]$), it shortens in the takeoff phase (first half of the swing phase, $\phi_i \in (2\beta\pi, (1+\beta)\pi)$) and lengthens in the landing phase (second half of the swing phase, $\phi_i \in [(1+\beta)\pi, 2\pi)$). The oscillator phase follows the following dynamics:

$$\frac{d\phi_i}{dt} = \omega + y_i, \quad (4)$$

where ω is the basic frequency of locomotion and y_i represents a sensory feedback. We used $\omega \ll \sqrt{\kappa/m_i}$ to make the model walk slowly.

Sensory feedback has been physiologically well studied in insects (Delcomyn, 2004; Büschges et al., 2008). Insects have mechanoreceptors that can sense various information, such as contact with the ground, joint angles, and mechanical load at the nearby leg joint (Tuthill and Wilson, 2016). Especially in stick insects, sensory feedback plays an important role for inter-joint coordination. Strain signals from the trochanter play a major role in shaping thorax-coxa (TC)-joint motoneuronal activity during walking and contribute to the coordination of the TC-joint movement with the stepping pattern of the distal leg joints (Akay et al., 2004). Centipedes also sense load information and stop their periodic leg movements when the terrain is removed (Yasui et al., 2017). Locomotion rhythm resetting and phase shifting in motorneuron activities by sensory feedback and perturbation (phase resetting) has been observed in insects (Büschges, 1995), as well as in mammals (Schomburg et al., 1998; Rybak et al., 2006). Because phase resetting is amenable to mathematical analysis to determine the essential functional role of sensory feedback, this study focuses on phase resetting based on load information. Based on our previous studies (Aoi et al., 2013; Ambe et al., 2015, 2018), we incorporated the phase resetting mechanism as

$$\tau\frac{dy_i}{dt} = -y_i + u_i \quad (5)$$

TABLE 1 | Parameters for simulation.

Parameter	Value	Parameter	Value	Parameter	Value
m_{B} [kg]	0.90	κ [N/m]	100	ω [rad/s]	$0.4 \ll \sqrt{\kappa/m}$
m [kg]	1.0	σ [Ns/m]	$2\sqrt{\kappa}$	g [m/s^2]	9.8
L [m]	1.0	K [N/m]	10^5	τ	0.5
a [m]	0.4	D [Ns/m]	$2\sqrt{K}$	β	0.8

$$u_i = \begin{cases} 0 & 0 \le \phi_i < (1+\beta)\pi \\ (2\pi - \phi_i)\,\delta(t - t_i^i) & (1+\beta)\pi \le \phi_i < 2\pi \end{cases} \tag{6}$$

where t_i^i is the time when Leg i touches the ground and $\delta()$ is Dirac's delta function. When Leg i touches the ground in the landing phase ($(1+\beta)\pi \le \phi_i < 2\pi$), the phase ϕ_i is reset to zero as shown in **Figure 2A**. In the present study, we used a first-order lag system with time constant τ to change the phase value continuously after the phase resetting for the simulation.

Because the leg movements of our model are determined by the oscillation phases, the relative phases between the oscillators $\psi_i \in [0, 2\pi)\ (\mathrm{mod}\ 2\pi)\,(i = 1, \ldots, N)$ explain the gait, which is given by

$$\psi_i = \phi_{i+1} - \phi_i. \tag{7}$$

We investigated where the relative phases converged through the mechanical dynamics (1) and phase dynamics (4).

2.3. Results

We conducted forward dynamic simulations of our model in case of $N = 3$ to find stable gaits. All simulations used the parameters in **Table 1**. To investigate the characteristics of the gaits, we defined a Poincaré section Σ^1 for the relative phases just before Leg 1 touches the ground, where we used $\boldsymbol{\Psi}^1 \equiv [\psi_1^1\ \psi_2^1\ \psi_3^1]^{\mathrm{T}}$ and $()^i$ represents the value just before Leg i touches the ground.

2.3.1. Periodic Solutions

First, we used six sets of the initial relative phases for $\boldsymbol{\Psi}^1$ to investigate if and how they converged. **Figure 3** shows the time profile of the relative phases on Σ^1 for the six sets of the initial relative phases. Some of the relative phases converged to identical values, but others converged to different values. These converged relative phases correspond to periodic solutions. These results suggest that there are many periodic solutions.

To illustrate details of the periodic solutions, **Figure 4A** uses thick colored lines (red, blue, and green) to show the relative phases converged from many initial values ($25 \times 25 \times 25$) for $\boldsymbol{\Psi}^1$. The solutions generally consist of three connected orthogonal line segments and lay close to two planes parallel to the ψ_1^1–ψ_2^1 and ψ_2^1–ψ_3^1 planes. **Figures 4B,C** show the solutions projected onto each plane. Near the connections between line segments, the segments are slightly bent. The three line segments correspond to the source-wave, retrograde-wave, and direct-wave gaits, as investigated below. The thin black line segments represent the analytical approximate solutions obtained in section 3.

Figures 5A–C show the slices of basin of attraction under the conditions $\psi_3^1 = 2(1-\beta)\pi$, π, and $2\beta\pi$, respectively. All the initial values (99×99) converged to one of the three gaits, and the basin of attraction was separated into three parts, each corresponding to one gait type.

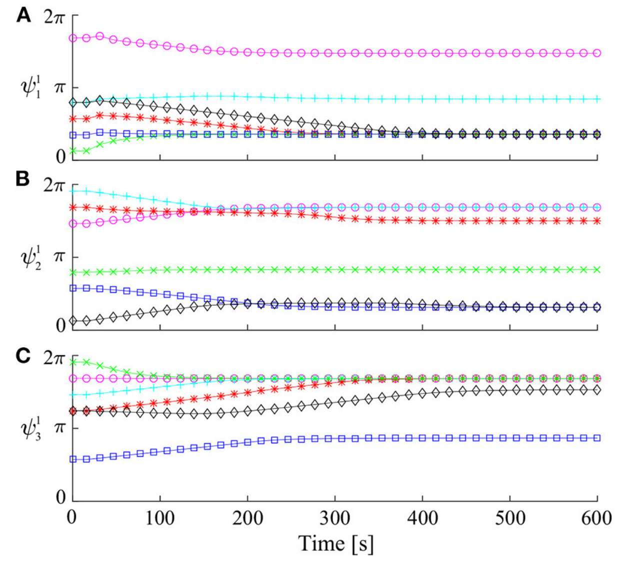

FIGURE 3 | Time profile of relative phases for $\boldsymbol{\Psi}^1$ simulated from six sets of initial values: **(A)** ψ_1^1, **(B)** ψ_2^1, and **(C)** ψ_3^1.

2.3.2. Characteristics of Three Types of Gaits

The obtained periodic solutions were categorized by three gaits: direct-, retrograde-, and source-wave gaits. The direct-wave gait has the following relative phases:

$$\hat{\psi}_1^1 \approx 2(1-\beta)\pi,\ \hat{\psi}_2^1 \approx 2(1-\beta)\pi, 2(1-\beta)\pi \lessapprox \hat{\psi}_3^1 \lessapprox 2\beta\pi$$

where $\hat{()}$ indicates the periodic solution. This gait appears as one line segment, as shown in **Figure 4**. **Figure 6A** shows the footprint diagram for $\hat{\boldsymbol{\Psi}}^1 = [1.13\ \ 0.98\ \ 1.50]^{\mathrm{T}}$ (point a in **Figure 4**). In this gait, the swing leg movement of Legs 1, 2, and 3 propagates from posterior to anterior with the same interval, as shown by red arrows. However, the relative phase of the swing leg movement between Legs 3 and 4 can vary within the range indicated by the violet arrow.

The retrograde-wave gait has the following relative phases:

$$2(1-\beta)\pi \lessapprox \hat{\psi}_1^1 \lessapprox 2\beta\pi,\ \hat{\psi}_2^1 \approx 2\beta\pi,\ \hat{\psi}_3^1 \approx 2\beta\pi.$$

This also appears as one line segment (to be precise, it is slightly curved) in **Figure 4**. **Figure 6B** shows the footprint diagram for $\hat{\boldsymbol{\Psi}}^1 = [3.97\ \ 5.29\ \ 5.29]^{\mathrm{T}}$ (point b in **Figure 4**). In this gait, the swing leg movement of Legs 2, 3, and 4 propagates from anterior to posterior with the same interval, as shown by green arrows. However, the relative phase of the swing leg movement between Legs 1 and 2 can vary in the range indicated by the violet arrow.

The source-wave gait has the following relative phases:

$$\hat{\psi}_1^1 \approx 2(1-\beta)\pi,\ 2(1-\beta)\pi \lessapprox \hat{\psi}_2^1 \lessapprox 2\beta\pi,\ \hat{\psi}_3^1 \approx 2\beta\pi.$$

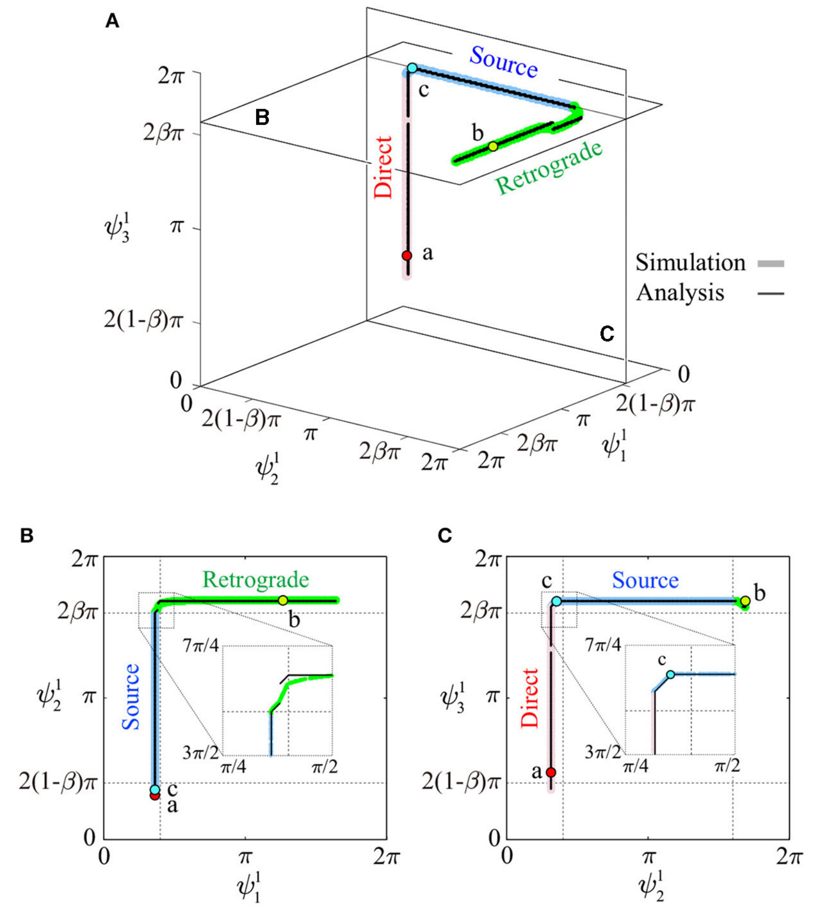

FIGURE 4 | Relative phases for Ψ^1 of periodic solutions: **(A)** shown in ψ_1^1-ψ_2^1-ψ_3^1 space, **(B)** projected to a plane parallel to the ψ_1^1-ψ_2^1 plane, and **(C)** projected to a plane parallel to the ψ_2^1-ψ_3^1 plane. Thick colored lines and thin black lines represent simulated and analytic solutions, respectively. Points a, b, and c are used to show footprint diagrams in **Figure 6**.

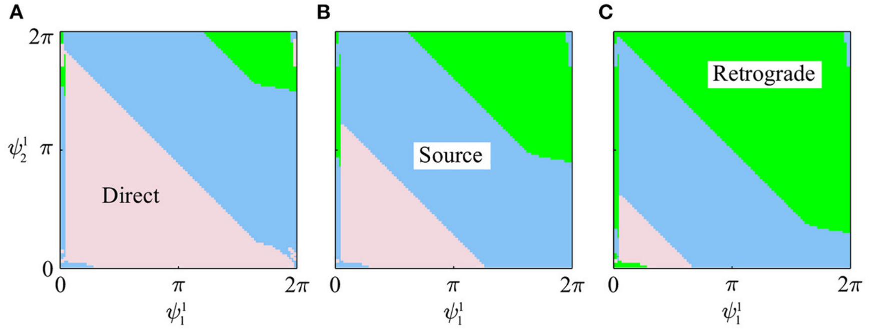

FIGURE 5 | Slices of basin of attraction for three gaits in simulation under three conditions: **(A)** $\psi_3^1 = 2(1-\beta)\pi$, **(B)** $\psi_3^1 = \pi$, and **(C)** $\psi_3^1 = 2\beta\pi$.

This also appears as one line segment (to be precise, it comprises two line segments) in **Figure 4**. **Figure 6C** shows the footprint diagram for $\Psi^1 = [1.13 \quad 1.10 \quad 5.28]^{\mathrm{T}}$ (point c in **Figure 4**). In this gait, the swing leg movement of Legs 1 and 2 propagates from posterior to anterior, as shown by red arrows, while that of Legs 3 and 4 propagates from anterior to posterior as shown by green arrows. However, the relative phase of the swing leg movement between Legs 2 and 3 can vary in the range indicated by the violet arrow.

These three types of gaits were not predetermined, but emerged through the mechanical and sensory interaction. These gaits are represented by line segments for Ψ^1, which are serially connected as shown in **Figure 4**.

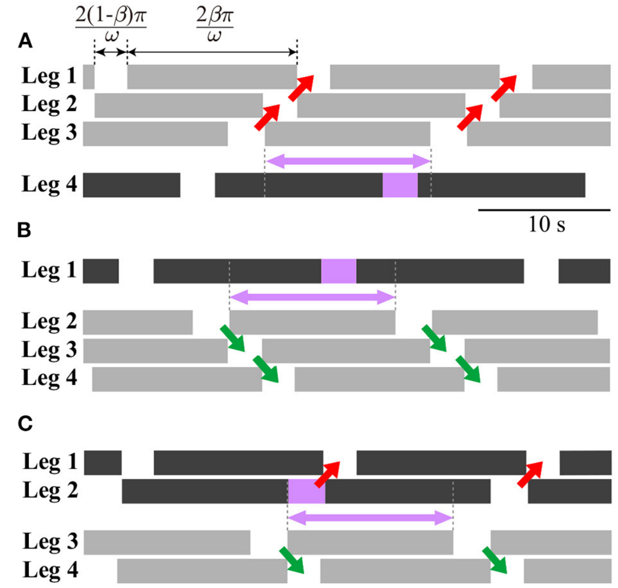

FIGURE 6 | Footprint diagrams of periodic solutions: **(A)** Direct-wave gait (point a in **Figure 4**), **(B)** retrograde-wave gait (point b in **Figure 4**), and **(C)** source-wave gait (point c in **Figure 4**). Black bars can change to gray bars as long as the violet box is in the range indicated by the violet arrow.

3. ANALYSIS

Three types of gaits were obtained via the mechanical and sensory interaction in simulations with a multi-mass spring model. Although the models described in section 2 used four mass points, these gaits are expected to appear in models with more mass points (attached **Supplementary Video 1**). **Figure 7** shows the three types of gaits for $N+1$ mass points. For the direct-wave gait (**Figure 7A**), the swing leg movements propagate anteriorly, where there is only one swing leg within one wavelength. While the phase difference between the neighboring legs for Legs 1 to N is around $2(1-\beta)\pi$, that between Legs N and $N+1$ is not unique and is variable from $2(1-\beta)\pi$ to $2\beta\pi$. For the retrograde-wave gait (**Figure 7B**), the swing leg movements propagate posteriorly, where there is only one swing leg within one wavelength. While the phase difference between the neighboring legs for Legs 2 to $N+1$ is around $2\beta\pi$, that between Legs 1 and 2 is not unique and is variable from $2(1-\beta)\pi$ to $2\beta\pi$. For the source-wave gait (**Figure 7C**), while the anterior swing leg movements (Legs 1 to $k-1$, $k \in [2,N]$) propagate anteriorly, those of the posterior part (Legs k to $N+1$) propagate posteriorly. Although the phase differences of the neighboring legs for the anterior and posterior parts are around $2(1-\beta)\pi$ and $2\beta\pi$, respectively, that between Legs $k-1$ and k is not unique and is variable from $2(1-\beta)\pi$ to $2\beta\pi$. To clarify the mechanism for generating these three gaits, we simplified our model by some physical assumptions to derive analytical solutions.

A concrete way to derive the analytical solutions is as follows. First, we simplify our mechanical and controller models. In particular, we assume that the natural frequencies of the mass points are larger than the gait frequency so that the vertical position of the mass points x_i $(i = 1, \ldots, N+1)$ is determined uniquely by the oscillator phase ϕ_i in section 3.1. We also assume that the time constant of our control model is smaller than the gait cycle duration found in section 3.2, which allows the Poincaré map to be obtained by determining the phase resetting value ϕ_i^i. These assumptions give a touchdown relation between ϕ_i^i, ϕ_{i-1}^i, and ϕ_{i+1}^i. In section 3.3, we determine the order of the touchdown events in the case of the source-wave gait based on the simulation results and rewrite the touchdown relation by $\phi_{i-1}^{i-1}, \phi_i^i, \phi_{i+1}^{i+1}$, and the relative phases between the oscillators, which gives periodic solutions of the source-wave gait. In section 3.4, we investigate the stability of the periodic solutions. In section 3.5, we derive the periodic solutions and stability of the direct-wave gait from the front–rear symmetry. In section 3.6, we compare the analytical results with the simulation results. In section 3.7, we describe the geometrical meaning of the obtained solutions.

3.1. Simplification of Mechanical Model

We used $\omega \ll \sqrt{\kappa/m_i}$ in (4) to make the model walk slowly in the simulation. Thus, we ignored the dynamics of the mass points and focused only on the equilibrium of forces by replacing the ground reaction forces with unknown variables. Then, (1) becomes

$$\begin{cases} \kappa(x_2-x_1)+R_1 = m_1 g & i=1 \\ \kappa(x_{i-1}-x_i)+\kappa(x_{i+1}-x_i)+R_i = m_i g & i \in [2,N] \\ \kappa(x_N-x_{N+1})+R_{N+1} = m_{N+1} g & i=N+1 \end{cases}, \qquad (8)$$

where R_i is the ground reaction force. The number of unknown variables is $2(N+1)$; $x_1, \ldots, x_{N+1}$ and $R_1, \ldots, R_{N+1}$. These variables depend on the foot contact conditions. In particular, when Leg i is in the air, $x_i \geq l(\phi_i)$ and $R_i = 0$. In contrast, when Leg i is in contact with the ground, $x_i = l(\phi_i)$ and $R_i > 0$. Therefore, when ϕ_i and foot contact conditions for all legs are given, the number of the unknown variables is reduced to $N+1$ and the unknown variables are solved by (8).

3.2. Simplification of Control Model

Although we used a first-order lag system in (9) for the simulation, the time constant τ is small compared with the gait period. Therefore, we set $\tau = 0$, which reduces (4) to

$$\frac{d\phi_i}{dt} = \omega + u_i. \qquad (9)$$

This gives

$$\frac{d\psi_i}{dt} = u_{i+1} - u_i \quad i = 1, \ldots, N. \qquad (10)$$

A Poincaré section Σ^j $(j = 1, \ldots, N+1)$ was defined for the relative phases just before the touchdown of Leg j and we used $\boldsymbol{\Psi}^j \equiv [\psi_1^j \ \ \psi_2^j \ \ \ldots \ \ \psi_N^j]^{\mathrm{T}}$. The Poincaré map for Σ^j was given by integrating (10) for one period. Under the assumption that

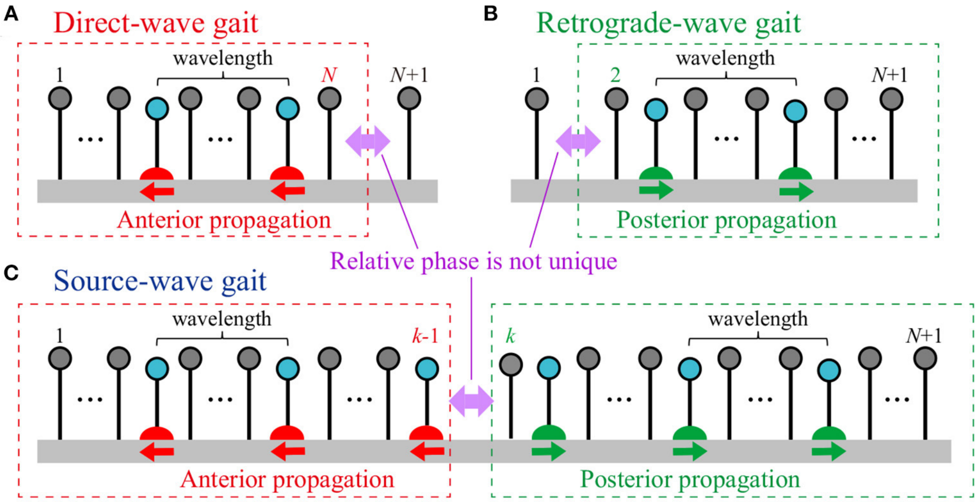

FIGURE 7 | Three types of gaits for $N+1$ mass points: **(A)** Direct-wave, **(B)** retrograde-wave, and **(C)** source-wave gaits. In the direct-wave (retrograde-wave) gait, while the swing leg movements of Legs 1 to N (Legs 2 to $N+1$) propagate anteriorly (posteriorly) with a constant relative phase, the relative phase between Legs N and $N+1$ (Legs 1 and 2) is not unique. In the source-wave gait, while the swing leg movements of the anterior part (Legs 1 to $k-1$, $k \in [2, N]$) propagate anteriorly, those of the posterior part (Legs k to $N+1$) propagate posteriorly. The relative phase between Legs $k-1$ and k is not unique. In these three gaits, there is only one swing leg within one wavelength.

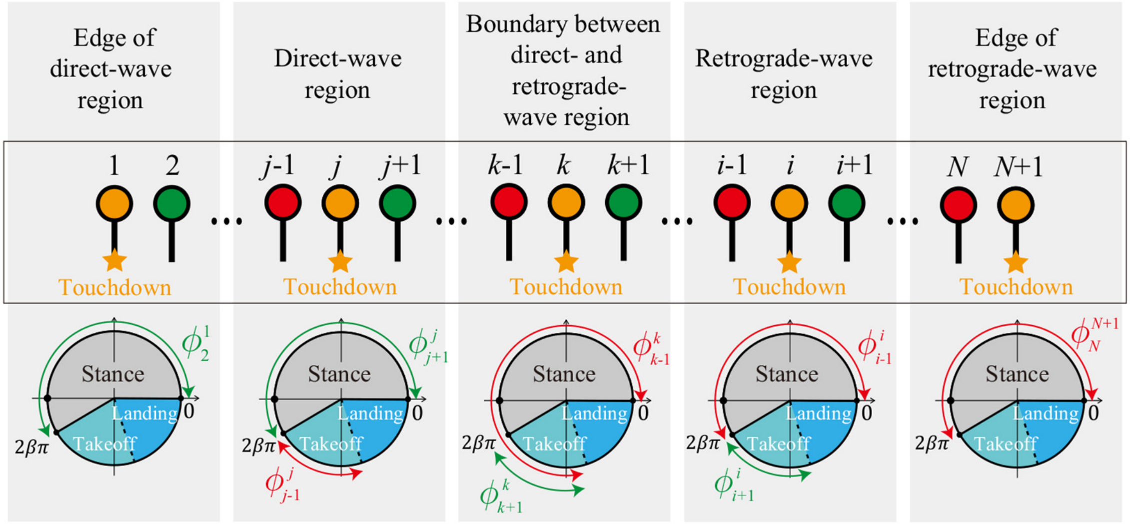

FIGURE 8 | Assumptions for the phases of the neighboring legs at each touchdown event for the source-wave gait.

each leg experiences phase resetting once each period, the map is given by

$$\psi_i^j \mapsto \psi_i^j + \phi_i^i - \phi_{i+1}^{i+1} \quad i = 1, \dots, N. \tag{11}$$

To obtain the Poincaré map, ϕ_i^i ($i = 1, \dots, N+1$) needs to be determined.

Based on the periodic solutions, we assume that there is only one swing leg within one wavelength, just before Leg i touches the ground ($i = 1, \dots, N+1$), the neighboring legs (Legs $i-1$ and $i+1$) are in contact with the ground. Therefore, $x_{i-1} = l(\phi_{i-1}^i)$, $x_i = l(\phi_i^i)$, $x_{i+1} = l(\phi_{i+1}^i)$, $R_{i-1} > 0$, $R_i = 0$, and $R_{i+1} > 0$ are satisfied just before the touchdown of Leg i. By substituting these variables into (8), we obtain

$$l(\phi_i^i) = \begin{cases} f_B(\phi_2^i) & i = 1 \\ f(\phi_{i-1}^i, \phi_{i+1}^i) & i \in [2, N] \\ f_B(\phi_N^i) & i = N+1 \end{cases}, \tag{12}$$

where

$$f(\phi_h, \phi_f) = \frac{1}{2}\left\{l(\phi_h) + l(\phi_f)\right\} - \frac{mg}{2\kappa} \tag{13}$$

$$f_{\mathrm{B}}(\phi) = l(\phi) - \frac{m_{\mathrm{B}}g}{\kappa}.$$

The substitution of (12) into (3) gives one relation between ϕ^i_{i-1}, ϕ^i_i, and ϕ^i_{i+1} for each i ($i = 1, \ldots, N+1$). Because we can write ϕ^i_{i-1} and ϕ^i_{i+1} as $\phi^{i-1}_{i-1}, \phi^i_i, \phi^{i+1}_{i+1}$, and $\mathbf{\Psi}^j$, as discussed in the following section, ϕ^i_i is obtained by $\mathbf{\Psi}^j$. As a result, we obtain the Poincaré map from (11).

3.3. Analytical Solution of Source-Wave Gait

Here, we derive the periodic solution of the source-wave gait characterized by Leg $k \in [2, N]$ that determines the boundary between the direct- and retrograde-wave regions (**Figure 7C**). The solution of the source-wave gait is useful for deriving those of the direct- and retrograde-wave gaits. In particular, the solution of the retrograde-wave gait is obtained by $k=2$ for the solution of the source-wave gait (**Figure 7B**). However, note that $k=N+1$ does not fully explain the solution of the direct-wave gait, which is instead derived by the front–rear symmetry and the solution of the retrograde-wave gait, as explained in section 3.5.

To derive the periodic solution of the source-wave gait, we first define the Poincaré section as Σ^k and transform the right-hand side of (12) to be represented by the relative phases $\mathbf{\Psi}^k$ and the touchdown phase ϕ^i_i ($i = 1, \ldots, N+1$). For that purpose, we assume some conditions for the phases of the neighboring legs at each touchdown event, determine the order of the touchdown events, and represent the relative phases of the neighboring legs of the touchdown leg using $\mathbf{\Psi}^k$ and ϕ^i_i by accounting for the effects of phase resetting. Second, we derive the conditions of ϕ^i_i for the periodicity. The reduced equation of (12) and the periodicity conditions yield the periodic solution.

Based on the simulation results obtained in section 2, we assume the following conditions for the phases of the neighboring legs at each touchdown event (**Figure 8**). For the touchdown of Leg k (boundary between direct- and retrograde-wave regions), ϕ^k_{k-1} is in the stance or takeoff phase ($0 \leq \phi^k_{k-1} < (1+\beta)\pi$), and ϕ^k_{k+1} is in the takeoff phase ($2\beta\pi \leq \phi^k_{k+1} < (1+\beta)\pi$). For the touchdown of Leg $j \in [2, k-1]$ (direct-wave region), ϕ^j_{j-1} is in the takeoff phase ($2\beta\pi \leq \phi^j_{j-1} < (1+\beta)\pi$) and ϕ^j_{j+1} is in the stance phase ($0 \leq \phi^j_{j+1} < 2\beta\pi$) because the swing movements of Legs 1 to $k-1$ propagate anteriorly. For the touchdown of Leg $i \in [k+1, N]$ (retrograde-wave region), ϕ^i_{i-1} is in the stance phase ($0 \leq \phi^i_{i-1} < 2\beta\pi$) and ϕ^i_{i+1} is in the takeoff phase ($2\beta\pi \leq \phi^i_{i+1} < (1+\beta)\pi$) because the swing movements of Legs k to $N+1$ propagate posteriorly. For the touchdown of Legs 1 and $N+1$ (edges of direct- and retrograde-wave regions), ϕ^1_2 and ϕ^{N+1}_N are in the stance phases ($0 \leq \phi^1_2, \phi^{N+1}_N < 2\beta\pi$).

These assumptions determine the order of touchdown events. In the retrograde-wave region, suppose that $n (> k)$ is the minimum value that satisfies $\phi^k_n \in (\phi^{n-1}_n, \phi^n_n]$, which means that Legs $(n-1)$, k, and n touch the ground sequentially (**Figure 9A**). Legs k to n correspond to almost one wavelength of the gait. Because the swing movement propagates posteriorly from Legs k to $N+1$, Leg n is in the swing phase when Leg k touches down. Thus, the order of touchdown events for Legs k to n is determined as being in the order k, n, $k+1$, $k+2$, $k+3$, …, $n-1$, as shown in **Figure 9A**. The order of touchdown events in the direct-wave region is determined similarly.

When the order of touchdown events is determined, the relative phases ψ^i_{i-1} and ψ^i_i just before touchdown of Leg i can be represented using $\mathbf{\Psi}^k$ and ϕ^{i-1}_{i-1}, and ϕ^{i+1}_{i+1} by accounting for the effects of phase resetting. Specifically, because phase resetting at each touchdown changes only the oscillator phase of the touchdown leg and the relative phases of the neighboring legs, ψ^i_{i-1} and ψ^i_i just before touchdown of Leg i can be represented using $\mathbf{\Psi}^k$, ϕ^{i-1}_{i-1}, and ϕ^{i+1}_{i+1}, depending on the experiences of the leg touchdowns. In the case of the retrograde-wave region, the evolution of the relative phases for Legs k to n at each touchdown event can be written as **Figure 9B**. For $i = k$ and n, ψ^i_{i-1} and ψ^i_i are given by $\psi^i_{i-1} = \psi^k_{i-1}$ and $\psi^i_i = \psi^k_i$, respectively (highlighted in orange at the touchdowns of Legs k and n in **Figure 9B**), because both neighboring legs do not experience phase resetting in the period between the touchdown events of Legs k and n. As a result, $\phi^i_{i-1} = \phi^i_i - \psi^k_{i-1}$ and $\phi^i_{i+1} = \phi^i_i + \psi^k_i - 2\pi$ (ϕ^i_{i+1} is subtracted by 2π to satisfy $0 \leq \phi^i_{i+1} < 2\pi$) are satisfied because $\psi^i_{i-1} = \phi^i_i - \phi^i_{i-1}$ and $\psi^i_i = \phi^i_{i+1} - \phi^i_i$. For $i \in [k+1, n-2]$, ψ^i_{i-1} and ψ^i_i are given by $\psi^i_{i-1} = \psi^k_{i-1} - (2\pi - \phi^{i-1}_{i-1})$ and $\psi^i_i = \psi^k_i$, respectively (highlighted in orange at the touchdown of Leg $k+1$ for $i = k+1$ in **Figure 9B**), because only the posterior Leg $i-1$ experiences phase resetting in the period between the touchdown events of Legs k and i. As a result, $\phi^i_{i-1} = \phi^i_i - \psi^k_{i-1} + 2\pi - \phi^{i-1}_{i-1}$ and $\phi^i_{i+1} = \phi^i_i + \psi^k_i - 2\pi$ are satisfied. For $i = n-1$, ψ^i_{i-1} and ψ^i_i are given by $\psi^i_{i-1} = \psi^k_{i-1} - (2\pi - \phi^{i-1}_{i-1})$ and $\psi^i_i = \psi^k_i + (2\pi - \phi^{i+1}_{i+1})$, respectively (highlighted in orange at the touchdown of Leg $n-1$ in **Figure 9B**), because both neighboring legs experience phase resetting in the interval between the touchdown events of Legs k and $n-1$. As a result, $\phi^i_{i-1} = \phi^i_i - \psi^k_{i-1} + 2\pi - \phi^{i-1}_{i-1}$ and $\phi^i_{i+1} = \phi^i_i + \psi^k_i - \phi^{i+1}_{i+1}$ are satisfied. This means that ϕ^i_{i-1} and ϕ^i_{i+1} can be represented by $\mathbf{\Psi}^k$, ϕ^{i-1}_{i-1}, ϕ^i_i, and ϕ^{i+1}_{i+1}. These analyses are also applicable to the direct-wave region.

By using these results, the right-hand side of (12) can be rewritten using ψ^k_i ($i=1, \ldots, N$) and ϕ^i_i ($i=1, \ldots, N+1$) as

$$l(\phi^i_i) = \begin{cases} f_{\mathrm{B}}(\phi^1_1 + \psi^k_1 - 2\pi) & i \in S^k_1 \\ f_{\mathrm{B}}(\phi^1_1 + \psi^k_1 - \phi^2_2) & i \in S^k_2 \\ f(\phi^i_i - \psi^k_{i-1},\ \phi^i_i + \psi^k_i - 2\pi) & i \in S^k_3 \\ f(\phi^i_i - \psi^k_{i-1} + 2\pi - \phi^{i-1}_{i-1},\ \phi^i_i + \psi^k_i - \phi^{i+1}_{i+1}) & i \in S^k_4 \\ f(\phi^i_i - \psi^k_{i-1},\ \phi^i_i + \psi^k_i - \phi^{i+1}_{i+1}) & i \in S^k_5 \\ f(\phi^i_i - \psi^k_{i-1} + 2\pi - \phi^{i-1}_{i-1},\ \phi^i_i + \psi^k_i - 2\pi) & i \in S^k_6 \\ f_{\mathrm{B}}(\phi^{N+1}_{N+1} - \psi^k_N) & i \in S^k_7 \\ f_{\mathrm{B}}(\phi^{N+1}_{N+1} - \psi^k_N + 2\pi - \phi^N_N) & i \in S^k_8 \end{cases} \tag{14}$$

where S^k_{1-8} are classified based on whether the neighboring legs (Legs $i-1$ and $i+1$) of Leg i experience phase resetting in the interval between the touchdown events of Legs k and i, as shown in **Table 2**. Specifically, $S^k_{1,2,7,8}$ are for $i = 1$ and $N+1$, which are given by

$$S^k_1 = \{i \mid i = 1\} \cap \{i \mid \phi^k_i \in (\phi^{i+1}_i, \phi^i_i]\}$$

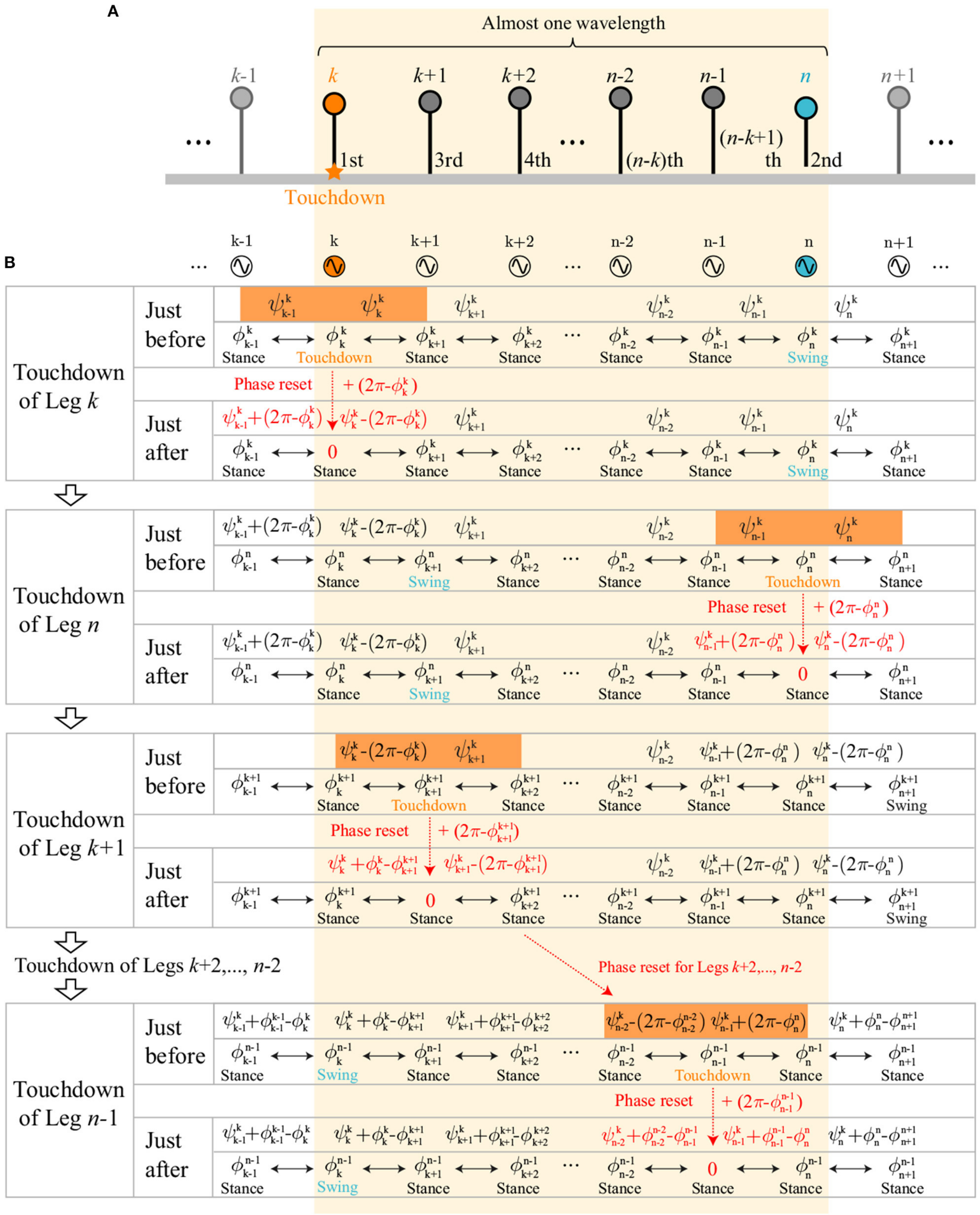

FIGURE 9 | Evolution of oscillator phases within one wavelength: **(A)** Order of touchdown events of Legs *k* to *n* in the retrograde-wave region. Legs *k*, *n*, *k*+1, *k*+2, *k*+3, . . . , *n*−1 touch down sequentially. **(B)** Evolution of oscillator phases and relative phases at touchdown events of Legs *k* to *n*. Phase resetting at each touchdown changes only the oscillator phase of the touchdown leg and the relative phases of the neighboring legs. ψ_{i-1}^{i} and ψ_{i}^{i} just before the touchdown of Leg *i* ($i = k, n, k+1, k+2, \ldots, n-2, n-1$) are represented by $\boldsymbol{\Psi}^{k}$, ϕ_{i-1}^{i-1}, and ϕ_{i+1}^{i+1}, as highlighted in orange.

TABLE 2 | Classification of sets S^k_{1-8}.

Set	Experience of phase resetting Leg $i-1$ (fore side)	 Leg $i+1$ (hind side)
S^k_1	–	No
S^k_2	–	Yes
S^k_3	No	No
S^k_4	Yes	Yes
S^k_5	No	Yes
S^k_6	Yes	No
S^k_7	No	–
S^k_8	Yes	–

$$\begin{aligned} S^k_2 &= \{i \mid i = 1\} \cap \{i \mid i \notin S^k_1\} \\ S^k_7 &= \{i \mid i = N+1\} \cap \{i \mid \phi^k_i \in (\phi^{i-1}_i, \phi^i_i]\} \\ S^k_8 &= \{i \mid i = N+1\} \cap \{i \mid i \notin S^k_7\}, \end{aligned}$$

$S^k_{3,4,5,6}$ are for $i = 2$ to N, which are given by

$$\begin{aligned} S^k_3 &= \{i \mid i = k\} \cup \{i \in [2, k-1] \mid \phi^k_i \in (\phi^{i+1}_i, \phi^i_i]\} \\ &\quad \cup \{i \in [k+1, N] \mid \phi^k_i \in (\phi^{i-1}_i, \phi^i_i]\} \\ S^k_4 &= \{i \in [2, k-1] \mid \phi^k_{i-1} \in (\phi^i_{i-1}, \phi^{i-1}_{i-1}]\} \\ &\quad \cup \{i \in [k+1, N] \mid \phi^k_{i+1} \in (\phi^i_{i+1}, \phi^{i+1}_{i+1}]\} \\ S^k_5 &= \{i \in [2, k-1] \mid i \notin S^k_3 \text{ and } i \notin S^k_4\} \\ S^k_6 &= \{i \in [k+1, N] \mid i \notin S^k_3 \text{ and } i \notin S^k_4\}. \end{aligned}$$

From (11), periodic solutions must satisfy

$$\hat{\phi}^1_1 = \hat{\phi}^2_2 = \cdots = \hat{\phi}^{N+1}_{N+1} \equiv \hat{\phi}^{\mathrm{td}}. \tag{15}$$

This means that the touchdown phase of all oscillators equals $\hat{\phi}^{\mathrm{td}}$. From (14) and (15), we obtain the periodic solution by $\hat{\phi}^{\mathrm{td}}$ and $\hat{\psi}^k_i$ $(i = 1, \ldots, N)$ as follows:

$$\hat{\phi}^{\mathrm{td}} = 2\pi - m_{\mathrm{B}} b \tag{16}$$

$$\hat{\psi}^k_i = \begin{cases} \hat{\psi}^k_{k-1} & i = k-1 \\ 2(1-\beta)\pi - (2m_{\mathrm{B}} - m)b & i \in T^k_1 \\ 2(1-\beta)\pi - (3m_{\mathrm{B}} - m)b & i \in [1, k-2] \text{ and } i \notin T^k_1 \\ \hat{\psi}^k_k & i = k \\ 2\beta\pi + (2m_{\mathrm{B}} - m)b & i+1 \in T^k_2 \\ 2\beta\pi + (3m_{\mathrm{B}} - m)b & \text{otherwise,} \end{cases} \tag{17}$$

where $b = ((1-\beta)g\pi)/(\kappa a)$. The first row, the following two rows, and the remaining rows of the right-hand side of (17) represent the relative phases on the boundary, in the direct-wave region, and in the retrograde-wave region, respectively. The sets $T^k_{1,2}$ are given by

$$\begin{aligned} T^k_1 &= \{i \in [1, k-2] | 2\beta\pi + (2m_{\mathrm{B}} - m)b < \hat{\phi}^k_i \le \hat{\phi}^{\mathrm{td}}\} \\ T^k_2 &= \{i \in [k+2, N+1] | 2\beta\pi + (2m_{\mathrm{B}} - m)b < \hat{\phi}^k_i \le \hat{\phi}^{\mathrm{td}}\}. \end{aligned} \tag{18}$$

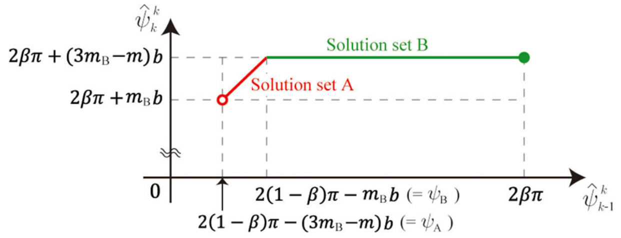

FIGURE 10 | Relation between $\hat{\psi}^k_{k-1}$ and $\hat{\psi}^k_k$.

T^k_1 is the set of legs (Leg i) in the direct-wave region whose neighboring legs (Legs $i-1$ and $i+1$) do not experience phase resetting between the touchdowns of Legs k and i (i.e., S^k_3 in the direct-wave region). T^k_2 is the set of legs (Leg i) in the retrograde-wave region whose neighboring legs (Legs $i-1$ and $i+1$) do not experience phase resetting between the touchdowns of Legs k and i (i.e., S^k_3 in the retrograde-wave region). $\hat{\psi}^k_{k-1}$ is not determined uniquely but satisfies

$$2(1-\beta)\pi - (3m_{\mathrm{B}} - m)b < \hat{\psi}^k_{k-1} \le 2\beta\pi. \tag{19}$$

This non-uniqueness is because the length of Leg i is constant in the stance phase (i.e., $l(\phi_i) = L$, which does not determine ϕ_i uniquely). $\hat{\psi}^k_k$ is represented using $\hat{\psi}^k_{k-1}$ as

$$\hat{\psi}^k_k = \begin{cases} \hat{\psi}^k_{k-1} + (4\beta - 2)\pi + (4m_{\mathrm{B}} - m)b & \psi_{\mathrm{A}} < \hat{\psi}^k_{k-1} < \psi_{\mathrm{B}} \\ 2\beta\pi + (3m_{\mathrm{B}} - m)b & \psi_{\mathrm{B}} \le \hat{\psi}^k_{k-1} \le 2\beta\pi \end{cases} \tag{20}$$

where $\psi_{\mathrm{A}} = 2(1-\beta)\pi - (3m_{\mathrm{B}} - m)b$ and $\psi_{\mathrm{B}} = 2(1-\beta)\pi - m_{\mathrm{B}} b$. Therefore, the relationship of $\hat{\psi}^k_{k-1}$ and $\hat{\psi}^k_k$ is explained by two connected segments, as shown in **Figure 10**. We call these segments solution sets A and B. Note that solution set A is smaller than solution set B, as shown in **Figure 4**, because $\kappa \gg 1$.

3.4. Stability of Source-Wave Gait

To discuss stability, we added perturbation $\Delta\psi^k_i$ $(i = 1, \ldots, N)$ to the obtained periodic solutions on Σ^k and evaluated the linear stability by analytically calculating the linear map of perturbation:

$$\Delta\boldsymbol{\Psi}^k \mapsto P_k \Delta\boldsymbol{\Psi}^k, \tag{21}$$

where $\Delta\boldsymbol{\Psi}^k = [\Delta\psi^k_1 \, \Delta\psi^k_2 \, \ldots \, \Delta\psi^k_N]^T$, and $P_k \in \mathbb{R}^{N \times N}$ is the Jacobian matrix of the Poincaré map. We assumed that the perturbation is too small to change the order of touchdown events and the sets S_i.

When we write the perturbed touchdown phase of Leg i as $\hat{\phi}^{\mathrm{td}} + \Delta\phi^i_i$ and substitute $\psi^k_i = \hat{\psi}^k_i + \Delta\psi^k_i$ and $\phi^i_i = \hat{\phi}^{\mathrm{td}} + \Delta\phi^i_i$ into (14), $\Delta\phi^i_i$ $(i = 1, \ldots, N+1)$ can be represented with $\Delta\psi^k_i$. The matrix P_k is derived by substituting $\phi^i_i = \hat{\phi}^{\mathrm{td}} + \Delta\phi^i_i$ into (11). The eigenvalues $\lambda_{\mathrm{S}k}$ of P_k for the source-wave gait are derived depending on solution sets A and B by

$$\lambda_{\mathrm{S}k} = \begin{cases} \{1, \, 1/2, \, 2/3, \, \ldots, \, 2/3\} & \psi_{\mathrm{A}} < \hat{\psi}^k_{k-1} < \psi_{\mathrm{B}} \\ \{1, \, 2/3, \, 2/3, \, \ldots, \, 2/3\} & \psi_{\mathrm{B}} \le \hat{\psi}^k_{k-1} \le 2\beta\pi \end{cases} \tag{22}$$

There is only one eigenvalue of 1 for both solution sets due to the non-uniqueness. However, the other eigenvalues are <1, which means that any initial points near the solution set will converge to the solution set.

3.5. Analytical Solution and Stability of Direct-Wave Gait

The solution of the direct-wave gait cannot be derived by substituting $k = N+1$ for those of the source-wave gaits. This is because part of the assumption regarding the phases of neighboring legs (specifically, that ϕ_{k-1}^k is in the takeoff phase, as in the middle figure of **Figure 8**) is not correct when $k=N+1$ for the direct-wave gait. Thus, we derive the solution of the direct-wave gait from the front–rear symmetry and the solution of the retrograde-wave gait.

We denote the flow of the oscillator phase i ($i = 1, \ldots, N+1$) with the initial value $(\tilde{\phi}_1^k, \tilde{\phi}_2^k, \ldots, \tilde{\phi}_{N+1}^k)$ just before the touchdown of Leg k by $\Phi_i(t;\ \tilde{\phi}_1^k, \tilde{\phi}_2^k, \ldots, \tilde{\phi}_{N+1}^k)$. From the front–rear symmetry of our model, the following equation is satisfied for the initial phases such that $\tilde{\phi}_i^k = \tilde{\phi}_i^{N+2-k}$ for $i = 1, \ldots, N+1$:

$$\begin{aligned}&\Phi_i(t;\ \tilde{\phi}_1^k, \tilde{\phi}_2^k, \ldots, \tilde{\phi}_{N+1}^k)\\ &\quad = \Phi_{N+2-i}(t;\ \tilde{\phi}_{N+1}^{N+2-k}, \tilde{\phi}_N^{N+2-k}, \ldots, \qquad \tilde{\phi}_1^{N+2-k})\end{aligned} \tag{23}$$

The periodic solution of the direct-wave gait $\hat{\psi}_i^N$ ($i = 1, \ldots, N$) on Σ^N, where $\hat{\phi}^{\mathrm{td}}$ is the same as (16), is derived from solution set B of the retrograde-wave gait ($k = 2$ for the source-wave gait) using the symmetry condition (symmetrical solution for solution set A of the retrograde-wave gait equals solution set A of the source-wave gait with $k = N$). Specifically, the substitution of $k = N$ into (23) yields $\Phi_i(t;\ \tilde{\phi}_{N+1}^N, \ldots, \tilde{\phi}_1^N) = \Phi_{N+2-i}(t;\ \tilde{\phi}_1^2, \ldots, \tilde{\phi}_{N+1}^2)$. When the periodic solution $\hat{\phi}_j^N$ ($j = 1, \ldots, N+1$) is used for the initial value $\tilde{\phi}_j^N$, we obtain $\hat{\phi}_i^N = \hat{\phi}_{N+2-i}^2$ ($i = 1, \ldots, N$). This yields $\hat{\psi}_i^N = 2\pi - \hat{\psi}_{N+1-i}^2$ because $\hat{\psi}_i^N = \hat{\phi}_{i+1}^N - \hat{\phi}_i^N$. By substituting solution set B of the retrograde-wave gait $\hat{\psi}_{N+1-i}^2$ ($k = 2$ in (17)), we obtain the solution of the direct-wave gait as

$$\hat{\psi}_i^N = \begin{cases}\hat{\psi}_N^N & i = N\\ 2(1-\beta)\pi - (2m_{\mathrm{B}} - m)b & i \in T_1^N\\ 2(1-\beta)\pi - (3m_{\mathrm{B}} - m)b & \text{otherwise.}\end{cases} \tag{24}$$

where $\hat{\psi}_N^N$ is an arbitrary constant fulfilling

$$2(1-\beta)\pi \le \hat{\psi}_N^N \le 2\beta\pi + m_{\mathrm{B}} b. \tag{25}$$

The linear stability of the solution can also be calculated using the symmetry condition (23). The symmetry condition gives the relation $\Delta\psi_i^N = -\Delta\psi_{N+1-i}^2$, which is represented as $\Delta\mathbf{\Psi}^N = -Q\Delta\mathbf{\Psi}^2$, where the matrix Q is an anti-diagonal matrix with all the anti-diagonal elements of 1. By using Q, the Jacobian matrix of the Poincaré map of the direct-wave gait P_{D} is calculated as $P_{\mathrm{D}} = QP_2Q^{-1}$. Thus, the eigenvalues λ_{D} of P_{D} are obtained by those of P_2 as

$$\lambda_{\mathrm{D}} = \{1,\ 2/3,\ 2/3,\ \ldots,\ 2/3\}. \tag{26}$$

There is only one eigenvalue of 1 due to the non-uniqueness. However, the other eigenvalues are <1, which means that any initial points near the solution set will converge to the solution set.

All the solution sets we derived were connected serially as a chain. Specifically, the boundary on solution set A of the source-wave gait with $k = i$ (left side of **Figure 10**) and the boundary on solution set B of the source-wave gait with $k = i+1$ (right side of **Figure 10**) are connected, as shown in **Figure 11A**. In addition, the boundary on solution set A of the source-wave gait with $k = i+1$ and the boundary on solution set B of the source-wave gait with $k = i+2$ are connected, as shown in **Figure 11A**. Furthermore, the boundary on solution set A of the source-wave gait with $k = N$ and the boundary of the direct-wave gait are connected, as shown in **Figure 11B**. The boundary on solution set B of the source-wave gait with $k=3$ and the boundary on solution set A of the source-wave gait with $k=2$ (retrograde-wave gait) are connected, as shown in **Figure 11C**. Thus, the obtained solution sets consist of many connected segments constrained in different planes, and the boundaries of the whole solution set correspond to the direct- and retrograde-wave gaits. Note that discontinuous jumps may exist on the analytical solution sets, as highlighted in **Figure 11A**. The jumps occur when the elements of the sets T_1 and T_2 change, that is, when the order of touchdown events of the neighboring legs changes. For example, when Leg s becomes an element of T_1^k, that is, when the order of touchdown events of the neighboring legs changes from Legs $s+1$, s, and $s-1$ to Legs s, $s-1$, and $s+1$, the relative phase $\hat{\psi}_s^k$ jumps from $2(1-\beta)\pi - (3m_{\mathrm{B}} - m)b$ to $2(1-\beta)\pi - (2m_{\mathrm{B}} - m)b$, as shown in (17).

3.6. Comparison With Simulation Results

To validate the analytical results, we compared the obtained solutions for $N = 3$ with the simulation results on Σ^1 in **Figure 4**, where the analytical solutions were derived using the same parameters of the simulation. In both the simulation and analytical results, source- and retrograde-wave gaits show two segments as solution sets A and B (although some discontinuous jumps appear). The segments of three gaits are serially connected, and their edges correspond to the direct- and retrograde-wave gaits. These characteristics were identical between the analytical and simulation results. Furthermore, the maximum distance between the solution sets of the simulation and analytical results was only 0.11 (1.8% of 2π). The errors mainly came from discontinuous jumps in the analytical solution, which are not shown in the simulation, because the first-order lag system in (5) smoothed the jumps.

3.7. Geometrical Features of Solutions

From the analytical solution (17), we found that the swing movements of the source-wave gait are isotropic waves and propagate forward from Leg $k-1$ (direct-wave region) and backward from Leg k (retrograde-wave region) with constant speeds. This gait is similar to that observed in millipedes (Tamura et al., 2016). When the interval between the legs is η, the wavelength ξ and velocity v of the swing movement are

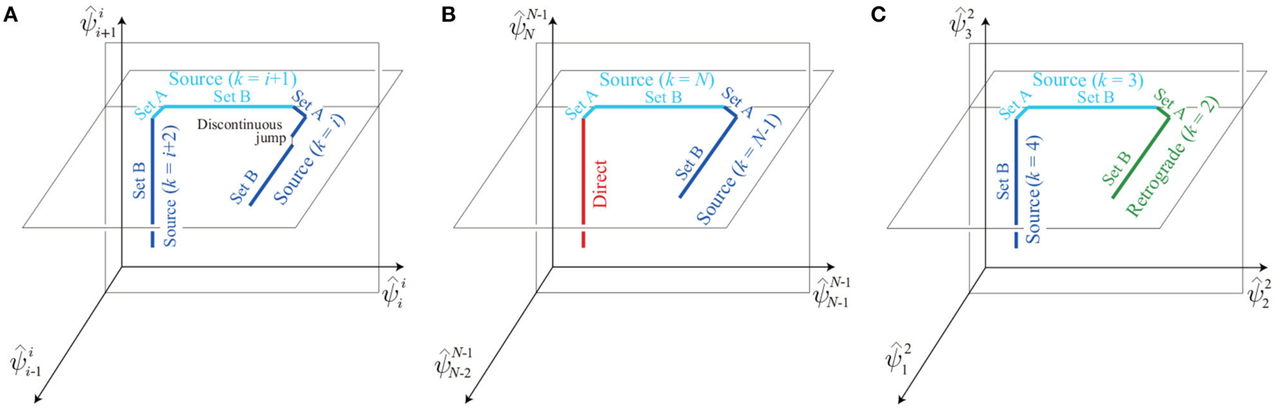

FIGURE 11 | Connection of the solution sets: **(A)** Source-wave gaits ($k = i, i+1, i+2$) projected onto the $\hat{\psi}^i_{i-1}$-$\hat{\psi}^i_i$-$\hat{\psi}^i_{i+1}$ space; **(B)** direct- and source-wave gaits ($k = N-1, N$) projected onto the $\hat{\psi}^{N-1}_{N-2}$-$\hat{\psi}^{N-1}_{N-1}$-$\hat{\psi}^{N-1}_N$ space; and **(C)** retrograde- ($k = 2$) and source-wave gaits ($k = 3, 4$) projected onto the $\hat{\psi}^2_1$-$\hat{\psi}^2_2$-$\hat{\psi}^2_3$ space.

derived by

$$\xi = \frac{\frac{1}{1-\beta} - \frac{m_{\mathrm{B}} g}{2\kappa a}}{1 - \frac{(3m_{\mathrm{B}} - m)g}{2\kappa a}}\eta, \tag{27}$$

$$v = \frac{\xi\omega}{2\pi}. \tag{28}$$

As the duty factor β increases, ξ and v increase.

When $k = 2$ and $\hat{\psi}_1 \approx 2\beta\pi$, the swing movements of the solution propagate from anterior to posterior with the wavelength from (27) and velocity from (28). This is similar to the retrograde-wave gait of centipedes (Full, 1997; Kuroda et al., 2014). In contrast, when $\hat{\psi}_N \approx 2(1-\beta)\pi$ in (24), the solution, whose front and rear parts are reversed from the solution of the retrograde-wave gait, is similar to the direct-wave gait of millipedes (Full, 1997; Kuroda et al., 2014). Our model has solutions corresponding to direct-, retrograde-, and source-wave gaits for $N \geq 3$.

4. DISCUSSION

4.1. Body Elasticity and Local Sensory Feedback Generate Interlimb Coordination

We assume that animal gaits can be represented as attractors of dynamic systems, as in Schöner et al. (1990), and that the essential structure of the dynamic system can be extracted by using a simple model (Full and Koditschek, 1999). Accumulating an understanding of such simple models allows us to understand actual complex phenomena. In the present study, we focused on the embodied sensorimotor interaction to generate multi-legged locomotion in a decentralized manner. We showed that the local sensory feedback and phase resetting generates the direct-, retrograde-, and source-wave gaits observed in multi-legged animals using a simple model to extract the essential features. We found that body elasticity is a key to generating the interlimb coordination. Specifically, the body natural frequency must be larger than the gait frequency ($\sqrt{\kappa/m_i} \gg \omega$). The analytical representation showed the existence of these gaits for $N \geq 3$, and revealed the parameter domain as follows: the boundary condition of the mass, $m/2 < m_{\mathrm{B}} < m$, and the amplitude of the swing leg movement, $mg/\kappa < a < L$. These findings improve our understanding of the mechanism of interlimb coordination in multi-legged locomotion.

So far, many studies have investigated the effects of sensory feedback on interlimb coordination. Owaki et al. (2012), Fukuoka et al. (2015), and Owaki and Ishiguro (2017) showed that quadruped robots, whose legs are controlled by distributed oscillators with load sensory feedback, generate walking, trotting, and galloping gaits depending on the speed. Tamura et al. (2016), Kano et al. (2017), and Yasui et al. (2017) also showed that load sensory feedback generates a millipede-like direct-wave gait. Our previous studies showed that phase resetting induces gait transitions in quadruped locomotion (Aoi et al., 2011, 2013) and hexapod locomotion (Fujiki et al., 2013; Ambe et al., 2015, 2018). In the present study, we also demonstrated that phase resetting generates retrograde-, source-, and direct-wave gaits in multi-legged locomotion. These findings are due to the embodied sensorimotor interaction, which is critical for the interlimb coordination regardless of the number of legs. Our analytical description using a simple model is helpful for clarifying the functional roles of the embodied sensorimotor interaction in interlimb coordination.

4.2. Relation With Intersegmental Coordination in Other Organisms

Other organisms also show intersegmental coordination in their locomotion, which appears as waves. For example, insect larvae and worms exhibit direct waves while crawling (Trimmer and Issberner, 2007; Paoletti and Mahadevan, 2014). Lampreys, leeches, and roundworms (*C. Elegans*) show body undulations that propagate backward during swimming. Motile cilia show metachronal waves. We discuss the relationship between our results and such intersegmental coordination by focusing on local sensory feedback.

Paoletti and Mahadevan (2014) developed an earthworm crawling model using mass points connected by spring dampers in an asymmetric friction environment. The model is controlled by neuro-muscular dynamics with the local sensory feedback, which contracts the segment muscles based on a stretch threshold and generates metachronal waves. Umedachi et al. (2016) proposed a similar model to reproduce the direct wave crawling motion of larvae in a decentralized manner. Each segment repeats stretching and contraction with distributed CPGs with local sensory feedback of the friction and velocity information for the segment. These results are similar to ours in the sense that metachronal waves are generated by local sensory feedback. However, their coordination is generated by asymmetric environmental friction, whereas ours is by different foot-contact timings.

The undulation patterns of lampreys and leeches as they swim are mainly generated by internal coupling of CPGs (Cohen et al., 1992; Grillner et al., 1995; KristanJr. et al., 2005). However, intersegmental coordination in leeches is not disrupted much even if the ganglion is cut (Yu et al., 1999), which suggests the importance of sensory feedback for segmental coordination. In addition, there is no clear evidence for the presence of CPGs in *C. Elegans*, and it has been suggested that proprioceptive receptors play a significant role in coordination (Wen et al., 2012). Boyle et al. (2012) modeled *C. Elegans* as a series of simple segments connected by elastic elements. They reproduced body undulations by neuro-muscular dynamics without CPGs. The dynamics of each segment is affected by the sensory feedback, which integrates several posterior segment stretches. When the feedback has only local interaction, such as stretch of the segment, no coordinated wave appears in a less viscous environment, such as water, and it appears only in a highly viscous fluid environment. That is, the fluid viscosity is responsible for generating the coordinated wave.

Motile cilia of organisms generate metachronal waves in a decentralized manner due to local interaction between the environmental fluid and the cilia (Elgeti and Gompper, 2013). Each cilium is controlled by simple switching inputs of power stroke and return stroke. These inputs switch when the cilium achieves a certain curvature; that is, it receives local sensory feedback about the curvature. Although each cilium moves independently, the metachronal wave for cilia motion appears through local interaction by the flow of the neighboring fluid.

An analytical description would help to understand these intersegmental coordination mechanisms. Thus, in the future, we would like to develop simple physical models for intersegmental coordination.

4.3. Physical Explanation of Countless Solutions

Our model has countless solutions as obtained by the serially connected set of the retrograde-, source-, and direct-wave gaits (**Figure 11**). This non-uniqueness is because our model has a conservative quantity as explained below.

We define E^j on the Poincaré section Σ^j ($j \in [1, N+1]$) by

$$E^j = \sum_{i=1}^{N} \psi_i^j. \tag{29}$$

From (11), the Poincaré map of E^j is represented as

$$E^j \mapsto E^j + \phi_1^1 - \phi_{N+1}^{N+1}. \tag{30}$$

The relation $\phi_1^1 = \phi_{N+1}^{N+1} = \hat{\phi}^{\mathrm{td}}$ holds if the neighboring legs (Legs 2 and N) are in the stance phases ($\phi_2^1 \in [0, 2\beta\pi]$ and $\phi_N^{N+1} \in [0, 2\beta\pi]$) when each leg (Legs 1 and $N+1$) touches the ground (this relation is also satisfied for the solution sets). In this case, (30) becomes $E^j \mapsto E^j$, where E^j is a conservative quantity, which produces countless solutions.

To explain the physical meaning of this conservative quantity, we represent ϕ_1^1 and ϕ_{N+1}^{N+1} using (3) and (12) when $\phi_2^1 \in [0, 2\beta\pi]$ and $\phi_N^{N+1} \in [0, 2\beta\pi]$.

$$\phi_1^1 = 2\pi - \frac{(1-\beta)m_1 g\pi}{\kappa a}, \tag{31}$$

$$\phi_{N+1}^{N+1} = 2\pi - \frac{(1-\beta)m_{N+1} g\pi}{\kappa a}. \tag{32}$$

These equations show that $\phi_1^1 = \phi_{N+1}^{N+1}$ is satisfied only when $m_1 = m_{N+1}$. Thus, this conservative quantity is derived from the symmetry between the front and tail masses ($m_1 = m_{N+1} = m_{\mathrm{B}}$). Strictly speaking, the symmetry of other parameters, such as κ and a, is also required for the conservative quantity.

Although our model generates multiple gaits because of the symmetry, animals prefer specific gaits. For example, centipedes prefer the retrograde-wave gait (Full, 1997; Kuroda et al., 2014). In contrast, millipedes prefer the direct-wave gait to move forward (Full, 1997; Kuroda et al., 2014) and use the source-wave gait when the body axis is bent like a U shape (Tamura et al., 2016). Our model does not explain these preferences. However, when the symmetry is broken, our model has no conservative quantity and generates a specific gait depending on the parameters. We would like to investigate the gait preference by incorporating asymmetries into our model in future studies.

4.4. Limitation of This Study

This study demonstrated that phase resetting generates direct-, retrograde-, and source-wave gaits in an elastic body whose natural frequency is larger than the gait frequency. However, our model did not replicate the details of animal gaits. For example, our model did not explain the gait preference of animals, as described above. While centipedes and millipedes use different contralateral interlimb coordination (i.e., left–right antiphase and in-phase movements, respectively), our model did not consider this behavior. Furthermore, although the swinging of multiple legs propagates simultaneously in millipedes and centipedes (Kuroda et al., 2014), only one leg swing is propagated in our model. These limitations and discrepancies come from the simple way in which our model extracts the essence of multi-leg motion, which was the focus in the present study. However, our results give clues to overcome these limitations and discrepancies. For example, the gait preference may be explained by introducing an asymmetry into our model, such as different masses between the head and tail, to eliminate the conservative quantity in our model. Better understanding of a simple model will provide insights for the design of a more complicated model. The extension of our model is one of our essential future tasks.

4.5. Application to Legged Robots

Multi-legged robots have been developed to extract the essence of dexterous traveling ability. On one hand, the flexible body axis contributes to rapid movement or ability to traverse rough terrain. In previous work (Aoi et al., 2016), we showed that high body-axis flexibility induces body undulations through Hopf bifurcation, which contributes to rapid turning. Hoffman and Wood (2011) showed that a passive undulatory gait increases the locomotion speed. Koh et al. (2010) and Kinugasa et al. (2017) demonstrated that multi-legged robots with a flexible body axis show high mobility in uneven terrain.

On the other hand, contacting the ground with many legs is useful for avoiding stumbling in various environments. Inagaki et al. (2010) proposed a distributed control method in which the legs follow the contact points of anterior legs, which allowed a robot to walk in various environments as long as the front legs choose solid footholds. Hayakawa et al. (2020) proposed a gait generation strategy to ensure static stability for single-legged modular robots to create a cluster with various leg configurations. Kano et al. (2017) showed the adaptability when part of the terrain is removed.

For static gaits, sensory feedback is useful for generating interlimb coordination, as in the present study, and to gain better adaptability to the environment (Kano et al., 2017; Yasui et al., 2017). To design a method for controlling multi-legged robots with sensory feedback, it is important to understand how and when the sensory feedback affects walking motion. The present study focused on phase resetting at foot contact as the sensory feedback and clarified the effects by using the analytical description of a simple model. We showed that phase resetting contributes to generating the coordinated gaits in a decentralized manner via embodied sensorimotor interaction when the model has an elastic body axis whose natural frequency is larger than the gait frequency. We also analytically derived the range of physical parameters where our analysis is valid. This helps when designing a controller to generate various gaits for multi-legged robots. In particular, when we design the leg movement using oscillator phases, as in Aoi et al. (2017) and Ambe et al. (2018), phase resetting will generate coordinated gaits regardless of the number of legs. We would like to investigate it through robot experiments in future studies.

5. CONCLUSION

This study used a simple model to analytically reveal that local sensory feedback, phase resetting, generates the direct-, retrograde-, and source-wave gaits observed in multi-legged animals in a decentralized manner via the embodied sensorimotor interaction. The model comprises massless legs and mass points connected by vertical springs to imitate a flexible body. The phase oscillators control the vertical movements of the legs independently, and the phases are only affected by phase resetting upon foot contact. The dynamic simulations show that countless periodic solutions of the three gaits emerge depending on the initial phase. Furthermore, these analytical solutions were derived under some assumptions deduced from the simulation results. They showed that all three gaits exist regardless the number of legs and revealed the parameter domain. The reason for the coexistence of the three gaits is explained by a conservative quantity due to the front–rear symmetry of our model. Because our model is limited to specific situations, such as the front–rear symmetry, permitting only vertical movements while ignoring the contralateral interlimb coordination, and propagation of only one swing leg within one wavelength, we need to incorporate more realistic situations into our model in the future.

DATA AVAILABILITY STATEMENT

The original contributions presented in the study are included in the article/**Supplementary Material**, further inquiries can be directed to the corresponding author/s.

AUTHOR CONTRIBUTIONS

YA conceived of the study, designed the study, carried out the simulation and theoretical analysis, and drafted the manuscript. SA helped conceiving and designing of the study, improved the theoretical analysis, and critically revised the manuscript. KT helped conceiving and designing of the study and critically revised the manuscript. FM helped conceiving and designing of the study, coordinated the study, and critically revised the manuscript. All authors gave final approval for publication and agree to be held accountable for the work performed therein.

FUNDING

This work was supported by JSPS KAKENHI Grant Number JP18K13723.

SUPPLEMENTARY MATERIAL

The Supplementary Material for this article can be found online at: https://www.frontiersin.org/articles/10.3389/fncir.2021.706064/full#supplementary-material

REFERENCES

Adachi, M., Aoi, S., Kamimura, T., Tsuchiya, K., and Matsuno, F. (2020). Body torsional flexibility effects on stability during trotting and pacing based on a simple analytical model. *Bioinspir. Biomim.* 15:055001. doi: 10.1088/1748-3190/ab968d

Akay, T., Haehn, S., Schmitz, J., and Büschges, A. (2004). Signals from load sensors underlie interjoint coordination during stepping movements of the stick insect leg. *J. Neurophysiol.* 92, 42–51. doi: 10.1152/jn.01271.2003

Ambe, Y., Aoi, S., Nachstedt, T., Manoonpong, P., Wörgötter, F., and Matsuno, F. (2018). Simple analytical model reveals the functional role of embodied sensorimotor interaction in hexapod gaits. *PLoS ONE*, Kyoto, 13:e0192469. doi: 10.1371/journal.pone.0192469

Ambe, Y., Nachstedt, T., Manoonpong, P., Wörgötter, F., and Matsuno, F. (2015). "Embodied sensorimotor interaction for insect locomotion," in *The First International Symposium on Swarm Behavior and Bio-Inspired Robotics*, 340–343.

Aoi, S., Katayama, D., Fujiki, S., Tomita, N., Funato, T., Yamashita, T., et al. (2013). A stability-based mechanism for hysteresis in the walk-trot transition in quadruped locomotion. *J. R. Soc. Interface* 10:20120908. doi: 10.1098/rsif.2012.0908

Aoi, S., Manoonpong, P., Ambe, Y., Matsuno, F., and Wörgötter, F. (2017). Adaptive control strategies for interlimb coordination in legged robots: a review. *Front. Neurorobot*. 11:39. doi: 10.3389/fnbot.2017.00039

Aoi, S., Tanaka, T., Fujiki, S., Funato, T., Senda, K., and Tsuchiya, K. (2016). Advantage of straight walk instability in turning maneuver of multilegged locomotion: a robotics approach. *Sci. Rep*. 6:30199. doi: 10.1038/srep30199

Aoi, S., Yamashita, T., and Tsuchiya, K. (2011). Hysteresis in the gait transition of a quadruped investigated using simple body mechanical and oscillator network models. *Phys. Rev. E* 83:061909. doi: 10.1103/PhysRevE.83.061909

Boyle, J. H., Berri, S., and Cohen, N. (2012). Gait modulation in *C. elegans*: an integrated neuromechanical model. *Front. Comput. Neurosci*. 6:10. doi: 10.3389/fncom.2012.00010

Büschges, A. (1995). Role of local nonspiking interneurons in the generation of rhythmic motor activity in the stick insect. *J. Neurobiol*. 27, 488–512. doi: 10.1002/neu.480270405

Büschges, A., Akay, T., Gabriel, J. P., and Schmidt, J. (2008). Organizing network action for locomotion: Insights from studying insect walking. *Brain Res. Rev*. 57, 162–171. doi: 10.1016/j.brainresrev.2007.06.028

Cohen, A. H., Ermentrout, G. B., Kiemel, T., Kopell, N., Sigvardt, K. A., and Williams, T. L. (1992). Modelling of intersegmental coordination in the lamprey central pattern generator for locomotion. *Trends Neurosci*. 15, 434–438. doi: 10.1016/0166-2236(92)90006-T

Cruse, H., Kindermann, T., Schumm, M., Dean, J., and Schmitz, J. (1998). Walknet-a biologically inspired network to control six-legged walking. *Neural Netw*. 11, 1435–1447. doi: 10.1016/S0893-6080(98)00067-7

Daun, S., Rubin, J., and Rybak, I. (2009). Control of oscillation periods and phase durations in half-center central pattern generators: a comparative mechanistic analysis. *J. Comput. Neurosci*. 27, 3–36. doi: 10.1007/s10827-008-0124-4

Daun-Gruhn, S., and Büschges, A. (2011). From neuron to behavior: dynamic equation-based prediction of biological processes in motor control. *Biol. Cybern*. 105, 71–88. doi: 10.1007/s00422-011-0446-6

Delcomyn, F. (2004). Insect walking and robotics. *Annu. Rev. Entomol*. 49, 51–70. doi: 10.1146/annurev.ento.49.061802.123257

Elgeti, J., and Gompper, G. (2013). Emergence of metachronal waves in cilia arrays. *Proc. Natl. Acad. Sci. U.S.A*. 110, 4470–4475. doi: 10.1073/pnas.1218869110

Fujiki, S., Aoi, S., Funato, T., Tomita, N., Senda, K., and Tsuchiya, K. (2013). Hysteresis in the metachronal-tripod gait transition of insects: a modeling study. *Phys. Rev. E* 88:012717. doi: 10.1103/PhysRevE.88.012717

Fukuoka, Y., Habu, Y., and Fukui, T. (2015). A simple rule for quadrupedal gait generation determined by leg loading feedback: a modeling study. *Sci. Rep*. 5:8169. doi: 10.1038/srep08169

Full, R. J. (1997). "Invertebrate locomotor system," in *The Handbook of Comparative Physiology*, ed W. Dantzler (Oxford: Oxford University Press), 853–930. doi: 10.1002/cphy.cp130212

Full, R. J., and Koditschek, D. E. (1999). Templates and anchors: neuromechanical hypotheses of legged locomotion on land. *J. Exp. Biol*. 202, 3325–3332. doi: 10.1242/jeb.202.23.3325

Grillner, S., Deliagina, T., el Manira, A., Hill, R. H., Lansner, A., Orlovsky, G. N., et al. (1995). Neural networks that co-ordinate locomotion and body orientation in lamprey. *Trends Neurosci*. 18, 270–279. doi: 10.1016/0166-2236(95)80008-P

Hayakawa, T., Kamimura, T., Kaji, S., and Matsuno, F. (2020). Autonomous distributed system for gait generation for single-legged modular robots connected in various configurations. *IEEE Trans. Robot*. 36, 1491–1510. doi: 10.1109/TRO.2020.2992983

Hoffman, K. L., and Wood, R. J. (2011). "Passive undulatory gaits enhance walking in a myriapod millirobot," in *2011 IEEE/RSJ International Conference on Intelligent Robots and Systems* (San Francisco, CA), 1479–1486. doi: 10.1109/IROS.2011.6048268

Hooper, S. L., Guschlbauer, C., Blümel, M., Rosenbaum, P., Gruhn, M., Akay, T., et al. (2009). Neural control of unloaded leg posture and of leg swing in stick insect, cockroach, and mouse differs from that in larger animals. *J. Neurosci*. 29, 4109–4119. doi: 10.1523/JNEUROSCI.5510-08.2009

Ijspeert, A. J. (2001). A connectionist central pattern generator for theaquatic and terrestrial gaits of a simulated salamander. *Biol. Cybern*. 84, 331–348. doi: 10.1007/s004220000211

Ijspeert, A. J. (2008). Central pattern generators for locomotion control in animals and robots: a review. *Neural Netw*. 21, 642–653. doi: 10.1016/j.neunet.2008.03.014

Inagaki, S., Niwa, T., and Suzuki, T. (2010). "Follow-the-contact-point gait control of centipede-like multi-legged robot to navigate and walk on uneven terrain," in *2010 IEEE/RSJ International Conference on Intelligent Robots and Systems* (Taipei), 5341–5346. doi: 10.1109/IROS.2010.5651324

Kamimura, T., Aoi, S., Higurashi, Y., Wada, N., Tsuchiya, K., and Matsuno, F. (2021). Dynamical determinants enabling two different types of flight in cheetah gallop to enhance speed through spine movement. *Sci. Rep*. 11:9631. doi: 10.1038/s41598-021-88879-0

Kano, T., Sakai, K., Yasui, K., Owaki, D., and Ishiguro, A. (2017). Decentralized control mechanism underlying interlimb coordination of millipedes. *Bioinspir. Biomim*. 12:036007. doi: 10.1088/1748-3190/aa64a5

Kinugasa, T., Osuka, K., Hayashi, R., Miyamoto, N., and Yoshida, K. (2017). Development of a small and lightweight myriapod robot using passive dynamics. *Artif. Life Robot*. 22, 429–434. doi: 10.1007/s10015-017-0378-x

Koh, D., Yang, J., and Kim, S. (2010). "Centipede robot for uneven terrain exploration: design and experiment of the flexible biomimetic robot mechanism," in *2010 3rd IEEE RAS EMBS International Conference on Biomedical Robotics and Biomechatronics* (Tokyo), 877–881. doi: 10.1109/BIOROB.2010.5627776

KristanJr., W. B., Calabrese, R. L., and Friesen, W. O. (2005). Neuronal control of leech behavior. *Prog. Neurobiol*. 76, 279–327. doi: 10.1016/j.pneurobio.2005.09.004

Kuroda, S., Kunita, I., Tanaka, Y., Ishiguro, A., Kobayashi, R., and Nakagaki, T. (2014). Common mechanics of mode switching in locomotion of limbless and legged animals. *J. R. Soc. Interface* 11:20140205. doi: 10.1098/rsif.2014.0205

Matsuoka, K. (1987). Mechanisms of frequency and pattern control inthe neural rhythm generators. *Biol. Cybern*. 56, 345–353. doi: 10.1007/BF00319514

Owaki, D., and Ishiguro, A. (2017). A quadruped robot exhibiting spontaneous gait transitions from walking to trotting to galloping. *Sci. Rep*. 7:277. doi: 10.1038/s41598-017-00348-9

Owaki, D., Kano, T., Nagasawa, K., Tero, A., and Ishiguro, A. (2012). Simple robot suggests physical interlimb communication is essential for quadruped walking. *J. R. Soc. Interface* 10:20120669. doi: 10.1098/rsif.2012.0669

Paoletti, P., and Mahadevan, L. (2014). A proprioceptive neuromechanical theory of crawling. *Proc. R. Soc. B* 281:20141092. doi: 10.1098/rspb.2014.1092

Pasemann F., Hild M., and Zahedi, K. (2003). "SO(2)-networks as neural oscillators," in *IWANN 2003: Computational Methods in Neural Modeling, Vol. 2686*, eds J. Mira and J. R. Álvarez (Springer), 141–151. doi: 10.1007/3-540-44868-3_19

Proctor, J. L., and Holmes, P. (2018). The effects of feedback on stability and maneuverability of aphase-reduced model for cockroach locomotion. *Biol. Cybern*. 112, 387–401. doi: 10.1007/s00422-018-0762-1

Rybak, I. A., Shevtsova, N. A., Lafreniere-Roula, M., and McCrea, D. A. (2006). Modelling spinal circuitry involved in locomotor patterngeneration:

insights from deletions during fictivelocomotion. *J. Physiol*. 577, 617–639. doi: 10.1113/jphysiol.2006.118703

Schilling, M., Hoinville, T., Schmitz, J., and Cruse, H. (2013). Walknet, a bio-inspired controller for hexapod walking. *Biol. Cybern*. 107, 397–419. doi: 10.1007/s00422-013-0563-5

Schomburg, E. D., Petersen, N., Barajon, I., and Hultborn, H. (1998). Flexor reflex afferents reset the step cycle during fictive locomotion in the cat. *Exp. Brain Res*. 122, 339–350. doi: 10.1007/s002210050522

Schöner, G., Jiang, W., and Kelso, J. (1990). A synergetic theory of quadrupedal gaits and gait transitions. *J. Theor. Biol*. 142, 359–391. doi: 10.1016/S0022-5193(05)80558-2

Seipel, J. E., Holmes, P. J., and Full, R. J. (2004). Dynamics and stability of insect locomotion: a hexapedal model for horizontal plane motions. *Biol. Cybern*. 91, 76–90. doi: 10.1007/s00422-004-0498-y

Shaw, K. M., Lyttle, D. N., Gill, J. P., Cullins, M. J., McManus, J. M., Lu, H., et al. (2015). The significance of dynamical architecture for adaptive responses to mechanical loads during rhythmic behavior. *J. Comput. Neurosci*. 38, 25–51. doi: 10.1007/s10827-014-0519-3

Spence, A. J., Revzen, S., Seipel, J., Mullens, C., and Full, R. J. (2010). Insects running on elastic surfaces. *J. Exp. Biol*. 213, 1907–1920. doi: 10.1242/jeb.042515

Steingrube, S., Timme, M., Wörgötter, F., and Manoonpong, P. (2010). Self-organized adaptation of a simple neural circuit enables complex robot behaviour. *Nat. Phys*. 6, 224–230. doi: 10.1038/nphys1508

Tamura, T., Satou, E., and Inoue, K. (2016). "Constructive understanding of decentralized leg motion control mechanism of myriapods," in *28th Sympsium of Destributed Autonomous System*, Hiroshima, 149–152. (in Japanese).

Tanase, M., Ambe, Y., Aoi, S., and Matsuno, F. (2015). A galloping quadruped model using left-right asymmetry in touchdown angles. *J. Biomech*. 48, 3383–3389. doi: 10.1016/j.jbiomech.2015.06.003

Ting, L. H., and Chiel, H. J. (2017). "Chapter 12: Muscle, biomechanics, and implications for neural control," in *Neurobiology of Motor Control: Fundamental Concepts and New Directions*, eds S. L. Hooper and A. Büschges (Hoboken, NJ: Wiley), 365–416. doi: 10.1002/9781118873397.ch12

Trimmer, B., and Issberner, J. (2007). Kinematics of soft-bodied, legged locomotion in manduca sexta larvae. *Biol. Bull*. 212, 130–142. doi: 10.2307/25066590

Tuthill, J. C., and Wilson, R. I. (2016). Mechanosensation and adaptive motor control in insects. *Curr. Biol*. 26, 1022–1038. doi: 10.1016/j.cub.2016.06.070

Umedachi, T., Kano, T., Ishiguro, A., and Trimmer, B. A. (2016). Gait control in a soft robot by sensing interactions with the environment using self-deformation. *R. Soc. Open Sci*. 3:160766. doi: 10.1098/rsos.160766

van der Pol, B. (1926). On relaxation oscillations. *Lond. Edinb. Dublin Philos. Mag. J. Sci*. 2, 978–992. doi: 10.1080/14786442608564127

Wen, Q., Po, M. D., Hulme, E., Chen, S., Liu, X., Kwok, S. W., et al. (2012). Proprioceptive coupling within motor neurons drives *C. elegans* forward locomotion. *Neuron* 76, 750–761. doi: 10.1016/j.neuron.2012.08.039

Yasui, K., Kano, T., Standen, E. M., Aonuma, H., Ijspeert, A. J., and Ishiguro, A. (2019). Decoding the essential interplay between central and peripheral control in adaptive locomotion of amphibious centipedes. *Sci. Rep*. 9:18288. doi: 10.1038/s41598-019-53258-3

Yasui, K., Sakai, K., Kano, T., Owaki, D., and Ishiguro, A. (2017). Decentralized control scheme for myriapod robot inspired by adaptive and resilient centipede locomotion. *PLoS ONE* 12:e171421. doi: 10.1371/journal.pone.0171421

Yu, X., Nguyen, B., and Friesen, W. O. (1999). Sensory feedback can coordinate the swimming activity of the leech. *J. Neurosci*. 19, 4634–4643. doi: 10.1523/JNEUROSCI.19-11-04634.1999

Conflict of Interest: The authors declare that the research was conducted in the absence of any commercial or financial relationships that could be construed as a potential conflict of interest.

frontiers
in Integrative Neuroscience

ORIGINAL RESEARCH
published: 07 January 2022
doi: 10.3389/fnint.2021.777741

Temporal Profile of Descending Cortical Modulation of Spinal Excitability: Group and Individual-Specific Effects

*Jiang Xu[1,2], Alejandro J. Lopez[2,3], Maruf M. Hoque[2], Michael R. Borich[2] and Trisha M. Kesar[2]**

[1]Department of Rehabilitation Medicine, Tongji Hospital, Tongji Medical College, Huazhong University of Science and Technology, Wuhan, China, [2]Division of Physical Therapy, Department of Rehabilitation Medicine, Emory University, Atlanta, GA, United States, [3]Neuroscience Graduate Program, Graduate Division of Biological and Biomedical Sciences, Emory University, Atlanta, GA, United States

Sensorimotor control is modulated through complex interactions between descending corticomotor pathways and ascending sensory inputs. Pairing sub-threshold transcranial magnetic stimulation (TMS) with peripheral nerve stimulation (PNS) modulates the Hoffmann's reflex (H-reflex), providing a neurophysiologic probe into the influence of descending cortical drive on spinal segmental circuits. However, individual variability in the timing and magnitude of H-reflex modulation is poorly understood. Here, we varied the inter-stimulus interval (ISI) between TMS and PNS to systematically manipulate the relative timing of convergence of descending TMS-induced volleys with respect to ascending PNS-induced afferent volleys in the spinal cord to: (1) characterize effective connectivity between the primary motor cortex (M1) and spinal circuits, mediated by both direct, fastest-conducting, and indirect, slower-conducting descending pathways; and (2) compare the effect of individual-specific vs. standard ISIs. Unconditioned and TMS-conditioned H-reflexes (24 different ISIs ranging from −6 to 12 ms) were recorded from the soleus muscle in 10 able-bodied individuals. The magnitude of H-reflex modulation at individualized ISIs (earliest facilitation delay or EFD and individual-specific peak facilitation) was compared with standard ISIs. Our results revealed a significant effect of ISI on H-reflex modulation. ISIs eliciting earliest-onset facilitation (EFD 0 ms) ranged from −3 to −5 ms across individuals. No difference in the magnitude of facilitation was observed at EFD 0 ms vs. a standardized short-interval ISI of −1.5 ms. Peak facilitation occurred at longer ISIs, ranging from +3 to +11 ms. The magnitude of H-reflex facilitation derived using an individual-specific peak facilitation was significantly larger than facilitation observed at a standardized longer-interval ISI of +10 ms. Our results suggest that unique insights can be provided with individual-specific measures of

OPEN ACCESS

Edited by:
Monica A. Daley,
University of California, Irvine,
United States

Reviewed by:
Nobuhiko Mori,
Osaka University, Japan
Giacomo Guidali,
San Giovanni di Dio Fatebenefratelli
Center (IRCCS), Italy

***Correspondence:**
Trisha M. Kesar
trisha.m.kesar@emory.edu

Received: 15 September 2021
Accepted: 21 December 2021
Published: 07 January 2022

Citation:
Xu J, Lopez AJ, Hoque MM, Borich MR and Kesar TM (2022) Temporal Profile of Descending Cortical Modulation of Spinal Excitability: Group and Individual-Specific Effects. Front. Integr. Neurosci. 15:777741. doi: 10.3389/fnint.2021.777741

Abbreviations: TMS, Transcranial magnetic stimulation; PNS, Peripheral nerve stimulation; ISIs, Inter-stimulus intervals; EFD, Early facilitation delay; EPSPs, Excitatory postsynaptic potentials; MVC, Maximal voluntary contraction; AMT, Active motor threshold; ANOVA, Analysis of variance.

top-down effective connectivity mediated by direct and/or fastest-conducting pathways (indicated by the magnitude of facilitation observed at EFD 0 ms) and other descending pathways that encompass relatively slower and/or indirect connections from M1 to spinal circuits (indicated by peak facilitation and facilitation at longer ISIs). By comprehensively characterizing the temporal profile and inter-individual variability of descending modulation of spinal reflexes, our findings provide methodological guidelines and normative reference values to inform future studies on neurophysiological correlates of the complex array of descending neural connections between M1 and spinal circuits.

Keywords: transcranial magnetic stimulation (TMS), spinal reflex excitability, lower extremity muscles, inter-stimulus interval (ISI), corticospinal pathways

INTRODUCTION

Motor evoked potentials (MEPs) generated in response to transcranial magnetic stimulation (TMS; Barker et al., 1985; Abbruzzese and Trompetto, 2002; Kobayashi and Pascual-Leone, 2003; Hallett, 2007; Kesar et al., 2018b) and Hoffman reflexes (H-reflexes) elicited in response to peripheral nerve stimulation (PNS; Schieppati, 1987; Pierrot-Deseilligny and Mazevet, 2000; Perez et al., 2007; Burke, 2016) have each been individually used to evaluate the excitability of cortical and spinal sensorimotor circuitry, respectively. Studies using TMS-evoked MEPs have shown modulation of corticospinal excitability with immobilization (Clark et al., 2008, 2010; Leukel et al., 2015; Opie et al., 2016), rehabilitation (Roosink and Zijdewind, 2010; Kantak et al., 2013; Keller et al., 2018), somatosensory stimulation (Meehan et al., 2008; Veldman et al., 2016; Brown et al., 2018), and motor learning (Stefan et al., 2005; Celnik, 2015; Kantak et al., 2018; Palmer et al., 2018). Similarly, H-reflex studies have demonstrated spinal circuit plasticity in response to electrical stimulation (Rozand et al., 2015; Bae and Kim, 2017; Kuck et al., 2018), aerobic exercise (Meunier et al., 2007; Hodapp et al., 2009; Tanuma et al., 2017), balance training (Taube et al., 2007; Behrens et al., 2015), operant conditioning (Thompson and Wolpaw, 2014, 2015) and immobilization (Lundbye-Jensen and Nielsen, 2008; Clark et al., 2010; Leukel et al., 2015). However, TMS-evoked MEPs or H-reflexes measured in isolation are limited in their ability to specifically elucidate whether the specific site of neuroplasticity is within the cortex, descending projections between M1 and the spinal cord (upper motor neurons), spinal segmental reflex circuits, or the spinal motoneuron pool, which is the final common pathway for both reflexive and voluntary motor commands (Hodgkin and Huxley, 1952; McNeil et al., 2013).

The H-reflex, providing an electrical analog of the excitability of spinal segmental reflexes, can be influenced or modulated by descending corticomotor volleys evoked by electrical or magnetic brain stimulation (Cowan et al., 1986; Nielsen et al., 1993). Therefore, the pairing of sub-threshold TMS and PNS has been used as a neurophysiologic technique to evaluate the strength of descending physiologic connections (i.e., effective connectivity) between M1 and spinal circuits (Crone et al., 2003; Urbin et al., 2017; Keller et al., 2018). TMS-conditioning of the H-reflex can index the excitability of fastest-conducting or direct as well as relatively slower or indirect descending corticomotor projections onto spinal motoneurons (Nielsen et al., 1993; Taube et al., 2017). The effect of pairing TMS with PNS manifests as a change in the amplitude of H-reflex response, when the PNS-induced ascending volley transmitted *via* the Ia afferents and TMS-induced descending volleys transmitted *via* descending corticomotor pathways converge at the level of the spinal motoneuron pool (Niemann et al., 2018). This paired, non-invasive stimulation technique can provide information about the ability of descending corticofugal pathways to modulate spinal reflex excitability in humans.

Many previous studies of TMS-conditioned H-reflexes have used two standardized inter-stimulus intervals (ISIs) to evaluate early and late interval facilitation (Nielsen et al., 1993; Nielsen and Petersen, 1995; Taube et al., 2017; Keller et al., 2018). For instance, when sub-threshold TMS is delivered 1–5 ms *after* PNS (ISI −1 to −5 ms), the resulting early onset facilitation of the H-reflex is thought to be mediated *via* direct, faster-conducting descending projections onto spinal motoneurons. When TMS is applied 5–10 ms *before* PNS (ISI +5 to +10), the resulting longer interval facilitation is hypothesized to modulate the H-reflex response through an array of relatively slower and/or indirect corticomotor descending pathways. By varying the relative timing of TMS-induced descending corticomotor volleys with respect to the PNS, varying magnitudes of H-reflex facilitation can be elicited and quantified, which in turn probe the excitability of multiple, descending pathways that influence the excitability of spinal segmental reflexes.

Previously, using a single or standard ISI, we showed moderate-to-good reliability of TMS-induced H-reflex facilitation over multiple test sessions (Gray et al., 2017). However, several methodological factors can influence the inter-individual variability and magnitudes of TMS-induced H-reflex facilitation. Previous studies have evaluated the effect of TMS intensity (Niemann et al., 2018), coil direction (Niemann et al., 2018), and muscle activation (Keller et al., 2018) on TMS-facilitation of H-reflexes. Recently, we demonstrated the effect of PNS intensity on H-reflex facilitation, albeit only at two standardized ISIs (−1.5 ms for early-onset facilitation and

+10 ms for longer interval facilitation; Lopez et al., 2020). The ISI is another important but relatively under-studied parameter that can affect the magnitude and reliability of facilitation (Nielsen et al., 1993; Geertsen et al., 2011; Taube et al., 2017). Several previous studies have used a single, standardized ISI for evaluation of TMS-induced H-reflex facilitation (Gray et al., 2017; Rio-Rodriguez et al., 2017), while others determined the ISI on an individual-subject basis (Urbin et al., 2017; Niemann et al., 2018). However, the influence of ISI on the magnitude of TMS-induced modulation of H-reflexes, and inter-individual variability in the timing and magnitude of facilitation across a range of ISIs is poorly understood. In addition to inter-individual differences in conduction velocity and segment length, optimizing or individualizing the ISI for eliciting H-reflex facilitation may be particularly important in neurological conditions (e.g., stroke, spinal cord injury, multiple sclerosis) given the changes in corticospinal excitability and transmission induced by the neurological lesion or injury (Knikou, 2017; Christiansen and Perez, 2018; Li et al., 2018). Thus, as an important first step toward understanding the influence of ISI, here, we varied the ISI between TMS and PNS to systematically manipulate the relative timing of convergence of descending TMS-induced volleys with respect to ascending PNS-induced afferent volleys in the spinal cord to characterize effective connectivity between the primary motor cortex (M1) and spinal circuits, mediated by both direct, fastest-conducting, as well as indirect, relatively slower-conducting descending pathways.

Furthermore, if individualization of ISIs is indeed an important methodological consideration, determining the optimum ISI for eliciting TMS-conditioning of H-reflexes for each study participant can be tedious and time-consuming, potentially limiting or constraining the application of this paired TMS-PNS stimulation technique in clinical trials or experimental studies investigating neuroplasticity (Taube et al., 2017). Therefore, the second objective of this study was to evaluate whether using an individualized, optimal ISI presented an advantage compared to the use of the same or "standardized" ISI for all participants in the group.

METHODS

Participants

Ten able-bodied, young individuals (eight females, age 22–28 years) participated in this study. All participants provided informed consent before study participation. Study procedures were approved by the Emory University Institutional Review Board (IRB).

Experimental Design

The soleus muscle of the right leg was tested in all participants. All data-collection procedures were performed with the participants seated in a semi-recumbent position with hips and knees at 30° of flexion, and the ankles secured in rigid boots (**Figure 1**). The lower leg, foot, and distal thighs were stabilized with inelastic straps to maintain consistent limb positioning during the experiment.

Electromyographic Recordings

Following standard skin preparation procedures, two surface electrodes (2-cm diameter, EL503, Biopac Systems Inc., Goleta, CA) were placed on the skin overlying the posterolateral aspect of the right soleus and the tibialis anterior (TA) muscle belly. A ground electrode was placed over the ipsilateral lateral malleolus. EMG signals were recorded at the sampling rate of 2,000 Hz with a 5–1,000 Hz bandpass filter. At the start of the experiment, participants were instructed to perform two isometric maximal voluntary contractions (MVCs) for 3–5 s into dorsiflexion and plantarflexion, separated by ∼30 s of rest. To control for the effects of varying background EMG activation, the participants were requested to maintain the right soleus background EMG activity at a low-level (10% EMG activation obtained during the MVC) during data collection. Throughout the experiment, the participant was provided real-time visual biofeedback on a display screen regarding his/her ongoing average rectified soleus and tibialis anterior EMG activity, as well as the target activation level (10% MVC; **Figure 1**). If the participant deviated from the 10% MVC EMG activation target, the investigator would pause and instruct the participant to adjust his/her EMG activation. This EMG visual feedback and experimenter's check on the ongoing EMG activation was implemented to ensure consistent soleus background EMG activation during the collection of both unconditioned and conditioned H-reflexes.

Peripheral Nerve Stimulation

A square electrode (5 cm by 5 cm, TSYR2020-20, Syrtenty, Titusville, FL) was attached to the anterior aspect of the knee and served as the anode. A pen electrode was used to search for the optimal nerve stimulation site in the popliteal fossa. Electrical stimulation was delivered to the posterior tibial nerve to evoke soleus H-reflexes. The optimal site for nerve stimulation was identified as the location that elicited stable soleus H-reflexes and a visible plantarflexion contraction at higher intensities. After confirming the optimal stimulation site, a self-adherent carbon rubber circular electrode (2.5 cm diameter, TSYR1000-40 round, Syrtenty, Titusville, FL) was attached, additional pressure was applied using a Styrofoam ball to maintain the electrode's contact with the skin, and the electrode and ball were tightly wrapped. The H-reflex recruitment curve was generated by administering approximately 50–60 single pulses with a pulse duration of 1 ms, which were delivered using an electrical stimulator controlled with custom-written MATLAB scripts (AcqKnowledge software Version 4.4, Biopac Systems Inc.). To acquire H-reflex and M-wave recruitment curves, electrical stimulation intensity was increased gradually until the maximal muscle response (M_{max}) was reached, as measured by the peak-to-peak amplitude of the raw M-wave responses. Using the H-reflex and M-wave curves, we also obtained the peripheral stimulation intensity required to elicit an H-reflex amplitude of 20% M_{max}.

Transcranial Magnetic Stimulation

To elicit soleus TMS-evoked motor evoked potentials (MEPs), single TMS pulses were delivered using a custom batwing, figure-of-eight coil with a posterior-anterior current direction connected to a monophasic TMS stimulator (Magstim 200^2;

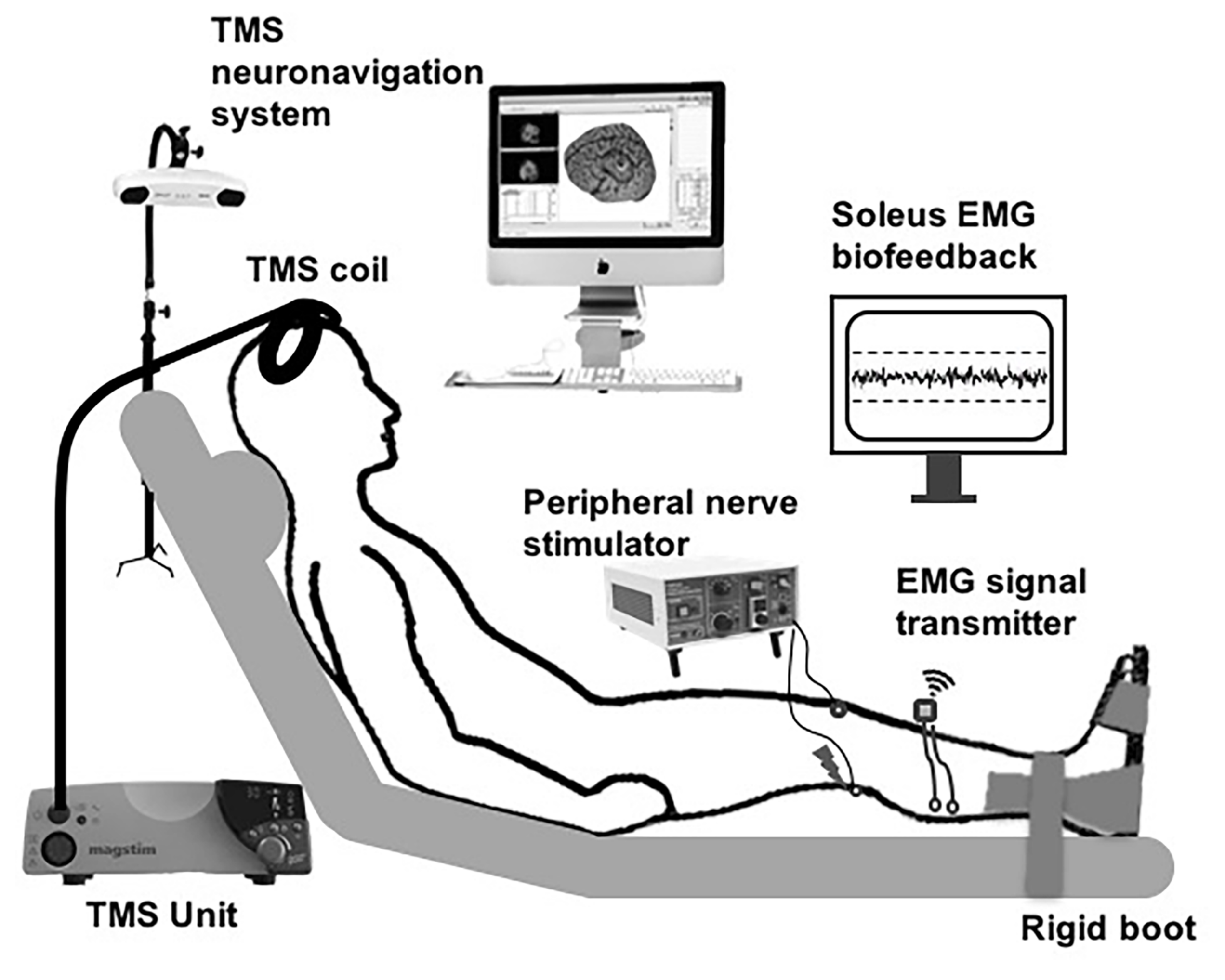

FIGURE 1 | Schematic of the experimental setup. Subthreshold transcranial magnetic stimulation (TMS) pulses applied over the soleus motor cortex hotspot were paired with peripheral nerve stimulation (PNS) delivered to the tibial nerve at a range of inter-stimulus intervals (ISIs). The participants were instructed to maintain low-level background soleus muscle EMG activation targeting 10% maximal voluntary contraction (MVC), with ongoing visual biofeedback of ongoing EMG activity was displayed to the participant throughout the session.

Gray et al., 2017; Kesar et al., 2018a; **Figure 1**). TMS pulses were delivered over the right soleus motor “hot spot” within left M1, defined as the optimal coil position that elicited maximal MEP responses in the soleus at the lowest TMS intensity. A stereotaxic neuronavigation system was used to track and maintain the accuracy of TMS coil positioning (Brainsight v. 2.2.14, Rogue Research Inc., Canada). To determine the active motor threshold (AMT), participants were requested to maintain low-level tonic EMG activity in the right soleus at 10% MVC EMG. AMT was determined as the lowest stimulator intensity needed to evoke a soleus MEP of $\geq$100 μV peak-to-peak amplitude in at least three out of five trials. We were able to elicit measurable MEPs from all study participants. For TMS-conditioning, the TMS intensity was maintained at 90% AMT (sub-threshold).

TMS-Conditioning of the Soleus H-Reflex

To investigate the influence of descending corticomotor projections on spinal reflex excitability, sub-threshold (90% AMT) TMS pulses were delivered at different timing intervals, or ISIs, relative to PNS of the posterior tibial nerve. The ISI between the conditioning TMS pulse (delivered over soleus hotspot on left M1) and the test PNS pulse (delivered in the right popliteal fossa) was varied from −6 to +12 ms. We collected conditioned H-reflex data at 24 different ISIs: −6, −5, −4, −3, −2.5, −2, −1.5, −1, 0, 1, 2, 3, 4, 5, 6, 7, 8, 9, 9.5, 10, 10.5, 11, 11.5 and 12 ms. Negative ISIs indicate that the PNS was delivered prior to TMS, and positive ISIs indicate that the PNS was delivered after the TMS. At each ISI, five conditioned H-reflexes were collected, interspersed with a total of 20 unconditioned (UC) H-reflexes. PNS-evoked responses were collected at a frequency of $\leq$0.25 Hz in random order. The intensity of tibial nerve stimulation was set to elicit an unconditioned H-reflex peak-to-peak amplitude equivalent to 20% of M_{max}, as H-reflexes of this size have been shown to be sensitive to inhibitory and facilitatory conditioning in previous publications (Taube et al., 2015, 2017; Gray et al., 2017).

Data Processing

Peak-to-peak amplitudes of unconditioned and conditioned H-reflexes at each ISI were extracted from raw EMG recorded. At each ISI, the magnitude of H-reflex facilitation or modulation was calculated as conditioned H-reflex amplitude as a percentage of the unconditioned H reflex amplitude. The earliest onset of facilitation indicates the ISI at which the fastest descending TMS-induced volleys arrive at the spinal motoneuron pools. The ISI of onset of earliest facilitation was identified for each participant as the first peak of facilitation that was followed by a period of decline before the facilitation curve resumed (Nielsen et al., 1993; Taube et al., 2015, 2017; Niemann et al., 2018; **Figure 2**). We plotted the relationship between ISI (normalized to EFD 0 ms) and the magnitude of H-reflex facilitation for each participant (**Figure 2**). Once we determined the onset of earliest facilitation, the ISI of this time point was redefined as 0 ms, and all previous and subsequent ISIs were normalized with reference to the earliest onset of facilitation, described as early facilitation delays (EFDs; **Figure 2**). We statistically compared unconditioned vs. conditioned H-reflex amplitudes at EFD 0 ms, as well as at EFD −1 ms to confirm that a significant facilitation occurred at EFD 0 ms (**Figure 3**).

In addition to the individualized determination of the onset of earliest facilitation and magnitude of facilitation at a range of EFDs, the individual-specific peak facilitation for each participant was determined at the ISI that generated maximal facilitation. Previous studies have defined standard early and longer interval or late ISIs as −1.5 ms and +10 ms, respectively. To compare facilitation observed at individualized (determined for each individual using their ISI curve) vs. standard ISIs (the same ISI used for all participants), we compared the magnitude of facilitation at: (i) individualized ISI where earliest facilitation was observed (EFD = 0 ms) vs. a standardized early ISI of −1.5 ms; and (ii) individualized maximal facilitation vs. longer interval facilitation at a standardized ISI of +10 ms.

Statistical Procedures

A repeated-measures analysis of variance (ANOVA) was performed to evaluate the effect of EFD (within-subjects factor with 18 levels, from EFD −2 ms to EFD 15 ms) on the dependent variable of H-reflex facilitation. We used paired t-tests to compare unconditioned vs. conditioned H-reflex amplitudes at EFD 0 ms and at EFD −1 ms. Additionally, to evaluate conditioning effects at standardized vs. individualized ISIs, paired t-tests were used to compare the magnitude of facilitation at: (i) the individual-specific ISI where the earliest onset of facilitation occurred (EFD 0 ms) vs. at a standard early ISI of −1.5 ms; (ii) the individual-specific maximal or peak facilitation vs. at a standard longer interval ISI of +10 ms. The Shapiro-Wilks test showed normal distribution at all except one ISI (EFD = 1 ms). All statistical tests were run in Statistical Package for the Social Sciences (IBM SPSS version 26) and the critical alpha level was set to $p < 0.05$.

RESULTS

Identification of the Earliest Onset of H-Reflex Facilitation in Individual Participants

To determine the influence of TMS-induced fastest descending volleys arriving at the spinal motoneurons, we identified the earliest onset of H-reflex facilitation for each participant. Relationships between ISI and H-reflex facilitation for each participant are shown in **Figure 2**. The onset of the earliest facilitation was observed at ISIs ranging from −3 to −5 ms (mean = −3.70 ± 0.67 ms) across study participants (**Figure 3B**). The average magnitude of facilitation at the earliest onset of facilitation was 158.00 ± 28.58% (**Figures 2**, **4**).

Each individual's data were normalized with reference to the ISI of earliest onset, which was referred to as EFD 0 ms). To confirm that EFD 0 ms was the first arrival of the fastest descending volley at spinal circuits, we statistically compared the unconditioned and conditioned soleus H-reflex amplitudes at EFD −1 ms and 0 ms (**Figures 3C,D**). At EFD −1 ms, there was no significant difference between the unconditioned and conditioned H-reflex amplitude [$p = 0.99$, paired Cohen's d −0.00056 (95.0%CI −0.262, 0.246)]. At EFD 0 ms, there the conditioned H-reflex amplitude was significantly larger than unconditioned [$p = 0.0018$, paired Cohen's $d = 0.709$ (95.0%CI 0.471, 1.04)] (**Figure 3**).

Influence of ISI on TMS-Conditioning of H-Reflex Facilitation

Overall, sub-threshold TMS conditioning facilitated the H-reflex from EFD 0 ms to EFD +15 ms (**Figure 2**). The repeated measures ANOVA evaluating the effect of EFD on H-reflex facilitation revealed a significant main effect for EFD ($F_{2.815,25.335} = 8.406$, $p < 0.01$, $\eta^2 = 0.483$).

Comparison of Early and Late Facilitation Measured at Individualized ISI vs. Standard ISI

To facilitate an individual-specific visualization of our study results, the magnitudes of H-reflex facilitation for each study participant (rows) at each ISI (columns) are demonstrated as a gray-scale gradient map (**Figure 4A**), with the different gray scale colors (from black to white) representing the rank of conditioned H-reflex amplitudes (from highest facilitation to lowest facilitation) for each participant. The onset of earliest facilitation and peak facilitation are both demarcated in the map for each participant, showing the inter-individual variability in these ISIs (**Figure 4A**). The paired t-test showed no significant difference between the facilitation magnitude at the individualized ISI where earliest onset facilitation was observed (EFD 0 ms) vs. facilitation at the standard early ISI of −1.5 ms [152.20 ± 23.05%, 171.78 ± 68.29%, $p = 0.30$, paired Cohen's $d = 0.384$ (95.0%CI −0.289, 1.1)] (**Figure 4B**). In contrast, the paired t-test showed a significantly greater magnitude of peak H-reflex facilitation when determined using an individualized peak ISI vs. the standard longer interval ISI of

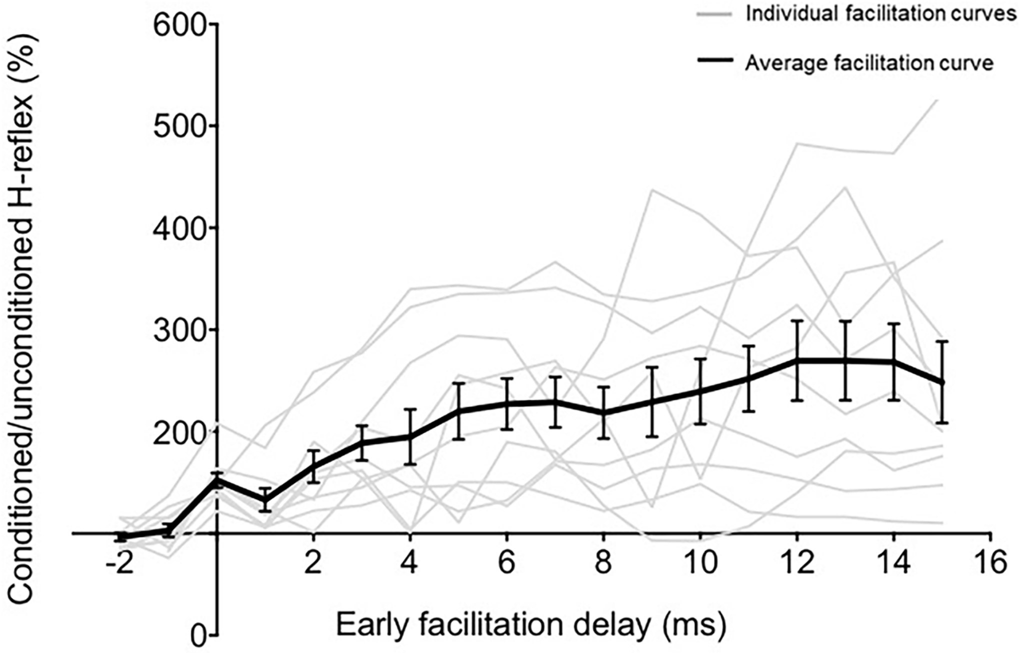

FIGURE 2 | The relationship between ISI and TMS-conditioning of Hoffmann's reflex (H-reflex). The graph demonstrates the relationship between different early facilitation delays (EFDs) and H-reflex facilitation (normalized as a percentage of unconditioned H-reflex amplitude), with gray lines representing data from individual participants and the black line representing the group average (error bars represent standard error). The ordinate (y-axis) shows the amplitude of the conditioned H-reflex as a percentage of the control (unconditioned) reflex amplitude. The abscissa (x-axis) shows the inter-stimulus timing between TMS and PNS normalized with reference to delay (in ms) from the ISI at which the earliest onset of facilitation occurred (EFD).

+10 ms [317.51 ± 134.54%, 269.83 ± 122.57%, $p < 0.01$, paired Cohen's d −0.332 (95.0%CI −0.515, −0.204)] (**Figure 4B**). The magnitude of peak facilitation at longer interval ISIs (both using individualized peak and standard ISI of +10 ms) was significantly greater than the magnitude of earliest onset facilitation observed at EFD 0 ms ($p < 0.01$; **Figure 4B**).

DISCUSSION

Here, we studied the temporal dynamics underlying pairing of TMS with PNS, a promising, non-invasive neurophysiologic approach for indexing the excitability of both direct or fast and indirect or relatively slower descending corticomotor projections onto spinal segmental circuitry. We systematically quantified the inter-individual variability in both the magnitude and timing of occurrence (i.e., ISI) of the earliest onset and peak TMS-induced H-reflex facilitation. Our results revealed substantial inter-individual variability in the timing of the earliest onset and the greatest magnitude of H-reflex facilitation, and support potential methodological advantages and mechanistic insights gained from utilizing individualized ISIs for measurement of earliest onset and longer-interval facilitation.

Mechanisms and Interpretation of Earliest Onset of Facilitation

Our findings show that the earliest onset of H-reflex facilitation occurred at the ISI of −3.70 ± 0.67 ms in healthy participants (**Figures 2**, **3**). The negative values for ISIs of early facilitation indicate that the TMS pulse was delivered after the PNS pulse. This earliest onset of facilitation is posited to represent the excitability of the fastest conducting or direct descending corticomotoneuronal connections (Nielsen et al., 1993; Taube et al., 2015, 2017). In our study, at these ISIs, the TMS-induced volley in these fastest or direct descending pathways produced sufficient depolarization in spinal motoneuron pools innervating the soleus, as evidenced by the larger amplitude of the conditioned H-reflex compared to an unconditioned H-reflex (Leukel et al., 2015; Taube et al., 2015). We identified the earliest onset of facilitation from the ISI curve as the first peak of facilitation followed by a decline in facilitation, based on methodology from previous literature (Keller et al., 2018; **Figure 2**). The decline following the first peak, while poorly understood, may be mediated by the activation of spinal inhibitory interneurons (Nielsen et al., 1993). In our study, the ISI at which we observed earliest facilitation is consistent with findings from a previous study that showed that early-onset or short-latency facilitation occurred in the −4 to −2 ms (−3.54 ± 0.66 ms) ISI range when the soleus was at rest (Taube et al., 2015, 2017). Another study, which used early-onset facilitation to evaluate the effects of ankle joint immobilization, revealed that early facilitation occurred at around the −3 ms ISI on average (Leukel et al., 2015). Similar to our current methods, a previous study recalibrated the ISI of early facilitation as 0 ms to synchronize the subsequent ISIs with respect to the ISI eliciting the earliest onset of facilitation (Aguiar and Baker, 2018). Based on our findings, future studies interested

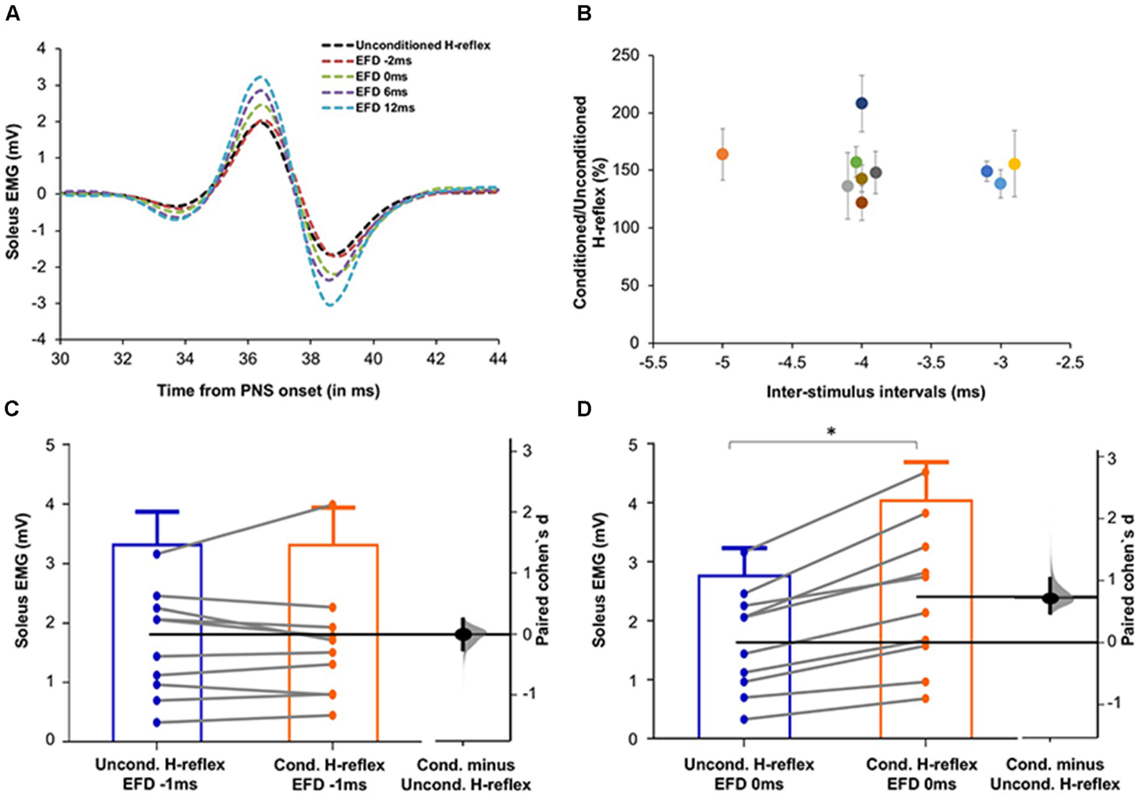

FIGURE 3 | (A) Raw H-reflex data. Raw H-reflex traces from a representative participant without (unconditioned H-reflex) and with TMS conditioning at multiple ISIs (conditioned H-reflexes at different delays with respect to the timing of earliest onset of facilitation, i.e., EFD). The conditioned H-reflexes are displayed at EFD −2 ms, 0 ms, 6 ms, and 12 ms. Note that in contrast to the absence of facilitation at EFD 0 ms, H-reflexes at the other EFD ISI intervals are facilitated (larger in amplitude) compared to the unconditioned H-reflex, showing modulation of the spinal reflex by the descending TMS-induced volleys. **(B)** Magnitude and timing of earliest onset of facilitation. The earliest onset of facilitation was observed at ISIs ranging from −3 to −5 ms (mean = −3.70 ± 0.67ms) across study participants (x-axis). The average magnitude of facilitation (y-axis) was 158.00 ± 28.58% but varied across different ISIs. **(C,D)** Graphs with estimation plots showing comparisons between unconditioned vs. conditioned H-reflex amplitudes at EFD −1 ms and EFD 0 ms. Unconditioned and conditioned H-reflexes (means with standard deviation as well as individual participant data) are shown at EFD −1 ms **(C)** and EFD 0 ms **(D)**. The paired mean difference (Cohen's d) is shown with a Gardner-Altman estimation plot on a floating axis on the right as a bootstrap sampling distribution; the mean difference is depicted as a dot; the 95% confidence interval is indicated by the ends of the vertical error bars. Note that while no significant increase in the conditioned H-reflex amplitudes was observed at EFD −1 ms, a significantly larger amplitude of conditioned vs. unconditioned (with a large effect size) was observed at EFD 0 ms. *Indicates statistically significant difference.

in evaluating the excitability of fastest and/or direct conducting descending projections can test ISIs in the −3 to −4 ms range, normalize individual ISI curves to the ISI of onset of earliest facilitation (EFD 0 ms), and to improve accuracy, if time permits, individually determine the ISI at which early facilitation is observed.

Although several previous studies used one standard ISI to investigate early H-reflex facilitation in their study cohort (Cortes et al., 2011; Leukel et al., 2012; Gray et al., 2017), early facilitation may show inter-individual variability due to physiological and anatomical differences influencing conduction velocities. In our study participant cohort, if we selected a single or standard ISI in the early facilitation range, a subset of participants may not demonstrate H-reflex facilitation (i.e., facilitation greater than 100%). Thus, in addition to evaluating the magnitude and timing of the earliest onset of facilitation, determining the individualized ISI that elicits the greatest magnitude of facilitation can be advantageous. For instance, the magnitude of earliest onset facilitation (i.e., % modulation of the conditioned H-reflex amplitude at EFD 0 ms) would provide a measure of the strength of effective connectivity of the fastest conducting and/or direct descending pathway between M1 and the spinal motoneuron pool. In conjunction, the ISI at which the earliest onset of facilitation occurs (i.e., ISI at which EFD 0 ms occurs) may provide insights into the underlying mechanism of descending cortical influences on spinal excitability. For example, if EFD 0 ms occurs at a longer ISI, showing a rightward shift with a neuropathology, it could indicate that the weakened effective connectivity is in part caused by delayed conduction or aberrant transmission in this fastest and/or direct descending pathway. Interestingly, recent work utilized shorter-interval ISIs with greater temporal resolution than our study (up to 0.1 ms differences between ISIs), and inferred that EFD 0 ms and EFD +0.6 ms were informative of changes in the excitability of circuits within infragranular and supragranular cortical layers, respectively (Leukel and Kurz, 2021).

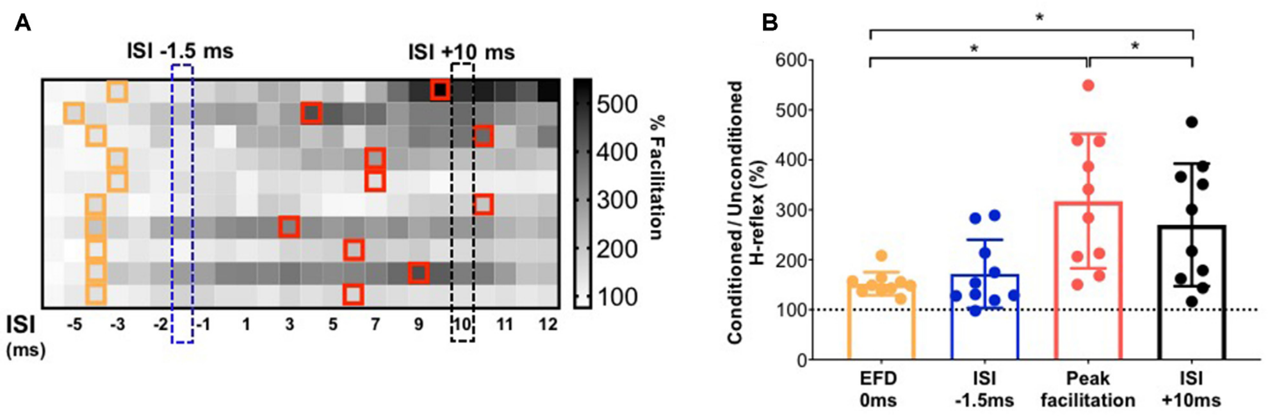

FIGURE 4 | Demonstration of individualized earliest onset of and peak magnitude of facilitation in comparison to standard ISIs. **(A)** The gradient map shows the gray-scale rank of the magnitude of facilitation for each study participant (rows) at each ISI (columns). The cells in the map filled with different gray scale colors (from white to black) represent the rank of conditioned H-reflexes amplitude (from highest facilitation to lowest facilitation) for each participant. For each participant, ISIs at which the earliest onset of facilitation was detected are demarcated with orange outlines. On the same color matrix, individualized ISIs that elicited peak facilitation are demarcated with red outlines. The chart shows the inter-individual variability in the location of ISI that elicits earliest or peak facilitation. **(B)** Comparison of the magnitude of facilitation for early facilitation at individualized EFD 0 ms vs. at a standard early ISI of −1.5 ms; and between individualized peak facilitation vs. at a longer interval standard ISI of +10 ms. *Indicates statistically significant difference.

Our results showing no significant difference in the measured magnitude of early facilitation when using a standardized (−1.5 ms) vs. individualized ISI suggest that at least for younger able-bodied individuals (**Figure 4**), the measurement of earliest onset of facilitation is robust and perhaps less susceptible to inter-trial or physiological variability. The Early onset facilitation measured at a single, standardized ISI such as −1.5 ms may provide a relatively quick and useful index of the overall excitability of relatively fast and direct descending projections. The statistically significant facilitation of the conditioned H-reflex measured at the −1.5 ms ISI also suggests that the coincidence of TMS-induced descending and PNS-induced ascending afferent volleys at the spinal motoneurons elicit robust H-reflex facilitation in able-bodied individuals, and probe the overall excitability or effective connectivity in the population of direct and/or fast descending projections (Cortes et al., 2011; Leukel et al., 2012).

Mechanisms and Interpretation of Longer-Interval and Maximal Facilitation

In addition to evaluating the timing and magnitude of the earliest onset of TMS-induced H-reflex facilitation, we also evaluated a wide range of longer interval ISIs and determined the ISI that elicits the greatest facilitation in our young able-bodied participant cohort (**Figure 2**). As expected, our results showed that the magnitude of peak facilitation was significantly higher than that of earliest onset facilitation (EFD 0 ms). We also showed a high degree of inter-individual variability in the individualized ISIs that elicited peak magnitude of facilitation (**Figure 4A**). This inter-individual variability in the magnitude and ISI of occurrence of peak facilitation perhaps reflects the complex and varied array of descending projections that may contribute to the facilitation measured at longer interval ISIs. The longer interval or late facilitation is hypothesized to be mediated by polysynaptic and/or relatively slower conducting, corticofugal descending pathways between M1 and the spinal motoneuron pool. While this method only provides indirect inference and limited anatomic specificity of these descending pathways, previous studies have hypothesized that they include cortico-reticulo-spinal, cortico-vestibular-spinal, cortico-propriospinal, and spinal interneurons that can synapse on multiple populations of spinal interneurons and motoneurons (Nielsen et al., 1993; Serranova et al., 2008).

In our study, similar to some previous works, we utilized the ISI of +10 ms as the standardized group ISI to measure longer interval facilitation. The challenge with the paired TMS-PNS technique, especially during the measurement of longer interval facilitation, is that multiple descending volleys may contribute additive EPSPs onto spinal motoneuron membranes, providing a varied spatial and temporal integration of membrane excitability at the spinal motoneuron pool, which could also be a potential explanation for the higher magnitude of facilitation observed at the longer interval ISIs. The conduction velocities and number of synapses in corticomotor projections may vary across individuals (Nielsen et al., 1993; Serranova et al., 2008). Also, the polysynaptic and multi-pathway neural circuit correlates underlying longer interval facilitation may result in greater variability in amplitudes of conditioned soleus H-reflexes (Nielsen et al., 1993; Nielsen and Petersen, 1995; Gray et al., 2017). The TMS-induced descending volleys within different corticofugal pathways may contribute to the inter-individual differences in both the ISI at which peak facilitation is observed and the magnitude of peak facilitation. Our results that a significantly larger magnitude of peak facilitation was observed at individualized ISIs vs. a standard 10 ms ISI, as well as the inter-individual variability in the ISI at which peak facilitation was observed, suggest that individualized ISIs may need to be determined for a comprehensive and rigorous measurement of

TMS-induced H-reflex facilitation mediated by slower and/or indirect descending pathways.

Based on our current results, we posit that the measurement of longer-interval facilitation (e.g., EFD 0 ms to 12 ms) at a range of ISIs can help to index the effective connectivity of relatively slower and/or indirect pathways. If the methodological or time constraints of a study necessitate a brief assessment of descending corticospinal effective connectivity, then peak facilitation at longer interval ISIs, even at a single ISI (e.g., +10 ms) may be sufficient to index the cumulative strength or excitability of the array of other descending connections between M1 and spinal motoneurons that are distinct from the fastest and/or direct descending pathways probed *via* earliest-onset facilitation. For a more refined or fine-grained characterization of descending corticospinal effective connectivity, a comprehensive longer-interval ISI curve for individual subjects (similar to **Figure 3**) can be collected, and also used to map changes in the ISI curve before vs. after an intervention or experimental manipulation. If the ISI vs. H-reflex facilitation curve shifts upward at longer intervals, that may suggest an increased effective connectivity in the slower or indirect descending pathways. If the peak or the entire curve shifts to the right, this may indicate a greater and perhaps compensatory reliance on a sub-population of relatively slower or indirect pathways (e.g., brain stem or propriospinal-mediated descending projections).

Potential Mechanisms and Implications of Inter-Individual Variability in Magnitude and Timing of TMS-Induced Facilitation

We posit that a neurophysiological assessment battery combining TMS, H-reflexes, and TMS-conditioned H-reflexes can probe site-specific changes in descending corticomotor circuits (Kurz et al., 2019), spinal reflex circuits (Niemann et al., 2018), and interactions between the two. Thus, utilization of paired TMS and PNS can provide more in-depth mechanistic insights into the specific site(s) and magnitude of training-induced plasticity in sensorimotor control circuitry. TMS-derived measures (e.g., MEP amplitude, motor threshold) and H-reflex data can be influenced by testing conditions such as posture, muscle activation, EMG sensor or stimulation electrode position, etc. In the current study, we controlled for and maintained consistency of, these methodological parameters, manipulating only the relative timing of delivery of TMS with respect to PNS, and collecting unconditioned H-reflexes as a control or reference for the TMS-conditioned H-reflex amplitudes. Inter-individual differences in H-reflex and MEP latencies, nerve conduction velocity, limb length, neuroanatomical structure, and strength of effective functional connectivity may explain the variability observed in the magnitude of facilitation as well as the ISIs eliciting earliest or peak facilitation. Additionally, for the same individual, the trial-to-trial variability in latencies and relative synchronization of TMS-induced descending volleys and PNS-induced ascending volleys may result in physiological variability in the arrival time of orthodromic and antidromic stimuli at the spinal motoneurons (Baudry et al., 2015), which can further contribute to the variability in TMS-induced facilitation. In recent work by Wiegel and Leukel, during TMS-conditioning of H-reflexes, different TMS intensities (e.g., above resting motor threshold), as well as transcranial electrical stimulation, were used in upper limb muscles to characterize different cortical pathways (Leukel and Kurz, 2021). Recent work in monkey and human models also underscores the possibility of measuring the excitability of different cortical circuits by TMS H-reflex conditioning (Wiegel et al., 2018; Kurz et al., 2019).

Limitations and Future Directions

The limitations of this study include the relatively small sample size, although it is consistent with samples in other similar studies (Gray et al., 2017; Lopez et al., 2020; Capozio et al., 2021). For the current study, a single nerve stimulation intensity was chosen (PNS intensity eliciting an H-reflex amplitude of 20% Mmax) based on previous literature, and facilitation was not measured at a range of intensities across the H-reflex recruitment curve. Similarly, a single subthreshold TMS intensity was used. For instance, in recent studies, H-reflex facilitation at certain EFDs was shown to be differentially influenced by specific movement tasks (Wiegel et al., 2020; Wiegel and Leukel, 2020). The stimulation parameters used here (e.g., 1 ms pulse width, the separation between consecutive ISIs, sub-threshold TMS according to active motor threshold), while mostly consistent with previous work, have been modified in recent studies, particularly to probe specific neural contributions at the ISIs eliciting early facilitation. Future studies can investigate factors influencing the optimal ISI (e.g., the latency of MEPs and H-reflexes) and develop a formula to enable individual-specific estimation of the optimal ISI for measuring earliest onset and peak facilitation.

Although earliest-onset and peak facilitation derived using paired TMS and PNS help to better localize the site of plasticity compared to TMS alone or H-reflexes alone, these techniques do not have the specificity to identify exactly which neural pathway is implicated in eliciting facilitation at different ISIs. As is true for many other non-invasive approaches, especially at longer ISIs, the observed H-reflex facilitation can be caused by many neural sources, spanning spinal, brain stem, and cortical sites, which are challenging to discriminate. Future work can combine TMS-facilitation of H-reflexes with neuroanatomical imaging or complementary neurophysiological techniques to determine relative contributions of specific descending pathways (e.g., cortico-reticulo-spinal, proprio-spinal) to these measures. Further, this method is limited to those muscles from which H-reflexes can be consistently elicited. The soleus and other lower limb muscles may have stronger spinal network contributions, which could influence our findings. Between-muscle differences in neuromotor circuit control can be investigated by applying similar methods in upper limb muscles and other lower limb muscles. We measured H-reflex facilitation in a seated active state for our study (i.e., while participants maintained low-level background EMG of ∼10% MVC); future work can compare facilitation in seated vs. standing, or during a dynamic postural or walking task (Nielsen et al., 1993; Nielsen and Petersen, 1995).

Evaluation of the effect of neuropathologies such as stroke or spinal cord injury on the magnitude and temporal profile of TMS-induced H-reflex facilitation is a promising area of future investigation. Understanding how the relationship between ISI and magnitude of H-reflex facilitation (i.e., the ISI curve similar to shown in **Figure 1**) is modulated by neuropathological conditions warrants more study. For example, one may postulate that in individuals with a cortical or subcortical lesion affecting the corticospinal pathway, the faster-conducting, direct descending projections may show greater disruption of effective connectivity compared to relatively slower, indirect descending projections that traverse through brain stem centers (Li and Francisco, 2015; Li et al., 2018). In fact, these relatively slower and indirect descending pathways, partly indexed using peak facilitation or area under the curve for longer-latency ISIs, may show a compensatory reorganization to mediate functional recovery following stroke (Wilkins et al., 2020; Hammerbeck et al., 2021). We therefore would hypothesize that post-stroke individuals may show a greater or preferential reduction in the magnitude of earliest onset of TMS-induced facilitation (i.e., EFD 0 ms).

CONCLUSIONS

Our study provides further evidence showcasing the advantage of TMS-induced H-reflex facilitation, especially when measured at a range of ISIs, as a unique non-invasive probe to differentially parse out the excitability of the array of direct, fast and indirect, slower descending corticomotor projections onto spinal reflex circuits. Our study findings can guide the methodology for use of the paired TMS-PNS technique in future investigations. Due to variability in conduction latencies of neuronal tracts in neurologically impaired individuals (such as stroke or multiple sclerosis), as well as inter-individual variability in physiological latencies, further development of methods and formulae to estimate the optimal ISI between TMS and PNS for each individual based on their baseline data merits further investigation.

DATA AVAILABILITY STATEMENT

The raw data supporting the conclusions of this article will be made available by the authors, without undue reservation.

ETHICS STATEMENT

The studies involving human participants were reviewed and approved by Emory University Institutional Review Board (IRB). The patients/participants provided their written informed consent to participate in this study.

AUTHOR CONTRIBUTIONS

TK and MB conceived and designed research. MH performed experiments with a group of graduate students. JX, AL, and MH analyzed data, prepared figures, and drafted manuscript. JX, AL, TK, MB, and MH interpreted results of experiments, prepared, edited and revised the manuscript, and approved the final version of manuscript. TK edited the final versions of the manuscript. All authors contributed to the article and approved the submitted version.

FUNDING

This work was supported by NIH NICHD grants (K01 HD079584, R01 HD09597) to TK, NIH NICHD grant (K12HD055931) and NIH grant (5R24HD050821-11) to MB, and NIH Diversity Supplement (3R01HD046922-13S1) to AL. JX was supported by China Scholarship Council (CSC, No. 201706165058).

ACKNOWLEDGMENTS

We would like to thank Dr. Manning Sabatier, Dr. Carly McMullen, Steven Eicholtz, Class of 2017 DPT students research group, and Kesar lab members for assistance with data collection.

REFERENCES

Abbruzzese, G., and Trompetto, C. (2002). Clinical and research methods for evaluating cortical excitability. *J. Clin. Neurophysiol.* 19, 307–321. doi: 10.1097/00004691-200208000-00005

Aguiar, S. A., and Baker, S. N. (2018). Descending inputs to spinal circuits facilitating and inhibiting human wrist flexors. *Front. Hum. Neurosci.* 12:147. doi: 10.3389/fnhum.2018.00147

Bae, S., and Kim, K. Y. (2017). Dual-afferent sensory input training for voluntary movement after stroke: a pilot randomized controlled study. *NeuroRehabilitation* 40, 293–300. doi: 10.3233/NRE-161417

Barker, A. T., Jalinous, R., and Freeston, I. L. (1985). Non-invasive magnetic stimulation of human motor cortex. *Lancet* 1, 1106–1107. doi: 10.1016/s0140-6736(85)92413-4

Baudry, S., Collignon, S., and Duchateau, J. (2015). Influence of age and posture on spinal and corticospinal excitability. *Exp. Gerontol.* 69, 62–69. doi: 10.1016/j.exger.2015.06.006

Behrens, M., Mau-Moeller, A., Wassermann, F., Bader, R., and Bruhn, S. (2015). Effect of balance training on neuromuscular function at rest and during isometric maximum voluntary contraction. *Eur. J. Appl. Physiol.* 115, 1075–1085. doi: 10.1007/s00421-014-3089-1

Brown, K. E., Neva, J. L., Feldman, S. J., Staines, W. R., and Boyd, L. A. (2018). Sensorimotor integration in chronic stroke: baseline differences and response to sensory training. *Restor. Neurol. Neurosci.* 36, 245–259. doi: 10.3233/RNN-170790

Burke, D. (2016). Clinical uses of H reflexes of upper and lower limb muscles. *Clin. Neurophysiol. Pract.* 1, 9–17. doi: 10.1016/j.cnp.2016.02.003

Capozio, A., Chakrabarty, S., and Astill, S. (2021). Reliability of the TMS-conditioned monosynaptic reflex in the flexor carpi radialis muscle. *Neurosci. Lett.* 745:135622. doi: 10.1016/j.neulet.2020.135622

Celnik, P. (2015). Understanding and modulating motor learning with cerebellar stimulation. *Cerebellum* 14, 171–174. doi: 10.1007/s12311-014-0607-y

Christiansen, L., and Perez, M. A. (2018). Targeted-plasticity in the corticospinal tract after human spinal cord injury. *Neurotherapeutics* 15, 618–627. doi: 10.1007/s13311-018-0639-y

Clark, B. C., Issac, L. C., Lane, J. L., Damron, L. A., and Hoffman, R. L. (2008). Neuromuscular plasticity during and following 3 wk of human forearm cast immobilization. *J. Appl. Physiol. (1985)* 105, 868–878. doi: 10.1152/japplphysiol.90530.2008

Clark, B. C., Taylor, J. L., Hoffman, R. L., Dearth, D. J., and Thomas, J. S. (2010). Cast immobilization increases long-interval intracortical inhibition. *Muscle Nerve* 42, 363–372. doi: 10.1002/mus.21694

Cortes, M., Thickbroom, G. W., Valls-Sole, J., Pascual-Leone, A., and Edwards, D. J. (2011). Spinal associative stimulation: a non-invasive stimulation paradigm to modulate spinal excitability. *Clin. Neurophysiol.* 122, 2254–2259. doi: 10.1016/j.clinph.2011.02.038

Cowan, J. M., Day, B. L., Marsden, C., and Rothwell, J. C. (1986). The effect of percutaneous motor cortex stimulation on H reflexes in muscles of the arm and leg in intact man. *J. Physiol.* 377, 333–347. doi: 10.1113/jphysiol.1986.sp016190

Crone, C., Johnsen, L. L., Biering-Sorensen, F., and Nielsen, J. B. (2003). Appearance of reciprocal facilitation of ankle extensors from ankle flexors in patients with stroke or spinal cord injury. *Brain* 126, 495–507. doi: 10.1093/brain/awg036

Geertsen, S. S., van de Ruit, M., Grey, M. J., and Nielsen, J. B. (2011). Spinal inhibition of descending command to soleus motoneurons is removed prior to dorsiflexion. *J. Physiol.* 589, 5819–5831. doi: 10.1113/jphysiol.2011.214387

Gray, W. A., Sabatier, M. J., Kesar, T. M., and Borich, M. R. (2017). Establishing between-session reliability of TMS-conditioned soleus H-reflexes. *Neurosci. Lett.* 640, 47–52. doi: 10.1016/j.neulet.2017.01.032

Hallett, M. (2007). Transcranial magnetic stimulation: a primer. *Neuron* 55, 187–199. doi: 10.1016/j.neuron.2007.06.026

Hammerbeck, U., Tyson, S. F., Samraj, P., Hollands, K., Krakauer, J. W., and Rothwell, J. (2021). The strength of the corticospinal tract not the reticulospinal tract determines upper-limb impairment level and capacity for skill-acquisition in the sub-acute Post-stroke period. *Neurorehabil. Neural Repair* 35, 812–822. doi: 10.1177/15459683211028243

Hodapp, M., Vry, J., Mall, V., and Faist, M. (2009). Changes in soleus H-reflex modulation after treadmill training in children with cerebral palsy. *Brain* 132, 37–44. doi: 10.1093/brain/awn287

Hodgkin, A. L., and Huxley, A. F. (1952). A quantitative description of membrane current and its application to conduction and excitation in nerve. *J. Physiol.* 117, 500–544. doi: 10.1113/jphysiol.1952.sp004764

Kantak, S., McGrath, R., Zahedi, N., and Luchmee, D. (2018). Behavioral and neurophysiological mechanisms underlying motor skill learning in patients with post-stroke hemiparesis. *Clin. Neurophysiol.* 129, 1–12. doi: 10.1016/j.clinph.2017.10.010

Kantak, S. S., Wittenberg, G. F., Liao, W. W., Magder, L. S., Rogers, M. W., and Waller, S. M. (2013). Posture-related modulations in motor cortical excitability of the proximal and distal arm muscles. *Neurosci. Lett.* 533, 65–70. doi: 10.1016/j.neulet.2012.10.048

Keller, M., Taube, W., and Lauber, B. (2018). Task-dependent activation of distinct fast and slow(er) motor pathways during motor imagery. *Brain Stimul.* 11, 782–788. doi: 10.1016/j.brs.2018.02.010

Kesar, T. M., Eicholtz, S., Lin, B. J., Wolf, S. L., and Borich, M. R. (2018a). Effects of posture and coactivation on corticomotor excitability of ankle muscles. *Restor. Neurol. Neurosci.* 36, 131–146. doi: 10.3233/RNN-170773

Kesar, T. M., Stinear, J. W., and Wolf, S. L. (2018b). The use of transcranial magnetic stimulation to evaluate cortical excitability of lower limb musculature: challenges and opportunities. *Restor. Neurol. Neurosci.* 36, 333–348. doi: 10.3233/RNN-170801

Knikou, M. (2017). Spinal excitability changes after transspinal and transcortical paired associative stimulation in humans. *Neural Plast.* 2017:6751810. doi: 10.1155/2017/6751810

Kobayashi, M., and Pascual-Leone, A. (2003). Transcranial magnetic stimulation in neurology. *Lancet Neurol.* 2, 145–156. doi: 10.1016/s1474-4422(03)00321-1

Kuck, A., Stegeman, D. F., van der Kooij, H., and van Asseldonk, E. H. F. (2018). Changes in H-reflex recruitment after trans-spinal direct current stimulation with multiple electrode configurations. *Front. Neurosci.* 12:151. doi: 10.3389/fnins.2018.00151

Kurz, A., Xu, W., Wiegel, P., Leukel, C., and S, N. B. (2019). Non-invasive assessment of superficial and deep layer circuits in human motor cortex. *J. Physiol.* 597, 2975–2991. doi: 10.1113/JP277849

Leukel, C., and Kurz, A. (2021). Determining the types of descending waves from transcranial magnetic stimulation measured with conditioned H-reflexes in humans. *Eur. J. Neurosci.* 54, 5038–5046. doi: 10.1111/ejn.15308

Leukel, C., Taube, W., Beck, S., and Schubert, M. (2012). Pathway-specific plasticity in the human spinal cord. *Eur. J. Neurosci.* 35, 1622–1629. doi: 10.1111/j.1460-9568.2012.08067.x

Leukel, C., Taube, W., Rittweger, J., Gollhofer, A., Ducos, M., Weber, T., et al. (2015). Changes in corticospinal transmission following 8weeks of ankle joint immobilization. *Clin. Neurophysiol.* 126, 131–139. doi: 10.1016/j.clinph.2014.04.002

Li, S., and Francisco, G. E. (2015). New insights into the pathophysiology of post-stroke spasticity. *Front. Hum. Neurosci.* 9:192. doi: 10.3389/fnhum.2015.00192

Li, S., Francisco, G. E., and Zhou, P. (2018). Post-stroke hemiplegic gait: new perspective and insights. *Front. Physiol.* 9:1021. doi: 10.3389/fphys.2018.01021

Lopez, A. J., Xu, J., Hoque, M. M., McMullen, C., Kesar, T. M., and Borich, M. R. (2020). Integration of convergent sensorimotor inputs within spinal reflex circuits in healthy adults. *Front. Hum. Neurosci.* 14:592013. doi: 10.3389/fnhum.2020.592013

Lundbye-Jensen, J., and Nielsen, J. B. (2008). Immobilization induces changes in presynaptic control of group Ia afferents in healthy humans. *J. Physiol.* 586, 4121–4135. doi: 10.1113/jphysiol.2008.156547

McNeil, C. J., Butler, J. E., Taylor, J. L., and Gandevia, S. C. (2013). Testing the excitability of human motoneurons. *Front. Hum. Neurosci.* 7:152. doi: 10.3389/fnhum.2013.00152

Meehan, S. K., Legon, W., and Staines, W. R. (2008). Paired-pulse transcranial magnetic stimulation of primary somatosensory cortex differentially modulates perception and sensorimotor transformations. *Neuroscience* 157, 424–431. doi: 10.1016/j.neuroscience.2008.09.008

Meunier, S., Kwon, J., Russmann, H., Ravindran, S., Mazzocchio, R., and Cohen, L. (2007). Spinal use-dependent plasticity of synaptic transmission in humans after a single cycling session. *J. Physiol.* 579, 375–388. doi: 10.1113/jphysiol.2006.122911

Nielsen, J., and Petersen, N. (1995). Evidence favouring different descending pathways to soleus motoneurones activated by magnetic brain stimulation in man. *J. Physiol.* 486, 779–788. doi: 10.1113/jphysiol.1995.sp020853

Nielsen, J., Petersen, N., Deuschl, G., and Ballegaard, M. (1993). Task-related changes in the effect of magnetic brain stimulation on spinal neurones in man. *J. Physiol.* 471, 223–243. doi: 10.1113/jphysiol.1993.sp019899

Niemann, N., Wiegel, P., Kurz, A., Rothwell, J. C., and Leukel, C. (2018). Assessing TMS-induced D and I waves with spinal H-reflexes. *J. Neurophysiol* 119, 933–943. doi: 10.1152/jn.00671.2017

Opie, G. M., Evans, A., Ridding, M. C., and Semmler, J. G. (2016). Short-term immobilization influences use-dependent cortical plasticity and fine motor performance. *Neuroscience* 330, 247–256. doi: 10.1016/j.neuroscience.2016.06.002

Palmer, J. A., Wolf, S. L., and Borich, M. R. (2018). Paired associative stimulation modulates corticomotor excitability in chronic stroke: a preliminary investigation. *Restor. Neurol. Neurosci.* 36, 183–194. doi: 10.3233/RNN-170785

Perez, M. A., Lundbye-Jensen, J., and Nielsen, J. B. (2007). Task-specific depression of the soleus H-reflex after cocontraction training of antagonistic ankle muscles. *J. Neurophysiol.* 98, 3677–3687. doi: 10.1152/jn.00988.2007

Pierrot-Deseilligny, E., and Mazevet, D. (2000). The monosynaptic reflex: a tool to investigate motor control in humans. Interest and limits. *Neurophysiol. Clin.* 30, 67–80. doi: 10.1016/s0987-7053(00)00062-9

Rio-Rodriguez, D., Iglesias-Soler, E., and Fernandez-Del-Olmo, M. (2017). Modulation of quadriceps corticospinal excitability by femoral nerve stimulation. *Neurosci. Lett.* 637, 148–153. doi: 10.1016/j.neulet.2016.11.033

Roosink, M., and Zijdewind, I. (2010). Corticospinal excitability during observation and imagery of simple and complex hand tasks: implications for motor rehabilitation. *Behav. Brain Res.* 213, 35–41. doi: 10.1016/j.bbr.2010.04.027

Rozand, V., Grospretre, S., Stapley, P. J., and Lepers, R. (2015). Assessment of neuromuscular function using percutaneous electrical nerve stimulation. *J. Vis. Exp.* 103:52974. doi: 10.3791/52974

Schieppati, M. (1987). The hoffmann reflex: a means of assessing spinal reflex excitability and its descending control in man. *Prog. Neurobiol.* 28, 345–376. doi: 10.1016/0301-0082(87)90007-4

Serranova, T., Valls-Sole, J., Munoz, E., Genis, D., Jech, R., and Seeman, P. (2008). Abnormal corticospinal tract modulation of the soleus H reflex in patients with pure spastic paraparesis. *Neurosci. Lett.* 437, 15–19. doi: 10.1016/j.neulet.2008.03.068

Stefan, K., Cohen, L. G., Duque, J., Mazzocchio, R., Celnik, P., Sawaki, L., et al. (2005). Formation of a motor memory by action observation. *J. Neurosci.* 25, 9339–9346. doi: 10.1523/JNEUROSCI.2282-05.2005

Tanuma, A., Fujiwara, T., Yamaguchi, T., Ro, T., Arano, H., Uehara, S., et al. (2017). After-effects of pedaling exercise on spinal excitability and spinal reciprocal inhibition in patients with chronic stroke. *Int. J. Neurosci.* 127, 73–79. doi: 10.3109/00207454.2016.1144055

Taube, W., Gruber, M., Beck, S., Faist, M., Gollhofer, A., and Schubert, M. (2007). Cortical and spinal adaptations induced by balance training: correlation between stance stability and corticospinal activation. *Acta Physiol. (Oxf)* 189, 347–358. doi: 10.1111/j.1748-1716.2007.01665.x

Taube, W., Leukel, C., Nielsen, J. B., and Lundbye-Jensen, J. (2015). Repetitive activation of the corticospinal pathway by means of rTMS may reduce the efficiency of corticomotoneuronal synapses. *Cereb. Cortex* 25, 1629–1637. doi: 10.1093/cercor/bht359

Taube, W., Leukel, C., Nielsen, J. B., and Lundbye-Jensen, J. (2017). Non-invasive assessment of changes in corticomotoneuronal transmission in humans. *J. Vis. Exp.* 123:52663. doi: 10.3791/52663

Thompson, A. K., and Wolpaw, J. R. (2014). Operant conditioning of spinal reflexes: from basic science to clinical therapy. *Front. Integr. Neurosci.* 8:25. doi: 10.3389/fnint.2014.00025

Thompson, A. K., and Wolpaw, J. R. (2015). Restoring walking after spinal cord injury: operant conditioning of spinal reflexes can help. *Neuroscientist* 21, 203–215. doi: 10.1177/1073858414527541

Urbin, M. A., Ozdemir, R. A., Tazoe, T., and Perez, M. A. (2017). Spike-timing-dependent plasticity in lower-limb motoneurons after human spinal cord injury. *J. Neurophysiol.* 118, 2171–2180. doi: 10.1152/jn.00111.2017

Veldman, M. P., Zijdewind, I., Maffiuletti, N. A., and Hortobagyi, T. (2016). Motor skill acquisition and retention after somatosensory electrical stimulation in healthy humans. *Front. Hum. Neurosci.* 10:115. doi: 10.3389/fnhum.2016.00115

Wiegel, P., Kurz, A., and Leukel, C. (2020). Evidence that distinct human primary motor cortex circuits control discrete and rhythmic movements. *J. Physiol.* 598, 1235–1251. doi: 10.1113/JP278779

Wiegel, P., and Leukel, C. (2020). Training of a discrete motor skill in humans is accompanied by increased excitability of the fastest corticospinal connections at movement onset. *J. Physiol.* 598, 3485–3500. doi: 10.1113/JP279879

Wiegel, P., Niemann, N., Rothwell, J. C., and Leukel, C. (2018). Evidence for a subcortical contribution to intracortical facilitation. *Eur. J. Neurosci.* 47, 1311–1319. doi: 10.1111/ejn.13934

Wilkins, K. B., Yao, J., Owen, M., Karbasforoushan, H., Carmona, C., and Dewald, J. P. A. (2020). Limited capacity for ipsilateral secondary motor areas to support hand function post-stroke. *J. Physiol.* 598, 2153–2167. doi: 10.1113/JP279377

Conflict of Interest: The authors declare that the research was conducted in the absence of any commercial or financial relationships that could be construed as a potential conflict of interest.

frontiers
in Integrative Neuroscience

ORIGINAL RESEARCH
published: 02 February 2022
doi: 10.3389/fnint.2021.796472

Translations of the Humeral Head Elicit Reflexes in Rotator Cuff Muscles That Are Larger Than Those in the Primary Shoulder Movers

Constantine P. Nicolozakes[1,2,3]*, **Margaret S. Coats-Thomas**[1,2,3], **Daniel Ludvig**[1,2], **Amee L. Seitz**[4] **and Eric J. Perreault**[1,2,5]

[1] Department of Biomedical Engineering, Northwestern University, Evanston, IL, United States, [2] Shirley Ryan AbilityLab, Chicago, IL, United States, [3] Feinberg School of Medicine, Northwestern University, Chicago, IL, United States, [4] Department of Physical Therapy & Human Movement Sciences, Northwestern University, Chicago, IL, United States, [5] Department of Physical Medicine and Rehabilitation, Northwestern University, Chicago, IL, United States

Edited by:
Richard Nichols,
Georgia Institute of Technology,
United States

Reviewed by:
Isaac Louis Kurtzer,
New York Institute of Technology,
United States
Ken Muramatsu,
Kyorin University, Japan
Beven Livingston,
University of North Florida,
United States

***Correspondence:**
Constantine P. Nicolozakes
constantine.nicolozakes@
northwestern.edu

Received: 16 October 2021
Accepted: 22 December 2021
Published: 02 February 2022

Citation:
Nicolozakes CP, Coats-Thomas MS, Ludvig D, Seitz AL and Perreault EJ (2022) Translations of the Humeral Head Elicit Reflexes in Rotator Cuff Muscles That Are Larger Than Those in the Primary Shoulder Movers. Front. Integr. Neurosci. 15:796472. doi: 10.3389/fnint.2021.796472

Muscle activation helps stabilize the glenohumeral joint and prevent dislocations, which are more common at the shoulder than at any other human joint. Feedforward control of shoulder muscles is important for protecting the glenohumeral joint from harm caused by anticipated external perturbations. However, dislocations are frequently caused by unexpected perturbations for which feedback control is essential. Stretch-evoked reflexes elicited by translations of the glenohumeral joint may therefore be an important mechanism for maintaining joint integrity, yet little is known about them. Specifically, reflexes elicited by glenohumeral translations have only been studied under passive conditions, and there have been no investigations of how responses are coordinated across the functional groupings of muscles found at the shoulder. Our objective was to characterize stretch-evoked reflexes elicited by translations of the glenohumeral joint while shoulder muscles are active. We aimed to determine how these responses differ between the rotator cuff muscles, which are essential for maintaining glenohumeral stability, and the primary shoulder movers, which are essential for the large mobility of this joint. We evoked reflexes using anterior and posterior translations of the humeral head while participants produced voluntary isometric torque in six directions spanning the three rotational degrees-of-freedom about the shoulder. Electromyograms were used to measure the stretch-evoked reflexes elicited in nine shoulder muscles. We found that reflex amplitudes were larger in the rotator cuff muscles than in the primary shoulder movers, in part due to increased background activation during torque generation but more so due to an increased scaling of reflex responses with background activation. The reflexes we observed likely arose from the diversity of proprioceptors within the muscles and in the passive structures surrounding the shoulder. The large reflexes observed in the rotator cuff muscles suggest that feedback control of the rotator cuff augments the feedforward control that serves to compress the humeral head into the glenoid. This coordination may serve to stabilize the shoulder rapidly when preparing for and responding to unexpected disturbances.

Keywords: stretch reflex, glenohumeral joint, glenohumeral stability, reflex amplitude, reflex latency, reflex gain-scaling, fine-wire intramuscular electromyography, surface electromyography

INTRODUCTION

The shoulder is the most mobile joint in the human body (Boone and Azen, 1979), allowing for the completion of complex functional and recreational activities. The anatomy of the glenohumeral joint, with few passive constraints on joint rotation (Soslowsky et al., 1992), facilitates the shoulder's expansive mobility but increases its susceptibility to instability, which is defined clinically as pain and discomfort due to excessive humeral head translation (Lippitt et al., 1991). The most severe consequence of instability is dislocation or translation of the entire humeral head beyond the rim of the glenoid fossa. Dislocations occur more commonly in the shoulder than in any other joint (Kerr et al., 2011). To maintain glenohumeral stability without compromising mobility, the muscles crossing the glenohumeral joint must provide active stability, which is achieved through a combination of voluntary feedforward control and involuntary feedback control (Labriola et al., 2005; Veeger and Van Der Helm, 2007). Feedforward control is particularly important for protecting the shoulder in response to predictable external perturbations that can cause humeral head translations. Shoulder dislocations, however, are more commonly caused by unexpected perturbations (Longo et al., 2011; Montgomery et al., 2019), for which feedback control is essential.

Stretch-evoked reflexes are a commonly studied form of feedback control that have been shown to increase the stiffness of several other joints (Sinkjaer and Hayashi, 1989; Carter et al., 1990; Kearney et al., 1997). A few studies have characterized stretch-evoked reflexes at the shoulder in response to rotations of the glenohumeral joint. These have demonstrated differences in the characteristics of reflex amplitudes and latencies between rotator cuff muscles and other muscles that primarily move the shoulder (Myers et al., 2003, 2004; Day et al., 2012; Nicolozakes, 2021). However, the feedback control most relevant to preventing shoulder dislocations is that which responds to unexpected translations, not rotations, of the shoulder. Translations of the humeral head will excite the varied proprioceptors in the ligaments and capsule surrounding the shoulder (Guanche et al., 1999; Witherspoon et al., 2014) as well as the muscle spindles most commonly associated with stretch-evoked reflexes. These translations elicit reflexively induced changes in muscle activation but have only been assessed during passive conditions (Latimer et al., 1998) that are less relevant to the functional states in which dislocations typically occur.

Rotator cuff muscles are believed to function as the primary stabilizers of the glenohumeral joint, complementing the role of primary shoulder movers that generate the torques required to move the shoulder through its range of motion. Rotator cuff muscles are regarded as active stabilizers because they have lines of action that pull the humeral head into the glenoid fossa (Lee et al., 2000), stabilizing the joint when activated voluntarily (Lippitt and Matsen, 1993; Lippitt et al., 1993). In contrast, the primary shoulder movers have more anterior or posterior lines of action that can destabilize the joint if agonists and antagonists are not activated in coordination (Ackland and Pandy, 2009). If rotator cuff muscles contribute to feedback stability, it would be expected that they would exhibit large reflexes in response to translational perturbations. However, their lines of action are likely to result in smaller muscle length changes in response to glenohumeral translations than would occur in the primary shoulder movers. It, therefore, remains unclear if the feedback control of the muscles crossing the shoulder is structured to leverage the anatomical differences between the rotator cuff muscles and the primary shoulder movers.

The purpose of this study was to compare stretch-evoked reflexes elicited by translations of the glenohumeral joint between rotator cuff muscles and primary shoulder movers. We hypothesized that reflexes would be larger in the rotator cuff muscles than in the primary shoulder movers based on the different functional roles of these groups. To test our hypothesis, we elicited reflexes by translating the humeral head anteriorly and posteriorly within the glenohumeral joint. Reflexes were recorded using electromyograms while participants produced isometric shoulder torques in multiple directions and at multiple levels of exertion to create a diverse set of active conditions that reflect daily shoulder use. Our results suggest that feedback control of the shoulder is organized to exploit the anatomical arrangement of muscles crossing the shoulder so as to protect against dislocations due to externally imposed translations.

METHODS

Overview

Our primary experiment was designed to elicit reflexes in shoulder muscles with translational perturbations, allowing us to compare the characteristics of these reflexes between rotator cuff muscles and primary shoulder movers. The deep rotator cuff muscles required fine-wire intramuscular electromyogram (EMG) recordings, whereas surface EMG recordings were made in all other muscles. We, therefore, conducted a secondary control experiment to determine if these different recording modalities influenced our measures of EMG, and in particular the latencies and amplitudes of the measured reflexes.

Participants

Fifteen healthy adults (eight female, seven male; mean age ± SD: 25.5 ± 4.2 years) participated in the primary experiment of this study. Seven healthy adults (three female, four male; mean age ± SD: 29.1 ± 5.8 years) participated in the control experiment. All participants reported no history of shoulder injury or shoulder pain in the 6 months prior to testing that prevented participation in overhead activities or required treatment from an allied health professional. All participants were right-hand dominant to accommodate for testing of the dominant arm in our robotic system. Participants gave written informed consent prior to the experiment. All procedures and protocols were approved by Northwestern University's Institutional Review Board (STU00208382).

Equipment

Stretch-evoked reflexes were elicited using a computer-controlled, single-degree-of-freedom linear motor (ThrustTube, Copley Controls Corporation; Canton, MA) with methods adapted from a prior protocol designed to estimate glenohumeral joint mechanics (Nicolozakes et al., 2021). Each participant was seated in a Biodex chair (Biodex Medical Systems; Shirley, NY). The right arm was attached midway between the acromion and the olecranon to the linear motor via a custom-made full-arm fiberglass cast. The upper arm was positioned at 90° shoulder abduction, 20° horizontal flexion, and 0° rotation (**Figure 1**). The elbow was held at 90° flexion, setting the forearm in the transverse plane. Each participant's scapula was stabilized with a form-fitting thermoplastic clamp over the acromion and posterior scapula to limit scapulothoracic movement and isolate displacements to the glenohumeral joint. The linear motor applied anterior-posterior displacements to translate the humerus within the glenoid fossa. The full-arm cast helped distribute the forces applied by the linear motor across the entire upper arm to minimize rotations at the glenohumeral joint. The motor was instrumented with a linear encoder (RGH24, Renishaw; Gloucestershire, UK) to record the displacements. Both mechanical and electrical safety stops were used to limit displacements within a safe range. Control of the linear motor was performed using xPC Target (MathWorks; Natick, MA).

EMGs were recorded to quantify the background activity and stretch-evoked reflexes elicited in each of the nine recorded shoulder muscles (**Table 1**). In our primary experiment, EMGs were recorded from nine total muscles. Bipolar surface electrodes (Delsys Inc.; Natick, MA) were used to record activity from six superficial muscles following standard skin preparation (Merletti and Cerone, 2020): *deltoid* (anterior, middle, and posterior heads), *pectoralis major* (clavicular head), *latissimus dorsi*, and *teres major*. These six muscles predominantly generate torque to rotate the shoulder when active, and we describe them throughout as primary shoulder movers. Fine-wire intramuscular electrodes (Motion Lab Systems; Baton Rouge, LA) were used to record activity from three deep rotator cuff muscles that are difficult to study with surface electrodes (Waite et al., 2010): *supraspinatus*, *infraspinatus*, and *subscapularis*. The rotator cuff muscles generate torque at the shoulder, but more importantly increase the stability of the glenohumeral joint when active by compressing the humeral head into the glenoid (Lee et al., 2000). The broad actions of each primary shoulder mover and rotator cuff muscle are summarized in **Table 1**.

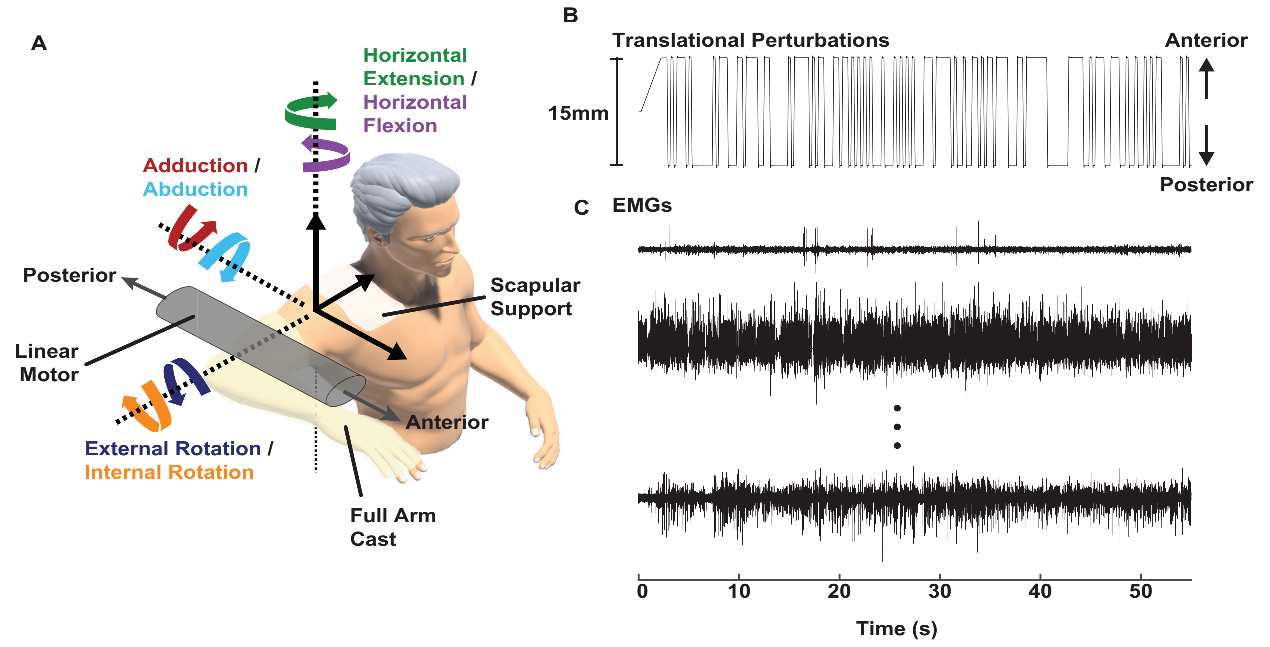

FIGURE 1 | Experimental setup. **(A)** A linear motor applied anterior-posterior perturbations to the glenohumeral joint while participants produced multiple levels of submaximal isometric torque in six directions. **(B)** Perturbations with a pseudorandom binary sequence and 15 mm peak-to-peak amplitude were applied to the glenohumeral joint. **(C)** Electromyograms (EMGs) were recorded in nine shoulder muscles while the participants held isometric torque and the linear motor applied perturbations. Representative samples are shown from the *supraspinatus, infraspinatus*, and *pectoralis major* (top to bottom).

TABLE 1 | Muscles recorded by EMG and their corresponding electrode placements.

	Muscle	Placement	Orientation	Muscle Actions at the Shoulder[d]
Intramuscular Electrodes	*Supraspinatus m*.	Two finger widths superior to the scapular spine at the midpoint between the posterior acromion angle and trigonum spinae.[a]	N/A	Abduction
	Infraspinatus m.	Two finger widths inferior to the scapular spine at the midpoint between the posterior acromion angle and trigonum spinae.[a]	N/A	External Rotation
	Subscapularis m.	Three finger widths anterior to the midpoint between the inferior angle of the scapula and the anterior axillary fold.[c]	N/A	Adduction, Internal Rotation
Surface Electrodes	*Anterior deltoid m*.	One finger width distal and anterior to the acromion.[b]	Along the line between the acromion and thumb.	Internal Rotation, Horizontal Flexion
	Medial deltoid m.	Over the greatest bulge in the muscle between the acromion and lateral epicondyle.[b]	Along the line between the acromion and the lateral epicondyle.	Abduction
	Posterior deltoid m.	Two finger widths posterior to the angle of the acromion.[b]	Along the line between the acromion and the little finger.	External Rotation, Horizontal Extension
	Pectoralis major m. (clavicular head)	Two finger widths inferior to the midpoint of the clavicle.[a]	Along the line between the sternoclavicular joint and anterior axillary fold.	Adduction, Internal Rotation
	Latissimus dorsi m.	Three finger widths distal to the posterior axillary fold.[a]	Along the line between the posterior axillary fold and L3 vertebra.	Adduction, Internal Rotation, Horizontal Extension
	Teres major m.	Three finger widths superior to the inferior angle of the scapula along the lateral border of the scapula.[a]	Along the line between the posterior axillary fold and the inferior angle of the scapula.	Adduction, Internal Rotation

[a]Perotto and Delagi (2011); [b]Hermens et al. (2000); [c]Nemeth et al. (1990); [d]Agur and Grant (2013).

In our control experiment, EMGs were recorded from the *anterior deltoid*, *posterior deltoid*, and *latissimus dorsi*. Surface electrodes and fine-wire intramuscular electrodes were used to simultaneously record activity in each muscle. Surface electrodes were placed as described in **Table 1**. Fine-wire intramuscular electrodes were inserted approximately 5 mm to the side of the surface electrode and angled so that the bare tips of the fine wires were below the middle of the surface electrode to ensure both electrodes recorded from the same area of muscle (Semciw et al., 2014).

Raw EMG signals were recorded using a Delsys Bagnoli-16 EMG system (Delsys Inc.; Natick, MA) and band-pass filtered by the EMG system at 20–450 Hz (surface electrodes) or 20–2,000 Hz (intramuscular electrodes). The gain for all EMG channels was set at 1 K unless a gain of 10 K was required to maximize the range of the data acquisition system. EMG data were then sampled at 5,000 Hz (PCI-6289 data acquisition card, National Instruments; Austin, TX).

Experimental Protocol

Prior to recording stretch-evoked reflexes, all participants produced isometric maximum voluntary contractions (MVC) in six directions (abduction/adduction, internal/external rotation, and horizontal flexion/extension) while in the experimental setup (**Figure 1**; Besomi et al., 2020). The torques measured during MVCs were used to normalize torque production in subsequent trials.

Stretch-evoked reflexes were elicited by applying small, stochastic, anterior-posterior perturbations at the glenohumeral joint with the linear motor. The perturbations were generated using a pseudorandom binary sequence. Individual perturbations had a peak-to-peak amplitude of 15 mm, a 100 ms long ramp, and a minimum switching time of 300 ms before the next perturbation (**Figure 1**). A 15 mm amplitude was large enough to elicit reflexes in all recorded shoulder muscles but small enough to ensure glenohumeral translations were safe for all participants. The midpoint of the perturbations coincided with the humeral head being centered in the glenoid fossa.

The experiment was designed to elicit stretch-evoked reflexes while participants produced volitional torque in different directions and at different levels of effort. Participants generated torque in six different directions to allow for the characterization of reflexes during different combinations of shoulder muscle activity. During each trial, participants maintained a constant isometric torque of either 5% or 10% MVC in one of six directions. The chosen torque levels produced muscle activations large enough to observe consistent stretch-evoked reflexes but without muscle fatigue. Passive trials, during which the

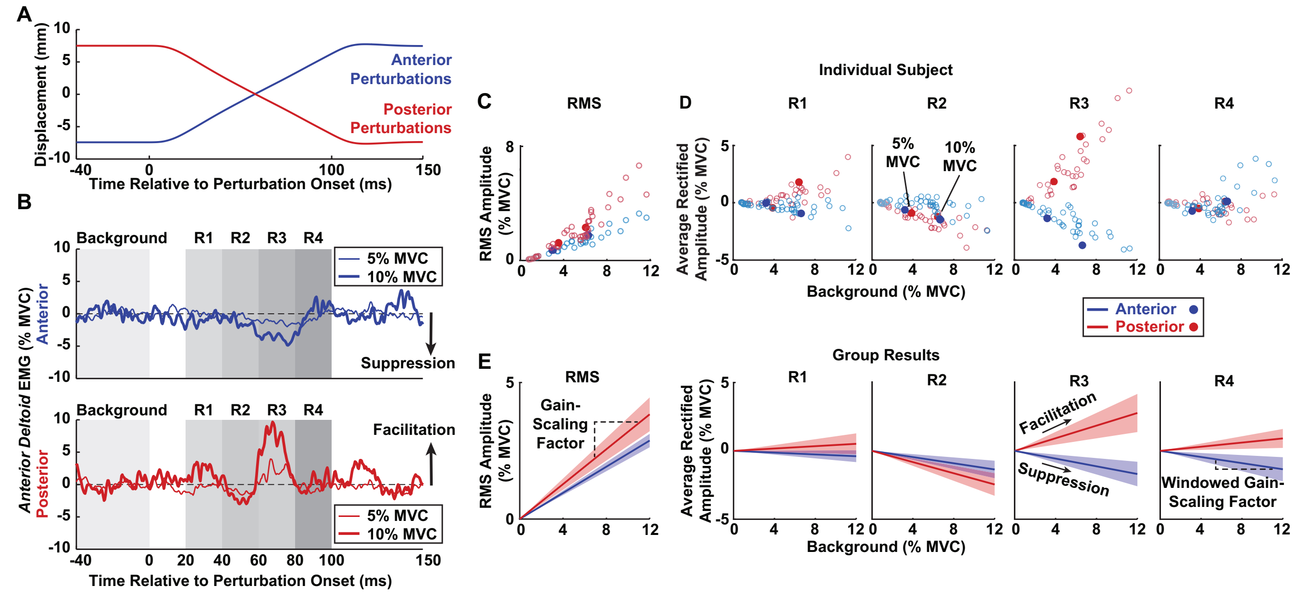

FIGURE 2 | Methods for estimating stretch-evoked reflexes. Sample data are displayed from a single participant to illustrate the methodology. **(A)** Anterior (blue) and posterior (red) perturbations were applied to the glenohumeral joint. Each perturbation had a peak-to-peak amplitude of 15 mm. **(B)** Average rectified EMGs of the *anterior deltoid* are displayed following anterior (top) and posterior (bottom) perturbations as participants generated torque at 5% (thin traces) and 10% (thick traces) MVC. Rectified EMGs were averaged across all perturbations in a trial and plotted relative to the average background EMG (0–40 ms prior to perturbation onset). RMS amplitudes were computed from the root mean square (RMS) of the reflex responses between 20 and 100 ms in each perturbation direction. Average rectified amplitudes in individual time windows (R1–4) were estimated by averaging the rectified EMG activity in four time windows post-perturbation onset. Reflexes that increased compared to background represented facilitation, and reflexes that decreased compared to background represented suppression. **(C)** RMS amplitudes of the *anterior deltoid* from all trials in an individual participant are plotted based on background activity, with the filled dots corresponding to the trials shown in panel **(B)**. **(D)** Average rectified amplitudes of the *anterior deltoid* from all trials in an individual participant are plotted for each reflex window based on background activity. The filled dots correspond to the trials shown in panel **(B)**. **(E)** The group results are displayed for *anterior deltoid* reflexes. The slopes between the RMS amplitudes and background activity were defined as the gain-scaling factors. The slope between the reflex responses in each window and background activity was defined as the windowed gain-scaling factor. Shaded regions represent the confidence intervals of the gain-scaling factors.

participants were instructed to relax and ignore the perturbations (0% MVC), were also recorded. Participants were aided by visual feedback to assist with acquiring and maintaining the target torque for each trial. They were instructed to maintain the target torque on average and to not respond to individual perturbations to minimize the influence of voluntary intervention (Shemmell et al., 2009). The order of torque magnitudes and directions was randomized for each participant. Each trial lasted 55 s. Data from the first 5 s of each trial were discarded to eliminate transient behaviors associated with the onset of the perturbation. Three trials were completed for each condition, resulting in 39 trials per participant (6 torque directions × 2 torque levels × 3 repetitions = 36 active trials + 3 passive trials). Participants rested for a minimum of 10 s between trials to prevent fatigue.

EMG Processing

EMG signals were used to measure background muscle activity prior to the onset of each perturbation and the reflexively elicited changes in muscle activation in response to each perturbation. All raw EMG signals were detrended, notch filtered at 60 Hz, and digitally band-pass filtered between 20 Hz and 500 Hz (surface) or 60 Hz and 1,500 Hz (intramuscular) with a 4th order Butterworth filter. We performed forward and backward digital filtering to avoid phase shifts. A high-pass cutoff of 60 Hz was used for intramuscular electrodes to reduce motion artifact created by the vibration of the fine-wires from the rapid perturbations. EMG data were rectified prior to any further processing. Rectified EMGs for each muscle were then normalized to the mean rectified value produced during MVCs at the beginning of the experiment. EMGs affected by uncommon or excessive noise during set up or testing were removed prior to analysis. Across the nine muscles recorded from each of our fifteen participants in our primary experiment, nine recordings were eliminated: 1 × *supraspinatus*, 2 × *infraspinatus*, 3 × *subscapularis*, 1 × *pectoralis major*, 1 × *latissimus dorsi*, and 1 × *teres major*. Across the three muscles recorded from each of our seven participants in our control experiment, four recordings were eliminated: 2 × *anterior deltoid* and 2 × *latissimus dorsi*.

EMG recordings from each trial were segmented and aligned to the onset of each anterior or posterior perturbation within the pseudorandom binary sequence. Each trial contained approximately 40 perturbations in each direction. Data between 40 ms prior to the perturbation onset and 100 ms after the perturbation onset were analyzed (**Figures 2A,B**). EMG after 100 ms were not considered to minimize contributions from voluntary interventions and the cessation of the ramp portion of the perturbation (Lewis et al., 2005; Honeycutt and Perreault, 2012). The aligned segments were averaged before further analysis. Background muscle activity was calculated as the mean average rectified EMG 0–40 ms prior to the onset of the perturbation. All reflex responses were measured relative to this background. We estimated reflex latencies for all active trials as the time after perturbation onset when the average rectified EMG diverged positively or negatively from the background by at least two standard deviations; these results were confirmed visually. Latencies were not measured for passive trials, which had inconsistent reflex responses.

We characterized the reflex amplitude in two ways. First, to capture the net change in muscle activity that resulted from perturbations in each direction, we computed the root mean square (RMS) amplitude as the RMS of the average rectified EMG relative to the background activity. This measure was computed over the period from 20 to 100 ms after perturbation onset. Second, we quantified the average rectified amplitude relative to the background activity in four separate time windows following perturbation onset to assess the sign (facilitatory or suppressive) and time evolution of the observed responses, as done in numerous other studies (Nakazawa et al., 1997; Pruszynski et al., 2009; Shemmell et al., 2009). The windows were: R1 (20–40 ms), R2 (40–60 ms), R3 (60–80 ms), and R4 (80–100 ms; **Figure 2B**). The R1 window likely included predominantly spinal contributions, and R2 to R4 likely contained contributions from both spinal and supraspinal pathways (Lewis et al., 2004; Shemmell et al., 2009).

Statistical Analysis

Our primary hypothesis was that the amplitudes of stretch-evoked reflexes in the rotator cuff muscles would be larger than those in the primary shoulder movers. This was assessed grossly by examining the RMS reflex amplitudes across all trials conducted at the largest tested voluntary contraction level of 10% MVC when reflexes were expected to be largest. The distribution of reflexes within each muscle from each participant was summarized by the 10th, 50th, and 90th percentiles to represent small, median, and large responses (Jonsson, 1978; Ludvig et al., 2019). This approach allowed for the comparison of reflex magnitudes beyond the simple mean or median of the data and accounted for the skewed distributions within each muscle and muscle group. A linear mixed effects model was used to determine if there were differences across muscle groups at each percentile. RMS amplitude was considered as the dependent variable. Muscle group and percentile were the fixed independent factors. Participants were treated as a random factor. *Post hoc* comparisons were used to compare amplitudes from the rotator cuff muscles to those in the primary shoulder movers.

Since reflexes scale with background activity (Matthews, 1986), we conducted two additional analyses to determine why reflex amplitudes may differ between rotator cuff muscles and primary shoulder movers. First, we compared the background activity between groups at 10% MVC using an analysis identical to that described for the RMS amplitudes. Next, we examined if the sensitivity of reflex amplitudes to background activity differed between muscle groups by computing a gain-scaling factor for each muscle, defined as the slope between background activity and RMS reflex amplitude. Reflex amplitudes from trials at contraction levels of 0%, 5%, and 10% MVC were included to maximize the range of each muscle's background activity. Separate gain-scaling factors were computed for each perturbation direction (**Figures 2C–E**). We compared gain-scaling factors in each muscle group using a linear mixed effects model with RMS reflex amplitude as the dependent variable, background activity as a continuous factor, and muscle and perturbation direction as fixed factors. Participants were treated as a random factor for both intercepts and slopes. The gain-scaling factors for each muscle group were compared using *post-hoc* comparisons. We compared gain-scaling factors between muscle groups separately for each perturbation direction and also stratified by perturbation directions that elicited facilitative or suppressive responses.

Our secondary hypothesis was that the latencies of stretch-evoked reflexes would differ in rotator cuff muscles compared to primary shoulder movers. We used a linear mixed effects model to quantify the average reflex latency for each muscle in each perturbation direction. Participants were treated as a random factor. We tested our hypothesis by comparing the average reflex latencies of the rotator cuff muscles to those of the primary shoulder movers.

In our control experiment, we compared reflexes recorded in the same muscle with surface and fine-wire intramuscular electrodes. First, we used a linear mixed effects model to determine if there were differences in RMS reflex amplitudes between electrode types at the 10th, 50th, and 90th percentiles. Second, we computed gain-scaling factors and compared them between electrode types using a linear mixed effects model. Finally, we used a linear mixed effects model to compare the average reflex latency between electrode types in each perturbation direction. All models included the same fixed, continuous, and random factors described above.

To compare parameters within each linear mixed effects model, we used the Wald t-test statistic with a Satterthwaite approximation to estimate P-values (Luke, 2017). All confidence limits reported in the text reflect 95% confidence intervals unless otherwise noted (mean ± CI). Bonferroni corrections were used to control for multiple comparisons.

RESULTS

Since there have been few studies examining shoulder reflexes elicited by translations of the glenohumeral joint, we begin by characterizing the nature of the elicited reflexes. We follow by providing a detailed evaluation of our hypotheses related to the stretch-evoked reflexes elicited in the rotator cuff muscles and primary shoulder movers. Finally, we describe the results of our control experiment comparing reflex characteristics recorded in the same muscle with surface and fine-wire intramuscular electrodes.

Nature of the Stretch-Evoked Reflexes Elicited by Glenohumeral Translations

Stretch-evoked reflexes were elicited by translations of the glenohumeral joint in all shoulder muscles recorded in our experiment. While no prior studies have described how shoulder muscles are stretched or shortened by translational perturbations, the expected length changes of the primary shoulder movers can be inferred from their anatomical orientation at the glenohumeral joint. We expect that muscles would be stretched by translations moving in a direction opposite of where they sit with respect to the glenohumeral joint, and the muscles would be shortened by translations moving in the same direction. For example, the *anterior deltoid* and *pectoralis major* sit anteriorly to the glenohumeral joint and are likely stretched by posterior perturbations. Accordingly, the *anterior deltoid* and *pectoralis major* displayed facilitatory reflexes in response to posterior perturbations and suppressive reflexes in response to anterior perturbations. In contrast, the *posterior deltoid*, *teres major*, and *latissimus dorsi* are oriented posteriorly to the glenohumeral joint and are likely stretched by anterior perturbations. Predictably, these three muscles displayed facilitatory reflexes in response to anterior perturbations and suppressive reflexes in response to posterior perturbations. Unlike the other primary shoulder movers, the *middle deltoid* is oriented superiorly to the glenohumeral joint. Reflexes in the *middle deltoid* did not consistently demonstrate facilitation or suppression responses to perturbations in either direction. It is more difficult to predict how translational perturbations would stretch or shorten the rotator cuff muscles given their compact anatomy around the glenohumeral joint. The *supraspinatus* and *infraspinatus* are roughly oriented posterosuperiorly and posteriorly, respectively, to the glenohumeral joint, yet both displayed facilitation in response to posterior perturbations and suppression in response to anterior perturbations. Likewise, the *subscapularis* is roughly oriented anteriorly to the joint but displayed facilitation in response to anterior perturbations and suppression in response to anterior perturbations. Overall, most facilitatory and suppressive reflexes were broad and monophasic, yet in some muscles such as the *supraspinatus*, *infraspinatus*, and *anterior deltoid*, brisk and biphasic facilitatory responses were observed. Examples of reflexes in each muscle can be observed for a typical participant in **Figure 3**.

Reflex Amplitudes Were Larger in Rotator Cuff Muscles Than in Primary Shoulder Movers

Due to the multiphasic nature of the reflexes observed in several muscles, we used the RMS of the average rectified EMG between 20 and 100 ms to assess the aggregate change in muscle activity elicited by translational perturbations of the shoulder. We found that this measure of reflex activity, or the RMS amplitude, was larger in the rotator cuff muscles than in the primary shoulder movers. This was evaluated by comparing distributions of RMS amplitudes elicited as participants generated voluntary torques of 10% MVC, the most active condition in our experimental design. Distributions were created for each muscle, incorporating all six volitional torque directions and both perturbation directions. Results for a typical participant are shown in **Figure 4A**. The difference in RMS amplitude between muscles groups was driven by large reflexes in the *supraspinatus* and *infraspinatus* and small reflexes in the *latissimus dorsi* and *teres major*. Across all participants, the median RMS amplitude was nearly twice as large in the rotator cuff muscles (2.0 ± 0.5% MVC) compared to the primary shoulder movers (1.0 ± 0.3% MVC; $P = 0.003$; **Figure 4B**). Similar differences were observed for the large (90th percentile) reflexes elicited in each group. The large reflexes in the rotator cuff muscles (6.1 ± 1.2% MVC) were approximately 50% greater than those in the primary movers (4.0 ± 1.1% MVC; $P = 0.03$). In contrast, minimal differences were observed between the small (10th percentile) reflexes in each group, where reflexes in the primary movers (0.3 ± 0.1% MVC) were slightly larger than those in the rotator cuff (0.2 ± 0.1%; $P = 0.45$). The largest reflexes were observed in the *supraspinatus* (median: 2.8 ± 0.9% MVC; large: 6.9 ± 1.8% MVC) and *infraspinatus* (median: 2.4 ± 0.8% MVC; large: 5.1 ± 1.3% MVC; **Figure 4B**). The smallest were observed in the *latissimus dorsi* (50th percentile: 0.6 ± 0.2% MVC; 90th percentile: 2.6 ± 0.7% MVC) and *teres major* (50th percentile: 0.7 ± 0.3% MVC; 90th percentile: 2.9 ± 1.0% MVC; **Figure 4B**).

The larger reflexes observed in the rotator cuff muscles may have been influenced by differences in background muscle activity between the two muscle groups, given that reflex amplitudes typically scale with background activity. However, across all participants, the median background activity at torque levels of 10% MVC barely differed between rotator cuff muscles (3.7 ± 1.2% MVC) and primary shoulder movers (3.4 ± 0.7% MVC; $P = 0.70$; **Figure 5**). The large (90th percentile) background activity in rotator cuff muscles (12.8 ± 2.5% MVC) was larger than in the primary shoulder movers (10.7 ± 1.3% MVC; $P = 0.13$), but the difference was still relatively small. In contrast, the small (10th percentile) background activity was larger in the primary shoulder movers (1.5 ± 0.4% MVC) than the rotator cuff muscles (0.5 ± 0.2% MVC; $P < 0.001$). Therefore, factors beyond the background activity of each muscle likely contributed to the differences in reflex amplitude between muscle groups.

Gain-Scaling Was More Prominent in Rotator Cuff Muscles Than in Primary Shoulder Movers

To determine if differences in reflex amplitude reported above were due to differences in reflex sensitivity to background activity, we computed the gain-scaling factor for each muscle, which defines the change in RMS amplitude resulting from a change in background activity. The gain-scaling factor was significantly different from zero in all muscles (all $P < 0.001$). Our data were described well by a model predicting RMS amplitudes based only on background activity, muscle type, and perturbation direction as the independent fixed factors ($R^2 = 0.89$). The gain-scaling factors ranged from 0.25 to 0.55 (Δ RMS amplitude/Δ background activity) across all muscles and perturbation directions (**Figure 6**). For a given muscle, gain-scaling factors were nearly always larger in the perturbation direction that elicited facilitatory reflexes than the perturbation direction that elicited suppressive reflexes. The only exception was in the *supraspinatus*, which displayed similar gain-scaling in both perturbation directions.

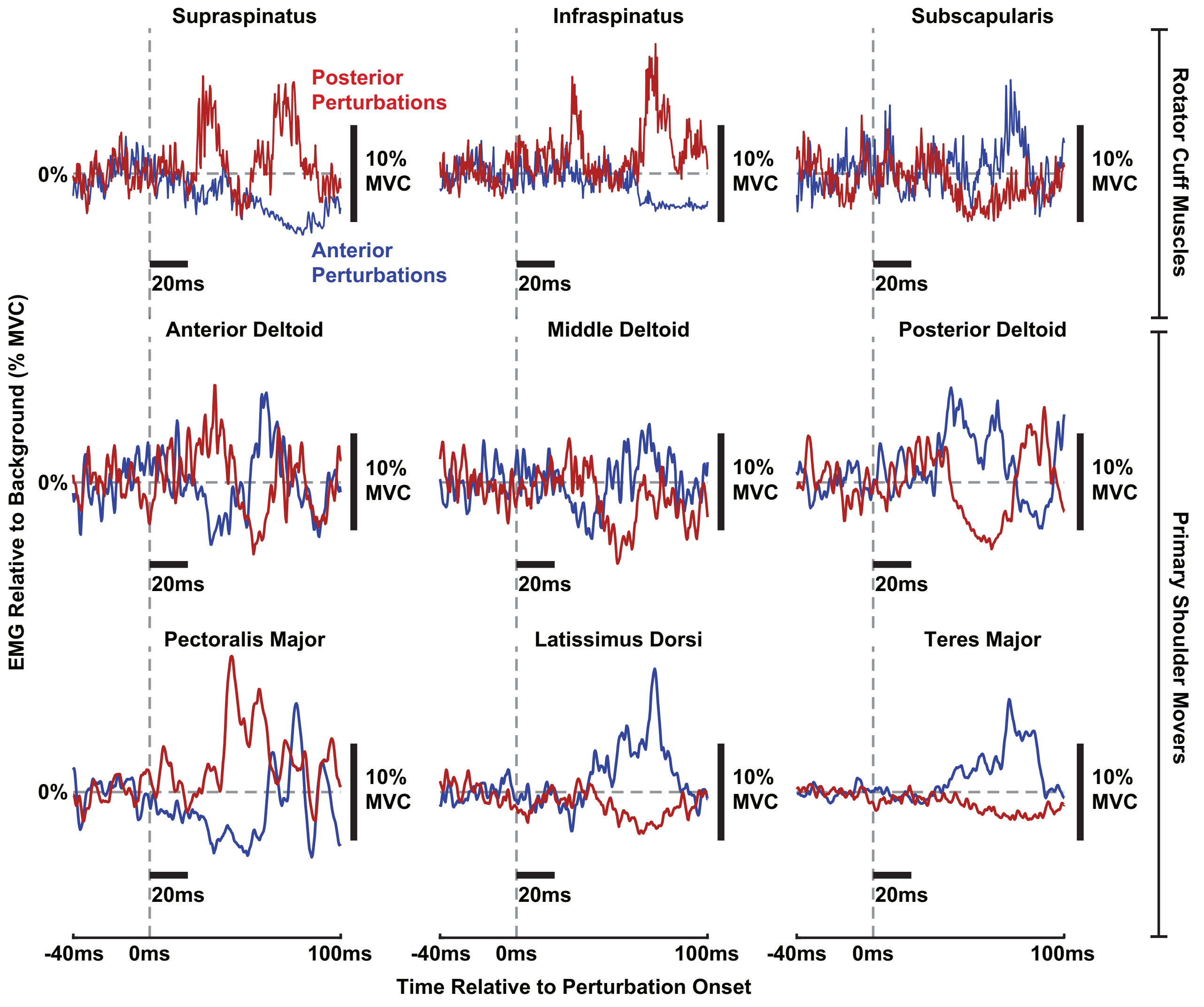

FIGURE 3 | Individual stretch-evoked reflexes responding to anterior (blue) and posterior (red) perturbations in all muscles from a typical participant. All trials shown are from torque levels of 10% MVC in a torque direction that generated a large background activity for each muscle. All EMGs are displayed relative to background activity. Thick black bars are included to display the scale of the x-axes (20 ms per horizontal bar) and y-axes (10% MVC of ΔEMG per vertical bar), respectively.

Gain-scaling was larger in the rotator cuff muscles than in the primary shoulder movers (**Figure 6**). Gain-scaling factors in the rotator cuff muscles were 0.43 ± 0.04 (Δ RMS amplitude/Δ background activity) for anterior perturbations and 0.41 ± 0.03 for posterior perturbations. In contrast, the values for the primary shoulder movers were 0.35 ± 0.03 and 0.35 ± 0.03 for anterior and posterior perturbations, respectively. The difference between muscle groups had a statistical significance of $P = 0.002$ for both perturbation directions. On average across both perturbation directions, gain-scaling factors in the cuff muscles were 0.07 ± 0.03 larger than in the primary shoulder movers ($P < 0.001$). Intercepts in the model were small but significant for the rotator cuff muscles (0.20 ± 0.03% MVC, $P < 0.001$) and primary shoulder movers (−0.11 ± 0.02% MVC, $P < 0.001$); these also differed significantly ($P < 0.001$). The similar degree of average gain-scaling following anterior and posterior perturbations suggests that shoulder muscles collectively generate balanced resistance to external disturbances coming from each direction. Gain-scaling factors were also larger in rotator cuff muscles than in primary shoulder movers when stratifying by perturbation directions that elicited facilitatory (0.47 ± 0.04 vs. 0.42 ± 0.04; $P = 0.008$) or suppressive reflexes (0.36 ± 0.04 vs. 0.30 ± 0.02; $P < 0.001$).

The time-course of the reflexes elicited in each muscle was quantified by examining the average rectified EMG in four time windows following perturbation onset: R1 (20–40 ms), R2 (40–60 ms), R3 (60–80 ms), and R4 (80–100 ms). We assessed the gain-scaling in each window, as described above for the RMS reflex amplitudes. The largest gain-scaling was typically observed

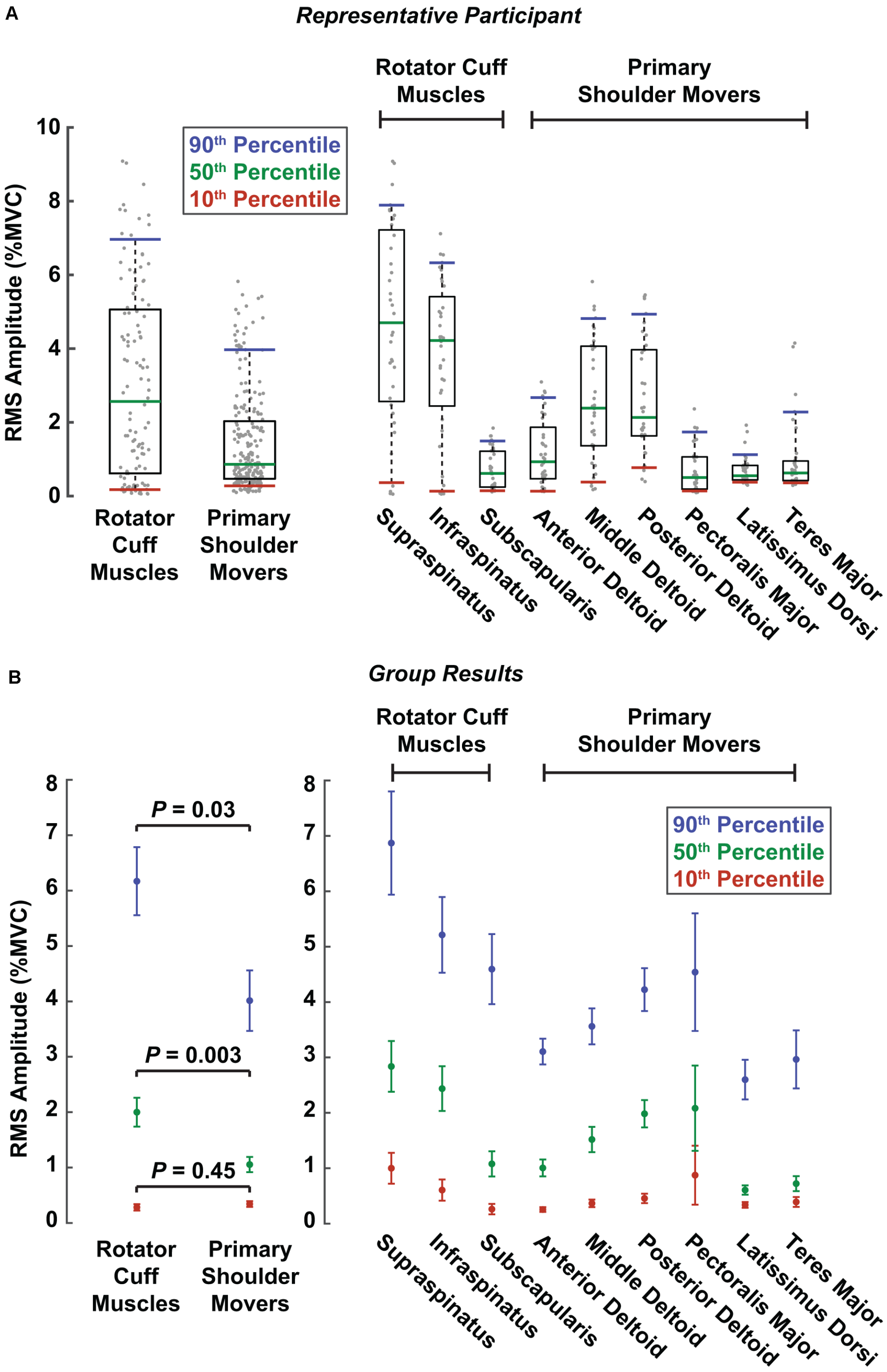

FIGURE 4 | Reflex amplitudes comparing muscle groups and individual muscles. Reflex amplitudes were summarized as RMS amplitudes, which were calculated from the root mean square of the reflexes in each perturbation direction for an individual trial. Colored lines represent the RMS amplitudes corresponding to the 10th (red), 50th (green), and 90th (blue) percentiles across all trials at torque levels of 10% MVC. The three percentiles correspond approximately to the small, median, and large amplitudes across all trials, respectively, for a given muscle or muscle group. **(A)** RMS amplitudes are displayed for a representative participant. Gray dots represent RMS amplitudes from all the participant's individual trials in both perturbation directions for a given muscle or muscle group. The boxes represent the interquartile range (25th and 75th percentiles), and the whiskers span from the 10th to 90th percentiles. **(B)** RMS amplitudes for all participants. Error bars represent the standard errors of the RMS amplitude estimates at each respective percentile.

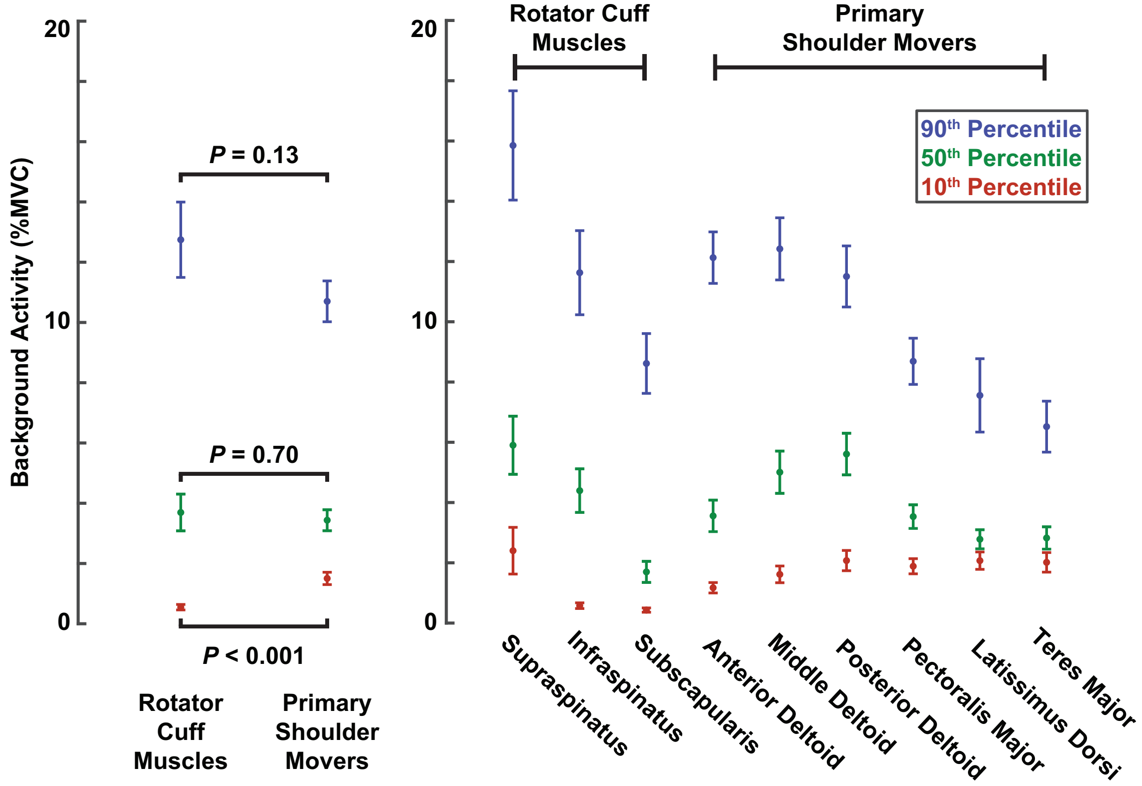

FIGURE 5 | Background activity comparing muscle groups and individual muscles. Colored dots represent background activities corresponding to the 10th (red), 50th (green), and 90th (blue) percentiles across all trials with torque levels of 10% MVC. Error bars represent the standard errors of each estimate.

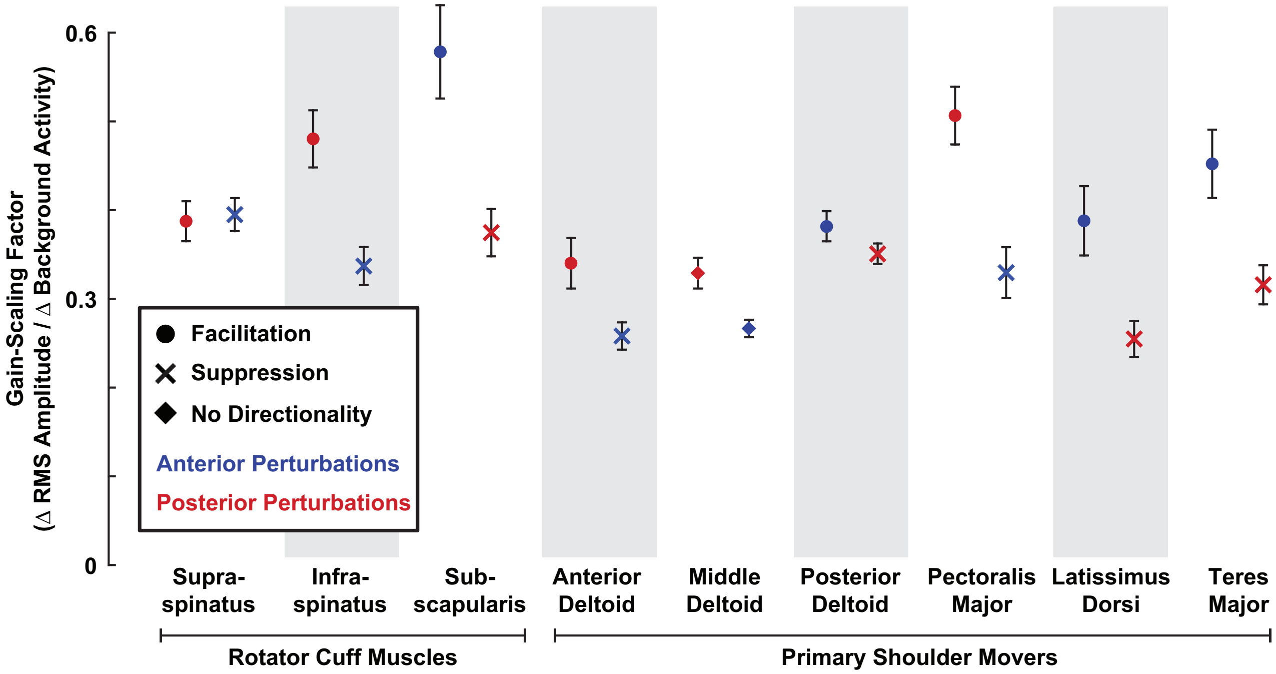

FIGURE 6 | Gain-scaling in all shoulder muscles. The gain-scaling factor for each muscle was estimated from the relationship between the RMS amplitude and background activity in each muscle stratified by perturbation direction. Error bars represent the standard errors of the estimated gain-scaling factors.

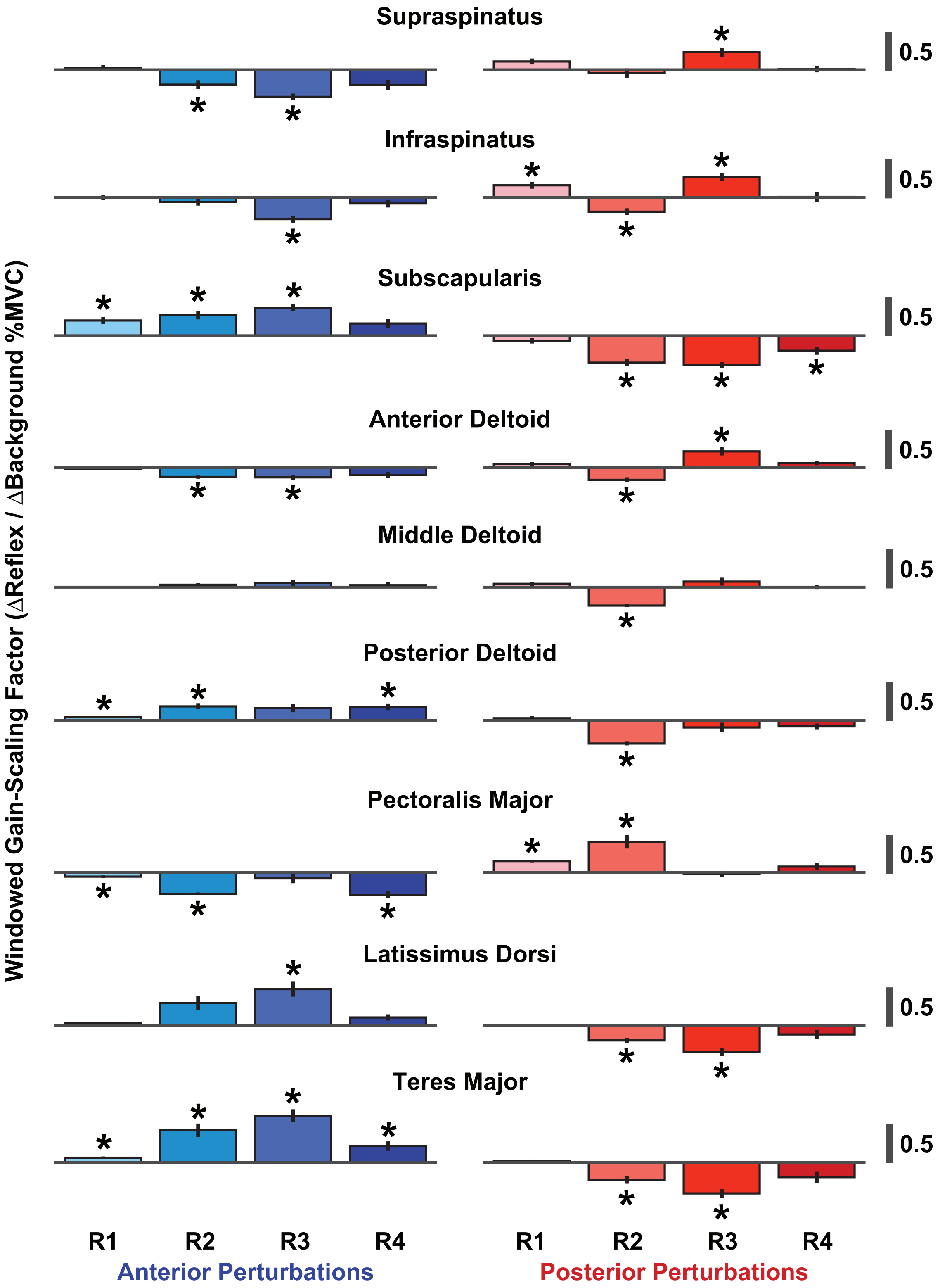

FIGURE 7 | Windowed gain-scaling factors for stretch-evoked reflexes in shoulder muscles responding to translations of the glenohumeral joint. The gain-scaling factor was computed from the relationship between a muscle's background activity and its reflex response in a given reflex window. Gain-scaling factors marked with an asterisk were significantly different from zero (α = 0.05/72). Vertical black lines represent the standard errors of the gain-scaling factors. Reflex windows: R1 (20–40 ms), R2 (40–60 ms), R3 (60–80 ms), R4 (80–100 ms).

in R2 or R3 (**Figure 7**). These results were obtained by grouping data across all six volitional torque directions.

Given that previous studies have shown that reflexes in shoulder muscles are affected by the specific tasks being performed (Pruszynski et al., 2008; Krutky et al., 2010; Nicolozakes, 2021), we also assessed gain-scaling in each window separately for each of the six torque directions used in our protocol. We quantified the improvement in goodness-of-fit between the models that estimated gain-scaling with and without grouping data across all six torque directions. The more complicated model led to only a modest improvement in the fit accuracy (median ΔR^2: +0.03, IQR: +0.02–0.06; **Supplementary Figure 1**). These findings suggest that the reflexes recorded in our study were most sensitive to changes in the background activity of the homonymous muscle rather than the coordinated activity of all muscles contributing to each of the tested torque directions. Interestingly, this is quite different than reflexes elicited by shoulder rotations (Nicolozakes, 2021).

Comparisons of Reflex Latencies Between Rotator Cuff Muscles and Primary Shoulder Movers

In addition to comparing reflex amplitudes between rotator cuff muscles and primary shoulder movers, we also compared reflex latencies, which represent a secondary measure relevant to the efficacy of the reflex response. The reflex latencies in the rotator cuff muscles were shorter than those in the primary shoulder movers. Specifically, reflex latencies in rotator cuff muscles were 5 ± 1 ms shorter, on average, than the latencies of the primary shoulder movers for facilitatory responses (29 ± 2 ms vs. 34 ± 2 ms; $P < 0.001$). The shortest mean facilitatory latencies were observed in the *supraspinatus* (27 ± 2 ms) and the *infraspinatus* (25 ± 2 ms), and the longest in the *latissimus dorsi* (43 ± 2 ms) and *teres major* (42 ± 2 ms; **Figure 8**).

Facilitatory reflex latencies became shorter with increased background activity in the three muscles that had the slowest facilitatory responses: the *subscapularis*, *latissimus dorsi*, and *teres major*. This decrease may be due to muscle activation creating a more effective transmission of the applied glenohumeral translation to the proprioceptors mediating the reflex response, or to decreasing the threshold of the relevant motoneurons. In these three muscles, facilitatory reflex latencies decreased by approximately 1 ms for each percentage increase in background activity (*subscapularis* Δ: −0.9 ± 0.6 ms/%MVC, $P = 0.003$; *latissimus dorsi* Δ: −1.1 ± 0.7 ms/%MVC, $P = 0.001$; *teres major* (Δ: −1.1 ± 0.8 ms/%MVC, $P = 0.005$). Smaller, nonsignificant changes in latency with increased muscle activation were observed in the other six muscles. Despite these activation-dependent changes, the differences in the facilitatory latencies were maintained at the highest activations tested.

Reflex latencies in rotator cuff muscles were also 5 ± 1 ms shorter than in primary shoulder movers for suppressive responses (32 ± 2 ms vs. 37 ± 2 ms; $P < 0.001$). A smaller range of latencies was observed for suppressive responses compared to facilitatory responses, with the shortest mean latency observed in the *supraspinatus* (30 ± 2 ms) and the longest in the *latissimus dorsi* (41 ± 2 ms). Within each muscle, reflexes elicited by posterior perturbations always occurred at a shorter latency than those elicited by anterior perturbations, regardless of the nature of the responses (facilitatory or suppressive; **Figure 8**). Such differences suggest a quicker overall response to posterior perturbations. In all nine muscles, only small, nonsignificant relationships between latency and muscle activation were observed for suppressive responses.

Recording Modality Influenced Measured Reflex Latencies

In our control experiment, we compared reflex latencies, amplitudes, and gain-scaling factors between reflexes recorded in the same muscle with surface or fine-wire electrodes. Across the three muscles, reflex latencies were on average 7 ± 2 ms shorter in reflexes recorded with fine-wire electrodes than those recorded with surface electrodes ($P < 0.001$; **Figure 9**). The differences were most pronounced in the *latissimus dorsi* (anterior: 8 ± 5 ms shorter, $P = 0.001$; posterior: 9 ± 4 ms shorter, $P < 0.001$) and least pronounced in the *posterior deltoid* (anterior: 4 ± 3 ms shorter, $P = 0.009$; posterior: 5 ± 3 ms shorter, $P = 0.002$). Differences in electrode type used to record reflexes from the rotator cuff muscles and primary shoulder movers may therefore have contributed to the differences in reflex latency recorded in our primary experiment.

Reflex amplitudes were impacted less by electrode type than were the reflex latencies. We found that our measures of reflex amplitude differed slightly or not at all between surface and fine-wire electrodes. Median RMS amplitudes (50th percentile) on average across muscles did not differ between electrode type (Δ fine-wire — surface = −0.05 ± 0.39% MVC; $P = 0.81$). Similar but slightly larger results were observed for the 90th percentile (Δ = 0.6 ± 0.7% MVC, $P = 0.14$), which were larger when recorded with fine-wire electrodes. This statistically insignificant bias across all muscles was due to small but significant increases in the anterior deltoid (Δ = 1.1 ± 0.5% MVC, $P < 0.001$) and latissimus dorsi (Δ = 0.5 ± 0.5% MVC, $P = 0.03$) amplitudes when using fine-wire electrodes. For smaller reflexes (10th percentile), amplitudes again did not differ between electrode type (Δ = −0.02 ± 0.20, $P = 0.87$). This difference only reached significance for the anterior deltoid (Δ = −0.11 ± 0.04% MVC, $P < 0.001$), which had larger amplitudes when recorded with surface electrodes. The average differences in gain-scaling between electrode type (anterior perturbations: Δ = 0.02 ± 0.12 Δ RMS amplitude/Δ background activity, $P = 0.76$; posterior perturbations: Δ = 0.05 ± 0.04, $P = 0.06$) were also less than we observed in our primary experiments. These results suggest that differences in electrode type may have influenced the magnitude of the amplitude effects reported in our primary experiment but not the overall conclusions.

DISCUSSION

The purpose of this study was to compare stretch-evoked reflexes elicited by translations of the glenohumeral joint between rotator cuff muscles and muscles that are primary movers of the

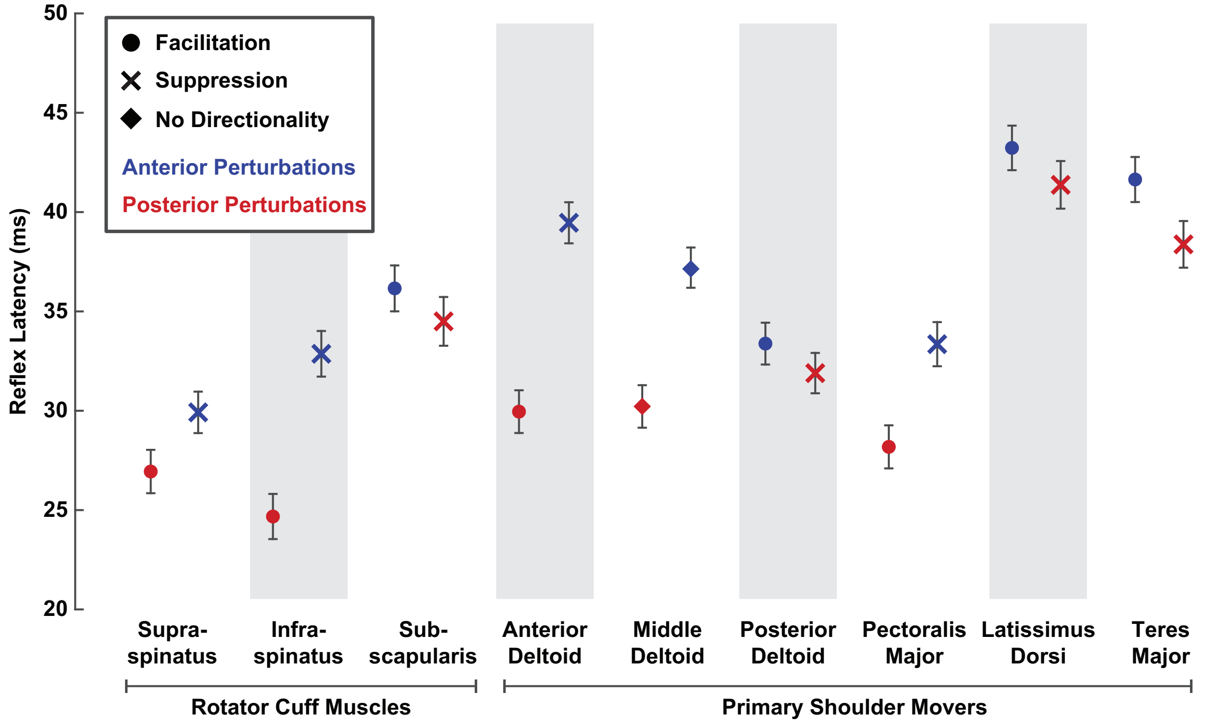

FIGURE 8 | Average latencies of stretch-evoked reflexes responding to translational perturbations of the glenohumeral joint. Reflex latencies were estimated as the time after perturbation onset when the average rectified EMG diverged positively or negatively from background activity by at least two standard deviations. Latencies were estimated separately for each perturbation direction. Only latency data from active trials (5% or 10% MVC) that elicited a reflex exceeding the threshold were included. Error bars represent the standard errors of the reflex latencies.

shoulder. Stretch-evoked reflexes were elicited in all muscles we studied. Reflex amplitudes were larger in the rotator cuff muscles than in the primary shoulder movers, with the highest amplitudes observed in the *supraspinatus* and *infraspinatus*. The increased amplitudes in these rotator cuff muscles were due to a larger level of background activity and an increased scaling with background activity, quantified by a gain-scaling factor for each muscle. Additionally, reflex latencies were shorter in rotator cuff muscles than in primary shoulder movers, but the differences observed may have been influenced by recording EMG with different types of electrodes. Our findings demonstrate that translations of the glenohumeral joint elicit strong stretch-evoked reflexes and that these reflexes are most vigorous in the rotator cuff muscles thought to be essential for shoulder stability. These involuntary responses likely arise from the diversity of proprioceptors within the muscles and passive structures surrounding the shoulder. Their actions serve to amplify the stabilizing properties of the rotator cuff muscles that have already been identified during volitional control, providing a brisk response to glenohumeral translations that should promote centering the humeral head within the glenoid fossa.

Factors Contributing to Different Reflex Amplitudes Between Shoulder Muscles

The shoulder is embedded with many proprioceptors that could have contributed to the reflexes observed in this study. While our study was not designed to identify the specific sensory organs contributing to reflexes elicited by glenohumeral translations, it is insightful to consider the potential sources of afferent information.

Muscle spindles are commonly assumed to be a primary source of afferent information when studying stretch-evoked reflexes. While we assume that they contributed to the responses we observed, it is unlikely that spindles alone accounted for the differences between the rotator cuff muscles and the primary movers of the shoulder. Muscle spindles are sensitive to changes in muscle length and its derivatives (Poppele and Bowman, 1970; Finley et al., 2013; Blum et al., 2020), and the amplitude of the elicited reflex increases with increasing changes in muscle length (Nichols and Houk, 1976; Neilson and Mccaughey, 1981; Cathers et al., 1999). The largest changes in muscle length for our study would be expected in muscles with lines of action that are most closely aligned to the anterior or posterior perturbations used to elicit reflexes, which are the primary shoulder movers (Ackland and Pandy, 2009). Contrary to what would be expected if the elicited reflexes were due solely to changes in muscle length, we observed that the muscles with lines of action nearly orthogonal to the applied perturbations, the *supraspinatus* and *infraspinatus* (Ackland and Pandy, 2009), had the largest reflex amplitudes. These larger amplitudes were not due simply to increased background activity in the rotator cuff muscles but also to an increased sensitivity of the elicited reflexes, which

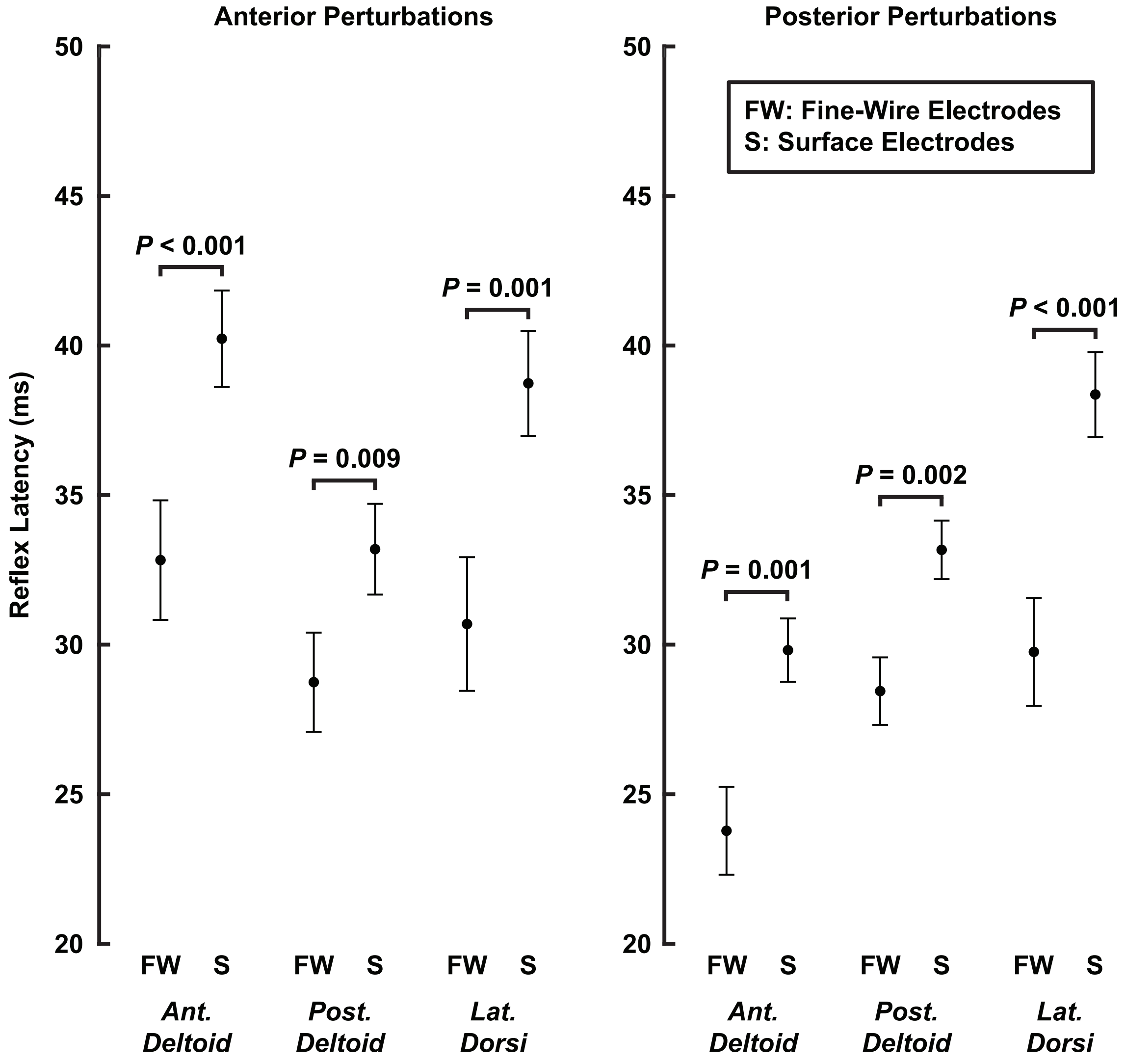

FIGURE 9 | Average latencies of stretch-evoked reflexes recorded in the same muscle with fine-wire intramuscular electrodes and surface electrodes. Latencies were estimated separately for each perturbation direction. Error bars represent the standard errors of the reflex latencies.

we quantified by the gain-scaling of the response in each muscle (Matthews, 1986). Hence, proprioceptors other than muscle spindles are likely to have contributed to the enhanced reflexes we observed in the rotator cuff muscles, though we cannot rule out differences in spindle density across muscle groups crossing the shoulder or differences in muscle-tendon compliance.

Additional proprioceptors that could be relevant to reflex activation of the shoulder musculature include the free nerve endings, Ruffini corpuscles, Golgi tendon organs, and Pacinian corpuscles within the glenohumeral capsule, its constituent ligaments, and the glenoid labrum (Bresch and Nuber, 1995; Vangsness et al., 1995; Gohlke et al., 1998; Guanche et al., 1999; Steinbeck et al., 2003; Witherspoon et al., 2014). These structures would be strained by translational perturbations of the glenohumeral joint (Brenneke et al., 2000), and the afferents within them have been shown to elicit strong reflexes in shoulder muscles that are most consistently observed in the rotator cuff (Voigt et al., 1998). Similar findings have been observed for stimulation of afferents from the coracoacromial ligament (Diederichsen et al., 2004) which, though external to the capsule, provides evidence for the broad innervation of passive structures within the shoulder. The reflexes we observed likely integrated afferent information from these passive structures along with those originating from muscle spindles, which may have contributed to the larger amplitudes observed in the rotator cuff muscles relative to those in the primary movers. Integration of afferent information from capsular proprioceptors would likely be much larger for reflexes elicited by glenohumeral translations compared to those elicited by glenohumeral rotations given that the latter should generate less strain on the passive structures. Interestingly, both the Voigt et al. (1998) and Diederichsen et al. (2004) studies noted strong suppressive responses in the shoulder muscles upon stimulation of the capsular and ligamentous afferents. In contrast, the translational perturbations used in our study elicited facilitative and suppressive reflexes. This difference may also result from the integrated effects of different sensory organs and pathways that are stimulated when the intact shoulder is translated as opposed to the more focused electrical stimulation used in prior work.

Factors Contributing to Different Reflex Latencies Between Shoulder Muscles

We found that reflex latencies were approximately 5 ms shorter in the rotator cuff muscles than in the primary shoulder movers. These findings were driven in part by long latencies in the *latissimus dorsi* and *teres major* and short latencies in the *supraspinatus* and *infraspinous*. However, in our control experiment, reflexes were approximately 7 ms shorter when recorded with fine-wire electrodes than with surface electrodes. While these instrumentation differences do not account for the full range of reflex latencies we observed (**Figure 8**), we cannot rule out the possibility that they are large enough to explain the average differences between rotator cuff muscles and primary movers. Interestingly, Day et al. (2012) also found reflexes in the rotator cuff muscles are faster than in the primary movers following unexpected internal and external rotation perturbations to the shoulder. They reported the fastest responses in the *infraspinatus* and *subscapularis*, and slower responses in the *anterior* and *posterior deltoid*. Notably, they also used fine-wire electrodes and surface electrodes to record reflexes in the rotator cuff muscles and primary shoulder movers, respectively, which may have contributed to their findings. A more careful assessment of any possible latency differences between these groups of muscles will require the consistent use of fine-wire electrodes.

The two muscles with the longest latencies in our study also demonstrated the largest negative correlation between muscle activation and reflex latency. The decrease in reflex latencies with increased muscle activity could arise from a more effective transmission of the perturbation to the muscles, a decreased threshold of the motoneuron pool, or increased spindle sensitivity arising from gamma activation (Vallbo, 1974). Similar to our activation-dependent measures, Myers et al. (2003) found that the latencies of reflexes in the *latissimus dorsi*, elicited by glenohumeral rotations in healthy shoulders, are also longer than in other shoulder muscles during relaxed conditions and decrease with increasing muscle activation; above 20% MVC, the latencies of the *latissimus dorsi* were comparable to those in other shoulder muscles. While the latencies of the *latissimus dorsi* and *teres major* in our study still were larger than most other shoulder muscles at higher activations, we did not approach the levels of activation tested by Myers et al. (2003). Higher activations may have led to the same result.

We are aware of only one other assessment of reflex latencies occurring from translational perturbations of the humeral head. Latimer et al. (1998) applied anterior translational forces to the humeral head using a pulley system that dropped weights onto an outstretched arm. Reflex latencies were recorded under passive conditions in multiple rotator cuff muscles and primary shoulder movers. Across all the tested shoulder muscles, they reported latencies of passive reflexes that ranged from 110 to 220 ms. The passive conditions of that study likely increased reflex times due to poor mechanical transmission along with the neural factors described above. Importantly, voluntary responses to perturbations can occur with latencies as short as 100 ms (Hammond, 1956; Honeycutt and Perreault, 2012; Forgaard et al., 2015), so it is unclear if the latencies reported by Latimer et al. (1998) represent reflex or volitional responses.

Across all muscles, reflexes in our study occurred at average latencies of 25–45 ms. While the fastest responses are similar in latency to stretch-evoked reflexes elicited by rotational perturbations of the shoulder (Perreault et al., 2008; Muraoka and Kurtzer, 2020; Nicolozakes, 2021), most are slower than would be expected for monosynaptic stretch-evoked reflexes. These longer latencies suggest that the reflexes elicited by translational perturbations may arise from structures other than muscle spindles, as discussed above. While the source of the reflex responses was not addressed in our work, it is interesting to note that reflexes elicited by electrical stimulation of the glenohumeral capsule have been measured to have latencies of approximately 33 ms, which are more consistent with the latencies observed in our study (Voigt et al., 1998). These slower responses provide further evidence that secondary afferents and the sensors they innervate likely contributed to the net reflexes observed in this study.

Methodological Considerations

Our study is among the first to assess reflexes elicited by translations of the glenohumeral joint, which can lead to dislocation when large enough to move the humeral head out of the glenoid fossa. These translations of the intact joint have the benefit of exciting all sensors that respond to joint translations during normal activities, and therefore could be considered more functional than the elegant mechanistic studies that have stimulated isolated elements within the sensory system of the shoulder. What is lost is the ability to identify the role of specific sensory systems in the net reflex responses we quantified. Modeling studies or more detailed experimental measures may help to bridge this gap.

In our control experiment, we found that reflex latencies were shorter when recorded with fine-wire intramuscular electrodes than when recorded with surface electrodes in the same muscle. These differences may have contributed to the shorter latencies we observed in the rotator cuff muscles since their anatomy, unlike the primary shoulder movers, required the use of fine-wire electrodes. Our results differ from those of prior comparisons of reflex latencies between surface and fine-wire electrodes, which found no differences between the two modalities (Wittek et al., 2001), although the standard deviations of their measurements were much higher than ours. Reflex amplitudes and gain-scaling factors were also slightly larger when recorded with fine-wire intramuscular electrodes. However, the differences were smaller than the differences we observed between rotator cuff muscles and primary shoulder movers in our primary experiment. Hence, these recording differences may have influenced the magnitude of the differences in reflex amplitude and gain-scaling we observed between muscle groups but not our overall conclusions. While studies analyzing shoulder muscle activity commonly record EMG with surface and fine-wire electrodes (Barden et al., 2005; Kibler et al., 2007; Day et al., 2012; Thomas et al., 2013), our results suggest that more consistent recording with fine-wire electrodes is warranted when the timing of EMG responses is of interest.

Our experiments were designed to assess shoulder reflexes elicited by glenohumeral translations. However, it was not possible to isolate our experimental perturbations solely to the glenohumeral joint, which would require a more direct interface with the bones of the humerus and scapula. We therefore cannot rule out small rotations occurring at the glenohumeral joint during the trials. We minimized soft tissue displacement by applying perturbations through a tight-fitting cast that interfaced with bony prominences on the humerus and by externally clamping the scapula. The comprehensive casting minimized glenohumeral rotations so that translations applied at the middle of the humerus were transmitted to the humeral head with minimal rotation of the humerus. This setup allowed us to use small, safe perturbations that avoided the possibility of dislocation, while still creating controlled translational strains at the glenohumeral joint.

It is also important to note that our results are limited to the posture we studied. We made all measurements with the shoulder oriented in 90° abduction, neutral rotation, and 20° horizontal flexion. Given that the tension of the glenohumeral capsule and the muscles' lines of action are unique to a shoulder's orientation (Turkel et al., 1981; Ackland and Pandy, 2009), reflexes are likely to vary at different shoulder postures. One example is the apprehension posture, which is linked to symptom reproduction in individuals with shoulder instability (Rowe and Zarins, 1981). We previously reported that the translational stiffness of the glenohumeral joint differs between the posture tested in our study and the apprehension posture (Nicolozakes et al., 2021). It is likely that reflexes also vary with posture due to differences in how shoulder muscles and passive glenohumeral structures are oriented in each posture (Turkel et al., 1981; Ackland and Pandy, 2009).

CONCLUSIONS

In summary, we found that stretch-evoked reflexes elicited by glenohumeral translations were larger in rotator cuff muscles than reflexes in primary shoulder movers. The strong reflexes elicited in the rotator cuff muscles, whose amplitudes ranged from 33% to 55% of background activity, could play a substantial role in maintaining shoulder stability, since the actions of the rotator cuff increase shoulder stability by pulling the humeral head into the glenoid fossa. While strong reflex activation of the rotator cuff muscles seems to be an appropriate response to mitigate the effects of unexpected translations, the mechanisms driving this response remain unclear since the muscles that have the largest reflex response to translations would also have relatively small length changes. This suggests a coordinated sensory response that integrates information from multiple structures within the shoulder, rather than only the muscle spindles commonly associated with stretch-evoked reflexes. Injury to the glenohumeral capsule that occurs following dislocation reduces shoulder proprioception and impacts reflexes elicited by joint rotations (Lephart et al., 1994; Zuckerman et al., 2003; Myers et al., 2004); what remains to be seen is if these disruptions also alter the reflexively elicited protective responses observed in this study. If so, our results can serve as a valuable benchmark to compare the translational reflexes present in healthy shoulders to those altered in individuals who have suffered dislocations or other injuries that alter the passive and active structures contributing to shoulder stability.

DATA AVAILABILITY STATEMENT

The raw data supporting the conclusions of this article will be made available by the authors upon request, without undue reservation.

ETHICS STATEMENT

The studies involving human participants were reviewed and approved by Northwestern University Institutional Review Board. The participants provided their written informed consent to participate in this study.

AUTHOR CONTRIBUTIONS

CN conceived the project, designed and performed the experiments, performed the analyses, and wrote the manuscript. MC-T performed the experiments and performed the analyses. DL designed the experiments and performed the analyses. AS and EP supervised the design of experiments and analyses of results. All authors contributed to the article and edited, revised, and approved the final submitted version of the manuscript.

FUNDING

This work was supported in part by the National Institutes of Health (NIAMS F31AR074288, NIGMS T32GM008152, NCATS UL1TR001422), The American Society of Biomechanics Graduate Student Grant-in-Aid, and Northwestern University.

ACKNOWLEDGMENTS

We would like to acknowledge Timothy Haswell and Julia Schmulewitz for their assistance with designing the experimental setup and collecting data.

SUPPLEMENTARY MATERIALS

The Supplementary Material for this article can be found online at: https://www.frontiersin.org/articles/10.3389/fnint.2021.796472/full#supplementary-material.

REFERENCES

Ackland, D. C., and Pandy, M. G. (2009). Lines of action and stabilizing potential of the shoulder musculature. *J. Anat.* 215, 184–197. doi: 10.1111/j.1469-7580.2009.01090.x

Agur, A. M. R., and Grant, J. C. B. (2013). *Grant's Atlas of Anatomy.* Philadelphia: Wolters Kluwer Health/Lippincott Williams & Wilkins.

Barden, J. M., Balyk, R., Raso, V. J., Moreau, M., and Bagnall, K. (2005). Atypical shoulder muscle activation in multidirectional instability. *Clin. Neurophysiol.* 116, 1846–1857. doi: 10.1016/j.clinph.2005.04.019

Besomi, M., Hodges, P. W., Clancy, E. A., Van Dieen, J., Hug, F., Lowery, M., et al. (2020). Consensus for experimental design in electromyography (CEDE) project: amplitude normalization matrix. *J. Electromyogr. Kinesiol.* 53:102438. doi: 10.1016/j.jelekin.2020.102438

Blum, K. P., Campbell, K. S., Horslen, B. C., Nardelli, P., Housley, S. N., Cope, T. C., et al. (2020). Diverse and complex muscle spindle afferent firing properties emerge from multiscale muscle mechanics. *eLife* 9:e55177. doi: 10.7554/eLife.55177

Boone, D. C., and Azen, S. P. (1979). Normal range of motion of joints in male subjects. *J. Bone Joint Surg. Am.* 61, 756–759.

Brenneke, S. L., Reid, J., Ching, R. P., and Wheeler, D. L. (2000). Glenohumeral kinematics and capsulo-ligamentous strain resulting from laxity exams. *Clin. Biomech. (Bristol, Avon)* 15, 735–742. doi: 10.1016/s0268-0033(00)00041-3

Bresch, J. R., and Nuber, G. W. (1995). Mechanoreceptors of the middle and inferior glenohumeral ligaments. *J. Shoulder and Elbow Surg.* 4, S63–S64. doi: 10.1016/S1058-2746(95)80219-3

Carter, R. R., Crago, P. E., and Keith, M. W. (1990). Stiffness regulation by reflex action in the normal human hand. *J. Neurophysiol.* 64, 105–118. doi: 10.1152/jn.1990.64.1.105

Cathers, I., O'dwyer, N., and Neilson, P. (1999). Dependence of stretch reflexes on amplitude and bandwidth of stretch in human wrist muscle. *Exp. Brain Res.* 129, 278–287. doi: 10.1007/s002210050898

Day, A., Taylor, N. F., and Green, R. A. (2012). The stabilizing role of the rotator cuff at the shoulder--responses to external perturbations. *Clin. Biomech. (Bristol, Avon)* 27, 551–556. doi: 10.1016/j.clinbiomech.2012.02.003

Diederichsen, L. P., Norregaard, J., Krogsgaard, M., Fischer-Rasmussen, T., and Dyhre-Poulsen, P. (2004). Reflexes in the shoulder muscles elicited from the human coracoacromial ligament. *J. Orthop. Res.* 22, 976–983. doi: 10.1016/j.orthres.2003.12.019

Finley, J. M., Dhaher, Y. Y., and Perreault, E. J. (2013). Acceleration dependence and task-specific modulation of short- and medium-latency reflexes in the ankle extensors. *Physiol. Rep.* 1:e00051. doi: 10.1002/phy2.51

Forgaard, C. J., Franks, I. M., Maslovat, D., Chin, L., and Chua, R. (2015). Voluntary reaction time and long-latency reflex modulation. *J. Neurophysiol.* 114, 3386–3399. doi: 10.1152/jn.00648.2015

Gohlke, F., Janssen, E., Leidel, J., Heppelmann, B., and Eulert, J. (1998). [Histopathological findings in the proprioception of the shoulder joint]. *Orthopade* 27, 510–517. doi: 10.1007/s001320050263

Guanche, C. A., Noble, J., Solomonow, M., and Wink, C. S. (1999). Periarticular neural elements in the shoulder joint. *Orthopedics* 22, 615–617. doi: 10.3928/0147-7447-19990601-12

Hammond, P. H. (1956). The influence of prior instruction to the subject on an apparently involuntary neuro-muscular response. *J. Physiol.* 132, 17–18P.

Hermens, H. J., Freriks, B., Disselhorst-Klug, C., and Rau, G. (2000). Development of recommendations for SEMG sensors and sensor placement procedures. *J. Electromyogr. Kinesiol.* 10, 361–374. doi: 10.1016/s1050-6411(00)00027-4

Honeycutt, C. F., and Perreault, E. J. (2012). Planning of ballistic movement following stroke: insights from the startle reflex. *PLoS One* 7:e43097. doi: 10.1371/journal.pone.0043097

Jonsson, B. (1978). Quantitative electromyographic evaluation of muscular load during work. *Scand. J. Rehabil. Med. Suppl.* 6, 69–74.

Kearney, R. E., Stein, R. B., and Parameswaran, L. (1997). Identification of intrinsic and reflex contributions to human ankle stiffness dynamics. *IEEE Trans. Biomed. Eng.* 44, 493–504. doi: 10.1109/10.581944

Kerr, Z. Y., Collins, C. L., Pommering, T. L., Fields, S. K., and Comstock, R. D. (2011). Dislocation/separation injuries among US high school athletes in 9 selected sports: 2005–2009. *Clin. J. Sport. Med.* 21, 101–108. doi: 10.1097/JSM.0b013e31820bd1b6

Kibler, W. B., Chandler, T. J., Shapiro, R., and Conuel, M. (2007). Muscle activation in coupled scapulohumeral motions in the high performance tennis serve. *Br. J. Sports Med.* 41, 745–749. doi: 10.1136/bjsm.2007.037333

Krutky, M. A., Ravichandran, V. J., Trumbower, R. D., and Perreault, E. J. (2010). Interactions between limb and environmental mechanics influence stretch reflex sensitivity in the human arm. *J. Neurophysiol.* 103, 429–440. doi: 10.1152/jn.00679.2009

Labriola, J. E., Lee, T. Q., Debski, R. E., and Mcmahon, P. J. (2005). Stability and instability of the glenohumeral joint: the role of shoulder muscles. *J. Shoulder Elbow Surg.* 14, 32S–38S. doi: 10.1016/j.jse.2004.09.014

Latimer, H. A., Tibone, J. E., Pink, M. M., Mohr, K. J., and Perry, J. (1998). Shoulder reaction time and muscle-firing patterns in response to an anterior translation force. *J. Shoulder Elbow Surg.* 7, 610–615. doi: 10.1016/s1058-2746(98)90009-x

Lee, S. B., Kim, K. J., O'driscoll, S. W., Morrey, B. F., and An, K. N. (2000). Dynamic glenohumeral stability provided by the rotator cuff muscles in the mid-range and end-range of motion. A study in cadavera. *J. Bone Joint Surg. Am.* 82, 849–857. doi: 10.2106/00004623-200006000-00012

Lephart, S. M., Warner, J. J., Borsa, P. A., and Fu, F. H. (1994). Proprioception of the shoulder joint in healthy, unstable and surgically repaired shoulders. *J. Shoulder Elbow Surg.* 3, 371–380. doi: 10.1016/S1058-2746(09)80022-0

Lewis, G. N., Perreault, E. J., and Mackinnon, C. D. (2005). The influence of perturbation duration and velocity on the long-latency response to stretch in the biceps muscle. *Exp. Brain Res.* 163, 361–369. doi: 10.1007/s00221-004-2182-9

Lewis, G. N., Polych, M. A., and Byblow, W. D. (2004). Proposed cortical and sub-cortical contributions to the long-latency stretch reflex in the forearm. *Exp. Brain Res.* 156, 72–79. doi: 10.1007/s00221-003-1767-z

Lippitt, S. B., Harryman, D. T. I., Sidles, J. A., and Matsen, F. a. I. (1991). Diagnosis and management of AMBRI syndrome. *Tech. Orthop.* 6, 61–74.

Lippitt, S., and Matsen, F. (1993). Mechanisms of glenohumeral joint stability. *Clin. Orthop. Relat. Res.* 291, 20–28. doi: 10.1097/00003086-199306000-00004

Lippitt, S. B., Vanderhooft, J. E., Harris, S. L., Sidles, J. A., Harryman 2nd, D. T., and Matsen 3rd, F. A. (1993). Glenohumeral stability from concavity-compression: a quantitative analysis. *J. Shoulder Elbow Surg.* 2, 27–35. doi: 10.1016/S1058-2746(09)80134-1

Longo, U. G., Huijsmans, P. E., Maffulli, N., Denaro, V., and De Beer, J. F. (2011). Video analysis of the mechanisms of shoulder dislocation in four elite rugby players. *J. Orthop. Sci.* 16, 389–397. doi: 10.1007/s00776-011-0087-6

Ludvig, D., Preuss, R., and Lariviere, C. (2019). The effect of extensible and non-extensible lumbar belts on trunk muscle activity and lumbar stiffness in subjects with and without low-back pain. *Clin. Biomech. (Bristol, Avon)* 67, 45–51. doi: 10.1016/j.clinbiomech.2019.04.019

Luke, S. G. (2017). Evaluating significance in linear mixed-effects models in R. *Behav. Res. Methods* 49, 1494–1502. doi: 10.3758/s13428-016-0809-y

Matthews, P. B. (1986). Observations on the automatic compensation of reflex gain on varying the pre-existing level of motor discharge in man. *J. Physiol.* 374, 73–90. doi: 10.1113/jphysiol.1986.sp016066

Merletti, R., and Cerone, G. L. (2020). Tutorial. Surface EMG detection, conditioning and pre-processing: best practices. *J. Electromyogr. Kinesiol.* 54:102440. doi: 10.1016/j.jelekin.2020.102440

Montgomery, C., O'briain, D. E., Hurley, E. T., Pauzenberger, L., Mullett, H., and Moran, C. J. (2019). Video analysis of shoulder dislocations in rugby: insights into the dislocating mechanisms. *Am. J. Sports Med.* 47, 3469–3475. doi: 10.1177/0363546519882412

Muraoka, T., and Kurtzer, I. (2020). Spinal circuits mediate a stretch reflex between the upper limbs in humans. *Neuroscience* 431, 115–127. doi: 10.1016/j.neuroscience.2020.02.007

Myers, J. B., Ju, Y. Y., Hwang, J. H., Mcmahon, P. J., Rodosky, M. W., and Lephart, S. M. (2004). Reflexive muscle activation alterations in shoulders with anterior glenohumeral instability. *Am. J. Sports Med.* 32, 1013–1021. doi: 10.1177/0363546503262190

Myers, J. B., Riemann, B. L., Ju, Y. Y., Hwang, J. H., Mcmahon, P. J., and Lephart, S. M. (2003). Shoulder muscle reflex latencies under various levels of muscle contraction. *Clin. Orthop. Relat. Res.* 407, 92–101. doi: 10.1097/00003086-200302000-00017

Nakazawa, K., Yamamoto, S. I., and Yano, H. (1997). Short- and long-latency reflex responses during different motor tasks in elbow flexor muscles. *Exp. Brain Res.* 116, 20–28. doi: 10.1007/pl00005740

Neilson, P. D., and Mccaughey, J. (1981). Effect of contraction level and magnitude of stretch on tonic stretch reflex transmission characteristics. *J. Neurol. Neurosurg. Psychiatry* 44, 1007–1012. doi: 10.1136/jnnp.44.11.1007

Nemeth, G., Kronberg, M., and Brostrom, L. A. (1990). Electromyogram (EMG) recordings from the subscapularis muscle: description of a technique. *J. Orthop. Res.* 8, 151–153. doi: 10.1002/jor.1100080120

Nichols, T. R., and Houk, J. C. (1976). Improvement in linearity and regulation of stiffness that results from actions of stretch reflex. *J. Neurophysiol.* 39, 119–142. doi: 10.1152/jn.1976.39.1.119

Nicolozakes, C. P. (2021). *Quantifying the Biomechanical and Neural Factors Contributing to Translational Shoulder Stability*. PhD Thesis. Northwestern University, Evanston, IL. Ann Arbor, MI: Proquest.

Nicolozakes, C. P., Ludvig, D., Baillargeon, E. M., Perreault, E. J., and Seitz, A. L. (2021). Muscle contraction has a reduced effect on Increasing glenohumeral stability in the apprehension position. *Med. Sci. Sports Exerc.* 53, 2354–2362. doi: 10.1249/MSS.0000000000002708

Perotto, A., and Delagi, E. F. (2011). *Anatomical Guide for the Electromyographer : The Limbs and Trunk*. Springfield, IL: Charles C. Thomas.

Perreault, E. J., Chen, K., Trumbower, R. D., and Lewis, G. (2008). Interactions with compliant loads alter stretch reflex gains but not intermuscular coordination. *J. Neurophysiol.* 99, 2101–2113. doi: 10.1152/jn.01094.2007

Poppele, R. E., and Bowman, R. J. (1970). Quantitative description of linear behavior of mammalian muscle spindles. *J. Neurophysiol.* 33, 59–72. doi: 10.1152/jn.1970.33.1.59

Pruszynski, J. A., Kurtzer, I., Lillicrap, T. P., and Scott, S. H. (2009). Temporal evolution of "automatic gain-scaling". *J. Neurophysiol.* 102, 992–1003. doi: 10.1152/jn.00085.2009

Pruszynski, J. A., Kurtzer, I., and Scott, S. H. (2008). Rapid motor responses are appropriately tuned to the metrics of a visuospatial task. *J. Neurophysiol.* 100, 224–238. doi: 10.1152/jn.90262.2008

Rowe, C. R., and Zarins, B. (1981). Recurrent transient subluxation of the shoulder. *J. Bone Joint Surg. Am.* 63, 863–872. doi: 10.2106/00004623-198163060-00001

Semciw, A. I., Neate, R., and Pizzari, T. (2014). A comparison of surface and fine wire EMG recordings of gluteus medius during selected maximum isometric voluntary contractions of the hip. *J. Electromyogr. Kinesiol.* 24, 835–840. doi: 10.1016/j.jelekin.2014.08.015

Shemmell, J., An, J. H., and Perreault, E. J. (2009). The differential role of motor cortex in stretch reflex modulation induced by changes in environmental mechanics and verbal instruction. *J. Neurosci.* 29, 13255–13263. doi: 10.1523/JNEUROSCI.0892-09.2009

Sinkjaer, T., and Hayashi, R. (1989). Regulation of wrist stiffness by the stretch reflex. *J. Biomech.* 22, 1133–1140. doi: 10.1016/0021-9290(89)90215-7

Soslowsky, L. J., Flatow, E. L., Bigliani, L. U., and Mow, V. C. (1992). Articular geometry of the glenohumeral joint. *Clin. Orthop. Relat. Res.* 285, 181–190. doi: 10.1097/00003086-199212000-00023

Steinbeck, J., Bruntrup, J., Greshake, O., Potzl, W., Filler, T., and Liljenqvist, U. (2003). Neurohistological examination of the inferior glenohumeral ligament of the shoulder. *J. Orthop. Res.* 21, 250–255. doi: 10.1016/S0736-0266(02)00155-9

Thomas, S. J., Swanik, C. B., Higginson, J. S., Kaminski, T. W., Swanik, K. A., Kelly, J. D., et al. (2013). Neuromuscular and stiffness adaptations in division I collegiate baseball players. *J. Electromyogr. Kinesiol.* 23, 102–109. doi: 10.1016/j.jelekin.2012.07.005

Turkel, S. J., Panio, M. W., Marshall, J. L., and Girgis, F. G. (1981). Stabilizing mechanisms preventing anterior dislocation of the glenohumeral joint. *J. Bone Joint Surg. Am.* 63, 1208–1217. doi: 10.2106/00004623-198163080-00002

Vallbo, A. B. (1974). Human muscle spindle discharge during isometric voluntary contractions. Amplitude relations between spindle frequency and torque. *Acta Physiol. Scand.* 90, 319–336. doi: 10.1111/j.1748-1716.1974.tb05594.x

Vangsness, C. T., Jr., Ennis, M., Taylor, J. G., and Atkinson, R. (1995). Neural anatomy of the glenohumeral ligaments, labrum and subacromial bursa. *Arthroscopy* 11, 180–184. doi: 10.1016/0749-8063(95)90064-0

Veeger, H. E., and Van Der Helm, F. C. (2007). Shoulder function: the perfect compromise between mobility and stability. *J. Biomech.* 40, 2119–2129. doi: 10.1016/j.jbiomech.2006.10.016

Voigt, M., Jakobsen, J., and Sinkjaer, T. (1998). Non-noxious stimulation of the glenohumeral joint capsule elicits strong inhibition of active shoulder muscles in conscious human subjects. *Neurosci. Lett.* 254, 105–108. doi: 10.1016/s0304-3940(98)00665-x

Waite, D. L., Brookham, R. L., and Dickerson, C. R. (2010). On the suitability of using surface electrode placements to estimate muscle activity of the rotator cuff as recorded by intramuscular electrodes. *J. Electromyogr. Kinesiol.* 20, 903–911. doi: 10.1016/j.jelekin.2009.10.003

Witherspoon, J. W., Smirnova, I. V., and Mciff, T. E. (2014). Neuroanatomical distribution of mechanoreceptors in the human cadaveric shoulder capsule and labrum. *J. Anat.* 225, 337–345. doi: 10.1111/joa.12215

Wittek, A., Ono, K., Kajzer, J., Ortengren, R., and Inami, S. (2001). Analysis and comparison of reflex times and electromyograms of cervical muscles under impact loading using surface and fine-wire electroces. *IEEE Trans. Biomed. Eng.* 48, 143–153. doi: 10.1109/10.909635

Zuckerman, J. D., Gallagher, M. A., Cuomo, F., and Rokito, A. (2003). The effect of instability and subsequent anterior shoulder repair on proprioceptive ability. *J. Shoulder Elbow Surg.* 12, 105–109. doi: 10.1067/mse.2003.4

Conflict of Interest: The authors declare that the research was conducted in the absence of any commercial or financial relationships that could be construed as a potential conflict of interest.

frontiers
in Integrative Neuroscience

MINI REVIEW
published: 21 February 2022
doi: 10.3389/fnint.2022.835852

Neural Control of Stopping and Stabilizing the Arm

***Shanie A. L. Jayasinghe*[1]*, Robert A. Scheidt*[2] *and Robert L. Sainburg*[1,3,4]**

[1] Department of Neurology, Pennsylvania State University College of Medicine, Hershey, PA, United States, [2] Department of Biomedical Engineering, Marquette University and Medical College of Wisconsin, Milwaukee, WI, United States, [3] Department of Kinesiology, Pennsylvania State University, State College, PA, United States, [4] Huck Institutes of the Life Sciences, Pennsylvania State University, State College, PA, United States

Stopping is a crucial yet under-studied action for planning and producing meaningful and efficient movements. In this review, we discuss classical human psychophysics studies as well as those using engineered systems that aim to develop models of motor control of the upper limb. We present evidence for a hybrid model of motor control, which has an evolutionary advantage due to division of labor between cerebral hemispheres. Stopping is a fundamental aspect of movement that deserves more attention in research than it currently receives. Such research may provide a basis for understanding arm stabilization deficits that can occur following central nervous system (CNS) damage.

Keywords: muscle, impedance control, upper limb, motor control, movement

OPEN ACCESS

Edited by:
Richard Nichols,
Georgia Institute of Technology,
United States

Reviewed by:
Warren G. Darling,
The University of Iowa, United States

Correspondence:
Shanie A. L. Jayasinghe
szj5408@psu.edu

Received: *15 December 2021*
Accepted: *17 January 2022*
Published: *21 February 2022*

Citation:
Jayasinghe SAL, Scheidt RA and Sainburg RL (2022) Neural Control of Stopping and Stabilizing the Arm. Front. Integr. Neurosci. 16:835852. doi: 10.3389/fnint.2022.835852

INTRODUCTION

When examining the neural mechanisms that underlie control of upper limb movements in humans, previous research has predominantly focused on how the nervous system specifies and actuates movement trajectories. However, an underappreciated yet critical aspect of motor control is the ability to stop movement at an intended and stable position, such as when a tennis player runs up to the net, stops, and hits a drop shot without falling through the net. Complex, graceful behaviors require that maneuverability of action be complemented with the ability to stabilize the body rapidly and precisely, and biological impedance control provides an elegant solution to the stopping problem.

Consider what would be needed to bring the hand to rest at a target without a specialized mechanism for controlling impedance. Precise joint torques would need to be planned and applied to decelerate a given motion, and inaccuracies due to "noise" and inaccurate predictions in motor commands and/or delays in sensory feedback would inevitably lead to instability. The arrangement of agonist and antagonist muscles across our joints allows two types of braking mechanisms—deceleration through the activation of task antagonists (imagine a car screeching to a halt at a traffic light), and position- and velocity-dependent impedance control through coactivation of agonist and antagonist muscles (similar to air brakes on an airplane that are used to reduce drag but not lift).

Mechanical impedance relates forces to resulting motions (velocities). As such, impedance can be characterized by the inertial, viscous, and elastic resistance to motion. Limb stiffness and viscosity can be modulated through muscle coactivation (i.e., simultaneous activation of opposing muscles at a joint) (Hogan, 1984; Lacquaniti et al., 1993) and through the modulation of proprioceptive reflex gains and thresholds (Takahashi et al., 2001; Pruszynski and Scott, 2012; Sainburg, 2014). Limb endpoint inertia is configuration-dependent (Hogan, 1985), and stiffness modulation *via* synergistic activation of muscles is used for postural coordination

(Mussa-Ivaldi et al., 1985). We propose that the action of stopping requires defining a specific limb configuration, and also defining parameters such as viscosity and stiffness.

HOW WE MOVE DEPENDS ON HOW WE STOP—AND *VICE VERSA*

There are two distinct ways in which movements can be "stopped." In one, inhibitory circuits in the brain suppress activity in cortical structures involved in movement planning and execution prior to the initiation of the movement (Nielson et al., 2002; Lemon and Kraskov, 2019). Inhibitory control is an aspect of executive functioning that is a focus of much research on decision making in health, normal aging, and disease (Rubia et al., 2001; Aron et al., 2007; Langenecker et al., 2007; Votruba et al., 2008; Mannarelli et al., 2020; Elverman et al., 2021). In this review, we limit our consideration to the second type of stopping—physical interaction between the motor periphery and the environment, that brings the limb to rest at a new stable posture after a movement has been initiated (c.f. Noorani and Carpenter, 2017).

Early studies of muscle activity during goal-directed reaching have demonstrated the role of antagonist muscle activity in stopping a ballistic movement. Studies of the classic triphasic electromyography (EMG) pattern commonly observed during fast goal-directed movements have identified notable stereotyped behaviors (Hallett et al., 1975; Ghez and Martin, 1982; Meinck et al., 1984; Hannaford and Stark, 1985). Specifically, at the beginning of a movement, any tonic activity in the functional antagonist ceases and a burst of activity in the functional agonist accelerates the limb toward its target. Around the time of peak movement velocity, the initial agonist burst ceases and antagonist activity rises to decelerate the limb. Shortly after the onset of the antagonist, agonist activity again arises as the limb is brought to rest at its intended target (Hallett et al., 1975).

In another seminal study examining the processes that underly transitions from movement to posture, Lestienne et al. (1981) examined the EMG patterns associated with a large range of single joint movements of various amplitudes, speeds, and directions made throughout the range of motion of the elbow and wrist joints. Their findings revealed reciprocal agonist-antagonist EMG patterns that characterized the early phase of motion, followed by coactivation patterns that characterized the later phase of movement. Coactivation patterns extended throughout the deceleration phase of movement into the postural stabilization phase and were characterized by a unique ratio of agonist to antagonist activity that varied with each final posture, a finding that could be explained partially by the differing muscle mechanical states associated with each final limb configuration. The fact that coactivation ratios varied directly with posture, but not with trajectory features such as movement direction, amplitude, or velocity led the authors to conclude: "The motor processes controlling final position and trajectory seem to be independent." These findings and conclusion support our hypothesis of independent mechanisms for control of trajectory and posture, which will be discussed later in this paper.

Studies with peripherally deafferented individuals have also shown the presence of the triphasic EMG pattern; however, the magnitude of the antagonist burst is not as strongly correlated to the magnitude of the first agonist burst as it is in neurologically intact individuals (Forget and Lamarre, 1987). Importantly, (Brown and Cooke, 1990) showed that humans can modify the triphasic EMG pattern when producing movements with different temporal profiles, such that the duration of initial agonist burst offset and antagonist burst onset can be modified. These studies show that online peripheral feedback is crucial for modulating the limb's mechanical interaction with the environment through the coordinated activity of functionally antagonistic muscles, and that neither peripheral mechanics nor central commands alone suffice.

In fact, numerous studies have demonstrated that the human central nervous system (CNS) is adept at achieving movement goals despite environmental changes impacting performance. This ability is facilitated by a phenomenon known as sensorimotor adaptation, which is a form of learning whereby the CNS adjusts motor behavior to restore performance in the presence of altered environmental conditions. Adaptation studies further highlight the importance of central influences on how the limb interacts physically with the environment. For example, when a ball is dropped from a specific height, we are able to infer an accurate time of interception and to modulate limb impedance accordingly (Lacquaniti et al., 1993); however, in conditions of reduced gravity, such as during space flight, the timing of interception is inaccurate because visual cues about the target are combined with an *a priori* model of the earth's gravitational acceleration (Lacquaniti et al., 2015). Adaptation also explains how we experience aftereffects from changing mechanical conditions. For example, when spending time on a boat, the CNS adapts to the rocking of the boat by implementing predictive and reactive mechanisms. Upon returning to stable ground, individuals experience "sea legs," which is the body countering the swaying that occurred on the boat to maintain balance, and reflects the CNS predicting waves that no longer exist. After a short time, however, this aftereffect goes away, due to readaptation to stable conditions. Such aftereffects have been shown in motor learning studies, and they reflect predictions of previously applied and adapted forces (Lackner and Dizio, 1994; Shadmehr and Mussa-Ivaldi, 1994; Sainburg and Kalakanis, 2000). A recent study showed that humans adapt their movement at different rates depending on the type of load placed on the upper limb—inertial, viscous, elastic—and that such adaptation may be explained by the existence of internal models of limb mechanics that are updated at different speeds (Oh et al., 2021). These studies have been interpreted to reflect a process that models the applied environment dynamics in order to control movements through predictive mechanisms involving neural structures widely distributed throughout the CNS (c.f. Scheidt et al., 2012). The study of central influence on peripheral interactions with the environment continues to be an important topic of research.

WHAT WE HAVE LEARNED FROM ENGINEERED SYSTEMS

Various computational models have been used to describe the neural control of movement and stopping. The CNS receives feedback from multiple sources, which suggests that it must decide how and when to integrate different types of feedback for movement planning. Limb movement can be stabilized through the use of neural feedback loops involving the CNS and muscles (Suminski et al., 2007), as well as through predictive control of mechanical impedance in the muscle (Burdet et al., 2001) and multi-articular limb (Hogan, 1985; Mah, 2001). A disadvantage of pure feedback control is that sensory information processing delays can be slow, leading to long loop delays. Therefore, in order to survive, we must be able to plan feedforward commands that are based on internal models (i.e., expectations) of the dynamic interactions between the limb and its environment and their sensory consequences. However, feedforward control also has limitations, including the inability to compensate in real-time for performance errors induced by environmental uncertainties, prediction errors, and potential noise in the motor execution system. Some combination of feedforward and feedback control schemes could have functional utility. How might this work?

One possibility is captured by the idea of model-free control, which has been used to describe biological movement. The equilibrium point hypothesis (Asatryan and Feldman, 1965) proposes that the CNS need not account for or control biomechanical nor environmental dynamics, but instead purports that centrally specified reference configurations (equilibrium positions or "set points") are a product of coactivation and reciprocal commands that result in stiffness about specified or "referent" configurations. Shifts in the referent configurations result in movement trajectories through the interaction of emergent muscle forces and joint torques interacting with mechanical loads. The utility of the model-free control approach was demonstrated by Buchli et al. (2011), who used a robotic system in which: (1) a model-free reward function implemented trial-and-error learning and (2) a variable impedance controller allowed adaptability to different task and environmental properties. This type of control learns both reference trajectory and feedback gain schedules simultaneously, purely through experience and without the need for an *a priori* model of body and/or environmental dynamics. Model-free, trial-and-error learning may indeed be a sufficient mechanism for controlling both movement and posture, but in itself, it fails to account for evidence of internal representations of mechanical conditions that appear to allow both adaptation in—and generalization to—novel dynamic environments, such as applied force or inertial fields (Sainburg, 2015). In addition, a large amount of evidence indicates that the CNS takes inertial dynamics of body segments into account when making point-to-point reaching movements (Cooke and Virji-Babul, 1995; Sainburg et al., 1995; Ketcham et al., 2004), that sensory feedback is used to control evolving movement (Flanders et al., 1986; Cordo, 1990), and that human-object interactions are planned based on information about the physical properties and mechanics of the object (Dingwell et al., 2002; Cothros et al., 2006).

Motor selection and motor planning mechanisms involve optimizing costs, such as smoothness, accuracy, mechanical energy, etc., to produce energetically efficient trajectories (Flash and Hogan, 1985; Alexander, 1997; Todorov, 2004; Nishii and Taniai, 2009; Huang et al., 2012). This type of control requires a model of limb dynamics and a cost function in order to be able to find optimal control trajectories and feedback gain schedules. Optimal feedback control assumes that the CNS is able to find the optimal solution for any given task by allowing variability in task-irrelevant dimensions while constricting variability that affects task goals (Todorov and Jordan, 2002). While this type of control may provide the ideal solution to an engineered system, this is not necessarily how the human CNS behaves, probably due to constraints imposed by evolution. Therefore, it is likely that we define a range of task-specific costs with different gains dependent on task conditions, and which allows us to rely on a local minimum that is "good enough," i.e., satisficing rather than looking for the "optimal" solution (Rosenbaum et al., 2001; De Rugy et al., 2012; Loeb, 2021). It is important to note here that neural control of movement is not "ideal" to begin with (i.e., our movements are not always the most energetically efficient or least erroneous choice), and any assumption of its ideal nature forms an incorrect basis for models of human movement. For example, (Gribble et al., 2003) showed that co-contraction of shoulder, elbow and biarticular muscles increased with reduced target size in order to improve movement accuracy, even though this was an energetically inefficient solution. The magnitude of co-contraction reduced over the course of learning, suggesting that internal models are formed by the CNS to regulate viscoelasticity of the musculoskeletal system by producing the necessary feedforward commands (Thoroughman and Shadmehr, 1999; Osu et al., 2002). Thus, we essentially balance a tradeoff between movement accuracy and efficiency.

We propose a hybrid model of motor control in which efficient movement is specified through the combination of control mechanisms that account for internal and environmental mechanics, are mediated by feedforward and feedback control circuits, and which provide for the ability to effectively achieve a stable posture at the end of movement (Sainburg, 2014). The hybridization of predictive and impedance control mechanisms has been shown to produce smooth movements that can quickly adapt to unexpected perturbations (Takahashi et al., 2001; Scheidt and Ghez, 2007; Yadav and Sainburg, 2014). The authors have separately modeled reaching using a serial hybrid model with a forward dynamic controller for specifying an initial trajectory based on environmental and task conditions, and a postural impedance controller for specifying a final equilibrium position (Scheidt and Ghez, 2007; Yadav and Sainburg, 2011). The serial hybrid model has been used to explain interlimb differences in reaching behavior related to the time of switch from trajectory control to impedance control, whereby the left hand switches from trajectory to impedance control early in the movement (Duff and Sainburg, 2007; Schabowsky et al., 2007). In contrast, the right hand's advantage in controlling intersegmental dynamics arises from a later shift to impedance control, which allows time for sensory feedback to be integrated into online trajectory control. These two control schemes differ in terms of computational and metabolic costs, which suggests that both schemes must work together. We speculate that the two control schemes arose due to an evolutionary advantage for a division of labor between cerebral hemispheres.

LESSONS FROM HUMAN PSYCHOPHYSICS

Even the most simple of actions, such as goal-directed reaching, appear to be implemented as a sequence of distinct control actions that specify movement trajectories and stabilized limb postures. Scheidt and Ghez (2007) designed two tasks that each emphasized one aspect of movement—control of ongoing trajectory (a slicing task) or final position (a point-to-point reaching task)—by providing knowledge of performance in the form of cursor feedback at the start or at the end of the movement. When participants adapted to a visuomotor rotation while completing either the reaching or slicing task, they only adapted to the specific feature of their performance that coincided with the provided feedback. Hence, participants only adapted the initial direction of their movements when provided (rotated) cursor feedback during movement but did not substantially adapt the final stabilized positions of those same movements. Similarly, they only adapted the location of their final stabilized hand position when provided (rotated) cursor feedback at the end of movement but did not substantially adapt the initial trajectory direction of those same movements. That is, adaptation of the spatial goal for movement did not transfer to the spatial goal for stabilizing the hand at the end of the same movement and *vice versa*. A second set of observations in these studies support the independence of control actions specifying the movement's initial trajectory and final position. After practicing accurate point-to-point reaches from a start position to a target, participants overshoot the target dramatically when asked to make an out-and-back slicing movement that was to reverse direction in that same spatial target (Scheidt et al., 2011). They did so because the initial plan for movement in the slicing task, which was transferred from the reaching task, failed to account for the *absence* of increased joint impedance caused by increased joint antagonist coactivations in the neighborhood of the spatial goal during reaching but not slicing. Learning to terminate a reaching movement accurately should have allowed individuals to perform the slicing task accurately if they were guided by a common control mechanism driven by a single spatial goal. However, the experimental results indicated that different neural representations of the target position are formed to specify an initial trajectory and a final posture (i.e., that the control of trajectory and final posture are in fact distinct), that these control actions are typically performed sequentially during point-to-point reaching, and that transfer of a movement trajectory plan from one task to another related task (i.e., from reaching to slicing) does not automatically account for differences in joint viscoelasticity anticipated in subsequent phases of the action sequence.

Interlimb differences in task performance arise from hemispheric specialization for control actions regulating limb movement trajectory and final posture. Although a prominent view of handedness is that the dominant hand-hemisphere system is better at movement coordination and execution than the non-dominant side, the non-dominant hand has been shown to be superior at specific aspects of performance, such as stopping at a fixed position. In an experiment that required participants to reach from a fixed start position to multiple targets vs. from multiple start positions to a fixed target, it was found that the dominant hand's performance was better for the former than the latter task, while the non-dominant hand's performance was better on the latter task (Wang and Sainburg, 2007). The dominant system aims to minimize errors associated with intersegmental coordination and is advantageous in adapting to novel dynamic conditions (Sainburg, 2002). The non-dominant system is specialized for responding to unexpected perturbations and reducing deviations from achieving steady state postures (Mutha et al., 2012). Further evidence of hemispheric specialization for these distinct control processes arises from studies conducted on individuals with unilateral brain damage due to stroke. During a reaching task, right hemisphere damaged individuals were able to make fairly linear reaching movements toward a spatial target, but produced large errors in final position accuracy compared to neurologically intact controls and left hemisphere damaged individuals (Schaefer et al., 2009). In contrast, left hemisphere damaged stroke survivors produced significantly more curved movements, but were more accurate at the end position compared to right hemisphere damaged individuals. These results have been replicated in the contralesional arm of hemiparetic chronic stroke survivors as well (Mani et al., 2013).

Based on psychophysics, the evidence suggests that human motor control *satisfices* not *optimizes*. Our CNS is an evolved system that does not necessarily conform to an optimal engineered system. Evolution has played a crucial role in the selection of structure and function of the human nervous system, and this may help delineate between what is ideal and what is practical. Although our control system may not yield the most elegant solution from an engineering perspective, it has ensured survival as a species; hence, when studying neural control of movement, we must allow for the possibility that sensorimotor responses to changing and often unpredictable environmental conditions may not be optimal, in the engineering sense.

WHY DOES ANY OF THIS MATTER?

Hemispheric specialization has allowed for effective and efficient bimanual control (e.g., holding a slice of bread with one hand while spreading butter on it with the other). An understanding of hemispheric control mechanisms can allow the design of more personalized treatment strategies for individuals with brain deficits. For example, training the ipsilesional arm of left hemisphere damaged stroke survivors on tasks that promote movement coordination while training right hemisphere damaged individuals on tasks that require online corrections, stabilization, and stopping can be beneficial for achieving functional independence (Maenza et al., 2021). In addition, lateralized motor control processes can affect the strategies employed for retraining the less-impaired arm (Sainburg and Duff, 2006) and impact functional outcomes differently in left and right hemisphere damaged stroke survivors (Jayasinghe et al., 2020). Such insights promise benefits of personalized therapeutic and compensatory interventions for chronic stroke survivors.

Stopping, in particular, is a fundamental aspect of movement that is complex and deserves more attention than it currently receives. Metabolic costs of stopping may be different from those of trajectory control, and future work may be able to address how this impacts movement strategies. A recent study from our lab showed that stabilizing behavior was similar between stroke survivors and neurologically intact adults during a mechanically coupled bimanual task (Jayasinghe et al., 2021) even though previous work using unilateral tasks have shown performance deficits in stroke survivors. There is clearly more to the story of stabilization than meets the eye, and future work can focus on different types of stabilization tasks—online correction, staying in a fixed position during perturbation to the same hand, bimanual stabilization, etc., to form a deeper understanding of this complex phenomenon and its specialization within the brain.

AUTHOR CONTRIBUTIONS

SALJ, RAS, and RLS interpreted findings and wrote the original draft of the manuscript. All authors contributed to the article, reviewed and approved the submitted version.

FUNDING

This work was supported by the National Institutes of Health R01HD059783 awarded to RLS and R01HD053727, R15HD093086, and R21NS121624 awarded to RAS.

REFERENCES

Alexander, R. M. (1997). A minimum energy cost hypothesis for human arm trajectories. *Biol. Cybern.* 76, 97–105. doi: 10.1007/s004220050324

Aron, A. R., Durston, S., Eagle, D. M., Logan, G. D., Stinear, C. M., and Stuphorn, V. (2007). Converging evidence for a fronto-basal-ganglia network for inhibitory control of action and cognition. *J. Neurosci.* 27, 11860–11864. doi: 10.1523/JNEUROSCI.3644-07.2007

Asatryan, D., and Feldman, A. (1965). Biophysics of complex systems and mathematical models: functional tuning of nervous system with control of movement or maintenance of a steady posture: I. mechanographic analysis of the work of the joint on execution of a postural task. *Biophysics* 10, 925–935.

Brown, S. H., and Cooke, J. D. (1990). Movement-related phasic muscle activation. I. Relations with temporal profile of movement. *J. Neurophysiol.* 63, 455–464. doi: 10.1152/jn.1990.63.3.455

Buchli, J., Stulp, F., Theodorou, E., and Schaal, S. (2011). Learning variable impedance control. *Int. J. Robot. Res.* 30, 820–833. doi: 10.3390/s18082539

Burdet, E., Osu, R., Franklin, D. W., Milner, T. E., and Kawato, M. (2001). The central nervous system stabilizes unstable dynamics by learning optimal impedance. *Nature* 414, 446–449. doi: 10.1038/35106566

Cooke, J., and Virji-Babul, N. (1995). Reprogramming of muscle activation patterns at the wrist in compensation for elbow reaction torques during planar two-joint arm movements. *Exp. Brain Res.* 106, 169–176. doi: 10.1007/BF00241366

Cordo, P. J. (1990). Kinesthetic control of a multijoint movement sequence. *J. Neurophysiol.* 63, 161–172. doi: 10.1152/jn.1990.63.1.161

Cothros, N., Wong, J., and Gribble, P. (2006). Are there distinct neural representations of object and limb dynamics? *Exp. Brain Res.* 173, 689–697. doi: 10.1007/s00221-006-0411-0

De Rugy, A., Loeb, G. E., and Carroll, T. J. (2012). Muscle coordination is habitual rather than optimal. *J. Neurosci.* 32, 7384–7391. doi: 10.1523/JNEUROSCI.5792-11.2012

Dingwell, J. B., Mah, C. D., and Mussa-Ivaldi, F. A. (2002). Manipulating objects with internal degrees of freedom: evidence for model-based control. *J. Neurophysiol.* 88, 222–235.

Duff, S. V., and Sainburg, R. L. (2007). Lateralization of motor adaptation reveals independence in control of trajectory and steady-state position. *Exp. Brain Res.* 179, 551–561. doi: 10.1007/s00221-006-0811-1

Elverman, K. H., Paitel, E. R., Figueroa, C. M., McKindles, R. J., and Nielson, K. A. (2021). Event-related potentials, inhibition, and risk for Alzheimer's disease among cognitively intact elders. *J. Alzheimers Dis.* 80, 1413–1428. doi: 10.3233/JAD-201559

Flanders, M., Cordo, P. J., and Anson, J. G. (1986). Interaction between visually and kinesthetically triggered voluntary responses. *J. Mot. Behav.* 18, 427–448.

Flash, T., and Hogan, N. (1985). The coordination of arm movements: an experimentally confirmed mathematical model. *J. Neurosci.* 5, 1688–1703. doi: 10.1523/JNEUROSCI.05-07-01688.1985

Forget, R., and Lamarre, Y. (1987). Rapid elbow flexion in the absence of proprioceptive and cutaneous feedback. *Hum. Neurobiol.* 6, 27–37.

Ghez, C., and Martin, J. (1982). The control of rapid limb movement in the cat. *Exp. Brain Res.* 45, 115–125.

Gribble, P. L., Mullin, L. I., Cothros, N., and Mattar, A. (2003). Role of cocontraction in arm movement accuracy. *J. Neurophysiol.* 89, 2396–2405. doi: 10.1152/jn.01020.2002

Hallett, M., Shahani, B. T., and Young, R. R. (1975). EMG analysis of stereotyped voluntary movements in man. *J. Neurol. Neurosurg. Amp. Psychiatry* 38:1154. doi: 10.1136/jnnp.38.12.1154

Hannaford, B., and Stark, L. (1985). Roles of the elements of the triphasic control signal. *Exp. Neurol.* 90, 619–634. doi: 10.1016/0014-4886(85)90160-8

Hogan, N. (1984). Adaptive control of mechanical impedance by coactivation of antagonist muscles. *IEEE Trans. Autom. Control* 29, 681–690. doi: 10.1109/tac.1984.1103644

Hogan, N. (1985). The mechanics of multi-joint posture and movement control. *Biol. Cybern.* 52, 315–331. doi: 10.1007/BF00355754

Huang, H. J., Kram, R., and Ahmed, A. A. (2012). Reduction of metabolic cost during motor learning of arm reaching dynamics. *J. Neurosci.* 32, 2182–2190. doi: 10.1523/jneurosci.4003-11.2012

Jayasinghe, S. A., Maenza, C., Good, D. C., and Sainburg, R. L. (2021). Deficits in performance on a mechanically coupled asymmetrical bilateral task in chronic stroke survivors with mild unilateral paresis. *Symmetry* 13:1366. doi: 10.3390/sym13081366

Jayasinghe, S. A. L., Good, D., Wagstaff, D. A., Winstein, C., and Sainburg, R. L. (2020). Motor deficits in the ipsilesional arm of severely paretic stroke survivors correlate with functional independence in left, but not right hemisphere damage. *Front. Hum. Neurosci.* 14:599220. doi: 10.3389/fnhum.2020.599220

Ketcham, C. J., Dounskaia, N. V., and Stelmach, G. E. (2004). Multijoint movement control: the importance of interactive torques. *Prog. Brain Res.* 143, 207–218. doi: 10.1016/S0079-6123(03)43021-5

Lackner, J. R., and Dizio, P. (1994). Rapid adaptation to Coriolis force perturbations of arm trajectory. *J. Neurophysiol.* 72, 299–313. doi: 10.1152/jn.1994.72.1.299

Lacquaniti, F., Bosco, G., Gravano, S., Indovina, I., La Scaleia, B., Maffei, V., et al. (2015). Gravity in the brain as a reference for space and time perception. *Multisens. Res.* 28, 397–426. doi: 10.1163/22134808-00002471

Lacquaniti, F., Carrozzo, M., and Borghese, N. (1993). Time-varying mechanical behavior of multijointed arm in man. *J. Neurophysiol.* 69, 1443–1464. doi: 10.1152/jn.1993.69.5.1443

Langenecker, S. A., Zubieta, J.-K., Young, E. A., Akil, H., and Nielson, K. A. (2007). A task to manipulate attentional load, set-shifting, and inhibitory control: convergent validity and test-retest reliability of the parametric Go/No-Go test. *J. Clin. Exp. Neuropsychol.* 29, 842–853. doi: 10.1080/13803390601147611

Lemon, R., and Kraskov, A. (2019). Starting and stopping movement by the primate brain. *Brain Neurosci. Adv.* 3:2398212819837149. doi: 10.1177/2398212819837149

Lestienne, F., Polit, A., and Bizzi, E. (1981). Functional organization of the motor process underlying the transition from movement to posture. *Brain Res.* 230, 121–131. doi: 10.1016/0006-8993(81)90396-6

Loeb, G. E. (2021). Learning to use muscles. *J. Hum. Kinet.* 76, 9–33. doi: 10.2478/hukin-2020-0084

Maenza, C., Wagstaff, D. A., Varghese, R., Winstein, C., Good, D. C., and Sainburg, R. L. (2021). Remedial training of the less-impaired arm in chronic stroke survivors with moderate to severe upper-extremity paresis improves functional independence: a pilot study. *Front. Hum. Neurosci.* 15:645714. doi: 10.3389/fnhum.2021.645714

Mah, C. D. (2001). Spatial and temporal modulation of joint stiffness during multijoint movement. *Exp. Brain Res.* 136, 492–506.

Mani, S., Mutha, P. K., Przybyla, A., Haaland, K. Y., Good, D. C., and Sainburg, R. L. (2013). Contralesional motor deficits after unilateral stroke reflect hemisphere-specific control mechanisms. *Brain* 136, 1288–1303. doi: 10.1093/brain/aws283

Mannarelli, D., Pauletti, C., Petritis, A., Delle Chiaie, R., Currà, A., Trompetto, C., et al. (2020). Effects of cerebellar tDCS on inhibitory control: evidence from a Go/NoGo task. *Cerebellum* 19, 788–798. doi: 10.1007/s12311-020-01165-z

Meinck, H.-M., Benecke, R., Meyer, W., Höhne, J., and Conrad, B. (1984). Human ballistic finger flexion: uncoupling of the three-burst pattern. *Exp. Brain Res.* 55, 127–133. doi: 10.1007/BF00240506

Mussa-Ivaldi, F. A., Hogan, N., and Bizzi, E. (1985). Neural, mechanical, and geometric factors subserving arm posture in humans. *J. Neurosci.* 5, 2732–2743. doi: 10.1523/JNEUROSCI.05-10-02732.1985

Mutha, P. K., Haaland, K. Y., and Sainburg, R. L. (2012). The effects of brain lateralization on motor control and adaptation. *J. Mot. Behav.* 44, 455–469. doi: 10.1080/00222895.2012.747482

Nielson, K. A., Langenecker, S. A., and Garavan, H. (2002). Differences in the functional neuroanatomy of inhibitory control across the adult life span. *Psychol. Aging* 17:56. doi: 10.1037//0882-7974.17.1.56

Nishii, J., and Taniai, Y. (2009). Evaluation of trajectory planning models for arm-reaching movements based on energy cost. *Neural Comput.* 21, 2634–2647.

Noorani, I., and Carpenter, R. (2017). Not moving: the fundamental but neglected motor function. *Philos. Trans. R. Soc. B Biol. Sci.* 372:20160190. doi: 10.1098/rstb.2016.0190

Oh, K., Rymer, W. Z., and Choi, J. (2021). The speed of adaptation is dependent on the load type during target reaching by intact human subjects. *Exp. Brain Res.* 239, 3091–3104. doi: 10.1007/s00221-021-06189-3

Osu, R., Franklin, D. W., Kato, H., Gomi, H., Domen, K., Yoshioka, T., et al. (2002). Short-and long-term changes in joint co-contraction associated with motor learning as revealed from surface EMG. *J. Neurophysiol.* 88, 991–1004. doi: 10.1152/jn.2002.88.2.991

Pruszynski, J. A., and Scott, S. H. (2012). Optimal feedback control and the long-latency stretch response. *Exp. Brain Res.* 218, 341–359.

Rosenbaum, D. A., Meulenbroek, R. J., Vaughan, J., and Jansen, C. (2001). Posture-based motion planning: applications to grasping. *Psychol. Rev.* 108:709. doi: 10.1037/0033-295x.108.4.709

Rubia, K., Russell, T., Overmeyer, S., Brammer, M. J., Bullmore, E. T., Sharma, T., et al. (2001). Mapping motor inhibition: conjunctive brain activations across different versions of go/no-go and stop tasks. *Neuroimage* 13, 250–261.

Sainburg, R. L. (2002). Evidence for a dynamic-dominance hypothesis of handedness. *Exp. Brain Res.* 142, 241–258. doi: 10.1007/s00221-001-0913-8

Sainburg, R. L. (2014). Convergent models of handedness and brain lateralization. *Front. Psychol.* 5:1092. doi: 10.3389/fpsyg.2014.01092

Sainburg, R. L. (2015). Should the Equilibrium Point Hypothesis (EPH) be considered a scientific theory? *Mot. Control* 19, 142–148.

Sainburg, R. L., and Duff, S. V. (2006). Does motor lateralization have implications for stroke rehabilitation? *J. Rehabil. Res. Dev.* 43, 311–322.

Sainburg, R. L., Ghilardi, M. F., Poizner, H., and Ghez, C. (1995). Control of limb dynamics in normal subjects and patients without proprioception. *J. Neurophysiol.* 73, 820–835. doi: 10.1152/jn.1995.73.2.820

Sainburg, R. L., and Kalakanis, D. (2000). Differences in control of limb dynamics during dominant and nondominant arm reaching. *J. Neurophysiol.* 83, 2661–2675. doi: 10.1152/jn.2000.83.5.2661

Schabowsky, C. N., Hidler, J. M., and Lum, P. S. (2007). Greater reliance on impedance control in the nondominant arm compared with the dominant arm when adapting to a novel dynamic environment. *Exp. Brain Res.* 182, 567–577.

Schaefer, S. Y., Haaland, K. Y., and Sainburg, R. L. (2009). Hemispheric specialization and functional impact of ipsilesional deficits in movement coordination and accuracy. *Neuropsychologia* 47, 2953–2966. doi: 10.1016/j.neuropsychologia.2009.06.025

Scheidt, R. A., and Ghez, C. (2007). Separate adaptive mechanisms for controlling trajectory and final position in reaching. *J. Neurophysiol.* 98, 3600–3613. doi: 10.1152/jn.00121.2007

Scheidt, R. A., Ghez, C., and Asnani, S. (2011). Patterns of hypermetria and terminal cocontraction during point-to-point movements demonstrate independent action of trajectory and postural controllers. *J. Neurophysiol.* 106, 2368–2382. doi: 10.1152/jn.00763.2010

Scheidt, R. A., Zimbelman, J. L., Salowitz, N. M., Suminski, A. J., Mosier, K. M., Houk, J., et al. (2012). Remembering forward: neural correlates of memory and prediction in human motor adaptation. *Neuroimage* 59, 582–600. doi: 10.1016/j.neuroimage.2011.07.072

Shadmehr, R., and Mussa-Ivaldi, F. A. (1994). Adaptive representation of dynamics during learning of a motor task. *J. Neurosci.* 14, 3208–3224. doi: 10.1523/JNEUROSCI.14-05-03208.1994

Suminski, A. J., Rao, S. M., Mosier, K. M., and Scheidt, R. A. (2007). Neural and electromyographic correlates of wrist posture control. *J. Neurophysiol.* 97, 1527–1545. doi: 10.1152/jn.01160.2006

Takahashi, C., Scheidt, R. A., and Reinkensmeyer, D. (2001). Impedance control and internal model formation when reaching in a randomly varying dynamical environment. *J. Neurophysiol.* 86, 1047–1051. doi: 10.1152/jn.2001.86.2.1047

Thoroughman, K. A., and Shadmehr, R. (1999). Electromyographic correlates of learning an internal model of reaching movements. *J. Neurosci.* 19, 8573–8588. doi: 10.1523/JNEUROSCI.19-19-08573.1999

Todorov, E. (2004). Optimality principles in sensorimotor control. *Nat. Neurosci.* 7, 907–915. doi: 10.1038/nn1309

Todorov, E., and Jordan, M. I. (2002). Optimal feedback control as a theory of motor coordination. *Nat. Neurosci.* 5, 1226–1235. doi: 10.1038/nn963

Votruba, K. L., Rapport, L. J., Vangel, S. J. Jr., Hanks, R. A., Lequerica, A., Whitman, R. D., et al. (2008). Impulsivity and traumatic brain injury: the relations among behavioral observation, performance measures, and rating scales. *J. Head Trauma Rehabil.* 23, 65–73. doi: 10.1097/01.HTR.0000314525.93381.69

Wang, J., and Sainburg, R. L. (2007). The dominant and nondominant arms are specialized for stabilizing different features of task performance. *Exp. Brain Res.* 178, 565–570. doi: 10.1007/s00221-007-0936-x

Yadav, V., and Sainburg, R. L. (2011). Motor lateralization is characterized by a serial hybrid control scheme. *Neuroscience* 196, 153–167. doi: 10.1016/j.neuroscience.2011.08.039

Yadav, V., and Sainburg, R. L. (2014). Limb dominance results from asymmetries in predictive and impedance control mechanisms. *PLoS One* 9:e93892.

Conflict of Interest: The authors declare that the research was conducted in the absence of any commercial or financial relationships that could be construed as a potential conflict of interest.

frontiers
in Neural Circuits

ORIGINAL RESEARCH
published: 03 March 2022
doi: 10.3389/fncir.2022.839521

Toward Assessing the Functional Connectivity of Spinal Neurons

Martin Zaback[1,2], Ekta Tiwari[2,3], Alexander J. Krupka[2,4], Francesca Marchionne[2], Francesco Negro[5], Michel A. Lemay[2] and Christopher K. Thompson[1,6]*

[1] Department of Health and Rehabilitation Sciences, College of Public Health, Temple University, Philadelphia, PA, United States, [2] Department of Bioengineering, College of Engineering, Temple University, Philadelphia, PA, United States, [3] School of Engineering, Brown University, Providence, RI, United States, [4] Department of Biology, DeSales University, Center Valley, PA, United States, [5] Department of Clinical and Experimental Sciences, Universita degli Studi di Brescia, Brescia, Italy, [6] Shriner's Hospital for Children, Philadelphia, PA, United States

Spinal interneurons play a critical role in motor output. A given interneuron may receive convergent input from several different sensory modalities and descending centers and relay this information to just as many targets. Therefore, there is a critical need to quantify populations of spinal interneurons simultaneously. Here, we quantify the functional connectivity of spinal neurons through the concurrent recording of populations of lumbar interneurons and hindlimb motor units in the *in vivo* cat model during activation of either the ipsilateral sural nerve or contralateral tibial nerve. Two microelectrode arrays were placed into lamina VII, one at L3 and a second at L6/7, while an electrode array was placed on the surface of the exposed muscle. Stimulation of tibial and sural nerves elicited similar changes in the discharge rate of both interneurons and motor units. However, these same neurons showed highly significant differences in prevalence and magnitude of correlated activity underlying these two forms of afferent drive. Activation of the ipsilateral sural nerve resulted in highly correlated activity, particularly at the caudal array. In contrast, the contralateral tibial nerve resulted in less, but more widespread correlated activity at both arrays. These data suggest that the ipsilateral sural nerve has dense projections onto caudal lumbar spinal neurons, while contralateral tibial nerve has a sparse pattern of projections.

Keywords: interneuron, motoneuron, high density arrays, single units, spinal cord circuitry

Edited by:
Richard Nichols,
Georgia Institute of Technology,
United States

Reviewed by:
Tuan Vu Bui,
University of Ottawa, Canada
Aritra Kundu,
University of Texas at Austin,
United States

Correspondence:
Christopher K. Thompson
ckt@temple.edu

Received: 20 December 2021
Accepted: 28 January 2022
Published: 03 March 2022

Citation:
Zaback M, Tiwari E, Krupka AJ, Marchionne F, Negro F, Lemay MA and Thompson CK (2022) Toward Assessing the Functional Connectivity of Spinal Neurons.
Front. Neural Circuits 16:839521.
doi: 10.3389/fncir.2022.839521

INTRODUCTION

Long range monosynaptic projections to spinal motoneurons are relatively rare in the mammalian motor system. Descending projections primarily terminate onto spinal interneurons in order to activate the spinal motoneurons—the classic exception to this are the cortical projections to motor pools which control distal muscles in phylogenetically advanced species (Lemon and Griffiths, 2005). Additionally, large diameter Ia afferents, which are exquisitely sensitive to vibration, have monosynaptic projections to nearly the entire homonymous motor pool (Mendell and Henneman, 1968). However, these specific cortical and reflex pathways are the minority of synaptic contacts on the spinal motoneuron and represent the exception, rather than the rule. Therefore, most synaptic contacts on the spinal motoneuron come from spinal interneurons.

Since the initial work of Lundberg, spinal interneurons have been shown to have a striking convergence across sensory modalities (Hultborn et al., 1976; Jankowska et al., 1981; Kniffki et al., 1981). In addition to this sensory convergence, spinal interneurons also receive and integrate descending drive (Brownstone and Bui, 2010). Thus, interneurons represent a "common path" integrating information from a wide range of sources (Jankowska and Lundberg, 1981). Further, these interneurons are sensitive to neuromodulation from brainstem centers (Schmidt and Jordan, 2000; Husch et al., 2015). This fundamental convergence of inputs and divergence of projections has the potential for high levels of functional connectivity across spinal neurons.

Given the complexities of this system, single or even paired spinal neuron recordings are likely insufficient to fully describe the function of spinal circuits. Spinal microelectrode arrays have been used to record the discharge of populations of individual spinal interneurons in the motor system. This work has been done in several species during a relatively small range of behaviors. Most of these have focused on quantifying interneuronal activity during endogenous behaviors, such as locomotion in the cat (AuYong et al., 2011a,b; Dominguez-Rodriguez et al., 2020; Musienko et al., 2020; McMahon et al., 2021), scratching in the turtle (Radosevic et al., 2019), or under anesthesia in the rat (McPherson and Bandres, 2021). While such behaviors are critical to understand input-output properties within and between interneurons and motoneurons, these relationships are difficult to extract in an intrinsically oscillating circuit. An approach using specific afferent inputs and combining recordings of interneurons and motoneurons would provide a neuronal ensemble view of the relationship between sensory feedback, interneuronal systems, and motor output.

Here, we describe the discharge of spinal interneurons and hindlimb motor units in response to specific forms of afferent drive. Neural recordings from high-density microelectrode arrays in the spinal cord and high-density electrodes arrays on the muscle surface were collected from three cats and decomposed into the individual discharge times of spinal interneurons and motor units. Our initial goal was to describe the functional connectivity of spinal neurons by quantifying short-term correlations within and between lumbar spinal interneurons and hindlimb motor unit discharge patterns. To accomplish this, two forms of afferent drive known to activate spinal interneurons and motoneurons were used—electrical stimulation of either the ipsilateral sural nerve and/or contralateral tibial nerve. Trains of electrical stimulation across a range of frequencies were used to evoke bouts of tonic motor output. Time and frequency domain correlations were used to examine differences in functional connectivity between spinal neurons. The reflex pathways arising from tibial nerve stimulation are thought to diffusely project to multiple spinal segments on the contralateral cord and involve more synapses before reaching the soleus motor pool compared to the reflex pathways arising from sural nerve stimulation (LaBella et al., 1989; Bannatyne et al., 2006). Since the more direct pathway arising from the ipsilateral sural nerve is more likely to have dense projections onto the soleus motor pool, it was expected that sural nerve stimulation would generate greater correlated activation of both spinal interneurons and motor units.

MATERIALS AND METHODS

Three adult female domestic shorthair cats (Liberty Research Inc., Waverly, NY, United States, weight: 2.52–3.56 kg) were used for this study. These animals underwent a terminal experiment to evaluate lumbar interneuronal firing and motoneuronal activity during stimulation of either the right (ipsilateral) sural nerve or left (contralateral) tibial nerve.

Cats were initially injected with atropine (0.05 mg/kg IM) and anesthetized with isoflurane (1.5–3.5% in oxygen) supplied through an endotracheal tube. Heart rate, blood pressure, end-tidal CO_2, tidal volume, arterial oxyhemoglobin saturation, respiration rate and temperature were monitored and recorded every 15 min. Intravenous fluids enriched with sodium bicarbonate (3.4 g/L) and sucrose (25 g/L) were administered throughout the experiment. Dexamethasone (2 mg/kg, IV) was given prior to surgery in order to reduce spinal swelling during the spinal laminectomy. The laminectomy was performed and the spinal cord was exposed at the lumbar level between the L3 and L7 spinal segments. Bipolar nerve cuffs were implanted around the right sural nerve and left tibial nerve at the level of the calcaneal tendon (Ollivier-Lanvin et al., 2011). One bifilar electrode was implanted into the lateral or medial gastrocnemius (LG, MG) muscle and the muscle activity was used to synchronize acquisition between the interneuronal [Tucker-Davis Technologies Inc., (TDT), Alachua, FL, United States] and motor unit [OT Bioelettronica (OTB), Turin, Italy] recording systems using cross correlation of this common signal. Following laminectomy, animals were transferred to a stereotaxic frame where the spinal vertebrae were securely clamped to the frame. The pia was opened to facilitate electrode insertion. The right soleus was exposed and dissected free of the surrounding muscles to facilitate placement of the high-density surface EMG electrode array (Thompson et al., 2018). Decerebration was then performed in order to discontinue anesthesia, which has been shown to affect the activity of the spinal circuitry (Jinks et al., 2005).

Extracellular Neural Recordings and Processing

One hour after decerebration, *in vivo* recordings of spinal extracellular signals were conducted using two 64 channels microelectrode arrays (model A8x8-5mm-200-200-177, Neuronexus, Ann Arbor, MI, United States) inserted at the dorsal root entry zone to depths of 3,000 to 3,500 μm into two lumbar segments. The planar 8 shaft arrays were inserted sagittally (i.e., in the rostrocaudal direction), so that the recording sites covered a range of 1,450 μm rostrocaudally and 1,450 μm dorsoventrally for each array The rostral electrode array was placed at L3, while the caudal array was placed at either L6 or L7. Interneuronal activity was recorded using the RZ2/RS4 TDT system for recording of 128 channels of multiunit activity (MUA) (sampling rate 24 KHz) and 2 analog channels of EMGs activity (LG/MG) and nerve stimuli (sampling rate 12 KHz).

Muscle activity was evoked in the ankle extensors using electrical stimulation of the right (ipsilateral) sural or left (contralateral) tibial nerve. Stimuli were pulse trains (biphasic 100 μs pulses) delivered continuously at one of five possible frequencies (5, 10, 20, 50, and 100 Hz). During each trial, two blocks of stimulation at the same frequency were delivered for 10–20 s with 10 s of rest between. The amplitude of stimulation was adjusted to the minimum current sufficient to evoke robust activity of the ankle extensors (range: 0.2–3 mA for the tibial nerve, and 0.1–1.5 mA for the sural nerve).

Neuronal extracellular activity was processed with customized Matlab scripts (The Mathworks, Natick, MA, United States). Raw multiunit data from the RS4 was first band-pass filtered between 300 Hz and 4,000 Hz (sampling rate 24 KHz). Filtered data were then processed using the UltraMegaSort2000 Matlab toolkit (Hill et al., 2011). The units chosen had an average firing frequency greater than 1 Hz throughout the trial, a number of refractory period violations (RPVs) less than 5% for a refractory period of 1.5 ms, and a signal to noise ratio greater than 1.5 (Joshua et al., 2007). **Figure 1A** depicts a subset of extracellular neural recordings (13/128) from one trial along with all decomposed interneuron spike trains that met the inclusion criteria for subsequent analysis.

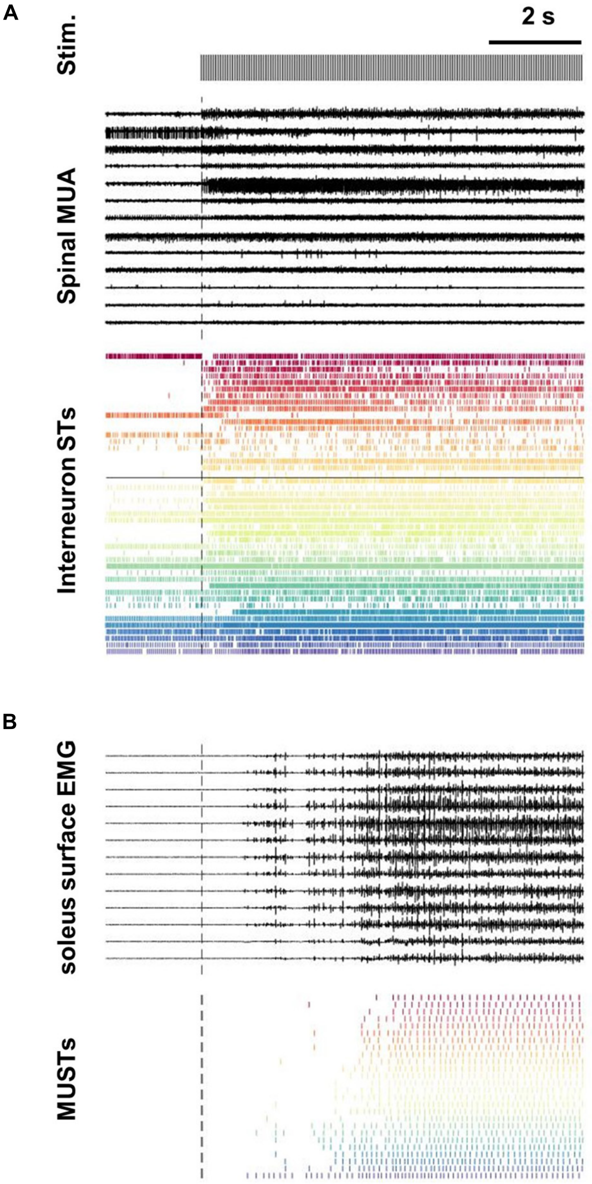

FIGURE 1 | Decomposition of spinal multi-unit and soleus surface electrode array recordings into interneuron and motor unit spike trains. **(A)** Subset of extracellular recordings (13/128 channels) from L3 and L6 spinal intermediate zones are shown along with the population of all interneurons spike trains (STs) decomposed from the array data ($n = 46$). The black horizontal line transecting the interneuron STs separates units decomposed from the L3 ($n = 27$) and L6 ($n = 19$) arrays. **(B)** Subset of surface EMG recordings (13/64 channels) along with the population of motor unit spike trains (MUSTs) decomposed from these array data ($n = 26$).

Electromyographic Recording and Processing

Electromyographic (EMG) activity of the soleus muscles were recorded using a 64 channel electrode array placed on the surface of the exposed muscle (Thompson et al., 2018). EMG data were filtered at 20–2,000 Hz, amplified at 150×, and digitized at 5.12 KHz using the Quattrocento system from OTB.

Decomposition of the EMG signal was performed using the well validated blind source separation approach (Holobar et al., 2009; Negro et al., 2016). Only spike trains with a silhouette measure >0.85 were used for further analyses (**Figure 1B**). Previous investigations have demonstrated the validity of this motor unit-decomposition approach during contractions evoked through cutaneous nerves in the cat, with a 96% rate of agreement with concurrent fine wire electrodes placed in the same muscle (Thompson et al., 2018).

Spike Train Analyses

Discharge rates of interneuron and motor unit spike trains were calculated during the first block of stimulation as well as during a 2-s period immediately prior to stimulation (**Figure 2A**). Coefficient variation (CoV) for each motor unit spike train was also calculated during the first block of stimulation after removal of interspike intervals (ISIs) greater than 400 ms.

Time- and frequency-domain correlations were performed to quantify the response of interneurons and motor units to the stimulus as well as the functional connectivity between interneurons and motor units. For time-domain analyses, the following peristimulus histograms (PSTH) were constructed: (1) interneuron spike times aligned to stimulus pulse times (Stim to IN); (2) motor units spike times aligned to stimulus pulse times (Stim to MU); (3) motor unit spike times aligned to interneuron spike times (IN to MU). For PSTH with motor unit spike times (i.e., Stim to MU and IN to MU), all motor unit spike times from a single trial were collapsed into a composite motor unit spike train (CST) (**Figure 3**). This was done to improve detection of response onsets. For each PSTH,

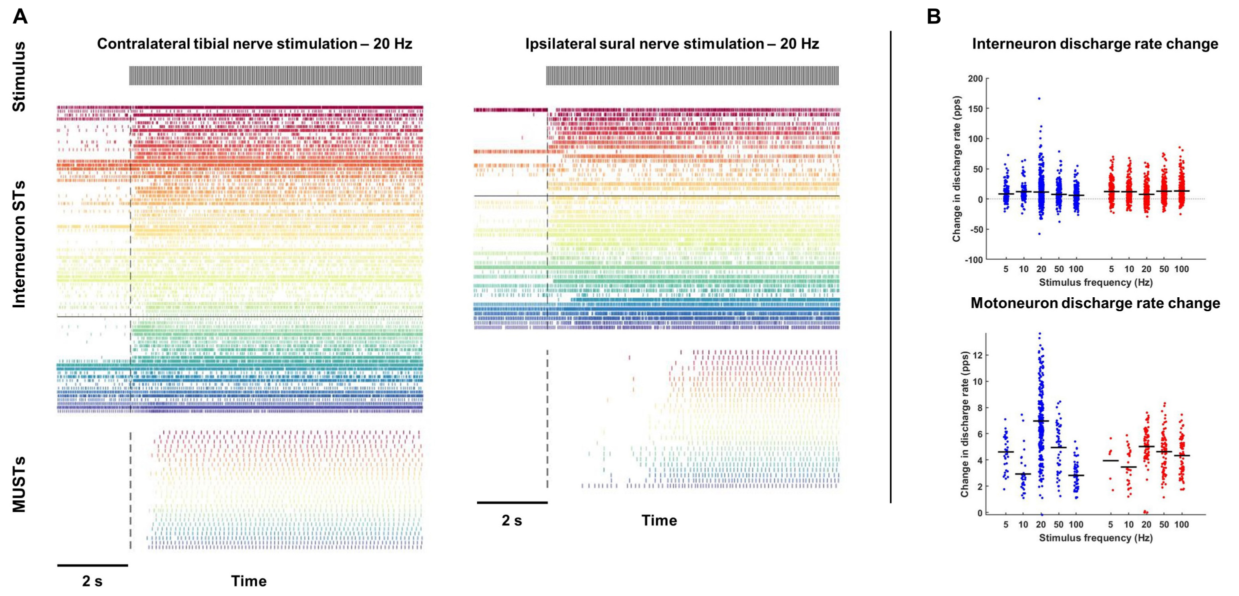

FIGURE 2 | Changes in interneuron and motoneuron spike times during tibial and sural nerve stimulation. **(A)** Population spike times of interneuron and motoneuron single units during exemplar trials of tibial (left) and sural (right) nerve stimulation at 20 Hz. **(B)** With both tibial and sural nerve stimulation, interneurons and motor units changed their discharge rate to a similar degree regardless of stimulation frequency. Motor units were almost exclusively quiescent during the pre-stimulation period and increased their discharge shortly after the onset of stimulation. Most interneurons had some baseline activity and displayed a more heterogeneous response to peripheral nerve stimulation.

the pre-stimulus period was 20 ms, the post-stimulus period was 80 ms, and the bin widths were 1 ms. To identify the onset and direction of the earliest response for each PSTH, a customized threshold crossing algorithm was used. From the pre-stimulus period, two separate thresholds were calculated: a LOW (±1 SD of mean baseline discharge) and HIGH threshold (±4 SD of mean baseline discharge). The algorithm then searched the post-stimulus period from 5 to 50 ms for any detectable response onset. A detectable response was identified when one of two criteria were met: (1) 6 of 8 consecutive bins exceeded the LOW threshold in the same direction or (2) 2 of 3 consecutive bins exceeded the HIGH threshold in the same direction. These two onset criteria were applied so the algorithm was able to identify small amplitude responses occurring over long durations and large amplitude responses occurring over short durations. The first bin where either of these criteria were met was identified as the response onset. Responses were identified as excitatory or inhibitory based on the direction of change in discharge relative to the pre-stimulus period. These time-domain analyses could only reliably be performed during trials with low frequency stimulation (see **Figure 4** and section "Time Domain Correlations Between Stimulus Pulse Train and Interneuron and Motor Unit Spike Trains" below).

The response of interneurons and motor units to the stimulus and connectivity between interneurons and motor units were examined using a coherence analysis based on the methods of Halliday et al. (1995). Coherence reflects linear dependence or correlation between two variables in the frequency domain. To calculate coherence, spike train data were separated into 401 ms disjoint segments (resulting in a frequency resolution of 2.49 Hz). Coherence $[C_{xy}(f)]$ was then calculated using equation:

$$\left|C_{xy}(f)\right| = \frac{|P_{xy}(f)|^2}{P_{xx}(f)\cdot P_{yy}(f)} \tag{1}$$

where $P_{xy}(f)$ is the averaged cross-power spectral density (PSD) function between the input and output spike trains, and $P_{xx}(f)$ and $P_{yy}(f)$ are the averaged auto-PSD functions of the same spike trains (Halliday et al., 1995).

To identify occurrence of significant coherence between pairs of spike trains, 99% confidence limits were calculated based on the number of segments used to derive the estimate of coherence. When coherence between a pair of spike trains exceeded the confidence limit at the stimulus frequency, they were considered significantly cohered (**Figures 5A–C**). For all significantly cohered spike trains, the magnitude of coherence was also calculated at the peak of coherence at the stimulus frequency after z-transformation:

$$Z = [\operatorname{atanh}\left(\sqrt{C_{xy}}(f)\right)/(\sqrt{0.5 \times L})] \tag{2}$$

Where C_{xy} is coherence at the frequency of stimulation (f) and L is the number of segments (**Figure 5E**).

This analysis of coherence was applied to the same combination of variables as the PSTH analyses, except individual motor unit spike trains instead of CSTs were analyzed. Thus, for each interneuron, the percentage of the motor unit population

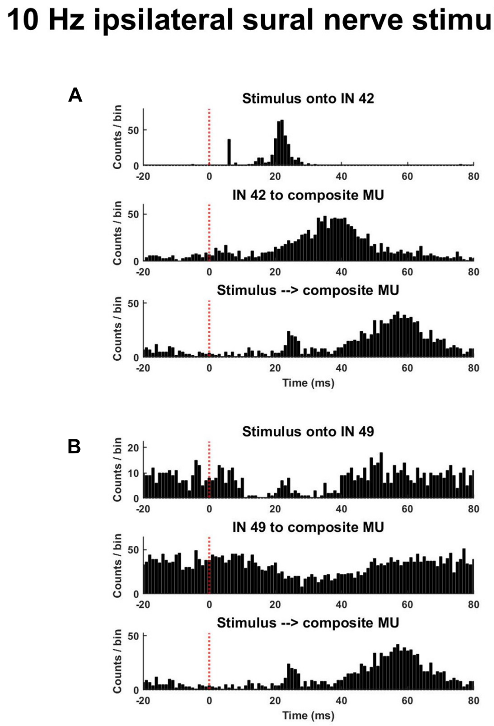

FIGURE 3 | Exemplar peristimulus time histograms during a trial of low frequency (10 Hz) ipsilateral sural nerve stimulation. **(A)** Shown is an interneuron that displayed an increased probability of discharge in response to the stimulus and whose discharge was associated with an increased probability of motor unit discharge [**(A)**, middle panel]. **(B)** Displayed is an interneuron that displayed a reduced probably of discharge and whose discharge was associated with a decreased probably of motor unit discharge [**(B)**, middle panel]. The same composite motor unit spike train in response to the stimulus is shown on the bottom panel of panels **(A,B)**.

it was cohered to could be calculated (**Figure 5D**). Similar coherence analyses were performed on pairs of interneurons.

Synchronization between pairs of interneurons was assessed using a PSTH analysis. For these PSTH, the discharge of one interneuron was aligned to the discharge of another interneuron. From a 15 ms pre-stimulus period, 95% confidence limits were constructed and changes in the discharge probability above or below this confidence limit occurring within 1 ms were identified as excitation and inhibition, respectively. This analysis was performed on all combinations of interneurons and the occurrence of excitatory and inhibitory synchrony for each pair of interneurons was calculated.

Statistical Analyses

All statistical models presented were implemented using SPSS v28 (IBM, Chicago IL, United States). To examine differences in interneuron and motor unit discharge rate as well as motor unit CoV between resting and stimulated states, full factorial linear mixed models of the changes in these variables pre- and post-stimulation onsets with nerve (Tibial vs. Sural) and frequency (5, 10, 20, 50, and 100 Hz) as factors were used (with animal as random factor). Main effects were compared using Bonferroni corrected *post hoc* comparisons between the means, and significant nerve × frequency interactions were followed-up by examining the overlap between the confidence limits of the estimated marginal means at each combination of nerve and frequency.

Linear mixed models were also used to examine how the different afferent drives (ipsilateral sural vs. contralateral tibial) influence the occurrence and magnitude of coherence between the stimulus and motor unit spike trains. Full-factorial linear mixed models with the percentage of significant coherence per trial or the magnitude of coherence for each motor unit significantly cohered with the stimulus as dependent variables, and nerve and frequency as factors (along with animal as a random factor) were conducted. Main effects were compared using Bonferroni corrected *post hoc* comparisons between the means for the factors and significant nerve × frequency interactions were evaluated based on the overlap between the confidence limits of the estimated marginal means at each combination of nerve and frequency.

Linear mixed models were also used to examine how the same afferent drives influence the occurrence and magnitude of coherence between the stimulus and interneurons, and interneurons and motor units. Linear mixed models with the percentage of significant coherence per trial (for Stim to IN) and interneuron (for IN to MU) and magnitude of coherence as dependent variables, and nerve, MUA location, and frequency as factors (along with their 2-way interactions, and animal a as random factor) were conducted to examine the effects of afferent drive on the occurrence and magnitude of these coherences. Main effects were compared using Bonferroni corrected *post hoc* comparisons between the means for the factors, and significant nerve × MUA location interactions were followed-up with an analysis of the effects of nerve and frequency at each MUA location by using a full factorial linear mixed model with nerve and frequency as factors (with animal as random factor) for the variable of interest at each MUA location.

Linear mixed models constructed using the same factors were used to examine how afferent drives influenced the percentage of interneurons time-locked or cohered to each other at each recording location and frequency of stimulation.

To examine the effect of interneuron depth on the occurrence of coherence between interneuron and motor unit spike trains, interneurons were divided into superficial or deep groups using median split based on the depth at which they were recorded. To improve power of these analyses, data were collapsed across stimulus frequency and linear mixed models were conducted separately for each MUA location with fixed effects of nerve and depth and animal as the random effect. For all model interaction and main effects, alpha was set at 0.05.

RESULTS

Changes in Interneuron and Motor Unit Firing With Peripheral Nerve Stimulation

Contralateral tibial nerve stimulation responses were measured over 9 trials in animal 1, 10 trials in animal 2, and 7 trials in animal 3, for a total of 26 trials. Ipsilateral sural nerve stimulation

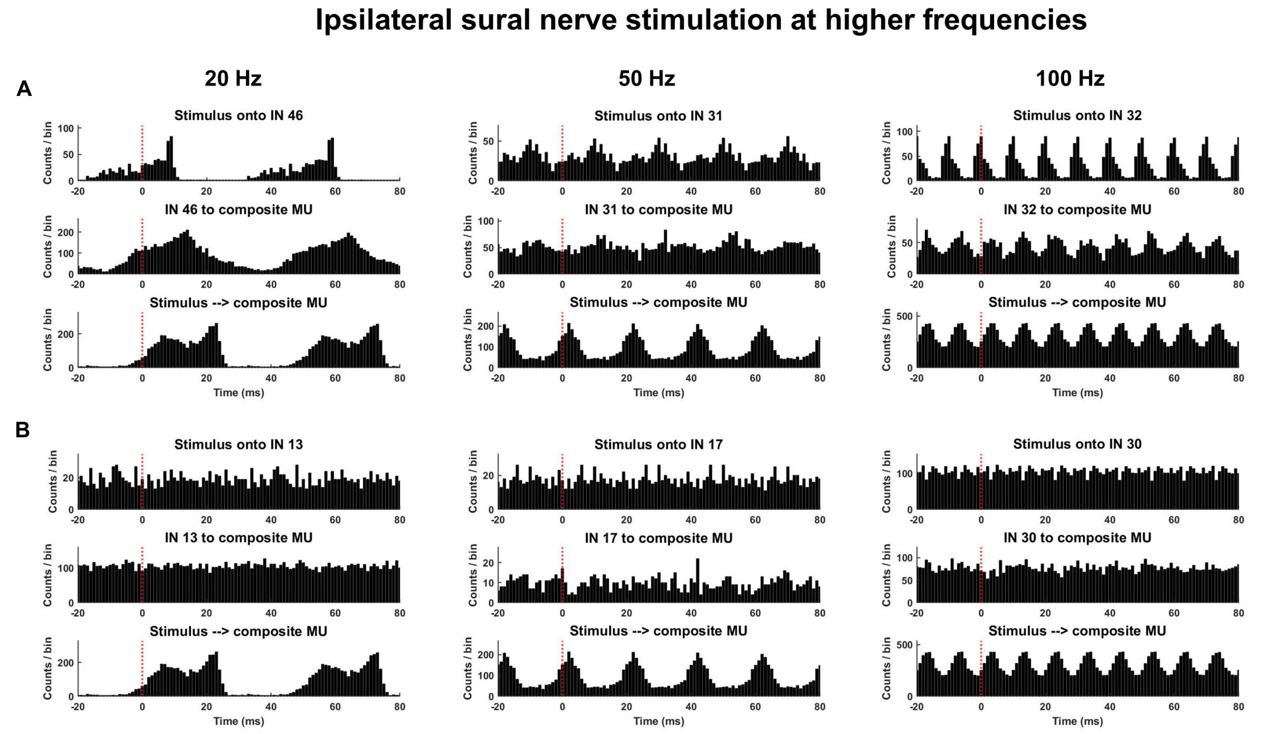

FIGURE 4 | Exemplar peristimulus time histograms during trials of higher frequency (≥20 Hz) ipsilateral sural nerve stimulation. **(A)** Clear responses entrained to the stimulus frequency can be observed; however, due to the long latency of the response and short inter-stimulus interval, the type (excitatory or inhibitory) and onset of response cannot be reliably determined from analysis of the PSTH. **(B)** Illustrates interneurons from the same trial that were not entrained to the stimulus frequency along with composite motor unit spike trains (CST) in response to the stimulus [bottom plots of panels **(A,B)** are repeated].

responses were measured over 19 trials in animal 1 and 2 trials in animal 2, for a total of 21 trials. From these trials, a total of 2,629 interneuron spike trains were decomposed from the L3 and L6/L7 multi-unit array recordings. Of these interneurons, 81.2% displayed some activity prior to peripheral nerve stimulation, while 67.8% changed their firing in response to stimulation (56.6% increased; 11.2% decreased). This change in firing was observed during both contralateral tibial and ipsilateral sural nerve stimulation (**Figure 2A**). On average, interneuron firing rate increased during stimulation by 7.1 and 7.9 pps during sural and tibial nerve stimulation, respectively (**Figure 2B**). There were no significant main effects of nerve ($F_{1,2448} = 0.769$, $p = 0.381$) or stimulation frequency ($F_{4,2608} = 1.759$, $p = 0.134$). There was a significant nerve × frequency interaction ($F_{4,2617} = 9.023$, $p < 0.001$) which appeared to be driven by interneuron firing rate increasing to a greater extent at 20 Hz during tibial compared to sural nerve stimulation. However, *post hoc* examination of the overlap of estimated marginal means 95% confidence limits revealed this effect was not significant.

A total of 678 motor unit spike trains were decomposed from the soleus EMG array data. Motor units were generally quiescent prior to peripheral nerve stimulation (**Figure 2A**). Only three units displayed some activity during the pre-stimulation baseline period, and all but one unit increased its firing rate during the first block of stimulation. On average, motor units increased their firing rate by 4.8 and 4.7 pps in response to sural and tibial nerve stimulation, respectively (**Figure 2B**). While there was no significant main effect of nerve ($F_{1,668} = 0.160$, $p = 0.689$), a frequency main effect was observed ($F_{4,667} = 35.072$, $p < 0.001$), with 20 and 50 Hz stimulation increasing motor unit firing rate to a greater extent than the other frequencies. There was a significant nerve × frequency interaction ($F_{4,667} = 13.54$, $p < 0.001$); however, *post hoc* examination of the overlap of estimated marginal means confidence limits revealed no significant effects.

Significant main effects of nerve ($F_{1,631} = 73.010$, $p < 0.001$) and frequency ($F_{1,654} = 30.761$, $p < 0.001$) were observed for motor unit CoV. Motor unit CoV was significantly lower during tibial nerve stimulation and was lowest during 20 Hz stimulation during both types of nerve stimulation. A significant nerve × frequency interaction was also observed ($F_{4,654} = 11.087$, $p < 0.001$). *Post hoc* analysis of estimated marginal means 95% confidence limits revealed this was due to significantly higher CoVs during sural compared to tibial nerve stimulation primarily at lower frequency stimulations (significantly different at 5 Hz).

Time Domain Correlations Between Stimulus Pulse Train and Interneuron and Motor Unit Spike Trains

Analysis of PSTHs revealed that interneurons displayed a heterogenous pattern of responsiveness to the stimulus pulse train. During low frequency stimulation (≤10 Hz), 36% of interneurons demonstrated an excitatory response to tibial

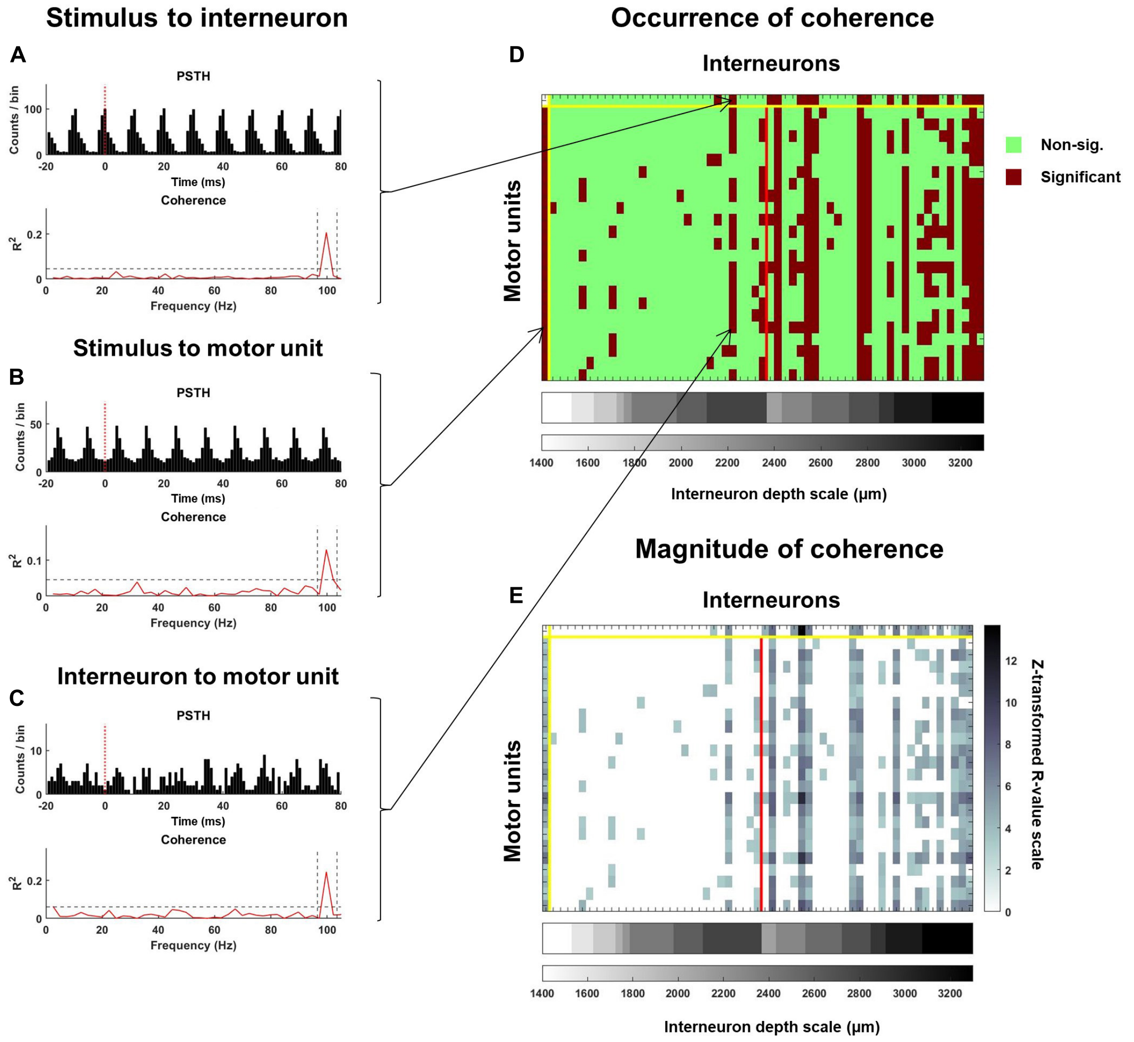

FIGURE 5 | Coherence analysis used to examine the response of interneurons and motoneurons to the stimulus pulse train as well as the functional connectivity between interneurons and motoneurons. Exemplar PSTH and coherence spectra for **(A)** an interneuron spike train relative to the stimulus, **(B)** a motor unit spike train relative to the stimulus, and **(C)** a motor unit spike train relative to an interneuron spike train. On each plot of the coherence spectra, a dashed horizontal line represents a 99% confidence limit. Coherence values exceeding this confidence limit at the stimulation frequency (identified with vertical dashed lines), were considered significant. The occurrence of significant coherence is mapped onto the matrix illustrated in panel **(D)**. The top row indicates interneurons that were and were not significantly cohered to the stimulus pulse times, while this same information for each motor unit is provided along the first column. All subsequent columns starting after the second row indicate instances where an interneuron was significantly cohered with a motor unit. The red vertical line separates interneurons that were recorded at the rostral (left) and caudal (right) spinal segments. Interneurons are further stratified according to depth, with deeper interneurons at each recording site being plotted further to the right. For all significant relations, the peak of coherence (after z-transformation) at the stimulation frequency was calculated. The magnitude of coherence between the stimulus and each interneuron and motor unit, and between each interneuron and motor unit for this exemplar trial is mapped onto the matrix in panel **(E)**.

(105/288) and sural (157/434) nerve stimulation. Inhibitory responses were observed in 23% (99/434) of interneurons during sural nerve stimulation and 15% (43/288) during tibial nerve stimulation. While multi-phasic responses could be observed (**Figure 3A**, top panel), the average onset of the earliest detectable responses were 13.7 ± 9.0 ms to sural stimulation and 14.5 ± 9.0 ms to tibial nerve stimulation.

Longer latency responses were typically observed in motor units (**Figure 3**, bottom panel). During low frequency stimulation (≤10 Hz), the earliest detectable change in discharge probability of the CSTs were 30.2 ± 12.5 ms and 30.4 ± 12.3 ms during sural and tibial nerve stimulation, respectively. The type of response was not consistent between these modes of stimulation; 100% of CSTs during sural nerve stimulation displayed an excitatory response (6/6), while CSTs during tibial nerve stimulation could display an early inhibitory (3/6) or excitatory (2/6) response.

During low frequency sural nerve stimulation (≤10 Hz), 25.2% (81/322) of CSTs increased their discharge in response to a given interneuron spike train, while 17.3% (56/322) displayed an inhibitory response. This is in contrast to tibial nerve stimulation,

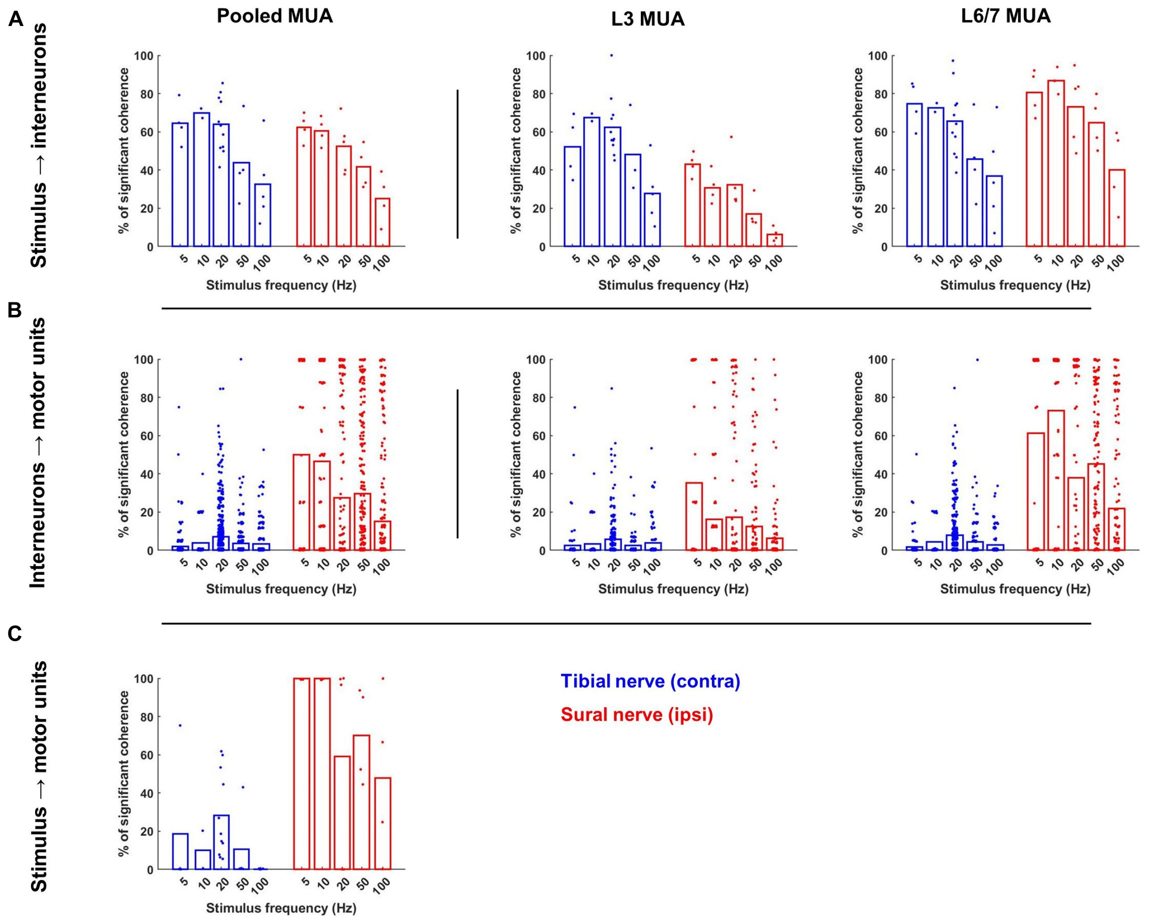

FIGURE 6 | Occurrence of significant coherence during contralateral tibial and ipsilateral sural nerve stimulation across frequencies. **(A)** Percentage of interneurons during each trial that were significantly cohered to the stimulus pulse train. The leftmost plot displays these percentage values for the entire interneuron population recorded during each trial, while the middle and right plots display the percentage of interneurons from each recording site that were cohered to the stimulus. **(B)** Percentage of the motor unit population that were significantly cohered to each interneuron during each trial across the entire population of interneurons (left) and population of interneurons at each recording site (right). **(C)** Percentage of motor pool that was significantly cohered to the stimulus pulse train. Bars represent the average percentage of significant coherence; individual data points have been jittered with uniformly distributed noise to minimize overlap.

during which only 2.1 % (6/288) of CST demonstrated a detectable excitatory response to interneuron discharge, while 2.4% (7/288) displayed an inhibitory response. When responses were observed, their onsets were at similar latencies for sural (23.6 ± 11.6 ms) and tibial (22.1 ± 13.3 ms).

Examination of the timing and type of response of interneurons and motor units to the stimulus pulse train as well as the response of motor units to interneuron spikes were only attempted at lower stimulus frequencies (≤10 Hz). This was because clear phase locking of both interneurons and motor units to the stimulus frequency was observed at higher frequencies (**Figure 4**). Since response latencies were typically greater than 10 ms, and changes to the probability of discharge could last upward of 40 ms (**Figure 3**), longer latency responses could fold over into the subsequent stimuli response at higher frequencies (≥20 Hz). This posed challenges for calculating true pre-stimulus firing rates and response latencies using the PSTH approach (**Figure 4**). The coherence analyses (**Figure 5**) presented below enabled us to examine relations between stimuli and motor units and interneurons and between interneurons and motor units across all frequencies used in this study.

Interneuron Coherence With Stimulus Pulse Train

During both sural and tibial nerve stimulation, a similar percentage of the interneurons were significantly cohered to the stimulus pulse train ($F_{1,76} = 0.310$, $p = 0.579$; **Figure 6A**). Significant main effects of frequency ($F_{4,75} = 25.166$, $p < 0.001$) and MUA location ($F_{1,75} = 90.150$, $p < 0.001$) indicated that the percentage of interneurons significantly cohered to the stimulus pulse train decreased as a function of increasing stimulus frequency and were greater at the L6/L7 recording site. A significant nerve × MUA location interaction ($F_{1,75} = 39.966$, $p < 0.001$) was also observed. Follow-up comparisons of the effect of nerve at each MUA location showed that a significantly greater percentage of interneurons recorded at the L3 site were cohered to the stimulus pulse train during tibial compared to sural nerve

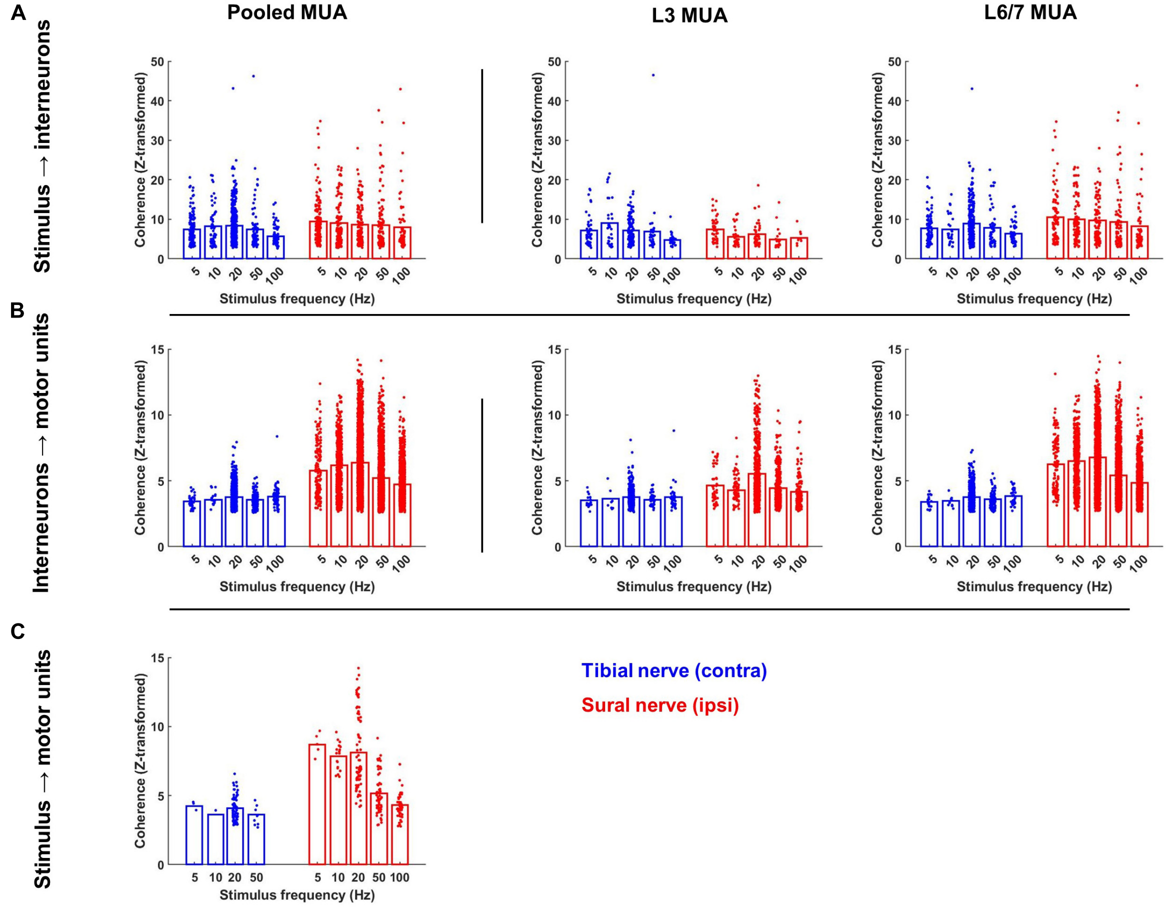

FIGURE 7 | Magnitude of significant coherence during contralateral tibial and ipsilateral sural nerve stimulation across frequencies. **(A)** Peak of coherence between the stimulus pulse train and each interneuron; **(B)** each interneuron and motor unit; and **(C)** the stimulus pulse train and each motor unit at the stimulation frequency. Bars represent the mean coherence value after z-transformation; individual data points have been jittered with uniformly distributed noise to minimize overlap.

stimulation ($F_{1,35} = 35.135$, $p < 0.001$; **Figure 6A** middle panel), while the opposite effect was observed for interneurons recorded at the L6/7 site ($F_{1,36} = 13.039$, $p < 0.001$; **Figure 6A** right panel).

A similar pattern of results was observed when the magnitude of coherence between the stimulus and each interneuron was analyzed (**Figure 7A**). On average, the magnitude of coherence did not significantly differ between sural and tibial nerve stimulation ($F_{1,437} = 0.004$, $p = 0.952$). However, a significant nerve × MUA location interaction was observed ($F_{1,1324} = 19.919$, $p < 0.001$). Follow-up comparisons of the effect of nerve at each MUA location showed that the magnitude of coherence recorded at the L3 site was significantly greater during tibial compared to sural nerve stimulation ($F_{1,179} = 8.940$, $p = 0.003$; **Figure 7A** middle panel), while the opposite effect was observed for interneurons recorded at the L6/7 site ($F_{1,156} = 11.224$, $p = 0.001$; **Figure 7A** right panel). At both MUA locations, there were significant main effects of frequency (L3: $F_{4,393} = 2.618$, $p = 0.035$; L6/7: $F_{4,800} = 3.316$, $p = 0.010$) due to coherence generally being weakest at 100 Hz.

Motor Unit Coherence With Interneuron Spike Trains

When compared to tibial nerve stimulation, a significantly greater proportion of the motor unit population was cohered to the discharge of individual interneurons during sural nerve stimulation ($F_{1,2355} = 311.520$, $p < 0.001$; **Figure 6B** left panel). Significant main effects of frequency ($F_{1,2409} = 32.131$, $p < 0.001$) and MUA location ($F_{1,2411} = 221.422$, $p < 0.001$) were also observed which resulted from a greater incidence of IN-MN coherence at lower frequencies and at the L6/7 recording site, respectively. A significant nerve × MUA location interaction was also observed ($F_{1,2411} = 154.839$, $p < 0.001$). Follow-up analyses of the effect of nerve and frequency for each MUA recording site revealed that there was a greater incidence of coherence at both spinal segments during sural nerve stimulation, although this effect was greater at the L6/7 recording site ($F_{1,1359} = 605.526$, $p < 0.001$) than the L3 recording site ($F_{1,1049} = 86.006$, $p < 0.001$; **Figure 6B**, middle and right panels). Significant nerve × frequency interactions were also observed at L3 ($F_{1,1049} = 9.758$, $p < 0.001$) and L6/7 ($F_{1,1359} = 23.946$,

$p < 0.001$) recording sites. In both cases, *post hoc* analysis of estimated marginal means confidence limits revealed this was due to the incidence of coherence decreasing as a function of stimulation frequency during only sural nerve stimulation.

A similar pattern of results was observed when the magnitude of coherence was analyzed. In particular, a main effect of nerve demonstrated that the magnitude of IN-MN coherence was significantly greater during sural compared to tibial nerve stimulation ($F_{1,1442} = 171.292$, $p < 0.001$). A main effect of MUA location was also observed due to the magnitude of coherence being significantly greater at the L6/7 recording site ($F_{1,6122} = 71.361$, $p < 0.001$). A significant nerve × MUA location interaction was also observed ($F_{1,5508} = 89.933$, $p < 0.001$). Follow-up analyses of the effects of nerve and frequency at each MUA location revealed that the magnitude of coherence was significantly greater during sural compared to tibial nerve stimulation at both MUA locations, although this effect was greater at L6/7 ($F_{1,4731} = 193.440$, $p < 0.001$) than L3 ($F_{1,855} = 29.277$, $p < 0.001$). Significant nerve × frequency interactions were also observed at L3 ($F_{1,1358} = 6.458$, $p < 0.001$) and L6/7 ($F_{1,4731} = 15.781$, $p < 0.001$) recording sites. *Post hoc* analysis of estimated marginal means confidence limits revealed that these interactions were due to the magnitude of coherence only changing as a function of stimulation frequency during sural nerve stimulation (**Figure 7B** middle and right panels).

Motor Unit Coherence With Stimulus Pulse Train

The proportion of the motor unit population significantly cohered to the stimulus pulse train was significantly greater during sural compared to tibial nerve stimulation ($F_{1,33} = 23.894$, $p < 0.001$; **Figure 6C**). A significant main effect of stimulation frequency was also observed ($F_{4,32} = 3.392$, $p = 0.020$), with most follow-up pairwise comparisons indicating that there was a significant reduction in the incidence of coherence during the highest frequency stimulation (100 Hz) independent of the nerve stimulated.

Similar effects were observed when analyzing the magnitude of coherence between the stimulus and motor unit spike trains. The magnitude of coherence was significantly greater during sural compared to tibial nerve stimulation ($F_{1,283} = 43.054$, $p < 0.001$). A significant main effect of frequency was also observed ($F_{1,283} = 30.118$, $p < 0.001$); follow-up pairwise comparisons revealed this was due to the magnitude of coherence being significantly lower at frequencies $\geq$50 Hz. *Post hoc* analysis of a significant nerve × frequency interaction ($F_{1,283} = 5.223$, $p = 0.002$) indicated that the main effect of frequency was driven primarily by the magnitude of coherence decreasing at higher frequencies during only sural nerve stimulation (**Figure 7C**).

Effect of Depth on Incidence of Coherence Between Interneurons and Motor Units

When a median split was used to classify interneurons as superficial ($\leq$2,400 μm) or deep (>2,400 μm), a significant main effect of depth was observed at the L3 recording site, indicating there was a greater incidence of coherence between motor units and L3 interneurons recorded from more ventral regions of the spinal cord ($F_{1,952} = 56.463$, $p < 0.001$; **Figure 8**). However, a significant nerve × depth interaction was also observed ($F_{1,1051} = 25.522$, $p < 0.001$). While the incidence of significant coherence tended to increase as a function of depth for both nerves, *post hoc* examination of the confidence limits for estimated marginal means revealed that the effect of depth was only significant during sural nerve stimulation.

In contrast to what was observed at the L3 recording site, when a similar median split was applied to interneurons recorded at L6/7 (superficial $\leq$ 2,500 μm; deep > 2,500 μm), no significant main effect of depth was observed for the occurrence of motor unit coherence with interneurons ($F_{1,1300} < 0.001$, $p = 0.985$). A significant nerve × depth interaction was observed ($F_{1,1338} = 8.866$, $p = 0.003$). However, *post hoc* analysis of the overlap of estimated marginal means confidence limits did not reveal any significant effects.

Coherence Between Interneurons

All the terms in the model had a significant effect on the percentage of interneurons significantly cohered with each other, with the overall mean for sural stimulation being higher than for tibial stimulation ($F_{1,2585} = 55.972$, $p < 0.001$) and coherence being twice as high for L6/7 interneurons [mean 37.8 ± 7.4% for L6/7 vs. 15.2 ± 7.4% for L3 ($F_{1,2585} = 650.459$, $p < 0.001$); **Figure 9B**]. A significant nerve × frequency interaction was observed for the percentage of interneurons significantly cohered with each other ($F_{4,2586} = 3.976$, $p = 0.003$). However, *post hoc* analysis of the overlap of the estimated marginal means confidence limits revealed no significant effects. A significant nerve × MUA location interaction was also observed ($F_{1,2585} = 187.774$, $p < 0.001$). Follow-up analyses of the effect of nerve at the L3 recording site demonstrated that a significantly greater percentage of interneurons were cohered to each other during tibial, compared to sural nerve stimulation ($F_{1,1071} = 68.022$, $p < 0.001$). By contrast, at the L6/7 recording site, the opposite effect was observed, as a significantly greater percentage of interneurons were cohered to each other during sural nerve stimulation ($F_{1,1442} = 180.581$, $p < 0.001$). At both MUA locations, significant main effects of frequency were also observed (L3: $F_{4,1138} = 41.476$, $p < 0.001$; L6/7: $F_{4,1441} = 36.141$, $p < 0.001$). Examination of pairwise comparisons revealed that in both cases, the percentage of interneurons significantly cohered to each other was significantly lower at higher frequencies ($\geq$50 Hz). Significant nerve × frequency interactions were also observed at the L3 ($F_{4,1140} = 12.739$, $p < 0.001$) and L6/7 ($F_{4,1441} = 3.424$, $p = 0.009$) recording sites. At the rostral recording site, *post hoc* analysis of the overlap of estimated marginal means confidence limits revealed that significantly more interneurons were cohered to each other during tibial compared to sural stimulation only at 10 Hz. *Post hoc* analyses at the L6/7 recording site did not reveal any significant effects.

Zero Lag Synchronization Between Interneurons

Analysis of interneuron synchronization during 5 and 10 Hz stimulation revealed a significantly greater percentage of

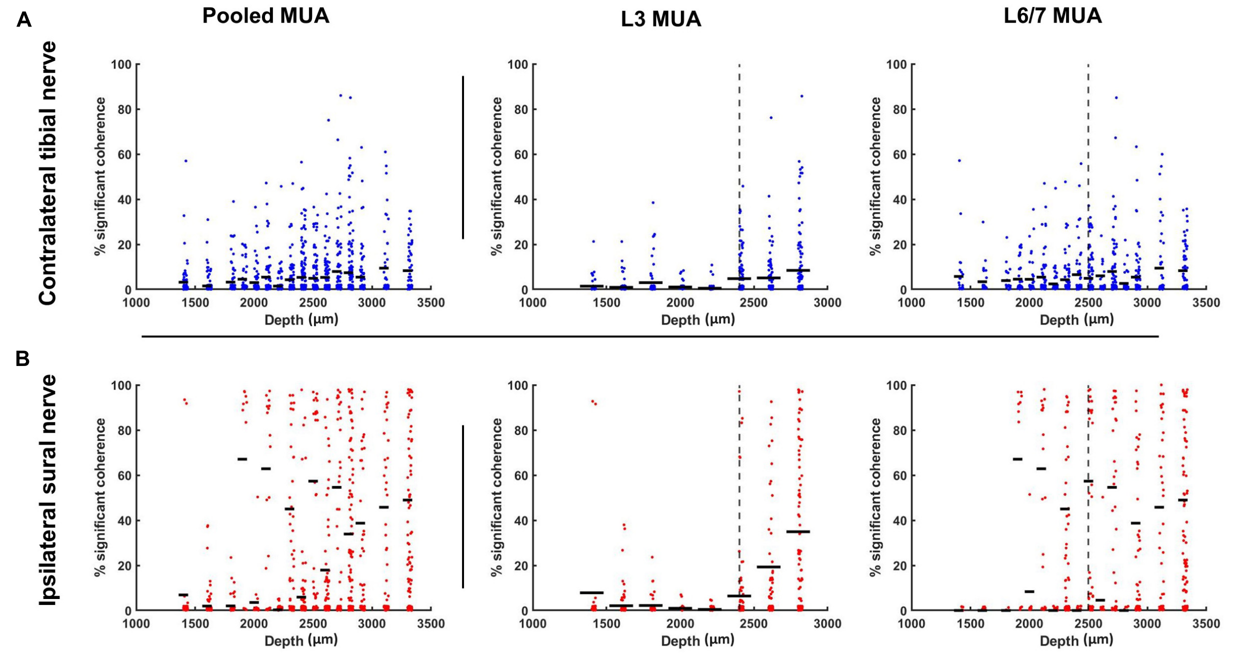

FIGURE 8 | Percentage of motor pool significantly cohered to discharge of individual interneurons (represented as single points) stratified as a function of interneuron depth for contralateral tibial [blue; **(A)**] and ipsilateral sural [red; **(B)**] nerve stimulation collapsed across frequencies. Horizontal dashes represent the mean percentage of motor unit cohered to individual interneurons within each depth bin. The vertical dashed line represents the median depth of the population of interneurons recorded at each spinal recording site. These median values were used to classify interneurons as superficial (≤median) or deep (>median) when examining the effect of interneuron depth on interneuron-motoneuron connectivity.

excitatory synchronization during sural compared to tibial nerve stimulation (sural: 7.15 ± 4.5%; tibial: 4.60 ± 4.9%; $F_{1,542} = 21.407$, $p < 0.001$; **Figure 10**). A significant nerve × MUA location interaction was also observed ($F_{1,722} = 46.698$, $p < 0.001$). Follow-up analyses revealed that the percentage of interneurons demonstrating synchronous excitation was significantly greater during sural compared to tibial nerve stimulation at the L6/7 recording site ($F_{1,95} = 31.716$, $p < 0.001$), but not at the L3 recording site ($F_{1,313} = 0.108$, $p = 0.743$).

Synchronous interneuron inhibition was observed less often than excitation, with 3.90 ± 1.7% and 4.15 ± 1.4% of interneurons displaying this behavior. No terms in the linear mixed model were significant, indicating that the occurrence of synchronous interneuron inhibition did not significantly differ between sural and tibial nerve stimulation ($F_{1,46} = 0.457$, $p < 0.502$), nor between the rostral and caudal recording sites ($F_{1,708} = 0.356$, $p < 0.551$).

DISCUSSION

Recordings from interneurons and motor units were made to quantify the functional connectivity of spinal neurons. Time and frequency domain correlations were performed within and across spinal interneurons and motor units in response to trains of stimulation of the ipsilateral sural or the contralateral tibial nerves. Despite interneuron and motor unit discharge patterns which, overall, were similar across modes of activation, the functional connectivity underlying this activation was different across nerves. In general, our observations are consistent with the hypothesis that the ipsilateral sural nerve has dense projections to the soleus motor pool, while the contralateral tibial nerve has sparse projections to the soleus motor pool.

Discharge Patterns of Spinal Interneurons and Motor Units

Both sural and tibial stimulation altered interneuron and motor unit discharge rates to similar extents. With both forms of stimulation, interneurons and motor units showed no difference in mean change in discharge rate, although the pattern of discharge was different between interneurons and motor units. A large majority of spinal interneurons were active at rest (McPherson and Bandres, 2021) and showed a heterogenous response to stimulation. Motor units were nearly exclusively quiescent at rest and therefore, necessarily, increased their discharge during stimulation, albeit at half the rate of spinal interneurons. This overall pattern was similar with both forms of afferent drive.

Likewise, the response frequency and latency of interneuronal responses were similar between nerves. Roughly one third of interneurons showed an initial excitatory response to the stimulation, while less than one third showed an initial inhibitory response. The initial response at the level of the motor unit was different between nerves. All the sural responses had an

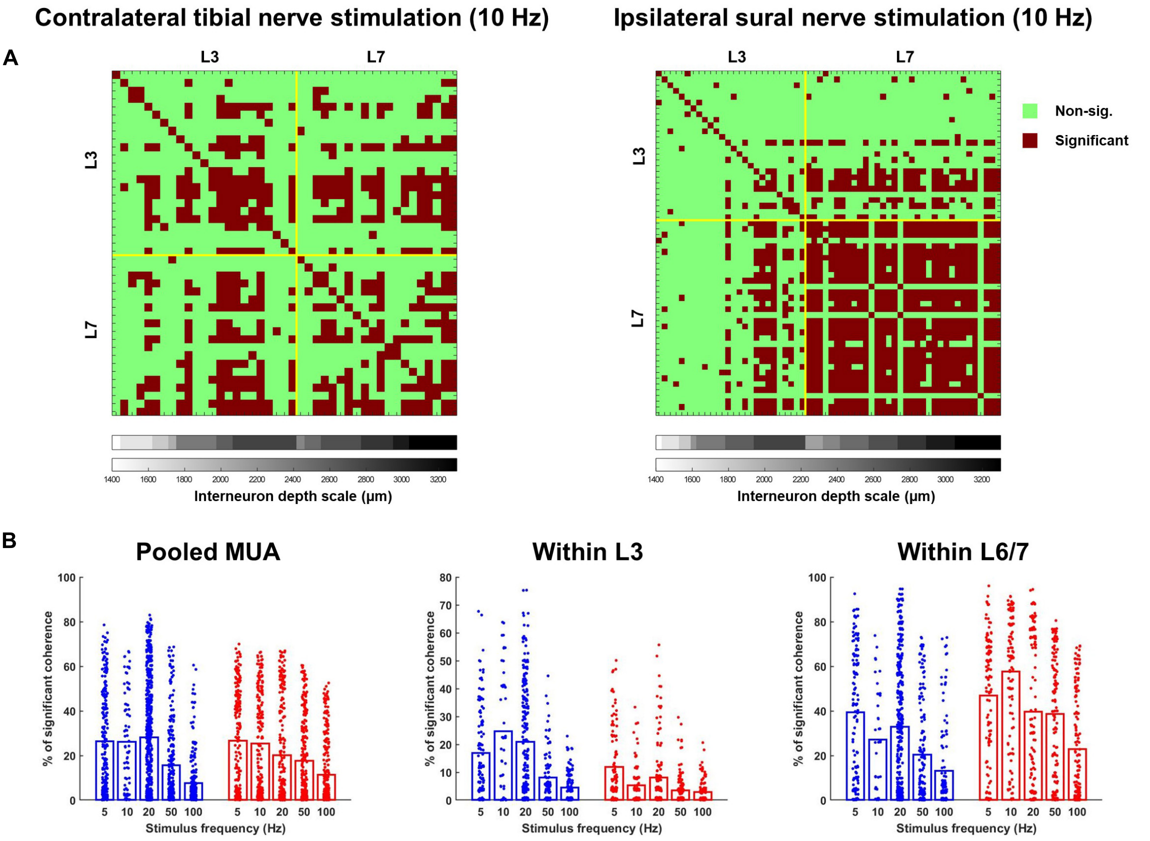

FIGURE 9 | (A) Matrices illustrating the incidence of significant coherence between interneurons during exemplar trials of 10 Hz tibial (left) and sural (right) nerve stimulation. Yellow lines separate units recorded at the rostral (L3) and caudal (L6/7) recording sites. Within each recording site, interneurons are stratified by depth, with deeper units plotted further to the right. **(B)** Percentage of interneuron population significantly cohered to discharge of individual interneurons across frequencies in response to contralateral tibial [blue; **(A)**] and ipsilateral sural [red; **(B)**] nerve stimulation. Bars represent means; data points are jittered with uniformly distributed noise to minimize overlap.

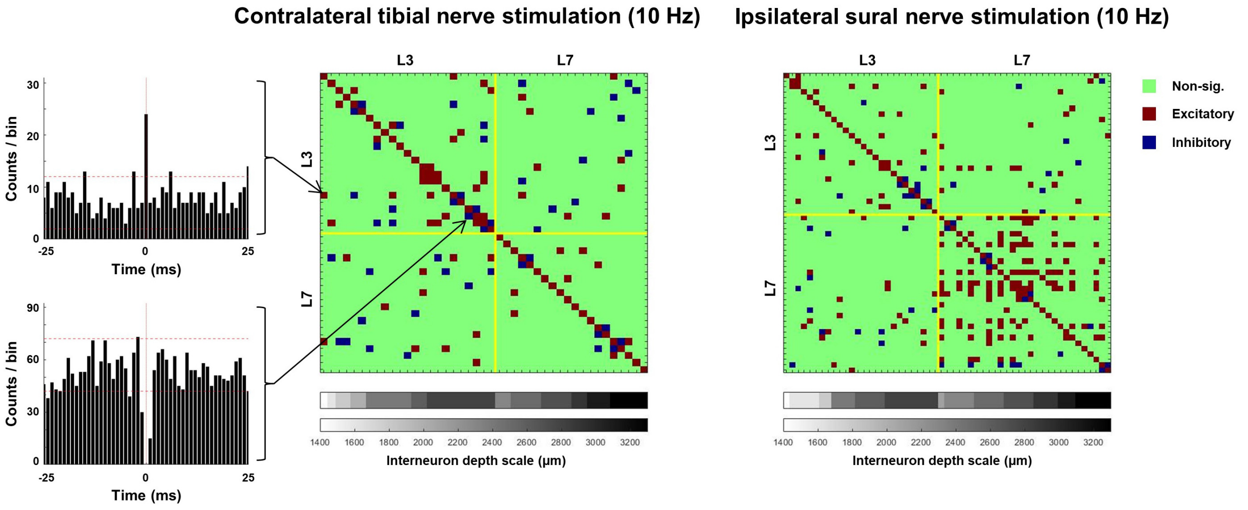

FIGURE 10 | Matrices illustrating the incidence of significant excitatory and inhibitory synchrony between interneurons during exemplar trials of tibial (left) and sural (right) nerve stimulation. PSTHs illustrate exemplar pairs of interneurons displaying excitatory (top) and inhibitory (bottom) synchrony. Dashed horizontal lines on PSTHs represent 95% confidence intervals calculated from a 15 ms pre-stimulus period.

initial excitatory response, while this was more equally split between initial excitatory and inhibitory responses during tibial stimulation. A mixed response is expected given the polysynaptic nature of these pathways (Harrison and Jankowska, 1985; LaBella et al., 1989; Cote and Gossard, 2004; Frigon and Rossignol, 2008). The exclusively excitatory motor unit response during sural nerve stimulation may potentially be explained by a fading of inhibition during trains of stimulation (Heckman et al., 1994).

The latencies of these initial responses were several tens of milliseconds and consistent with previous work on cutaneous reflexes in the cat (Cote and Gossard, 2004; Frigon and Rossignol, 2008). Given such a latency, the afferent pathway responsible for the initial response is likely Aβ fibers, though it is likely that smaller fibers contribute to the later responses. Because of these long latencies, at higher frequencies the response of one stimulation folded over into the response of the next stimulation. This made the analysis of baseline discharge, confidence limits, and response latencies unable to be calculated in a meaningful manner for frequencies greater than 10 Hz. As such, a frequency domain approach was used to better quantify the response across a range of frequencies, however, with these approaches it is difficult to ascertain latencies and if the response is excitatory or inhibitory.

Differences in Functional Connectivity Between Afferent Pathways

Despite these similarities in change in discharge rate and interneuron response type and latency, stark differences were observed in the correlated activity of spinal neurons during ipsilateral sural and contralateral tibial nerve stimulation. The occurrence and magnitude of coherence was significantly greater for sural stimulation as compared to tibial stimulation. Thus, ipsilateral sural stimulation induced greater entrainment of spinal network activity to the stimulation frequency compared to contralateral tibial stimulation. Further, the occurrence of short latency excitatory synchronous activity among spinal interneurons was greater during sural stimulation than tibial stimulation. Nevertheless, the occurrence of correlated interneuron activity (∼30%) was observed to a greater extent than excitatory and inhibitory synchronous interneuron activity (<10%). This suggests that the network entrainment was more dominant than the putative relatively direct anatomical connections underlying zero latency synchronization.

The location of correlated activity was different between nerves. Sural stimulation evoked greater coherence and excitatory interneuron synchrony in the caudal array, whereas tibial stimulation was no different at L3 as compared to L6/7. While the dorsal root entry for sural and tibial are at or near the L6/L7 spinal level, it is likely that the commissural interneurons needed for the contralateral pathway are more dispersed and have sparse projections to multiple spinal segments (Bannatyne et al., 2006). Consistent with differing projection patterns between the two nerves, these data suggest that the ipsilateral sural nerve has dense projections onto segmental networks of spinal neurons whereas the tibial nerve contralateral pathway, which must synapse onto commissural interneurons since afferents do not cross the midline, show more sparse and spatially distributed projections onto spinal neuron networks (Harrison et al., 1986). Such anatomical organization is consistent with the functional consequence of activation of these pathways—activation of the ipsilateral sural tends to activate ankle extensors, while activation of the contralateral tibial may activate extensors throughout the hindlimb.

The frequency of stimulation had several significant relationships. In general, there is a decrease in correlated activity with increased frequency. This decay is more prevalent in the sural nerve, whereas the tibial nerve has relatively small and uniform coherence across frequencies. As such is it possible that this nerve and frequency interaction plays a critical role the ability of these pathways to transfer information. With its sparse projections, it is difficult for tibial nerve to relay the frequency content of the afferent drive to the soleus motor pool.

Limitations of the Approach

In the current study, the contralateral tibial and ipsilateral sural nerves were stimulated as means to tonically activate the SOL motor pool (Heckman et al., 1994). This was critical since it was necessary to generate tonic discharge of both interneurons and motor units to examine their connectivity. The methods used in the current study were able to demonstrate clear differences in the pattern of connectivity between these different modes of afferent drive. However, because each of these pathways relay different types of sensory information (i.e., pure cutaneous vs. mixed muscle and cutaneous inputs) from different sides of the body, it is difficult to determine how each of these factors contribute to the differences in connectivity of spinal neurons. Therefore, future studies employing similar methods with a larger sample size should attempt to explore more granular differences in the pattern of connectivity between a variety of afferent pathways.

It is likely that a cutaneous nerve will result in a mixture of inhibition and excitation occurring at different time scales—indeed a subpopulation of interneurons were firing at baseline and decreased their discharge. Our ability to detect such a mixture of excitation and inhibition is limited with the PSTH approach. Because of this, we only characterized the initial response at relatively low frequencies ($\leq$10 Hz). Secondary effects are difficult to observe in the PSTH of motor units due to synchronization of the long after hypolarization of the spinal motoneuron. The after hypolarization in spinal interneurons is likely shorter in duration and it is possible that secondary synaptic events will faithfully be reflected as change in probability of discharge. Peristimulus frequency grams may be used in conjunction with the PSTH approach to better quantify a mixture of excitatory and inhibitory drive at different timescales (Turker and Powers, 2003). Further, recordings from dorsal roots and identification of each interneurons' preferred activation would be helpful in this regard. This would allow us to gain some measure of the occurrence and latencies of afferent projections to the spinal cord and allow for classification of interneurons. Such information would allow us to more accurately model the neuronal circuitry of the spinal cord.

Additionally, we used the CST to quantify the motor unit response rather than individual motor units. As motor units discharge at much lower rates than spinal interneurons, using the CST increased the number of occurrences and allowed for detection of events. While visual observation of the individuals motor units suggested a homogenous, though noisy, response across the motor pool, recording for longer periods and tracking the same unit would help identify potential non-uniform distributions of synaptic input to the motor pool. Further, as the general change discharge rate was similar between nerves, but the functional connectivity was substantially different between nerves, detailed assessments of individual motoneurons may allow for the detection of features of the state of interneurons using motor unit discharge patterns. Being able to use these motor unit discharge patterns to infer the state of the spinal cord circuitry could provide an important means to non-invasively quantify the state of spinal cord circuitry in humans.

In the current study, estimates of coherence were derived from segments of the data that were weighted equally over the entire duration of the stimulation period. However, it is unclear if the strength of coherence was consistent over time. Repetitive stimulation may cause changes in input-output properties of spinal neurons lasting several tens of seconds due to several factors, including neurotransmitter depletion (Regehr, 2012), impaired vesicle fusion (Neher and Sakaba, 2008), desensitization of post-synaptic receptors (Xu-Friedman and Regehr, 2004), and/or summation of somatic currents (Powers and Binder, 2000; Cushing et al., 2005). Thus, it is possible there may have been time-dependent changes in the magnitude of coherence between the stimulus pulse train and interneuron and motor unit spike times. Future studies should attempt to apply time-frequency analyses to assess time-dependent changes in coherence during periods of repetitive stimulation.

Here we quantified the discharge patterns of spinal interneurons and motor units using time and frequency domain correlations to quantify the functional connectivity of spinal neurons during trains of afferent drive from two different nerves. Our data support the notion that the ipsilateral sural nerve has dense projections to the soleus motor pool, while contralateral tibial nerve has sparce projections. Understanding the activation patterns of spinal neurons during precisely controlled afferent drive will allow for future investigations to quantify how this circuitry changes following neurological injury, such as spinal cord injury.

DATA AVAILABILITY STATEMENT

The raw data supporting the conclusions of this article will be made available by the authors, without undue reservation.

ETHICS STATEMENT

The animal study was reviewed and approved by Temple University Institutional Animal Care and Use Committee.

AUTHOR CONTRIBUTIONS

ML and CT: conception and experimental design. AK, FM, ML, and CT: data collection. MZ, ET, FN, ML, and CT: data analysis. MZ and CT: preparation of figures. MZ, ML, and CT: interpretation of results, manuscript preparation, and critical revisions. All authors contributed to the article and approved the submitted version.

FUNDING

This work was supported by an NIH/NINDS grant (NS110605) to ML. Publication of this article was funded in part by the Temple University Open Access Publishing Fund.

REFERENCES

AuYong, N., Ollivier-Lanvin, K., and Lemay, M. A. (2011a). Preferred locomotor phase of activity of lumbar interneurons during air-stepping in subchronic spinal cats. *J. Neurophysiol.* 105, 1011–1022. doi: 10.1152/jn.00523.2010

AuYong, N., Ollivier-Lanvin, K., and Lemay, M. A. (2011b). Population spatiotemporal dynamics of spinal intermediate zone interneurons during air-stepping in adult spinal cats. *J. Neurophysiol.* 106, 1943–1953. doi: 10.1152/jn.00258.2011

Bannatyne, B. A., Edgley, S. A., Hammar, I., Jankowska, E., and Maxwell, D. J. (2006). Differential projections of excitatory and inhibitory dorsal horn interneurons relaying information from group II muscle afferents in the cat spinal cord. *J. Neurosci.* 26, 2871–2880. doi: 10.1523/JNEUROSCI.5172-05.2006

Brownstone, R. M., and Bui, T. V. (2010). Spinal interneurons providing input to the final common path during locomotion. *Prog. Brain Res.* 187, 81–95. doi: 10.1016/B978-0-444-53613-6.00006-X

Cote, M. P., and Gossard, J. P. (2004). Step training-dependent plasticity in spinal cutaneous pathways. *J. Neurosci.* 24, 11317–11327. doi: 10.1523/JNEUROSCI.1486-04.2004

Cushing, S., Bui, T., and Rose, P. K. (2005). Effect of nonlinear summation of synaptic currents on the input-output properties of spinal motoneurons. *J. Neurophysiol.* 94, 3465–3478. doi: 10.1152/jn.00439.2005

Dominguez-Rodriguez, L. E., Stecina, K., Garcia-Ramirez, D. L., Mena-Avila, E., Milla-Cruz, J. J., Martinez-Silva, L., et al. (2020). Candidate interneurons mediating the resetting of the locomotor rhythm by extensor group i afferents in the cat. *Neuroscience* 450, 96–112. doi: 10.1016/j.neuroscience.2020.09.017

Frigon, A., and Rossignol, S. (2008). Short-latency crossed inhibitory responses in extensor muscles during locomotion in the cat. *J. Neurophysiol.* 99, 989–998. doi: 10.1152/jn.01274.2007

Halliday, D. M., Rosenberg, J. R., Amjad, A. M., Breeze, P., Conway, B. A., and Farmer, S. F. (1995). A framework for the analysis of mixed time series/point process data–theory and application to the study of physiological tremor, single motor unit discharges and electromyograms. *Prog. Biophys. Mol. Biol.* 64, 237–278. doi: 10.1016/s0079-610700009-0

Harrison, P. J., and Jankowska, E. (1985). Sources of input to interneurones mediating group I non-reciprocal inhibition of motoneurones in the cat. *J. Physiol.* 361, 379–401. doi: 10.1113/jphysiol.1985.sp015651

Harrison, P. J., Jankowska, E., and Zytnicki, D. (1986). Lamina VIII interneurones interposed in crossed reflex pathways in the cat. *J. Physiol.* 371, 147–166. doi: 10.1113/jphysiol.1986.sp015965

Heckman, C. J., Miller, J. F., Munson, M., Paul, K. D., and Rymer, W. Z. (1994). Reduction in postsynaptic inhibition during maintained electrical stimulation of different nerves in the cat hindlimb. *J. Neurophysiol.* 71, 2281–2293. doi: 10.1152/jn.1994.71.6.2281

Hill, D. N., Mehta, S. B., and Kleinfeld, D. (2011). Quality metrics to accompany spike sorting of extracellular signals. *J. Neurosci.* 31, 8699–8705. doi: 10.1523/JNEUROSCI.0971-11.2011

Holobar, A., Farina, D., Gazzoni, M., Merletti, R., and Zazula, D. (2009). Estimating motor unit discharge patterns from high-density surface electromyogram. *Clin. Neurophysiol.* 120, 551–562. doi: 10.1016/j.clinph.2008.10.160

Hultborn, H., Illert, M., and Santini, M. (1976). Convergence on interneurones mediating the reciprocal Ia inhibition of motoneurones. I. Disynaptic Ia inhibition of Ia inhibitory interneurones. *Acta Physiol. Scand.* 96, 193–201. doi: 10.1111/j.1748-1716.1976.tb10188.x

Husch, A., Dietz, S. B., Hong, D. N., and Harris-Warrick, R. M. (2015). Adult spinal V2a interneurons show increased excitability and serotonin-dependent bistability. *J. Neurophysiol.* 113, 1124–1134. doi: 10.1152/jn.00741.2014

Jankowska, E., Johannisson, T., and Lipski, J. (1981). Common interneurones in reflex pathways from group 1a and 1b afferents of ankle extensors in the cat. *J. Physiol.* 310, 381–402. doi: 10.1113/jphysiol.1981.sp013556

Jankowska, E., and Lundberg, A. (1981). Interneurones in the spinal cord. *Trends Neurosci.* 4, 230–233.

Jinks, S. L., Atherley, R. J., Dominguez, C. L., Sigvardt, K. A., and Antognini, J. F. (2005). Isoflurane disrupts central pattern generator activity and coordination in the lamprey isolated spinal cord. *Anesthesiology* 103, 567–575. doi: 10.1097/00000542-200509000-00020

Joshua, M., Elias, S., Levine, O., and Bergman, H. (2007). Quantifying the isolation quality of extracellularly recorded action potentials. *J. Neurosci. Methods* 163, 267–282. doi: 10.1016/j.jneumeth.2007.03.012

Kniffki, K. D., Schomburg, E. D., and Steffens, H. (1981). Convergence in segmental reflex pathways from fine muscle afferents and cutaneous or group II muscle afferents to alpha-motoneurones. *Brain Res.* 218, 342–346. doi: 10.1016/0006-8993

LaBella, L. A., Kehler, J. P., and McCrea, D. A. (1989). A differential synaptic input to the motor nuclei of triceps surae from the caudal and lateral cutaneous sural nerves. *J. Neurophysiol.* 61, 291–301. doi: 10.1152/jn.1989.61.2.291

Lemon, R. N., and Griffiths, J. (2005). Comparing the function of the corticospinal system in different species: organizational differences for motor specialization? *Muscle Nerve.* 32, 261–279. doi: 10.1002/mus.20333

McMahon, C., Kowalski, D. P., Krupka, A. J., and Lemay, M. A. (2021). Single cell and ensemble activity of lumbar intermediate and ventral horn interneurons in the spinal air-stepping cat. *J. Neurophysiol.* 2021:21. doi: 10.1152/jn.00202.2021

McPherson, J. G., and Bandres, M. F. (2021). Spontaneous neural synchrony links intrinsic spinal sensory and motor networks during unconsciousness. *Elife* 10:66308. doi: 10.7554/eLife.66308

Mendell, L. M., and Henneman, E. (1968). Terminals of single Ia fibers: distribution within a pool of 300 homonymous motor neurons. *Science* 160, 96–98. doi: 10.1126/science.160.3823.96

Musienko, P. E., Lyalka, V. F., Gorskii, O. V., Merkulyeva, N., Gerasimenko, Y. P., Deliagina, T. G., et al. (2020). Comparison of operation of spinal locomotor networks activated by supraspinal commands and by epidural stimulation of the spinal cord in cats. *J. Physiol.* 598, 3459–3483. doi: 10.1113/JP279460

Negro, F., Muceli, S., Castronovo, A. M., Holobar, A., and Farina, D. (2016). Multi-channel intramuscular and surface EMG decomposition by convolutive blind source separation. *J. Neural Eng.* 13:26027. doi: 10.1088/1741-2560/13/2/026027

Neher, E., and Sakaba, T. (2008). Multiple roles of calcium ions in the regulation of neurotransmitter release. *Neuron* 59, 861–872. doi: 10.1016/j.neuron.2008.08.019

Ollivier-Lanvin, K., Krupka, A. J., AuYong, N., Miller, K., Prilutsky, B. I., and Lemay, M. A. (2011). Electrical stimulation of the sural cutaneous afferent nerve controls the amplitude and onset of the swing phase of locomotion in the spinal cat. *J. Neurophysiol.* 105, 2297–2308. doi: 10.1152/jn.00385.2010

Powers, R. K., and Binder, M. D. (2000). Summation of effective synaptic currents and firing rate modulation in cat spinal motoneurons. *J. Neurophysiol.* 83, 483–500. doi: 10.1152/jn.2000.83.1.483

Radosevic, M., Willumsen, A., Petersen, P. C., Linden, H., Vestergaard, M., and Berg, R. W. (2019). Decoupling of timescales reveals sparse convergent CPG network in the adult spinal cord. *Nat. Commun.* 10:2937. doi: 10.1038/s41467-019-10822-9

Regehr, W. G. (2012). Short-term presynaptic plasticity. *Cold Spring Harb. Perspect. Biol.* 4:a005702. doi: 10.1101/cshperspect.a005702

Schmidt, B. J., and Jordan, L. M. (2000). The role of serotonin in reflex modulation and locomotor rhythm production in the mammalian spinal cord. *Brain Res. Bull.* 53, 689–710. doi: 10.1016/s0361-923000402-0

Thompson, C. K., Negro, F., Johnson, M. D., Holmes, M. R., McPherson, L. M., Powers, R. K., et al. (2018). Robust and accurate decoding of motoneuron behaviour and prediction of the resulting force output. *J. Physiol.* 2018:276153. doi: 10.1113/JP276153

Turker, K. S., and Powers, R. K. (2003). Estimation of postsynaptic potentials in rat hypoglossal motoneurones: insights for human work. *J. Physiol.* 551, 419–431. doi: 10.1113/jphysiol.2003.044982

Xu-Friedman, M. A., and Regehr, W. G. (2004). Structural contributions to short-term synaptic plasticity. *Physiol. Rev.* 84, 69–85. doi: 10.1152/physrev.00016.2003

Conflict of Interest: The authors declare that the research was conducted in the absence of any commercial or financial relationships that could be construed as a potential conflict of interest.

The handling editor declared a past collaboration with one of the author ML.

frontiers
in Integrative Neuroscience

ORIGINAL RESEARCH
published: 21 March 2022
doi: 10.3389/fnint.2022.802608

Leveraging Joint Mechanics Simplifies the Neural Control of Movement

Daniel Ludvig[1,2]*, *Mariah W. Whitmore*[1,2] *and Eric J. Perreault*[1,2,3]

[1] Department of Biomedical Engineering, Northwestern University, Evanston, IL, United States, [2] Shirley Ryan AbilityLab, Chicago, IL, United States, [3] Department of Physical Medicine and Rehabilitation, Northwestern University, Chicago, IL, United States

Behaviors we perform each day, such as manipulating an object or walking, require precise control of the interaction forces between our bodies and the environment. These forces are generated by muscle contractions, specified by the nervous system, and by joint mechanics, determined by the intrinsic properties of the musculoskeletal system. Depending on behavioral goals, joint mechanics might simplify or complicate control of movement by the nervous system. Whether humans can exploit joint mechanics to simplify neural control remains unclear. Here we evaluated if leveraging joint mechanics simplifies neural control by comparing performance in three tasks that required subjects to generate specified torques about the ankle during imposed sinusoidal movements; only one task required torques that could be generated by leveraging the intrinsic mechanics of the joint. The complexity of the neural control was assessed by subjects' perceived difficulty and the resultant task performance. We developed a novel approach that used continuous estimates of ankle impedance, a quantitative description of the joint mechanics, and measures of muscle activity to determine the mechanical and neural contributions to the net ankle torque generated in each task. We found that the torque resulting from changes in neural control was reduced when ankle impedance was consistent with the task being performed. Subjects perceived this task to be easier than those that were not consistent with the impedance of the ankle and were able to perform it with the highest level of consistency across repeated trials. These results demonstrate that leveraging the mechanical properties of a joint can simplify task completion and improve performance.

Keywords: joint mechanics, mechanical impedance, neural control, muscle activation, perceived difficulty, task performance

Edited by:
Richard Nichols,
Georgia Institute of Technology,
United States

Reviewed by:
Elliott J. Rouse,
University of Michigan, United States
Takahiro Kagawa,
Aichi Institute of Technology, Japan

****Correspondence:***
Daniel Ludvig
daniel.ludvig@mail.mcgill.ca

Received: *26 October 2021*
Accepted: *31 January 2022*
Published: *21 March 2022*

Citation:
Ludvig D, Whitmore MW and Perreault EJ (2022) Leveraging Joint Mechanics Simplifies the Neural Control of Movement.
Front. Integr. Neurosci. 16:802608.
doi: 10.3389/fnint.2022.802608

INTRODUCTION

Completing motor tasks that require contact is dependent on an ability to regulate the relationship between limb motions and interaction forces with the environment. The nature of this relationship depends on the requirements of each task. For example, continuous hopping requires joint torques that increase sufficiently upon impact to launch the hopper into the air (Farris and Sawicki, 2012), whereas landing from a jump requires a decrease in joint torques after the initial impact to cease motion and stabilize the body (Decker et al., 2003). The flexibility to perform these similar but contrasting actions arises from our ability to coordinate joint motions and torques across a range of functionally relevant situations.

Two strategies for coordinating limb motions and interaction forces are leveraging the mechanical properties of the limb associated with the current state of the neuromuscular system, and actively regulating joint torques or motions by changing the state of the neuromuscular system as can occur through changes in muscle activation. The mechanical properties of a limb or joint are often quantified by estimates of impedance, the dynamic relationship between imposed motions and the resulting torques (Hogan, 1985b). By setting impedance to a desired value, it is possible to achieve a variety of motion-torque relationships, though these are of course limited to relationships that are physiologically plausible. For example, the static component of limb impedance—often referred to as stiffness—serves to generate torques that oppose externally applied motions. Impedance control might therefore be sufficient for hopping, in which joint torques must increase with increasing joint excursion (Farris and Sawicki, 2012). However, for landing from a jump in which joint torques tend to decrease—following an initial increase—with increasing joint excursion (Decker et al., 2003), an impedance control strategy alone would not be possible. The alternative is to change muscle activity continuously throughout the task to achieve the desired motion-torque relationship; this is the only feasible solution when the impedance established by the current state of the neuromuscular system is not sufficient for the demands of the task being performed.

There are many conditions in which impedance regulation provides a simple and effective control strategy for stabilizing limb posture or movement trajectories. Impedance has been shown to be regulated in many postural tasks (Finley et al., 2012; Krutky et al., 2013; Zenzeri et al., 2014), often to stabilize the human limb against unpredictable disturbances. These adaptations can occur through changes in limb configuration (Mussa-Ivaldi et al., 1985; Tsuji et al., 1995; Trumbower et al., 2009; Krutky et al., 2013), volitional muscle activation (Hogan, 1984; De Serres and Milner, 1991; Mirbagheri et al., 2000), or involuntary activation through reflex pathways (Sinkjaer et al., 1988; Doemges and Rack, 1992; Mirbagheri et al., 2000; van der Helm et al., 2002). The same mechanisms can be used to stabilize a limb during movement (Burdet et al., 2001; Franklin et al., 2007; Ludvig et al., 2017). However, it remains unknown whether a similar strategy of impedance regulation would be advantageous for the coordination of motion and torque when stability is not a primary concern.

Impedance control is not a viable strategy for coordinating torque with motion when task demands are not compatible with the intrinsic mechanical properties of a joint or limb. In these cases, it is necessary to regulate joint torques through changes in muscle activation. This approach has the advantage of being flexible enough to generate arbitrary torque profiles independent of the movement of the joint, even profiles that are inconsistent with the inherent mechanical properties of the joint, such as those that emulate a negative stiffness. However, such a strategy may require more complex neural control and associated decreases in performance or increases in cognitive demand relative to an impedance control strategy. These complexities may arise from external factors such as the unpredictable mechanical properties of the environment (Johansson and Westling, 1988), or internal factors such as the non-linear length-tension (Gordon et al., 1966) and force-velocity (Hill, 1938; Wickiewicz et al., 1984) properties of muscle or the inherent noisiness of muscle activation (Carlton et al., 1985; Harris and Wolpert, 1998; Jones et al., 2002; Tracy et al., 2005). Despite these potential disadvantages, controlling torque through changes in muscle activation could be more intuitive, and may result in tasks that are perceived to be easy and can be completed accurately (Corbett et al., 2011). Thus, it remains unclear which strategy would be more advantageous in terms of neural simplicity, task performance and metabolic cost.

The purpose of this study was to determine if humans leverage the impedance of a limb to complete a motor task more simply, which we defined as perceived to be easier and more consistent, when that impedance is aligned with task demands. We evaluated this by determining how the strategy chosen by the subject influenced the perception of difficulty and task performance. All experiments were performed on the human ankle. Subjects were required to complete three tasks differing in the required coordination between ankle motions and ankle torques. Specifically, the three tasks had different slopes associated with their motion-torque profiles. These slopes have been described as the "quasi-stiffness" of a joint, as they characterize a spring-like behavior that can be different from the actual mechanical properties of the joint (Latash and Zatsiorsky, 1993; Rouse et al., 2013). One of the tasks had a positive quasi-stiffness consistent with the physiological impedance of the ankle, allowing it to be completed either by leveraging the impedance of the ankle or actively regulating ankle torques through changes in muscle activation. The other two tasks had zero or negative quasi-stiffness and could only be completed by explicitly regulating ankle torques through changes in muscle activation, allowing us to evaluate the influence of this strategy on task performance. We computed ankle impedance continuously throughout the experiment while simultaneously measuring the activity of the major muscles crossing the ankle. These measures were used to determine the contributions of ankle impedance and changes in neural control to the net ankle torque. We expected that when impedance of the ankle was consistent with the task requirements there would be less ankle torque due to muscle activity. We hypothesized that this increased reliance on joint impedance and lesser reliance on cyclic muscle activation would result in a task that was perceived easier and more consistent to perform. These results clarify the conditions in which impedance control is used and demonstrate the impact of that use on task difficulty and performance.

Portions of this work have been previously presented in abstract form (Ludvig et al., 2020).

MATERIALS AND METHODS

Ethical Approval

Twenty unimpaired adults (7 female, 13 male; 27 ± 3 years) participated in this study. All subjects provided informed consent

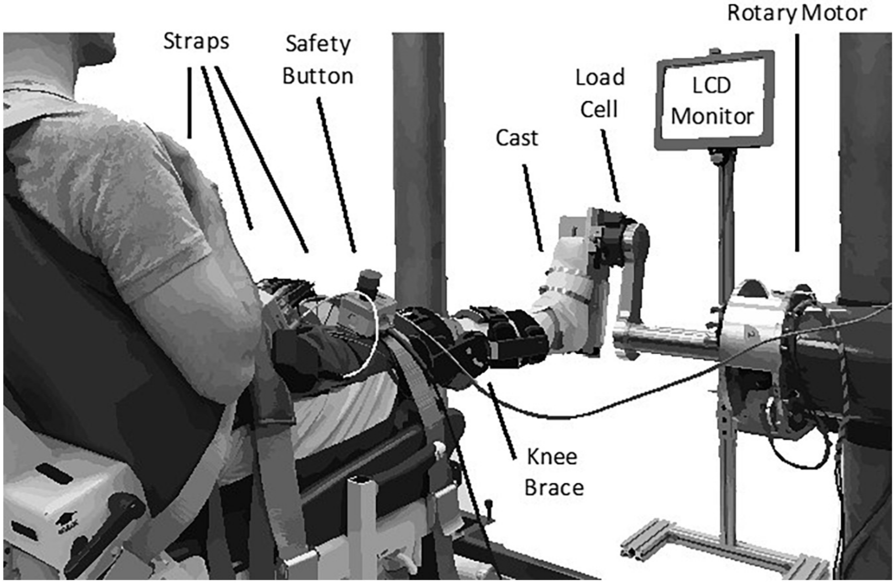

FIGURE 1 | Experimental apparatus.

to the protocol, which was approved by the Northwestern University Institutional Review Board.

Apparatus

We secured each subject's right ankle to an electric rotary motor (BSM90N-3150AF, Baldor, Fort Smith, AR) via a custom fiberglass cast (**Figure 1**). The cast encased the entire foot but did not cover the ankle joint, preserving full range-of-motion. We aligned the ankle to the center of rotation of the motor and restricted movement to the sagittal plane. Subjects sat reclined with their hips at 135 deg and their right leg extended in front of them. We fixed the right knee at 15 deg of flexion using a brace (Innovator DLX, Össur, Reykjavik, Iceland) and secured it, along with the torso, to the chair using straps. We recorded the ankle angle using an encoder integrated with the motor. We used a 6-degree-of-freedom load cell (45E15A4, JR3, Woodland, CA, United States) to acquire force and torque data about the ankle. We controlled the motor using a position control scheme, so the position of the subject's ankle was always dictated by the position of the motor.

We measured electromyograms (EMGs) from four muscles crossing the ankle—medial and lateral gastrocnemius (MG and LG), soleus (SOL), and tibialis anterior (TA). Measurements were made using bipolar surface electrodes (Noraxon 272, Scottsdale, AZ), and amplified (AMT-8, Bortec, Calgary, AB) as needed to maximize the range of the data acquisition system. The analog data were anti-alias filtered at 500 Hz using a 5-pole Bessel filter and sampled at 2.5 kHz (PCI-DAS1602/16, Measurement Computing, Norton, MA, United States). Ankle position was simultaneously recorded using a 24-bit quadrature encoder card (PCI-QUAD04, Measurement Computing, Norton, MA, United States). Data acquisition and motor control were executed using xPC target (The Mathworks Inc., Natick, MA, United States).

Protocol

Two different experimental sessions were conducted. A unique set of 10 subjects participated in each session. The goal of the first session was to characterize the contribution of impedance and muscle activation to torque generation during movement. The goal of the second session was to evaluate the perceived difficulty of the three tasks performed in both sessions.

The first session began with the collection of maximum voluntary contractions (MVCs) to normalize the recorded EMG and to scale the torque for the later trials (Besomi et al., 2020). A MVC was collected for plantarflexion and dorsiflexion, with the ankle fixed at the neutral posture, set to be 1.75 rad between the shank and the foot. We defined ankle angle to be positive when dorsiflexed from the neutral position, consistent with previous work that has quantified ankle impedance (Mirbagheri et al., 2000). Since the goal of the experiment was to produce torques in the plantarflexion direction, we defined plantarflexion torque to be positive.

Subjects completed three tasks: (1) a positive quasi-stiffness task (+K); (2) a zero quasi-stiffness task (0K); (3) and a negative quasi-stiffness task (–K). The +K task required subjects to produce torques as if they were "resisting" an imposed movement, while the –K task required subjects to produce torques as if they were "assisting" the imposed movement. For all tasks, the actuator moved the ankle through a sinusoidal motion with a frequency of 0.5 Hz and an amplitude of 0.18 rad, centered about the neutral position (**Figure 2A**). This frequency and amplitude were selected as they are similar to the ankle kinematics during walking (Borghese et al., 1996). For the +K and –K tasks, subjects were instructed to produce a 0.5-Hz

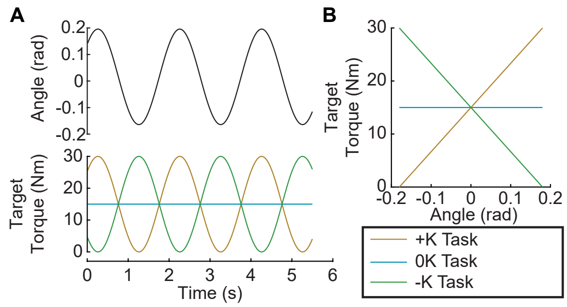

FIGURE 2 | Experimental Protocol. Subjects performed 3 tasks: A positive-quasi-stiffness task (+K); a zero-quasi-stiffness task (0K) and negative-quasi-stiffness task (–K). **(A)** In the +K task the target torque was in phase with the imposed sinusoidal ankle rotation, while it was out of phase for the –K task. **(B)** In the +K task, the slope of the target torque-angle trace is positive, thus we termed it a positive-quasi-stiffness task. Similarly, the slope of the target torque-angle trace is zero in the zero-quasi-stiffness (0K) task, and negative in the negative-quasi-stiffness (–K) task.

sinusoidal plantarflexion torque ranging from 0 to 30% MVC and were aided by visual feedback. The magnitude of the target torque was selected to be feasible without fatigue over the duration of our experiments. For the +K task, the desired torque was in phase with the movement, while for the –K task the desired torque was 180° out of phase with the movement. For the 0K task, subjects were instructed to maintain plantarflexion torque constant at 15%. Maintaining this level ensured that the average torque was consistent across all three tasks. The +K task resulted in an angle-torque relationship with a positive slope (**Figure 2B**) and hence a quasi-stiffness that was consistent with the impedance of the ankle. In contrast, the 0K and –K tasks had zero and negative slopes, respectively, and could not be achieved simply by altering the mechanical impedance of the ankle. In all tasks, subjects were provided visual feedback of their torque and the target torque trajectory. Prior to beginning each task, subjects were given a minimum of 2 150-s trials (1 without and 1 with perturbations) where they practiced coordinating their torque with the imposed movement. Once subjects were able to track the desired torque with an error that had a standard deviation of less than 3% MVC, we proceeded to the experimental trials. All subjects required only two trials for the +K and –K tasks, but some found the 0K task more difficult. On average 2.6 ± 1.0 trials were required for complete training for the 0K task. We subsequently collected five 150-s trials for each of the three tasks. An additional trial was collected to determine the passive mechanics of the ankle. This involved applying the same sinusoidal movement to the ankle while subjects remained relaxed. A small pseudo-random binary sequence (PRBS) perturbation was imposed on the larger sinusoidal movement to estimate ankle impedance. The PRBS perturbation had an amplitude of 0.035 rad, a velocity of 1.75 rad/s, and a switching time of 0.153 s (**Figure 3**). Finally, each subject tracked the sinusoidally varying target torque while the ankle position was held constant. The data from this isometric trial was used to estimate the relationship between changes in muscle activation and ankle torque.

Task difficulty was assessed in a separate group of subjects who completed the same three tasks as in the first session, but without superimposed perturbations. Subjects completed one 60-s trial for each task, and the order of the trials was randomized. After completing all trials, subjects assigned a difficulty score to each task using a continuous scale from 1 to 5, with 1 defined as very easy and 5 as very hard.

Estimating Contributions of Impedance and Muscle Activation to Ankle Torque

Prior to analysis, the recorded EMGs were notch-filtered to remove 60-Hz noise and full-wave rectified. The angle, torque and rectified EMG signals were digitally filtered to prevent aliasing and decimated to 100 Hz. Ankle impedance was estimated using an ensemble system identification algorithm that requires numerous replications of a repeatable behavior (Ludvig and Perreault, 2012). We therefore segmented all signals into overlapping three-period long segments, with each segment beginning one period (2 s) after the previous one. This resulted in approximately 370 segments for each task. We used the 200 segments with the lowest mean-squared error between measured torque and the target torque to maximize the similarity of our repetitions used for system identification. Finally, torque and EMG were normalized by each subject's MVC torque/EMG to facilitate comparisons across subjects. **Figure 4A** shows a 10-s snippet of recorded data from a representative subject, with the average of the 200 segments superimposed.

Estimation of Impedance Contributions to Torque

Following this pre-processing, the torque due to impedance was computed as follows (numbers correspond to the steps shown in **Figure 3**):

1. The large sinusoidal movement and small random perturbations—as well as the torque due to the sinusoidal movement and the random perturbations—were separated by removing the ensemble mean of the ankle angle and torque from each periodic segment.
2. Ankle impedance was estimated by computing a non-parametric, time-varying impulse response function (IRF) at each point within the periodic ankle motion (Ludvig and Perreault, 2012). This impulse response described the relationship between the small PRBS perturbations and the ankle torques opposing them. Two-sided IRFs (Kearney and Hunter, 1990; Westwick and Perreault, 2012) were estimated with a duration ranging from −0.06 to 0.06 s relative each instance in time; the estimation used a 0.1-s window of data centered about this same time point (the mean %VAF of the time-varying IRFs in all subjects and tasks was 81 ± 10%, $n = 30$). The non-parametric IRFs were subsequently parameterized using a second order model consisting of a stiffness, viscosity, and inertia (Ludvig et al., 2011; Ludvig and Perreault, 2012). **Figure 4B** shows the stiffness estimate of the impedance, which we will show to be the dominant component of the impedance at the frequencies relevant to the completion of the three tasks.

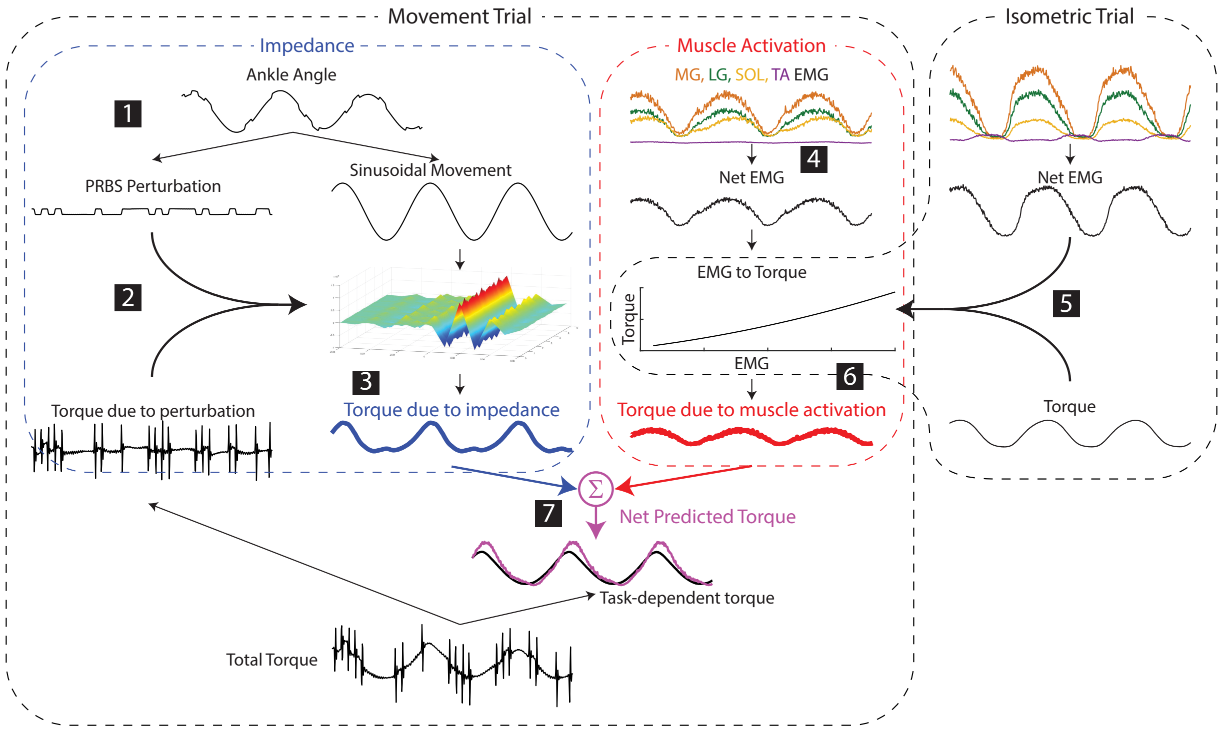

FIGURE 3 | Estimating the contributions of impedance and muscle activation to the net torque about the ankle. (1) Small pseudorandom binary sequence perturbations (PRBS) were superimposed on the larger sinusoidal movement. (2) Ankle impedance was estimated by fitting a time-varying impulse response function between the small perturbation and the resultant torque. (3) The torque due to the impedance was computed by convolving the larger sinusoidal movement with the estimated impedance. (4) The net muscle activity about the ankle was approximated as the difference between the average of the plantarflexor activity and the dorsiflexor activity. (5) The torque due to muscle activation was predicted by a static relationship between the net EMG and ankle torque, estimated from data collected in a separate isometric experiment for each subject. (6) The torque due to muscle activation in the movement trials was computed using this static relationship and the EMGs measured in the movement trial. (7) The net predicted torque was computed as the sum of the torques due to impedance and muscle activation.

3. The torque due to the impedance (Tq_I) was computed by convolving the estimated time-varying IRF ($h(t,t)$) with the imposed sinusoidal movement (q).

$$Tq_I\left(t\right) = \iint_{0}^{t} h\left(t,\tau\right)\frac{d\theta}{dt}\left(t-\tau\right)d\tau dt \qquad (1)$$

This time-varying convolution allows for the impedance to vary non-linearly with torque or ankle angle, and assumes an initial equilibrium position at 0, the center angle of the imposed movement. This computation of impedance torque is insensitive to changes in the equilibrium position throughout the movement. The validity of this assumption, which allows us to distinguish torque due to impedance from that due to muscle activation, is assessed by evaluating the accuracy of the modeled torque across all experimental conditions.

This procedure was done for all three tasks, as well as the data collected in the passive trial.

Estimation of Muscle Activation Contributions to Torque

Following the initial EMG pre-processing outlined above, the torque due to muscle activation was computed as follows:

4. For all tasks, the net EMG was computed by computing the difference between the average plantarflexor (LG, MG, SOL) EMG activity and the dorsiflexor (TA) EMG activity.
5. A 2nd order polynomial was fit between the net EMG and the torque measured in the isometric task (%VAF = 98.0 ± 0.8%, n = 10) to create a model of the EMG to torque relationship.
6. The torque due to muscle activity during the movement trials was predicted from the EMGs measured in these trials and the isometric model.
7. The net predicted torque was computed by summing the torque due to muscle activity with the torque due to impedance computed in step 3. It is important to note that the models used to predict torques due to both impedance and muscle activation were estimated from data separate from that on which the full model was evaluated. The torque response to small perturbations was used to estimate impedance, and isometric contractions were used to estimate the EMG-torque relationship. We then used these estimated models to predict the net torque during each of the three tasks involving sinusoidal movements (**Figure 3**).

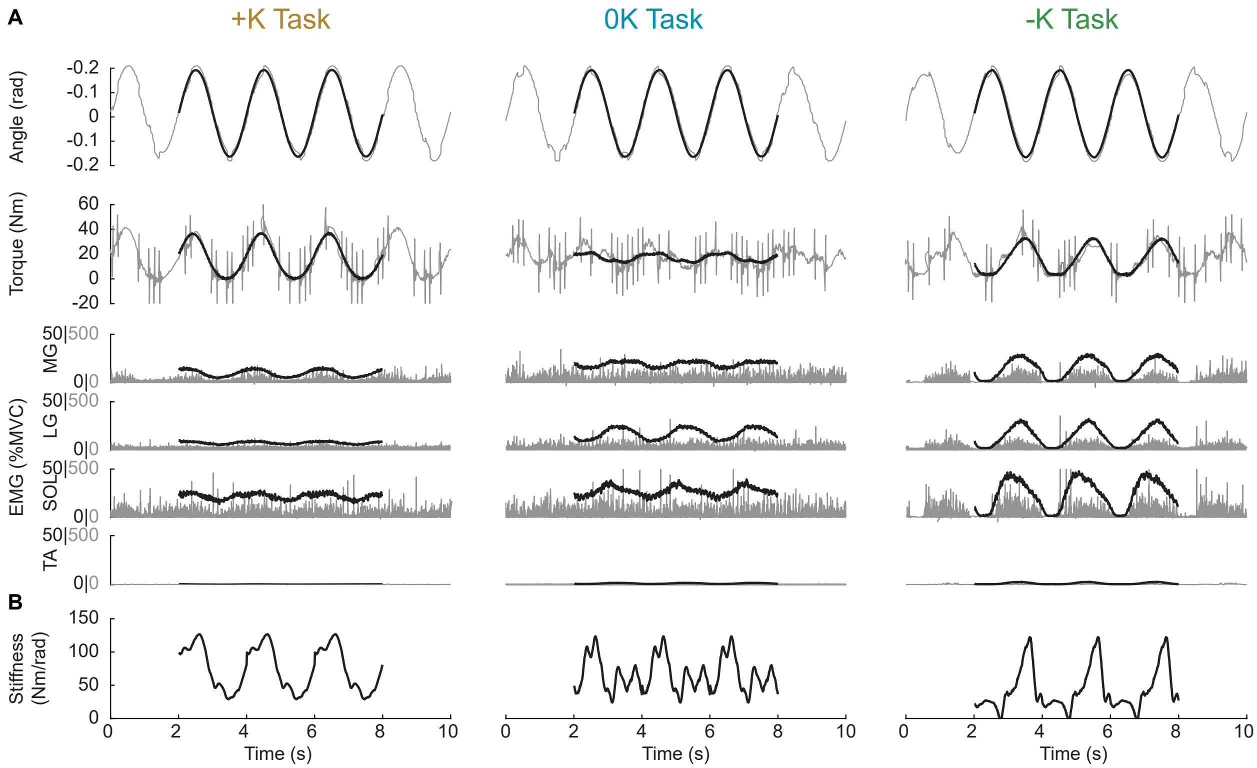

FIGURE 4 | Sample data from a representative subject. **(A)** 10-s snippet of raw data (gray) along with the average of the best 200 segments gathered from the data (black line) for all three tasks. **(B)** Estimates of the stiffness component of impedance throughout the task. Impedance, and hence stiffness, could only be computed with the ensemble of the 200 segments, thus we do not have estimates for a single trial, to match the 10-s snippets shown in **(A)**.

Evaluation of Task Performance

Task performance was evaluated by how well subjects matched the target torque, how consistent they were from trial to trial, and whether they had any consistent deviations from the target. Overall performance was quantified by the total error, which described how well the subjects followed the desired torque trajectory. It was computed by the root mean square (RMS) of the tracking error between desired and actual torque trajectories. This total error was then broken down into two components: random error and bias error. Random error was a measure of consistency, as it quantified how much trial-to-trial variability there was in the torque trajectories. It was computed by finding the RMS of the torque trajectories after removing the average torque trajectory. Finally, the bias error, was used to quantify consistent deviations from the target torque. It was computed by finding the RMS of error between the desired and average torque trajectories.

Statistical Analysis

The goal of this study was to determine how leveraging joint impedance when feasible simplified the neural control of movement. Specifically, we tested the hypothesis that tasks that leveraged the impedance of the ankle would be completed with an easier perceived difficulty and consistently. We compared three metrics across the three tasks that were studied: the torque due muscle activation, perceived difficulty across the tasks, and performance in each of the three torque-tracking tasks. We used a repeated measures ANOVA to test for differences in each of these metrics across the three tasks. *Post hoc* analyses were computed using Tukey's Honest Significant Difference when needed. Additionally, we ran paired *t*-tests to determine whether impedance or muscle activation was greater in each task. For all tests, significance was set to $p = 0.05$. Results are presented as the mean and 95% confidence intervals (mean ± 47.5% confidence interval), unless otherwise specified. We completed the data analysis in MATLAB (2017a, MathWorks).

RESULTS

A Model of Torques Due to Impedance and Muscle Activation Described Experimental Data

We found that the experimentally measured ankle torque was modeled well by our simple model predicting the torques due to impedance and muscle activation. **Figure 5A** shows the experimentally measured torque, the predicted torques due to impedance and muscle activation, and the net predicted torque (impedance + muscle activation) for a typical subject. Across all

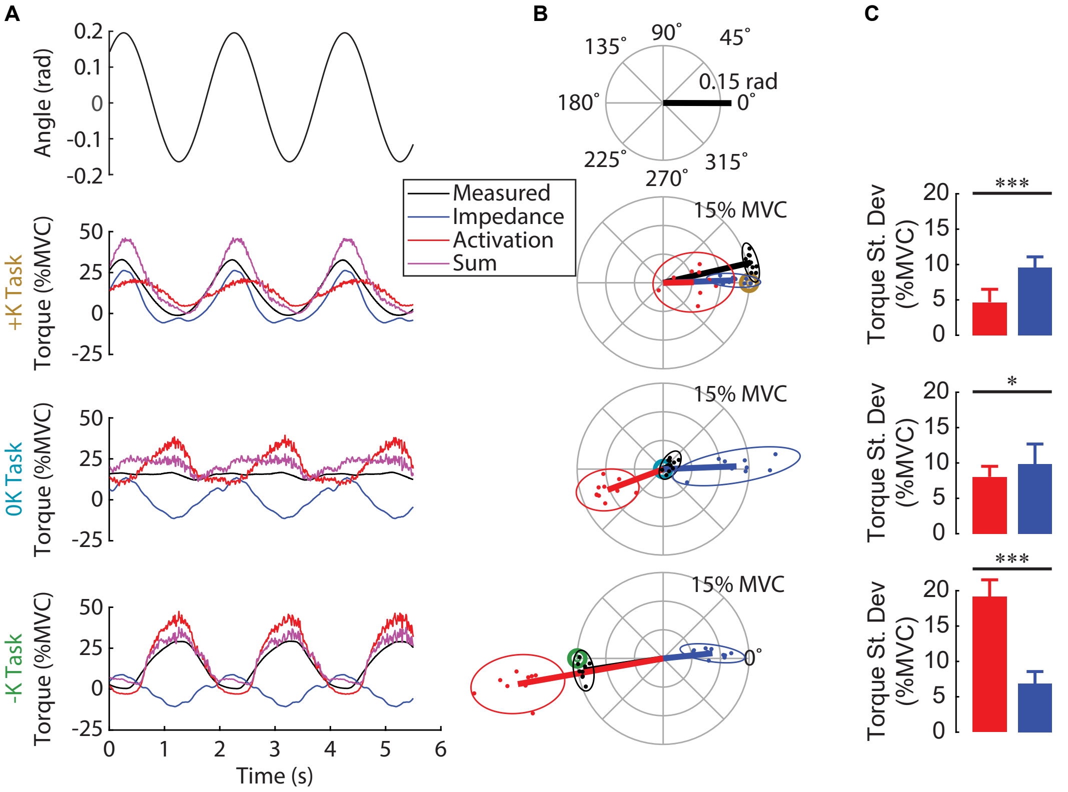

FIGURE 5 | Contribution of impedance and muscle activation to the torque generated in the three tasks. **(A)** Ankle angle, measured torque, torque due to impedance, torque due to muscle activation and their sum for all three tasks for one subject. The sum of the two modeled torque components was a good fit for the measured torque for this subject in all three tasks. **(B)** Polar plot showing the phase and magnitude of the different torque components for all subjects. For each task, the target torque is denoted by a bullseye. Since the torque due to impedance was always in phase with the imposed movement, muscle activation was required to compensate for the impedance when it was not beneficial to task performance. **(C)** The torque due to impedance was greater than the torque due to muscle activation in the +K task, whereas these torques were of similar magnitude in the 0K task, and had a reversed order of dominance in the –K task ($*p < 0.05$, $**p < 0.01$; $***p < 0.001$). We conclude that subjects completed the +K task by relying more on ankle impedance and reducing muscle activity compared to the other two tasks.

movement trials, the standard deviation of the residual error of this model was 4.0 ± 1.6% MVC (mean ± S.D.; $n = 30$). This was a rather small error relative to the large torques produced in certain movement trials that were up to 30% MVC. Furthermore, these errors were consistent across the three tasks [+K: 3.6 ± 0.8% MVC, 0K: 4.2 ± 1.0% MVC, –K: 4.3 ± 1.5% MVC; $F_{(2,\,18)} = 0.58$, $p = 0.58$]. These results suggest that the assumptions inherent in the model are appropriate for the tested experimental conditions. Separating the measured torque into these two components allowed us to investigate how these two potential mechanisms for regulating motion-torque coordination were employed in each of the tested tasks.

Tasks That Leverage Limb Impedance Reduce the Need for Muscle Activation

We examined the contributions of ankle impedance and changes in muscle activation to the net torque at the ankle to determine the strategies that subjects employed in each task. **Figure 5A** shows the measured torque, the torques attributed to the impedance and muscle activation and the sum for a representative subject. **Figure 5B** shows the magnitude and the phase of the 0.5 Hz component of these torques for all subjects. For both the representative subject and the entire group, the torque due to impedance closely matched the measured torque in the +K task, where subjects produced torques "resisting" the imposed movement. For this task, the impedance torque accounted for 88 ± 5% (mean ± S.D.; $n = 10$) of the measured torque variance. In contrast, in the 0K task, the torque from impedance was a sinusoid of similar magnitude to the +K task, but not helpful as the 0K task required no sinusoidal torque component. Finally, in the –K task, where subjects produced torques to "assist" the imposed movement, the torque from impedance was a sinusoid out of phase with the measured torque, and therefore counterproductive.

In all tasks, the torque due to impedance was dominated by the stiffness, resulting in an impedance torque that was in phase with the movement. The non-parametric IRFs quantifying ankle impedance were parameterized by second-order models with stiffness, viscosity, and inertia (**Figure 6**). The torque due to stiffness (+K: 10.9 ± 1.1% MVC; 0K: 11.2 ± 1.8% MVC; –K: 7.9 ± 1.4% MVC) was an order of magnitude greater

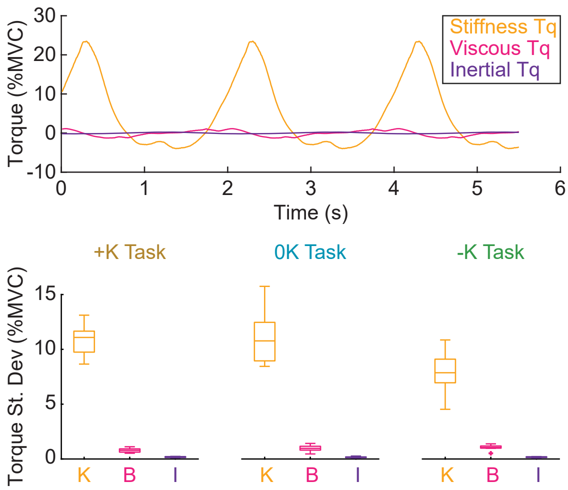

FIGURE 6 | Stiffness was the dominant contributor to the impedance torque. **(A)** The torque due to, stiffness (orange) viscosity (magenta) and inertia (purple) for a single task in a representative subject. **(B)** The torque due to stiffness was approximately an order of magnitude greater than the torque due to viscosity and two orders of magnitude greater than the torque due to inertia for all tasks.

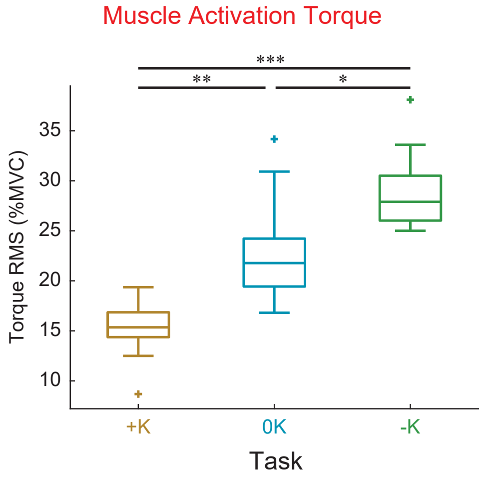

FIGURE 7 | The +K task required subjects to generate less torque due to muscle activation compared to the other two tasks. This was seen both in the mean torque as well as the standard deviation of torque about the mean value. **p* < 0.05; ***p* <0.01; ****p* < 0.001.

than the torque due to viscosity (+K: 0.79 ± 0.14% MVC; 0K: 0.96 ± 0.20% MVC; –K: 1.06 ± 0.16% MVC) and two orders of magnitude greater than the torque due to inertia (0.16 ± 0.04% MVC in all tasks) in all three tasks.

Subjects used changes in muscle activation to compensate for counterproductive impedance torques. Since for all tasks, the torque from ankle impedance was in phase with the movement (**Figure 5B**), the presence or timing of the impedance torque was therefore counterproductive in the 0K and –K tasks, respectively. This required subjects to compensate for these counterproductive torques in the 0K and –K tasks through changes in muscle activation. The consequence was that subjects produced less cyclic torque from changes in muscle activation during the +K task and more torque due to ankle impedance ($\Delta = 4.9 \pm 2.1\%$ MVC, $t_9 = 5.3$, $p = 0.0005$) (**Figure 5C**). These contributions to the net cyclic ankle torque were more comparable in the 0K task ($\Delta = 1.8 \pm 1.5\%$ MVC, $t_9 = 2.8$, $p = 0.02$), while there was greater cyclic torque due to muscle activation in the –K Task ($\Delta = -12.3 \pm 1.6\%$ MVC, $t_9 = -17.5$, $p < 0.0001$). Together, these results suggest that subjects relied more heavily on the impedance of the ankle to meet the task demands when impedance was consistent with the task requirements.

We compared the torque from muscle activation across the three tasks (**Figure 7**), to confirm our expectation that tasks which aligned with the impedance of the joint would require less muscle activation. We found that the torque due to muscle activation was smallest in the +K task. The torque due to muscle activation, as measured by the root mean square, varied between the different tasks [$F_{(2,\ 18)} = 27$, $p < 0.0001$]. The torque from muscle activation was significantly lower in the +K task compared to the –K task ($\Delta = 13.9 \pm 4.9\%$ MVC, $p < 0.0001$) and the 0K task ($\Delta = 7.9 \pm 4.9\%$ MVC, $p = 0.002$). These results confirm our expectation that the +K task resulted in a task which required less torque due to muscle activation, allowing us to link any changes in perceived difficulty and task performance to a decreased reliance on neurally controlled muscle activation.

To rule out the possibility that co-contraction resulted in an increase in muscle activation with no increase in joint torque, we verified that the plantarflexor EMG activity was lower in the +K task. We found that the mean plantarflexor EMG was significantly lower in the +K task compared to the 0K task ($\Delta = 5.8 \pm 3.2\%$ MVC, $p = 0.0005$) or the –K task ($\Delta = 4.4 \pm 3.2\%$ MVC, $p = 0.006$). This lesser amount of plantarflexor EMG in the +K task indicates that co-contraction of the plantarflexors and dorsiflexors did not result in low levels of torque due to muscle activation despite high levels of muscle activity.

Tasks That Can Leverage Limb Impedance Are Perceived as Easy to Perform

We asked subjects to rate the difficulty of each task to determine how the different strategies we observed changed the perception of task difficulty. Difficulty was rated, from 1 to 5 on a continuous scale. These subjective measures were obtained from a new set of subjects so that previous exposure to the three torque-tracking tasks did not alter perceived difficulty. Eight of the 10 subjects perceived the +K task to be easiest, while 2 subjects found the –K task to be easiest. All subjects found the 0K task to be most difficult. Using the subjects' reported perceived difficulty scores (**Figure 8**), we found that the there was a significant perceived difficulty between the three tasks [$F_{(2,\ 18)} = 38$, $p < 0.0001$]. The +K task was found to be significantly easier than both the

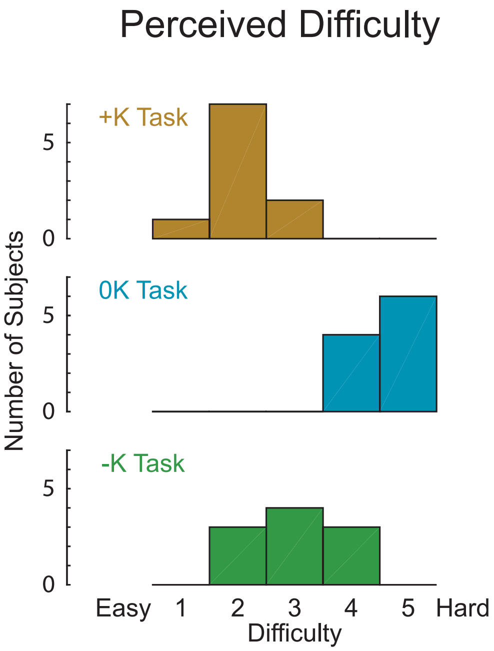

FIGURE 8 | The +K task was perceived to be easier by the subjects, as rated on a 1–5 difficulty scale.

–K ($\Delta = 1.0 \pm 0.7$, $p = 0.009$) and the 0K tasks ($\Delta = 2.5, \pm 0.7$, $p < 0.0001$).

Tasks That Leverage Limb Impedance Can Be Performed More Consistently Than Others

We assessed the torque-tracking errors to evaluate how the different control strategies influenced performance in each task. Specifically, we quantified the total, random, and bias tracking errors for the original groups of subjects (**Figure 9**) in which we estimated the impedance from. Both random and bias error varied cyclically with the imposed movement, resulting in a total torque error that was approximately proportional to the torque applied by each subject. As a result, we saw no difference in the total tracking error across tasks [$F_{(2,\ 18)} = 1.6$, $p = 0.223$]. This similar performance may be due to fact that subjects were trained to achieve a certain level of proficiency in matching the torque. However, we did observe differences in random error [$F_{(2,\ 18)} = 16$, $p = 0.0001$], which assesses the consistency of task performance across repeated cycles of movement. There was significantly less random error in the +K task compared to the –K (Δ root mean square error = 1.0 ± 0.5% MVC, $p = 0.0004$) and 0K tasks ($\Delta = 1.0 \pm 0.5$% MVC, $p = 0.0003$). We also saw differences in the steady state or bias error across repeated movements in each of the three tasks [$F_{(2,\ 18)} = 20$, $p < 0.0001$]. There was greater bias error in the +K task compared to the –K ($\Delta = 0.7 \pm 0.5$% MVC, $p = 0.01$) and 0K tasks ($\Delta = 1.4 \pm 0.5$% MVC, $p < 0.0001$).

The decrease in random error in the +K task may suggest a neural control strategy that required fewer cycle-to-cycle corrective actions by the subject. We assessed this possibility by computing the cycle-to-cycle variation in the plantarflexor muscle activity, which was quantified by the power of plantarflexor EMG following removal of the ensemble mean (**Figure 10**). Similar to the random error, the +K task had the lower cycle-to-cycle variability in EMG compared to both the 0K ($\Delta = -1.2 \pm 0.9$% MVC, $p = 0.005$) and –K tasks ($\Delta = -1.3 \pm 0.9$% MVC, $p = 0.005$), while the –K and 0K task had similar amounts of variability ($\Delta = 0.0\% \pm 0.8$% MVC, $p = 0.99$). Across all subjects we see a strong correlation between the random error and the cycle-to-cycle EMG variability ($r = 0.78$, $p < 0.0001$; **Figure 10C**), indicating that the increased cycle-to-cycle tracking errors in the –K and 0K tasks were associated with increased variability in how subjects controlled muscle activation across cycles of movement. The reduced need for cycle-to-cycle changes in neural control could be another way in which leveraging the impedance in the +K task resulted in a simpler task to complete.

DISCUSSION

The purpose of this study was to determine if leveraging the impedance of a limb results in an easier and more consistent task performance. We had subjects complete three torque-tracking tasks using their ankle, only one of which could be achieved by leveraging their impedance (the +K task). We evaluated the control strategy used in each task by estimating the contributions of ankle impedance and muscle activation to the net torque that was produced. We found that subjects generated less torque from muscle activation in the +K task, the task in which subjects had to produce torques to “resist” the imposed movement. Subjects perceived the +K task to be easiest and were able to complete it more consistently than the other two tasks. These differences were not simply the result of the reduced muscle activation required to complete the +K task, as the task that required the most muscle activity was not perceived as most difficult, nor did it exhibit the lowest performance. These results demonstrate that when subjects can leverage joint impedance to complete a motor task, it results in a strategy that is easier and more consistent to perform.

Tasks That Leverage Limb Impedance Reduce the Need for Muscle Activation

In the +K task when the ankle impedance was consistent with the task demands, subjects produced more torque via ankle impedance and less through muscle activation. While this finding on its own was not too surprising it provided a confirmation of expectations, and a means to quantify how much impedance could help or hinder neural control. In contrast, both other tasks were completed by increasing the torque arising from muscle activation, as neither could be completed using only impedance modulation. This is because the dominant component of impedance in these tasks was stiffness, which is a finite positive value (Hunter and Kearney, 1982) and generates a torque that

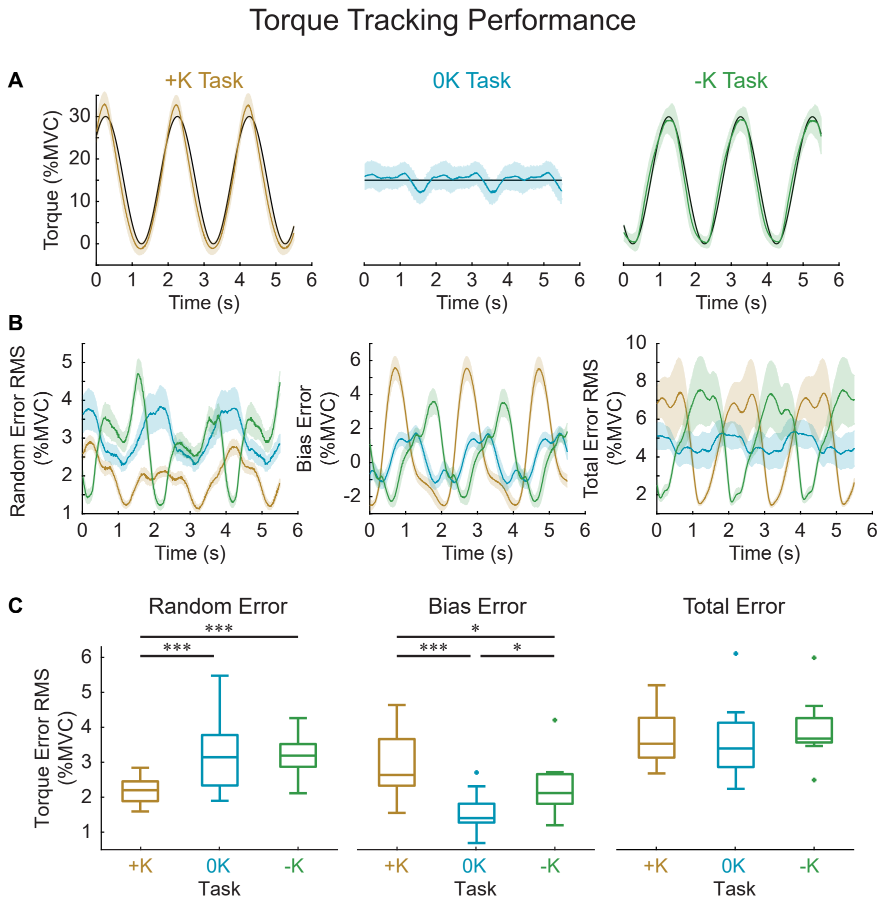

FIGURE 9 | Task performance was quantified by how well the measured torque matched the torque target in all three tasks. **(A)** Representative data for one subject, showing the target (black), the average measured torque (colored lines) and standard deviation across all the cycles of the movement (shaded area). **(B)** Computed random, bias and total error and their variation throughout the imposed movement. Solid shows group average, shaded area shows 95% confidence interval of the group average. **(C)** While the total error did not differ between the three tasks, the +K task did show less random error, indicating a more consistent task behavior when subjects could rely more heavily on impedance. *$p < 0.05$; ***$p < 0.001$.

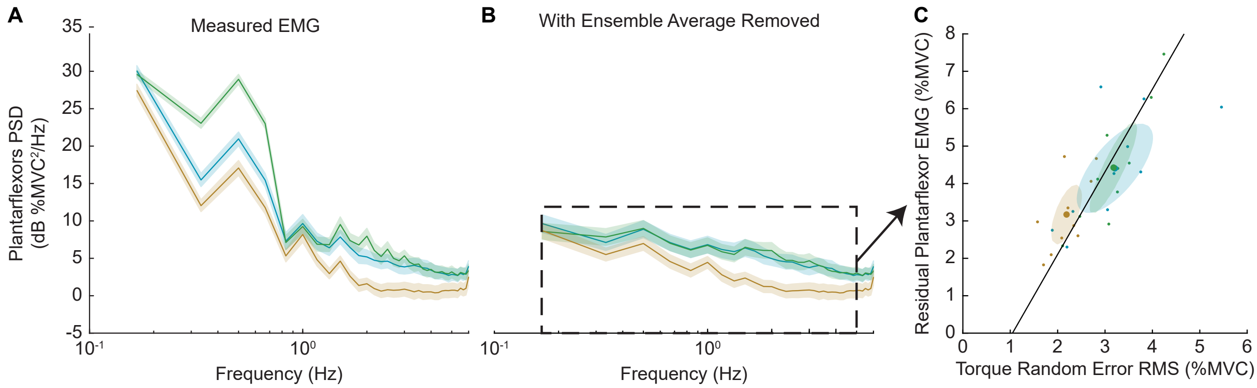

FIGURE 10 | Random error was correlated with increased cycle-to-cycle muscle activity variability. **(A)** Power spectra of the plantarflexor EMGs for all three tasks. Solid line shows group average, shaded areas show 95% confidence internals. As expected, the –K task had the greatest EMG activity. **(B)** Removing the ensemble average allowed us to investigate the EMG activity that differed from cycle-to-cycle. The +K task had less EMG than the other two tasks at all frequencies. **(C)** This residual EMG correlated strongly with the amount of random torque error across all subjects and tasks (black line). As a result, in the +K task subjects had less random torque error and less cycle-to-cycle variability in their EMGs.

resists the imposed sinusoidal motion. Generating a constant level of torque (0K task) or a torque that assists the imposed motion (–K task) requires muscle activation to counter the torque due to impedance. Our results agree with this expectation, as there were nearly equivalent torques from impedance and changes in muscle activation in the 0K task and substantially more torque due to muscle activation in the –K task.

Even though subjects could have completed the +K task by setting their impedance to a value appropriate for generating the target torque, few used only this strategy. Completing the +K task through impedance modulation alone would have required our subjects to set their ankle stiffness to constant values ranging from 49 to 94 Nm/rad, depending on each individual's MVC. This is well within the range of achievable ankle stiffnesses (Hunter and Kearney, 1982; Loram and Lakie, 2002; Loram et al., 2007). Subjects were able to rely on their impedance to generate the majority of the necessary torque as the impedance torque accounted for 88% of the measured torque. However, they did not rely exclusively on an impedance control strategy, as the impedance torque was on average 2.6 times greater than the muscle activation torque (**Figure 5C**). Thus, while subjects did rely on their impedance to complete the +K task, they did not use an impedance control strategy exclusively.

Tasks That Leverage Impedance Are Perceived to Be Easier

Subjects perceived the +K task to be the easiest to complete. Two factors have been associated with the perceived difficulty in completing force or torque production tasks: physical and psychological factors (Slobounov et al., 2004). The leveraging of impedance in the +K task resulted in less muscle activation torque and that may partly explain why most subjects found this task easier to perform. However, that explanation is not consistent with the results of the 0K and –K tasks; subjects universally found the 0K task to be most difficult despite that it required less muscle activation torque than the –K task. Therefore, the perceived difficulty may be related more to psychological factors. The verbal feedback provided by the subjects demonstrates this decreased mental challenge in completing the +K task, as several described this task as "easier" or "more natural." The strategies they employed also suggest a simpler approach to completing the +K task, in which some subjects found it easy to "hold their foot still" in the +K task as opposed to needing to "find the rhythm" in the 0K and –K tasks. However, it remains unknown as to why subject perceived the 0K task to be the most difficult.

Tasks That Leverage Impedance Are Completed More Consistently

Subjects completed the +K task more consistently than the other two tasks. While overall performance was similar in all three tasks, subjects generated torques that were more consistent from cycle-to-cycle in the +K task. Some of this decreased variability might be explained by signal dependent noise. Muscle activation is an inherently noisy process (Carlton et al., 1985; Harris and Wolpert, 1998; Jones et al., 2002; Tracy et al., 2005) and thus the tasks that require more muscle activation would have more variability. Signal dependent noise could explain the decreased random error in the +K task, but it cannot explain the similar levels of random error in the 0K and –K tasks since the –K task had higher levels of muscle activity than the 0K task (**Figures 7**, **10A**).

The cycle-to-cycle variability in matching the torque target (i.e., the random error) correlated with the variability in muscle activation across cycles. This correlation suggests that subjects were generating corrective bursts of muscle activity in response to deviating from the target torque trajectory (Hu et al., 2017), and that these corrections were largest for the 0K and –K tasks. This suggestion of increased cycle-to-cycle corrections is consistent with the finding that steady-state or bias errors were largest for the +K task. These differences in error performance across tasks demonstrates how leveraging impedance can simplify neural control. Once an appropriate level of limb impedance is established, changes in neural control can be minimized as long as the interaction torques required for task completion remain consistent over time.

Implications

The mechanical impedance of human limbs has been studied extensively in the context of maintaining stability during postural control (Hogan, 1984; Mussa-Ivaldi et al., 1985; De Serres and Milner, 1991; Trumbower et al., 2009; Krutky et al., 2013) and movement (Gomi and Kawato, 1996; Burdet et al., 2001; Franklin et al., 2007; Zenzeri et al., 2014). When stability is compromised by unexpected disturbances or the exertion of forces on the environment, we are able regulate impedance so as to complete the task at hand (Hogan, 1985a). Impedance regulation has also proven to be an important concept for robot control (Anderson and Spong, 1988; Vanderborght et al., 2013), as it can be used to generate stable motions and postures along with reliable and forceful contact with the environment. Impedance in robotics has been implemented both through software (Semini et al., 2015) and hardware (Pratt and Williamson, 1995; Vanderborght et al., 2013), analogous to the roles of muscle activation and joint impedance play in generating torques in our study, respectively. Using a hardware based approach can be simpler as it reduces the complexity of the required control algorithms (Vanderborght et al., 2013). We believe that our experimental findings are the first to demonstrate that humans can also leverage the impedance of their limbs to simplify the control required to generate forceful interactions with the environment.

Many common locomotor tasks require joint motion-torque relationships, or quasi-stiffnesses, that are consistent with the impedance of our limbs. Due to the ability of our central nervous system to precisely control muscle activation, humans can generate a variety of motion-torque patterns at each joint. One behavior that arises in many lower-limb movements is a spring-like behavior, or a positive quasi-stiffness, for which the generated joint torques or limb forces act to oppose changes in length. Positive quasi-stiffness can be seen at the whole limb level (Blickhan, 1989; Ferris and Farley, 1997) and at the joint level (Farley and Morgenroth, 1999; Shamaei et al., 2013a) during human locomotion. For example, the ankle, knee, and hip exhibit positive quasi-stiffness in a variety of tasks including, walking (Shamaei et al., 2013a,b,c; Rouse et al., 2014), running (Stefanyshyn and Nigg, 1998; Arampatzis et al., 1999; Kuitunen et al., 2002), and hopping (Farley and Morgenroth, 1999). This positive quasi-stiffness is also present at the muscle-tendon level during many phases of animal locomotion (Tu and Dickinson, 1996; Roberts et al., 1997; Biewener et al., 1998). A simple and efficient way to achieve this quasi-stiffness would be to match the impedance of the joint to the behavioral demands so that the demands on changes in muscle activation are minimized. Our results demonstrate that task-appropriate impedance simplifies neural control. An important complementary experiment would be to evaluate if impedance is actively regulated to simplify neural control.

Limitations

Our results were obtained using a novel method for decomposing the net torque about the ankle into components arising from impedance and from muscle activation. This was useful for estimating the relative contributions of these two strategies for controlling the net torque about the ankle, but potential errors in the estimation process should be considered. However, it is important to note that any errors in estimating either torque due to impedance and muscle activation would not alter our primary conclusions that the +K task was completed more consistently and perceived as easier to perform, as these primary outcomes were independent of our decomposition technique.

The model used to estimate the torque from muscle activation was constructed from data measured during isometric contractions rather than the cyclical movements in which it was eventually used. We chose to use an isometric model to estimate the EMG-torque relationship to limit the assumptions made and to avoid directly fitting models to the data. Directly fitting the data would require us to remove the contribution of the impedance from the measured torque, and any errors in our estimation of the impedance torque could bias our estimates of the torque due to muscle activation. While using isometric data to determine the EMG-torque relationship has the advantage of not being confounded by impedance torque it did have limitations. Specifically, there was little activity in the dorsiflexor muscle during the isometric trial and the EMG-torque relationship changes during movement, as this relationship is sensitive to the angle of the joint (Liu et al., 2013, 2015) and the velocity of movement (Wickiewicz et al., 1984). These effects may have introduced errors in our predictions of muscle activation torque during our movement conditions, but the residuals of our model suggest that these errors were modest and consistent across all tested conditions. There was little activity in the dorsiflexor muscles during the three cyclic movement tasks, thus inaccuracies in modeling the contribution of the dorsiflexor would not greatly affect our prediction of the torque due to muscle activation. As can be seen in the sample data shown in **Figure 4**, the muscle activity in the dorsiflexor muscle (TA), is substantially smaller than the activity in the plantarflexor muscles for all tasks. Across all subjects, the average activity in the plantarflexor muscles was 11 ± 2, 10 ± 2, and 6 ± 1 times greater than the activity in the dorsiflexor muscles in the +K, 0K, and –K tasks, respectively. Thus, any errors in modeling the torque due to the dorsiflexor muscles would be overshadowed by the much larger torques generated by the plantarflexor muscles. We further determined error bounds, by directly fitting a model between the EMG and torque following removal of the impedance. This model, which was directly fit to the data, did predict less torque due to muscle activation compared to the isometric model we used for our main results, but this decrease in predicted torque due to muscle activation was consistently lower in all tasks [+K: 5 ± 3% MVC; 0K: 7 ± 3% MVC; –K: 7 ± 3% MVC; $F_{(2,\ 18)} = 1.0$, $p = 0.37$], and thus would not have affected our conclusions.

Our estimates of impedance were obtained during cyclical movements, but the use of these estimated to compute the torque due to impedance relied on an important assumption. This was that any changes in torque arising from changes in the set-point or equilibrium position were captured by the muscle activation torque component. The accuracy of our modeled torque, which was not fit to the experimental measures, suggests that any errors in the estimated impedance torque were modest (4.0% MVC). In addition, it is important to note that any errors that did exist would not alter our primary conclusions that the +K task was completed more consistently and perceived as easier to perform, as these primary outcomes were independent of our decomposition technique.

Our study only focused on leveraging joint mechanics in the ankle to simplify neural control. It is remains unknown if our findings generalize to other joints, especially to those of the upper limb. Different brain areas are known to control the upper and lower limbs (Luft et al., 2002). While impedance control has been shown in both upper (Krutky et al., 2013) and lower limbs (Finley et al., 2012), we do not know if our specific findings generalize across limbs.

CONCLUSION

In summary, we found that humans can leverage the impedance of the ankle to simplify neural control when that impedance is consistent with the motion-torque demands of the task. Such a strategy reduced the required muscular effort, leading to performance that was perceived to be easier and was completed more consistently. These findings were enabled by the novel method we developed that allowed us to separately estimate the contributions of ankle impedance and changes in neural control to the net ankle torque during large movements. These results suggest that relying on impedance could be a simple way to complete many tasks that require spring-like motion-torque profiles from the joints within the human body.

DATA AVAILABILITY STATEMENT

The raw data supporting the conclusions of this article will be made available by the authors, without undue reservation.

ETHICS STATEMENT

The studies involving human participants were reviewed and approved by the Northwestern University Institutional Review Board. The patients/participants provided their written informed consent to participate in this study.

AUTHOR CONTRIBUTIONS

DL and MW collected and analyzed the data. DL and EP interpreted the results. DL, MW, and EP drafted the manuscript, while DL generated all the figures. All authors have approved the final version of the manuscript and have agreed to be accountable for all aspects of the work and contributed to the conceptual design of the study, and confirm that all listed authors qualify to be listed as authors, and that no one else qualifies to be an author of this manuscript.

FUNDING

This research has been supported in part by the U.S. Army Telemedicine and Advanced Technology Research Center (W81XWH-09-2-0020), and the U.S. Army Joint Warfighter Program (W81XWH-14-C-0105).

REFERENCES

Anderson, R. J., and Spong, M. W. (1988). Hybrid impedance control of robotic manipulators. *IEEE J. Robot. Autom.* 4, 549–556. doi: 10.1109/56.20440

Arampatzis, A., Bruggemann, G. P., and Metzler, V. (1999). The effect of speed on leg stiffness and joint kinetics in human running. *J. Biomech.* 32, 1349–1353. doi: 10.1016/s0021-9290(99)00133-5

Besomi, M., Hodges, P. W., Clancy, E. A., Van Dieen, J., Hug, F., Lowery, M., et al. (2020). Consensus for experimental design in electromyography (CEDE) project: Amplitude normalization matrix. *J. Electromyogr. Kinesiol.* 53:102438. doi: 10.1016/j.jelekin.2020.102438

Biewener, A. A., Konieczynski, D. D., and Baudinette, R. V. (1998). In vivo muscle force-length behavior during steady-speed hopping in tammar wallabies. *J. Exp. Biol.* 201(Pt 11), 1681–1694. doi: 10.1242/jeb.201.11.1681

Blickhan, R. (1989). The spring-mass model for running and hopping. *J. Biomech.* 22, 1217–1227. doi: 10.1016/0021-9290(89)90224-8

Borghese, N. A., Bianchi, L., and Lacquaniti, F. (1996). Kinematic determinants of human locomotion. *J. Physiol.* 494(Pt 3), 863–879. doi: 10.1113/jphysiol.1996.sp021539

Burdet, E., Osu, R., Franklin, D. W., Milner, T. E., and Kawato, M. (2001). The central nervous system stabilizes unstable dynamics by learning optimal impedance. *Nature* 414, 446–449. doi: 10.1038/35106566

Carlton, M. J., Robertson, R. N., Carlton, L. G., and Newell, K. M. (1985). Response timing variability: coherence of kinematic and EMG parameters. *J. Mot. Behav.* 17, 301–319. doi: 10.1080/00222895.1985.10735351

Corbett, E. A., Perreault, E. J., and Kuiken, T. A. (2011). Comparison of electromyography and force as interfaces for prosthetic control. *J. Rehabil. Res. Dev.* 48, 629–641. doi: 10.1682/jrrd.2010.03.0028

De Serres, S. J., and Milner, T. E. (1991). Wrist muscle activation patterns and stiffness associated with stable and unstable mechanical loads. *Exp. Brain Res.* 86, 451–458. doi: 10.1007/BF00228972

Decker, M. J., Torry, M. R., Wyland, D. J., Sterett, W. I., and Richard Steadman, J. (2003). Gender differences in lower extremity kinematics, kinetics and energy absorption during landing. *Clin. Biomech.* 18, 662–669. doi: 10.1016/s0268-0033(03)00090-1

Doemges, F., and Rack, P. M. (1992). Task-dependent changes in the response of human wrist joints to mechanical disturbance. *J. Physiol.* 447, 575–585. doi: 10.1113/jphysiol.1992.sp019019

Farley, C. T., and Morgenroth, D. C. (1999). Leg stiffness primarily depends on ankle stiffness during human hopping. *J. Biomech.* 32, 267–273. doi: 10.1016/s0021-9290(98)00170-5

Farris, D. J., and Sawicki, G. S. (2012). Linking the mechanics and energetics of hopping with elastic ankle exoskeletons. *J. Appl. Physiol.* 113, 1862–1872. doi: 10.1152/japplphysiol.00802.2012

Ferris, D. P., and Farley, C. T. (1997). Interaction of leg stiffness and surfaces stiffness during human hopping. *J. Appl. Physiol.* 82, 15–22. doi: 10.1152/jappl.1997.82.1.15

Finley, J. M., Dhaher, Y. Y., and Perreault, E. J. (2012). Contributions of feed-forward and feedback strategies at the human ankle during control of unstable loads. *Exp. Brain Res.* 217, 53–66. doi: 10.1007/s00221-011-2972-9

Franklin, D. W., Liaw, G., Milner, T. E., Osu, R., Burdet, E., and Kawato, M. (2007). Endpoint stiffness of the arm is directionally tuned to instability in the environment. *J. Neurosci.* 27, 7705–7716. doi: 10.1523/Jneurosci.0968-07.2007

Gomi, H., and Kawato, M. (1996). Equilibrium-point control hypothesis examined by measured arm stiffness during multijoint movement. *Science* 272, 117–120. doi: 10.1126/science.272.5258.117

Gordon, A. M., Huxley, A. F., and Julian, F. J. (1966). The variation in isometric tension with sarcomere length in vertebrate muscle fibres. *J. Physiol.* 184, 170–192. doi: 10.1113/jphysiol.1966.sp007909

Harris, C. M., and Wolpert, D. M. (1998). Signal-dependent noise determines motor planning. *Nature* 394, 780–784. doi: 10.1038/29528

Hill, A. V. (1938). The heat of shortening and the dynamic constants of muscle. *Proc. R. Soc. London. Series B Biol. Sci.* 126, 136–195. doi: 10.1152/advan.00072.2005

Hogan, N. (1984). Adaptive control of mechanical impedance by coactivation of antagonist muscles. *IEEE Trans. Autom. Control* 29, 681–690. doi: 10.1109/tac.1984.1103644

Hogan, N. (1985a). Impedance Control: An Approach to Manipulation: Part I—Theory. *J. Dyn. Syst. Meas. Control* 107, 1–7. doi: 10.1115/1.3140702

Hogan, N. (1985b). The mechanics of multi-joint posture and movement control. *Biol. Cybern.* 52, 315–331. doi: 10.1007/BF00355754

Hu, X., Ludvig, D., Murray, W. M., and Perreault, E. J. (2017). Using Feedback Control to Reduce Limb Impedance during Forceful Contractions. *Sci. Rep.* 7:9317. doi: 10.1038/s41598-017-10181-9

Hunter, I. W., and Kearney, R. E. (1982). Dynamics of human ankle stiffness: variation with mean ankle torque. *J. Biomech.* 15, 747–752. doi: 10.1016/0021-9290(82)90089-6

Johansson, R. S., and Westling, G. (1988). Coordinated isometric muscle commands adequately and erroneously programmed for the weight during lifting task with precision grip. *Exp. Brain Res.* 71, 59–71. doi: 10.1007/BF00247522

Jones, K. E., Hamilton, A. F., and Wolpert, D. M. (2002). Sources of signal-dependent noise during isometric force production. *J. Neurophysiol.* 88, 1533–1544. doi: 10.1152/jn.2002.88.3.1533

Kearney, R. E., and Hunter, I. W. (1990). System identification of human joint dynamics. *Crit. Rev. Biomed. Eng.* 18, 55–87.

Krutky, M. A., Trumbower, R. D., and Perreault, E. J. (2013). Influence of environmental stability on the regulation of end-point impedance during the maintenance of arm posture. *J. Neurophysiol.* 109, 1045–1054. doi: 10.1152/jn.00135.2012

Kuitunen, S., Komi, P. V., and Kyrolainen, H. (2002). Knee and ankle joint stiffness in sprint running. *Med. Sci. Sports Exerc.* 34, 166–173. doi: 10.1097/00005768-200201000-00025

Latash, M. L., and Zatsiorsky, V. M. (1993). Joint Stiffness - Myth or Reality. *Hum. Mov. Sci.* 12, 653–692. doi: 10.1016/0167-9457(93)90010-M

Liu, P., Liu, L., and Clancy, E. A. (2015). Influence of Joint Angle on EMG-Torque Model During Constant-Posture, Torque-Varying Contractions. *IEEE Trans. Neural. Syst. Rehabil. Eng.* 23, 1039–1046. doi: 10.1109/TNSRE.2015.2405765

Liu, P., Liu, L., Martel, F., Rancourt, D., and Clancy, E. A. (2013). Influence of joint angle on EMG-torque model during constant-posture, quasi-constant-torque contractions. *J. Electromyogr. Kinesiol.* 23, 1020–1028. doi: 10.1016/j.jelekin.2013.06.011

Loram, I. D., and Lakie, M. (2002). Direct measurement of human ankle stiffness during quiet standing: the intrinsic mechanical stiffness is insufficient for stability. *J. Physiol.* 545, 1041–1053. doi: 10.1113/jphysiol.2002.025049

Loram, I. D., Maganaris, C. N., and Lakie, M. (2007). The passive, human calf muscles in relation to standing: the short range stiffness lies in the contractile component. *J. Physiol.* 584(Pt 2), 677–692. doi: 10.1113/jphysiol.2007.140053

Ludvig, D., and Perreault, E. J. (2012). System identification of physiological systems using short data segments. *IEEE Trans. Biomed. Eng.* 59, 3541–3549. doi: 10.1109/TBME.2012.2220767

Ludvig, D., Plocharski, M., Plocharski, P., and Perreault, E. J. (2017). Mechanisms contributing to reduced knee stiffness during movement. *Exp. Brain. Res.* 235, 2959–2970. doi: 10.1007/s00221-017-5032-2

Ludvig, D., Visser, T. S., Giesbrecht, H., and Kearney, R. E. (2011). Identification of time-varying intrinsic and reflex joint stiffness. *IEEE Trans. Biomed. Eng.* 58, 1715–1723. doi: 10.1109/TBME.2011.2113184

Ludvig, D., Whitmore, M. W., and Perreault, E. J. (2020). Contributions of joint mechanics and neural control to the generation of torque during movement. *Annu. Int. Conf. IEEE Eng. Med. Biol. Soc.* 2020, 3807–3810. doi: 10.1109/EMBC44109.2020.9175898

Luft, A. R., Smith, G. V., Forrester, L., Whitall, J., Macko, R. F., Hauser, T. K., et al. (2002). Comparing brain activation associated with isolated upper and lower limb movement across corresponding joints. *Hum. Brain Mapp.* 17, 131–140. doi: 10.1002/hbm.10058

Mirbagheri, M. M., Barbeau, H., and Kearney, R. E. (2000). Intrinsic and reflex contributions to human ankle stiffness: variation with activation level and position. *Exp. Brain Res.* 135, 423–436. doi: 10.1007/s002210000534

Mussa-Ivaldi, F. A., Hogan, N., and Bizzi, E. (1985). Neural, mechanical, and geometric factors subserving arm posture in humans. *J. Neurosci.* 5, 2732–2743. doi: 10.1523/JNEUROSCI.05-10-02732.1985

Pratt, G. A., and Williamson, M. M. (1995). "Series elastic actuators," in *Proceedings 1995 IEEE/RSJ International Conference on Intelligent Robots and Systems*, Vol.391, (Piscataway, NJ: Institute of Electrical and Electronics Engineers), 399–406.

Roberts, T. J., Marsh, R. L., Weyand, P. G., and Taylor, C. R. (1997). Muscular force in running turkeys: the economy of minimizing work. *Science* 275, 1113–1115. doi: 10.1126/science.275.5303.1113

Rouse, E. J., Gregg, R. D., Hargrove, L. J., and Sensinger, J. W. (2013). The difference between stiffness and quasi-stiffness in the context of biomechanical modeling. *IEEE Trans. Biomed. Eng.* 60, 562–568. doi: 10.1109/TBME.2012.2230261

Rouse, E. J., Hargrove, L. J., Perreault, E. J., and Kuiken, T. A. (2014). Estimation of human ankle impedance during the stance phase of walking. *IEEE Trans. Neural. Syst. Rehabil. Eng.* 22, 870–878. doi: 10.1109/TNSRE.2014.2307256

Semini, C., Barasuol, V., Boaventura, T., Frigerio, M., Focchi, M., Caldwell, D. G., et al. (2015). Towards versatile legged robots through active impedance control. *Int. J. Robot. Res.* 34, 1003–1020. doi: 10.1177/0278364915578839

Shamaei, K., Sawicki, G. S., and Dollar, A. M. (2013a). Estimation of quasi-stiffness and propulsive work of the human ankle in the stance phase of walking. *PLoS One* 8:e59935. doi: 10.1371/journal.pone.0059935

Shamaei, K., Sawicki, G. S., and Dollar, A. M. (2013b). Estimation of quasi-stiffness of the human hip in the stance phase of walking. *PLoS One* 8:e81841. doi: 10.1371/journal.pone.0081841

Shamaei, K., Sawicki, G. S., and Dollar, A. M. (2013c). Estimation of quasi-stiffness of the human knee in the stance phase of walking. *PLoS One* 8:e59993. doi: 10.1371/journal.pone.0059993

Sinkjaer, T., Toft, E., Andreassen, S., and Hornemann, B. C. (1988). Muscle stiffness in human ankle dorsiflexors: intrinsic and reflex components. *J. Neurophysiol.* 60, 1110–1121. doi: 10.1152/jn.1988.60.3.1110

Slobounov, S., Hallett, M., and Newell, K. M. (2004). Perceived effort in force production as reflected in motor-related cortical potentials. *Clin. Neurophysiol.* 115, 2391–2402. doi: 10.1016/j.clinph.2004.05.021

Stefanyshyn, D. J., and Nigg, B. M. (1998). Dynamic Angular Stiffness of the Ankle Joint during Running and Sprinting. *J. Appl. Biomech.* 14, 292–299. doi: 10.1123/jab.14.3.292

Tracy, B. L., Maluf, K. S., Stephenson, J. L., Hunter, S. K., and Enoka, R. M. (2005). Variability of motor unit discharge and force fluctuations across a range of muscle forces in older adults. *Muscle Nerve* 32, 533–540. doi: 10.1002/mus.20392

Trumbower, R. D., Krutky, M. A., Yang, B. S., and Perreault, E. J. (2009). Use of self-selected postures to regulate multi-joint stiffness during unconstrained tasks. *PLoS One* 4:e5411. doi: 10.1371/journal.pone.0005411

Tsuji, T., Morasso, P. G., Goto, K., and Ito, K. (1995). Human hand impedance characteristics during maintained posture. *Biol. Cybern.* 72, 475–485. doi: 10.1007/BF00199890

Tu, M. S., and Dickinson, M. H. (1996). The control of wing kinematics by two steering muscles of the blowfly (Calliphora vicina). *J. Comp. Physiol. A* 178, 813–830. doi: 10.1007/BF00225830

van der Helm, F. C., Schouten, A. C., de Vlugt, E., and Brouwn, G. G. (2002). Identification of intrinsic and reflexive components of human arm dynamics during postural control. *J. Neurosci. Methods* 119, 1–14. doi: 10.1016/S0165-0270(02)00147-4

Vanderborght, B., Albu-Schaeffer, A., Bicchi, A., Burdet, E., Caldwell, D. G., Carloni, R., et al. (2013). Variable impedance actuators: A review. *Robot. Autom. Syst.* 61, 1601–1614. doi: 10.1016/j.robot.2013.06.009

Westwick, D. T., and Perreault, E. J. (2012). Estimates of acausal joint impedance models. *IEEE Trans. Biomed. Eng.* 59, 2913–2921. doi: 10.1109/TBME.2012.2213339

Wickiewicz, T. L., Roy, R. R., Powell, P. L., Perrine, J. J., and Edgerton, V. R. (1984). Muscle architecture and force-velocity relationships in humans. *J. Appl. Physiol. Respir. Environ. Exerc. Physiol.* 57, 435–443. doi: 10.1152/jappl.1984.57.2.435

Zenzeri, J., De Santis, D., and Morasso, P. (2014). Strategy switching in the stabilization of unstable dynamics. *PLoS One* 9:e99087. doi: 10.1371/journal.pone.0099087

Conflict of Interest: The authors declare that the research was conducted in the absence of any commercial or financial relationships that could be construed as a potential conflict of interest.

frontiers
in Integrative Neuroscience

ORIGINAL RESEARCH
published: 30 March 2022
doi: 10.3389/fnint.2022.810139

Emergence of Extreme Paw Accelerations During Cat Paw Shaking: Interactions of Spinal Central Pattern Generator, Hindlimb Mechanics and Muscle Length-Depended Feedback

Boris I. Prilutsky[1]*, Jessica Parker[2], Gennady S. Cymbalyuk[2] and Alexander N. Klishko[1]

[1] Laboratory of Biomechanics and Motor Control, School of Biological Sciences, Georgia Institute of Technology, Atlanta, GA, United States, [2] Dynamical Neuroscience Laboratory, Neuroscience Institute, Georgia State University, Atlanta, GA, United States

Cat paw shaking is a spinal reflex for removing an irritating stimulus from paw by developing extremely high paw accelerations. Previous studies of paw shaking revealed a proximal-to-distal gradient of hindlimb segmental velocities/accelerations, as well as complex inter-joint coordination: passive motion-dependent interaction moments acting on distal segments are opposed by distal muscle moments. However, mechanisms of developing extreme paw accelerations during paw shaking remain unknown. We hypothesized that paw-shaking mechanics and muscle activity might correspond to a whip-like mechanism of energy generation and transfer along the hindlimb. We first demonstrated in experiments with five intact, adult, female cats that during paw shaking, energy generated by proximal muscle moments was transmitted to distal segments by joint forces. This energy transfer was mostly responsible for the segmental velocity/acceleration proximal-to-distal gradient. Distal muscle moments mostly absorbed energy of the distal segments. We then developed a neuromechanical model of hindlimb paw shaking comprised a half-center CPG, activating hip flexors and extensors, and passive viscoelastic distal muscles that produced length/velocity-depended force. Simulations reproduced whip-like mechanisms found experimentally: the proximal-to-distal velocity/acceleration gradient, energy transfer by joint forces and energy absorption by distal muscle moments, as well as atypical co-activation of ankle and hip flexors with knee extensors. Manipulating model parameters, including reversal of segmental inertia distal-to-proximal gradient, demonstrated important inertia contribution to developing the segmental velocity/acceleration proximal-to-distal gradient. We concluded that extreme paw accelerations during paw shaking result from interactions between a spinal CPG, hindlimb segmental inertia, and muscle length/velocity-depended feedback that tunes limb viscoelastic properties.

Keywords: central pattern generator, inter-segmental energy transfer, cat paw-shake response, EMG activity, whip-like motion, neuromechanical modeling, AnimatLab

Edited by:
Monica A. Daley,
University of California, Irvine,
United States

Reviewed by:
Arthur H. Dewolf,
Catholic University of Louvain,
Belgium
Giovanna Catavitello,
Catholic University of Louvain,
Belgium

Correspondence:
Boris I. Prilutsky
boris.prilutsky@biosci.gatech.edu

Received: *06 November 2021*
Accepted: *14 February 2022*
Published: *30 March 2022*

Citation:
Prilutsky BI, Parker J, Cymbalyuk GS and Klishko AN (2022) Emergence of Extreme Paw Accelerations During Cat Paw Shaking: Interactions of Spinal Central Pattern Generator, Hindlimb Mechanics and Muscle Length-Depended Feedback. Front. Integr. Neurosci. 16:810139. doi: 10.3389/fnint.2022.810139

INTRODUCTION

Cats produce fast paw oscillations to remove water or adhesive tape on the paw (Prochazka et al., 1977, 1989; Smith et al., 1980; Abraham and Loeb, 1985; Pearson and Rossignol, 1991; Hodson-Tole et al., 2012; Mehta and Prilutsky, 2014). This is a spinal reflex, paw-shake response (Koshland and Smith, 1989; Pearson and Rossignol, 1991), aimed to remove an irritating light object stuck to the paw or foot. Previous studies have demonstrated that cats during this motor behavior develop extremely high paw velocities and accelerations, the latter often exceeding gravitational acceleration by more than 10 times (Hoy et al., 1985). There is a proximal-to-distal gradient of segmental and joint angular velocities and accelerations, with foot velocities and accelerations exceeding those of the shank and thigh by several times (Hoy et al., 1985; Hoy and Zernicke, 1986). Previous studies have also documented complex inter-joint coordination and atypical muscle synergies during paw shaking, which are dramatically different from kinematic and EMG activity patterns observed during locomotion. For example, although most of flexor and extensor hindlimb muscles demonstrate reciprocal EMG activity, as in locomotion, there is atypical co-activation between ankle flexor tibialis anterior and knee extensors vasti (Smith et al., 1985). Distal muscle moments at the ankle and knee act to counteract passive motion-depended interaction moments applied to the foot and shank (Hoy et al., 1985; Hoy and Zernicke, 1986). Thus, ankle and knee muscles are active mostly during their lengthening (Hoy et al., 1985; Fowler et al., 1988; Prochazka et al., 1989; Mehta and Prilutsky, 2014) and therefore primarily absorb energy of the foot and shank. The above description suggests that energy increase of distal segments (and their velocity and acceleration) is provided by passive interaction motion-depended forces and moments acting on the distal segments. Similar increases in angular velocity of distal limb segments have been observed in fast motor actions such as passive knee extensions during the swing phase of locomotion and kicking or throwing a ball (Bernstein, 1940; Phillips et al., 1983; Martin and Cavanagh, 1990; Wisleder et al., 1990; Putnam, 1991; Hirashima et al., 2003). The mechanism of energy transfer from proximal to distal limb segments and enhancement of velocity and acceleration of distal segments is called a whip-like mechanism, and inverse dynamics analysis has been used to quantify it (Robertson and Winter, 1980; Aleshinsky, 1986; Putnam, 1991). In whip-like motion, mechanical energy is mostly generated by muscle moments at proximal joints of the limb and is transferred to distal segments primarily by the action of joint forces that do not generate energy for the motion by themselves. Muscle moments of the distal joints primarily decelerate distal segments at the end of motion range to prevent joint overextension by absorbing energy of the distal segments (Robertson and Winter, 1980; Chapman and Caldwell, 1983; Putnam, 1991).

To achieve the proximal-to-distal gradient of segmental angular velocities and accelerations during whip-like movements, the nervous system needs to precisely regulate activities of multiple muscles and inter-joint coordination. Neural control of paw shaking is still poorly understood. Although it has been established that paw-shake-like rhythmic activity of hindlimb flexor and extensor motoneurons can be generated by spinal interneuronal networks, called central pattern generators (CPG), without motion-depended sensory feedback (Pearson and Rossignol, 1991) and that the activity of spindle group Ia afferents from muscles crossing the ankle (triceps surae) and knee joints (hamstrings) is extremely high during paw shaking (Prochazka et al., 1989), it is not known how central and feedback neural mechanisms interact to produce highly coordinated paw shaking. Previously, we proposed a neuromechanical model of cat hindlimbs controlled by a simple CPG (Parker et al., 2018), generating rhythmic reciprocal inputs to flexor and extensor motoneurons, and by motion-dependent sensory feedback, modulating the CPG and motoneuronal activity (Bondy et al., 2016). This model reproduced basic paw-shake kinematics and muscle activity patterns (i.e., reciprocal activation of hip and ankle flexors and extensors and atypical co-activation of knee extensors and ankle flexors). However, complexity of that model, in which all hindlimb muscles were activated by both the CPG and somatosensory feedback and contributed to hindlimb energy generation and transfer, did not allow us to isolate and investigate in details the two major components of a whip-like motion. These components are (i) the generation of mechanical energy for motion by proximal hindlimb muscles and (ii) the energy transfer to the paw and creating the proximal-to-distal gradient of segmental angular velocities/accelerations by passive dynamics of distal muscles and body segments. Therefore, the goal of this study was twofold: (1) examine in intact cats if paw-shake mechanics correspond to the whip-like mechanism and (2) develop and analyze a simplified neuromechanical model of a cat hindlimb with a CPG, activating only hip muscles, and passive viscoelastic muscles of the knee, ankle, and metatarsophalangeal (MTP) joints that produce length/velocity-depended force. We hypothesized that cat paw shaking is organized as a whip-like motion and that specific muscle and inter-joint coordination in this motor behavior can emerge in interactions between a spinal CPG, hindlimb mechanical properties and muscle length/velocity-depended feedback.

MATERIALS AND METHODS

Animal Experiments

All animal surgeries and chronic experiments were in compliance with the "Guide for the Care and Use of Laboratory Animals. Eighth Edition" (National Research Council of the National Academies, 2011) and were approved by the Institutional Animal Care and Use Committee of the Georgia Institute of Technology (protocol number A13063). Five adult female cats (mass 3.27 ± 0.55 kg, **Table 1**) participated in this and our previous studies and underwent previously described surgical and experimental procedures (Maas et al., 2010; Hodson-Tole et al., 2012; Mehta and Prilutsky, 2014; Gregor et al., 2018; Klishko et al., 2021). Briefly, the animals were trained to walk on a plexiglass enclosed walkway using food rewards. Major muscles of the right hindlimb were implanted with Teflon-insulated

TABLE 1 | Animal characteristics.

Cat	Mass, kg	Thigh length, mm	Shank length, mm	Tarsals length, mm	Digits length, mm	Paw-shake cycles analyzed
BL	3.00	100	100	77	31	23
BO	3.90	98	106	67	36	8
CO	3.83	95	119	66	30	2
JU	2.80	98	100	64	30	5
QL	2.80	93	103	59	30	3
Mean ± SD	3.27 ± 0.55	96.6 ± 2.7	105.5 ± 7.9	66.5 ± 6.6	31.4 ± 2.6	Total: 41

Each animal is indicated by a 2-letter code. Recorded kinematics of these animals were used in the analysis of energy generation, transfer and absorption by joint forces and muscle moments. EMG recordings of cats BL, BO, CO and JU were also used in the analysis of EMG burst onset and offset times (see ***Table 2****).*

multistranded stainless-steel fine wires (CW5402; Cooner Wire, Chatsworth, CA) under sterile conditions and general isoflurane anesthesia. The animals recovered from surgery for 2 weeks with pain medication and antibiotics administered.

We recorded kinematics of paw shaking using a 3D high-speed video motion-capture system (Vicon, United Kingdom) and reflective markers placed on the iliac crest, greater trochanter, knee joint, lateral malleolus, 5th metatarsophalangeal joint, and tip of 5th toe using double-sided adhesive tape. Prior to recordings, we attached a small piece of adhesive tape (2 × 3 cm) on the plantar surface of the right hindpaw and placed the cat inside the walkway. The cat walked across the walkway and periodically shook the hindlimb after initiating the swing phase; during paw shaking, the cat interrupted walking and was standing on the other three limbs. We recorded hindlimb kinematics and muscle electromyographic (EMG) activity at sampling rate of 120 and 3,000 Hz, respectively.

Data Analysis

We used inverse dynamics analysis to compute resultant joint forces and joint (muscle) moments in the sagittal plane using recorded kinematics and inertial properties of cat hindlimb segments as described previously (Prilutsky et al., 2005; Farrell et al., 2014). Specifically, recorded vertical and horizontal marker displacements were low-pass filtered (Butterworth zero-lag filter, cut-off frequency 15 Hz). The recorded knee marker position was recalculated using measured lengths of the shank and thigh (**Table 1**) and recorded coordinates of the hip and ankle to reduce effects of skin movement around the knee (Goslow et al., 1973). We computed linear and angular velocities and accelerations of hindlimb segments using numerical differentiation. For further analysis, we selected only paw-shake episodes performed approximately in a sagittal plane (deviations of the thigh from the sagittal plane was within ∼25°). We then calculated the resultant joint forces and muscle moments using the computed accelerations and inertial properties of hindlimb segments; for review of inverse dynamics computations see, for example, Zatsiorsky (2002) and Winter (2004). The mass, position of the center of mass (COM) and moment of inertia with respect to COM of each hindlimb segment were calculated from the measured cat mass and body segment lengths (**Table 1**) using the regression equations developed in Hoy and Zernicke (1985).

To quantify energy generation and absorption by resultant muscle moments and energy transfer by resultant joint forces in the sagittal plane, we computed power produced by the resultant joint force and muscle moment at each hindlimb joint, as well as the rate of total energy change of each hindlimb segment (Robertson and Winter, 1980; see also **Figure 1**):

Rate of energy change of segment s due to power developed by joint force F at joint j ($\dot{E}_{F,s,j}$):

$$\dot{E}_{F,s,j} = F_{x,s,j}v_{x,s,j} + F_{y,s,j}v_{y,s,j}, \tag{1}$$

where $F_{x,s,j}$ and $F_{y,s,j}$ are two components of the force vector at joint j of segment s; $v_{x,s,j}$ and $v_{y,s,j}$ are two components of the linear velocity vector of joint j of segment s. Note that segments thigh, shank, and tarsals have a proximal and a distal joint (hip and knee for the thigh, knee and ankle for the shank, and ankle and MTP for the tarsals), while hindpaw (hind digits) has only the proximal MTP joint.

Rate of energy change of segment s due to power developed by muscle moment M at joint j ($\dot{E}_{M,s,j}$):

$$\dot{E}_{M,s,j} = M_{s,j}\omega_s, \tag{2}$$

where $M_{s,j}$ is muscle moment at joint j of segment s and ω_s is angular velocity of segment s.

The rate of total energy change of segment s due to power of joint forces and muscle moments ($\dot{E}_s$):

$$\dot{E}_s = \sum_j (\dot{E}_{F,s,j} + \dot{E}_{M,s,j}). \tag{3}$$

The rate of total energy change of segment s computed as the time derivative of the total energy of segment s ($\dot{E}_s^{'}$):

$$\dot{E}_s^{'} = \frac{d}{dt}\left(\frac{m_s v_{x,s}^2}{2} + \frac{m_s v_{y,s}^2}{2} + \frac{I_s\omega_s^2}{2} + m_s\mathbf{g}y_s\right), \tag{4}$$

where m_s and I_s are segment mass and moment of inertia of segment s with respect to the segment COM, respectively; $v_{x,s}$ and $v_{y,s}$ are two components of the linear velocity vector of the COM of segment s; ω_s is the angular velocity of segment s; y_s is vertical coordinate of the COM of segment s; and $\boldsymbol{g}$ is gravitational acceleration. Note that $\dot{E}_s = \dot{E}_s^{'}$ (Robertson and Winter, 1980; Aleshinsky, 1986; Zatsiorsky, 2002).

For these calculations, we used relatively steady-state paw-shake cycles (between 2 and 5) in the middle of each paw-shake episode [although there is a drift in the cycle duration (Smith et al., 1985; Parker et al., 2021)] and discarded the cycles in the beginning and the end. A cycle was defined as the period between two consecutive time onsets of a hip flexion moment (**Figure 2**).

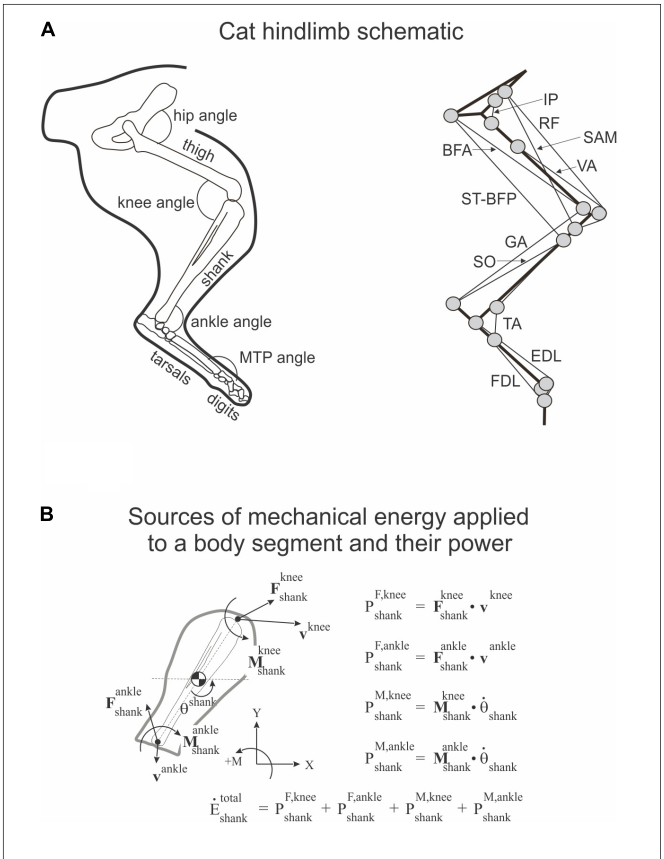

FIGURE 1 | Schematic of cat hindlimb and sources of mechanical energy. **(A)** Cat hindlimb schematic. Left panel: Hindlimb segments and joint angles. MTP is metatarsophalangeal joint. Right panel: Schematic of the hindlimb musculoskeletal model. Thick and thin black lines denote limb segments and muscles, respectively; gray circles indicate locations of muscle origin, insertion and *via* points. IP, iliopsoas (hip flexor); BFA, biceps femoris anterior (hip extensor); SAM, sartorius medial (hip flexor and knee flexor); RF, rectus femoris (hip flexor and knee extensor); ST-BFP, semitendinosus-biceps femoris posterior (hip extensor and knee flexor); VA, vasti (knee extensor); GA, gastrocnemius (ankle extensor and knee flexor); SO, soleus (ankle extensor); TA, tibialis anterior (ankle flexor); EDL, extensor digitorum longus (flexor of digits; its ankle flexion action is neglected in the model); FDL, flexor digitorum longus (extensor of digits, its ankle extension action is neglected in the model). **(B)** Sources of mechanical energy applied to a body segment (shank) and their power (see section "Materials and Methods" and Eqs 1–4 for details).

To determine EMG burst onset and offset times during paw shaking, we analyzed EMG activity of 4 out of 5 cats from this study (BL, BO, CO, JU; **Table 1**) as well as EMG activity of additional 8 intact cats (**Table 2**) recorded in our previous study (Parker et al., 2021). We band-pass filtered (30–1,500 Hz), demeaned and full-wave rectified the recorded EMG signals. To reduce motion-depended noise, we slightly smoothed the rectified EMG signal using a zero-lag, moving average with an 8-ms window. We then determined EMG burst onset and offset times using 3 standard deviations (SD) from the EMG baseline and a condition of the minimum EMG burst duration of 25 ms. We defined the EMG baseline as the signal during a EMG inter-burst interval of at least 200 ms in duration. We determined the EMG burst onset and offset time of each muscle with respect to the EMG burst onset of the medial gastrocnemius muscle (GA) because this muscle was recorded in the largest number of paw-shake cycles.

Neuromechanical Modeling of Paw Shaking

To simulate a whip-like motion of cat paw shaking, we simplified our previous neuromechanical model of the hindlimb with a half-center CPG and feedback signals (Bondy et al., 2016) developed using software for neuromechanical simulations AnimatLab (Cofer et al., 2010). We modeled hindlimb as a planar system of 5 rigid segments (pelvis fixed in place, thigh, shank, tarsals, and digits) that were interconnected by frictionless hinge joints and actuated by major hindlimb muscles crossing the hip, knee, ankle, and MTP joints (**Figure 1A**). Points of muscle origin and attachment, as well as the via points along the muscle paths, were selected to approximately match those described in the literature and to reproduce reported muscle moment arms with respect to the joints (Goslow et al., 1973; Prilutsky et al., 1996; Boyd and Ronsky, 1998; Burkholder and Nichols, 2004; MacFadden and Brown, 2007). Selected parameters of the hindlimb model segments and muscles are listed in **Tables 3**, **4**, respectively. Hindlimb segments' length and mass (**Table 3**) were selected to be within small ranges (5–20%) of the corresponding characteristics of the experimental cats (**Table 1**). Muscle parameters, including parameters of the three-element Hill-type muscle model (contractile element, parallel elastic element, series elastic element) were originally selected to match cat muscle properties reported in the literature (Goslow et al., 1977; Sacks and Roy, 1982; Herzog et al., 1992; Baratta et al., 1995; Scott and Loeb, 1995; Brown et al., 1996; Prilutsky et al., 1996). These muscle parameters included the optimal length of the muscle-tendon unit, parameters of the isometric force-length relationship, and muscle viscosity (the mean slope of the force-velocity relationship); resting length and stiffness of the parallel elastic element; stiffness of the series elastic element; and others (see **Table 4** and AnimatLab model in **Data Sheet 1** of **Supplementary Material**). These parameters were adjusted by hand within biologically realistic ranges to reproduce as close as possible joint angle patterns of real paw shaking (**Figure 2**).

In the simplified model, the half-center CPG provided rhythmic reciprocal excitatory inputs to motoneurons of one-joint hip flexor iliopsoas (IL) and one-joint hip extensor biceps femoris anterior (BFA). The other more distal hindlimb muscles in the model were considered passive and did not receive any excitatory or inhibitory inputs. The model was actuated by active contractions of the hip flexor and extensor muscles. Stiffness coefficients of the parallel and series elastic components, as well as a viscosity coefficient of the contractile component of the passive muscles allowed them to produce length- and stretch velocity-depended force. This model design was implemented to simulate a whip-like mechanism of movement organization more precisely. In this model, mechanical energy for motion is supplied only by most proximal hip muscles, whereas the other

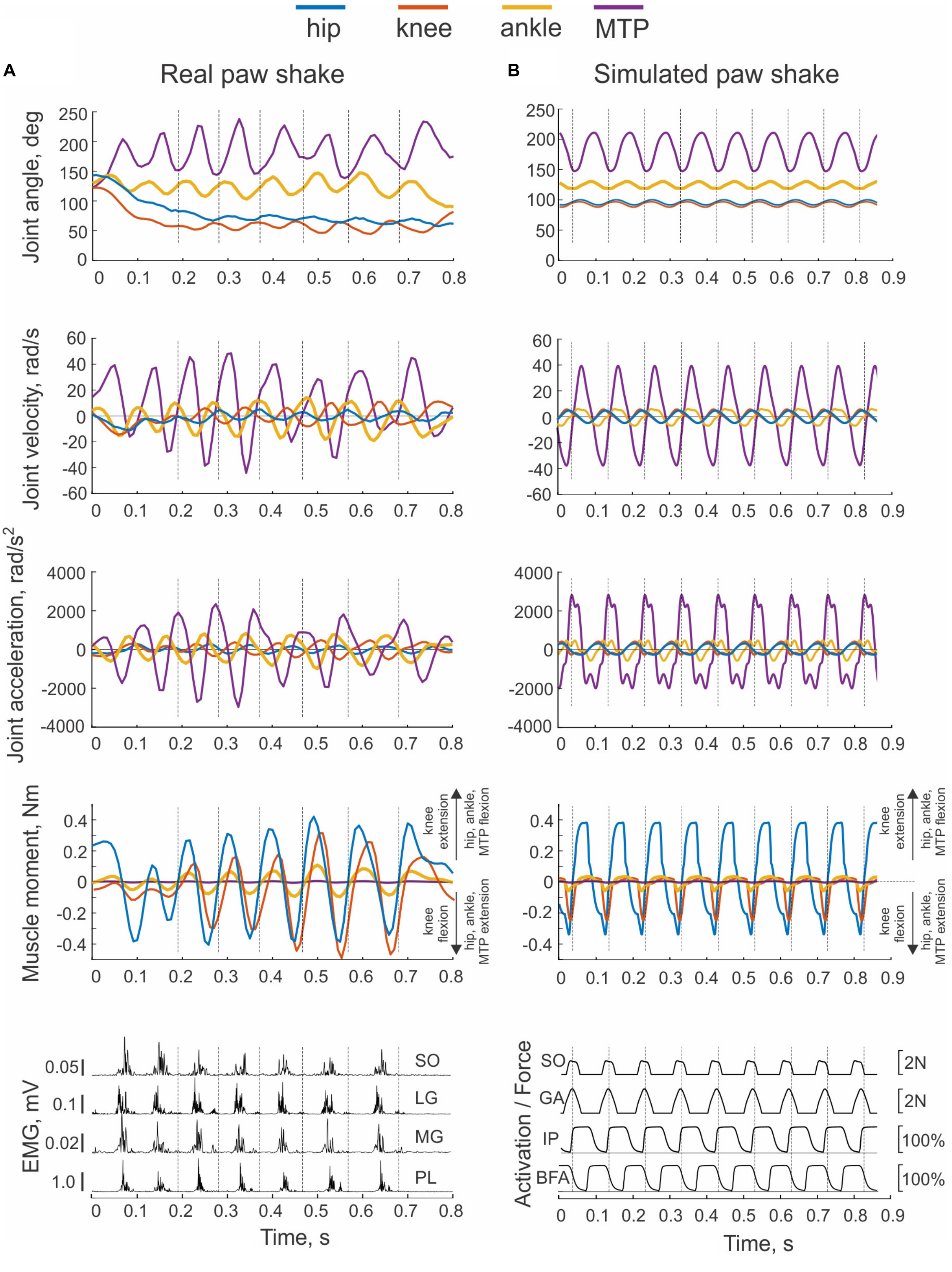

FIGURE 2 | Examples of real and simulated paw shaking. Time periods separated by vertical dashed lines indicate cycles selected for analysis (cycle onset corresponds to the onset of the flexion hip moment). **(A)** A representative episode of real paw shaking of cat BL (**Table 1**). Panels from top to bottom: joints angles, joint angular velocities, joint accelerations, muscle moments, and EMG activities of ankle extensors SO (soleus), lateral gastrocnemius (LG), medial gastrocnemius (MG), and plantaris (PL). Positive muscle moment values correspond to flexion at the hip, ankle, and MTP joints, and to extension at the knee; negative moment values correspond to joint extension at the hip, ankle, and MTP joints, and to flexion at the knee. MTP is metatarsophalangeal joint. **(B)** Example of simulated paw shaking. The first 4 panels show the same mechanical variables as in **(A)**. Last bottom panel shows force produced by ankle extensors SO and GA, as well as activation of hip flexor IP and hip extensor BFA as % of maximal activation (see **Figure 1** for muscle definition).

TABLE 2 | EMG burst onset and offset times of selected hindlimb muscles during a paw-shake cycle.

Cats	GA	SO		BFA		VA		TA		IP	
	Offset	Onset	Offset	Onset	Offset	Onset	Offset	Onset	Offset	Onset	Offset
BL	17.5 ± 1.2 / 6	1.9 ± 1.6 / 6	20.2 ± 2.2 / 6								
BO	45.4 ± 4.9 / 9	–3.3 ± 3.5 / 6	41.8 ± 7.0 / 6	7.2 / 3	29.0 / 3	13.0 / 1	27.0 / 1			31.5 ± 1.4 / 6	102.3 ± 13.6 / 6
BR	63.9 ± 10.0 / 24	–2.7 ± 4.4 / 21	48.3 ± 4.0 / 21			76.7 ± 16.4 / 5	127.1 ± 9.6 / 5			44.9 ± 7.5 / 15	117.2 ± 13.3 / 15
CO	38.3 / 3										
CR	56.4 ± 11.1 / 18	1.5 ± 8.4 / 15	40.9 ± 6.2 / 15	–1.1 ± 11.8 / 18	42.9 ± 13.6 / 18	80.7 ± 8.7 / 8	123.4 ± 5.8 / 8			28.5 ± 3.5 / 12	99.6 ± 8.7 / 12
JU	38.9 / 3	6.57 / 3	33.0 / 3					51.7 / 2	104.4 / 2	23.0 / 2	98.3 / 2
MO	51.4 ± 6.3 / 18							48.7 ± 4.1 / 12	102.0 ± 9.4 / 12	26.3 ± 7.2 / 5	88.9 ± 11.4 / 5
NA	62.4+11.4 / 6	2.7 ± 5.2 / 6	47.7+6.7 / 6	18.7 ± 5.9 / 6	33.5 ± 6.6 / 6						
SQ	79.2 / 3										
ST	42.1 ± 13.5 / 6	–20.3 / 3	45.6 / 3								
VE	53.8 ± 9.3 / 6					69.7 / 3	102.7 / 3	68.0 ± 3.8 / 6	149.2 ± 11.9 / 6		
WE	51.7 ± 11.4 / 21	–13.2 ± 6.9 / 18	43.8 ± 6.9 / 18							21.3 ± 4.61 / 6	123.9 ± 8.3 / 6
All	52.8 ± 14.6 / 123	–3.9 ± 9.0 / 78	42.4 ± 9.3 / 78	4.2 ± 13.0 / 27	39.3 ± 12.6 / 27	73.5 ± 19.1 / 17	115.2 ± 25.1 / 17	54.8 ± 9.7 / 20	116.5 ± 24.0 / 20	32.8 ± 10.4 / 46	107.6 ± 15.6 / 46

Onset and offset measurements for all muscles were taken with respect to the EMG burst onset of the medial gastrocnemius muscle (GA) recorded in the same paw-shake cycles. The numerator shows the mean ± SD in ms; the denominator is the number of cycles included in the analysis. Standard deviations (SD) were not computed when the number of analyzed cycles was $n \leq 3$. GA, gastrocnemius; SO, soleus; BFA, biceps femoris anterior; VA, vasti; TA, tibialis anterior; IP, iliopsoas. Independent factors muscle and cat significantly affected EMG burst onset and offset times [linear mixed model analysis; $F(5, 275) = 284.1–393.6$, $p < 0.001$ and $F(11, 275) = 21.9–36.1$, $p < 0.001$, respectively].

TABLE 3 | Hindlimb model segment parameters.

Segment	Length, mm	Mass, kg	Modified mass, kg
Thigh	92.7	0.146	0.006
Shank	98.6	0.059	0.019
Foot	59.3	0.019	0.059
Digits	25.0	0.006	0.146

*Length and mass of the model segments are within 5–10% of the values for the experimental cats, except the digits (20%) (see **Table 1**).*

more distal muscles can only dissipate or return some of this energy to the system.

The model of a half-center CPG was described in detail elsewhere (Bondy et al., 2016; Parker et al., 2018). Briefly, each half-center was a spiking Hodgkin-Huxley neuron with six ionic currents. The half-centers interacted through an inhibitory synaptic current. The low voltage of half-inactivation and large time constant of inactivation of this current prevent large calcium currents during high frequency (~10 Hz) paw-shake-like rhythmic activities. Parameters of this CPG model generating paw-shake-like activity can be found in Bondy et al. (2016) and Parker et al. (2018).

We used simulated kinematics and kinetics of paw shaking generated in AnimatLab forward simulations to compute power of joint forces and muscle moments, as well as the rate of total energy change as described by Eqs (1)–(4). We also investigated effects of mass distribution along the hindlimb on the proximal-to-distal gradient of segmental angular velocities and accelerations. The mass and cross-section gradient of a real whip is critical for developing an extremely high velocity of the whip tip (Krehl et al., 1998; McMillen and Goriely, 2003). To this end, we reversed the gradient of segmental masses in the hindlimb model (**Table 3**) and ran AnimatLab forward simulations using the same CPG input and muscle properties. In addition, we conducted simulations in which we changed muscle stiffness parameters (**Table 4**) by ± 20% from the nominal values and kept all other model parameters unchanged. This relatively small range of muscle stiffness changes led to a large increase in the joint angle movement magnitudes exceeding in some joints the physiologically feasible ranges (e.g., the knee joint was slightly overextended). Similar simulations were performed to investigate the role of muscle viscosity after changing it by ± 90%.

Statistics

We tested effects of hindlimb segments and joints (independent factors) on experimentally determined peaks of joint and segmental angular velocity and acceleration, muscle moments, and segmental energy changes due to joint forces and muscle moments (depended variables). We used a linear mixed-effects model (MIXED) with paw shaking cycle as a random factor (IBM SPSS Statistics 27, Chicago). We used a similar linear-mixed model to test effects of independent factors muscle and cat on the EMG burst onset and offset time, as well as on the EMG burst duration in a cycle (depended variables). Pairwise comparisons

TABLE 4 | Hindlimb model muscle parameters.

Muscle	Maximum force, N	Optimal muscle-tendon length, mm	Muscle fiber length relative to the muscle-tendon unit length, %	Stiffness of parallel elastic element, kN/m	Stiffness of series elastic element, kN/m	Contractile element viscosity, Ns/m
IP	100	39.7	55	3.17	17.3	53.5
BFA	20	104.81	36	0.89	6.46	21.8
SAM	100	96.61	91	0.188	2.97	22.7
RF	100	93.0	20	0.5	50.0	197.5
ST-BFP	100	103.98	56	2.5	34.8	607.8
VA	100	94.58	27	7.9	37.3	534
GA	10	102.1	23	0.545	4.55	100
SO	10	74.65	58	0.062	0.99	100
TA	100	77.0	57	0.241	6.1	104
EDL	100	96.62	35	3.77	5.5	19.6
FDL	10	92.5	17	0.05	5.0	105

*These muscle parameters were first taken from the literature (Goslow et al., 1977; Sacks and Roy, 1982; Herzog et al., 1992; Baratta et al., 1995; Scott and Loeb, 1995; Brown et al., 1996; Prilutsky et al., 1996) and then adjusted by hand within biologically realistic ranges to reproduce joint angle patterns of paw shaking (see **Figure 2**). IP, iliopsoas (hip flexor); BFA, biceps femoris anterior (hip extensor); SAM, sartorius medial (hip and knee flexor); RF, rectus femoris (hip flexor and knee extensor); ST-BFP, semitendinosus-biceps femoris posterior (hip extensor, knee flexor); VA, vastus (knee extensor); GA, gastrocnemius (ankle extensor, knee flexor); SO, soleus (ankle extensor); TA, tibialis anterior (ankle flexor); EDL, extensor digitorum longus (ankle flexor, digits flexor); FDL, flexor digitorum longus (ankle extensor, digits extensor).*

were performed using Bonferroni adjustments. The significance level was set at 0.05.

RESULTS

Real Paw Shaking in the Cat

General Characteristics

Kinematic variables of paw shaking of a single cat shown in **Figure 2A** were representative of all 5 cats. The cycle of steady-state paw shaking averaged across all cycles and animals was 0.098 ± 0.014 s, which corresponded approximately to 10 Hz. The range of joint angles and peak joint velocities increased from proximal to distal joints. For example, mean peaks of MTP and ankle flexion velocities were 34.2 ± 16.3 rad/s and 12.9 ± 3.7 rad/s, respectively, while the peak of hip flexion velocity was 3.1 ± 1.8 rad/s (joint angles are defined in **Figure 1A**). The effect of joint as an independent factor on the peaks of flexion joint velocities was significant; [F(3, 144) = 57.297, $p < 0.001$]. Similar trends occurred for peaks of extension velocities in these joints (25.3 ± 11.1 rad/s, 12.1 ± 2.9 rad/s and 3.1 ± 2.4, for MTP, ankle and hip joints, respectively; [F(3, 144) = 80.128, $p < 0.001$]. Peaks of joint moments had the opposite tendency—higher peaks occurred in proximal joints (**Figure 2A**). For example, on average across all cats and cycles, peaks of flexion MTP and ankle moments (0.005 ± 0.002 Nm and 0.073 ± 0.018 Nm) were significantly lower of the peak hip flexion moment [0.292 ± 0.091 Nm; F(3, 144) = 209.4, $p < 0.001$]. Note that in the first half of the paw-shake cycle, a combination of MTP flexion, ankle flexion, knee extension and hip flexion joint moments occurred, whereas in the second half, these moments changed direction to MTP extension, ankle extension, knee flexion and hip extension (**Figure 2A**). Activity of distal muscles started when the joint was moving in the direction opposite to the muscle action. For example, ankle extensors (soleus, lateral and medial gastrocnemius and plantaris) demonstrated EMG burst in the middle of each cycle when the ankle was flexing (negative ankle angular velocity; **Figure 2A**).

All 5 cats demonstrated a proximal-to-distal gradient of segmental angular velocity and acceleration peaks in both flexion and extension directions during paw shaking (**Figure 3**). The mean peak of flexion velocity and acceleration across all cats and cycles increased from 3.491 ± 1.595 rad/s and 152.5 ± 84.2 rad/s^2 for the thigh to 42.6 ± 17.1 rad/s and 1992.2 ± 874.5 rad/s^2 for the digits (paw) [see **Figure 3** and **Data Sheet 2** in **Supplementary Material**; F(3, 144) = 71.4–71.9, $p < 0.001$]. The corresponding peaks of extension angular velocity and acceleration were 2.635 ± 2.237 rad/s and 161.7 ± 79.3 rad/s^2 for the thigh to 32.1 ± 10.5 rad/s and 2200.9 ± 807.4 rad/s^2 for the digits [**Figure 3**; F(3, 144) = 92.4–120.3, $p < 0.001$].

Energy Generation and Transfer by Muscle Moments and Joint Forces in Real Paw Shaking

Typical patterns of power of joint forces and muscle moments applied to each hindlimb segment are shown in **Figures 4A,B**, respectively. Power of forces at the thigh joints during steady-state paw shaking had mostly negative values, indicating that the thigh energy was reduced by the joint forces applied to this segment. The hip and knee joint forces decelerated the thigh, which is confirmed by the decrease of thigh energy obtained by integration of thigh power due to joint forces over time (**Figure 4C**). The energy decrease in the thigh due to the actions of the hip and knee forces corresponds to energy transferred to the neighboring segments, including the shank, by these forces. However, total power of joint forces applied to the shank was more negative than positive (**Figure 4A**) as confirmed by the decrease of the shank energy over the whole paw-shake episode due to the action of the knee and ankle joint forces applied to the shank (**Figure 4C**). This means that energy transferred from

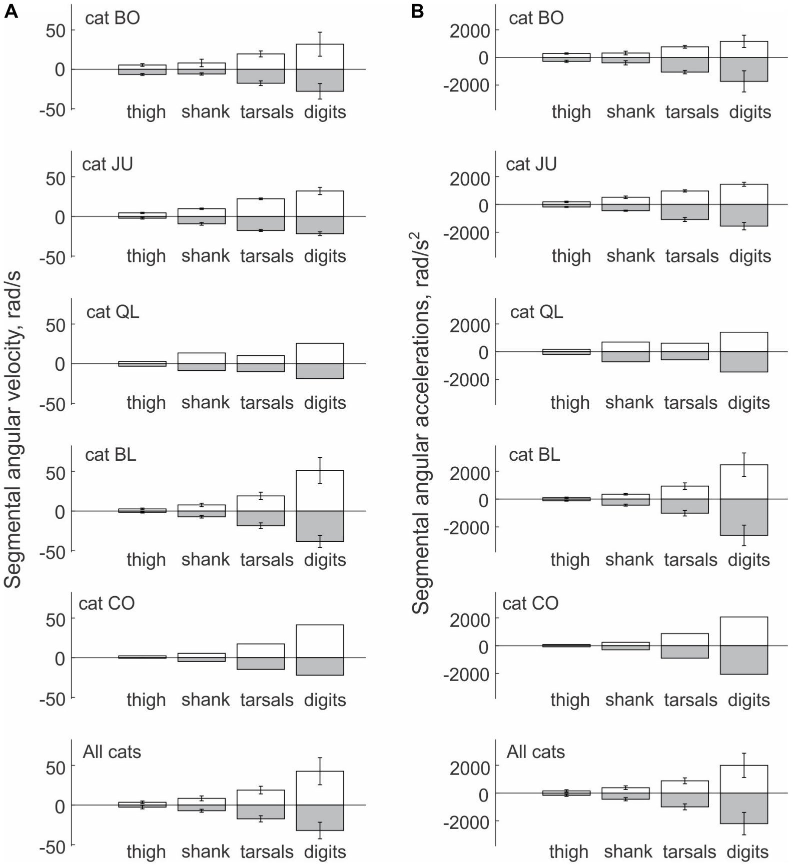

FIGURE 3 | Mean (± SD) peak values of segmental angular velocity **(A)** and acceleration **(B)** computed across individual paw-shake cycles of individual cats and all cats together. Standard deviations (SD) for cats QL and CO were not computed because of the small number of cycles analyzed (see **Table 1** for the number of analyzed cycles).

the thigh to the shank was further transferred to the tarsals by the ankle joint force. Although the tarsals receive energy from the shank, energy of tarsals decreased (**Figure 4C**) due to its transfer by the MTP joint force to the digits, whose energy during paw shaking increased (**Figure 4C**). Energy transferred from the thigh, shank and tarsals to the digits was generated by muscle moments at the hip, knee and tarsals, which is evident from mostly positive power of muscle moments acting on the thigh, shank and tarsals (**Figure 4B**) and from growing energy of these segments over the paw shaking episode (**Figure 4D**). Power of the muscle moment applied to the digits is negative (**Figure 4B**), i.e., muscles at the MTP joint absorb and dissipate energy of the digits.

We observed similar patterns of energy generation, absorption and transfer in all cats. The energy change of the thigh, shank and tarsals in each paw-shake cycle due to the action of joint forces was negative in most cases (**Figure 5A**). The digits received energy (positive energy change) through joint forces in 3 out 5 cats, while two cats showed essentially no change in energy on average. On average across all cats and cycles (**Table 1**), the thigh, shank and tarsals lost energy due to the action of joint forces—the corresponding values were 8.5 ± 0.4 mJ, 6.2 ± 9.7 mJ and 6.6 ± 7.9 mJ (**Figure 5A** and **Data Sheet 2** in **Supplementary Material**). The joint force at the MTP increased energy of the digits, 5.0 ± 4.7 mJ. The effect of the segment factor on the energy transfer was significant [$F(3, 144) = 14.3$, $p < 0.001$] with significant differences among all segments ($p < 0.011$), except between the shank and tarsals ($p = 0.696$). Mostly opposite trends of segmental energy change were caused by muscle moments (**Figure 5B**). Muscle moments increased energy of the most proximal segments, i.e., the thigh (in 4 cats), shank (in 2 cats) and tarsals (in 3 cats); energy of the most distal segment, the digits, was absorbed by muscle moments in all 5 cats. On average across all cats and cycles, the energy changes in the thigh, shank, tarsals and digits were 4.9 ± 6.6 mJ, 2.7 ± 11.8 mJ, 6.7 ± 8.3 mJ and –4.0 ± 2.0 mJ (**Figure 5B**). The effect of the segment factor on these energy changes was significant [$F(3, 144) = 7.698$, $p < 0.001$]. Pairwise comparisons revealed significant differences in energy change between the digits and thigh ($p < 0.001$), the digits and tarsals ($p = 0.001$), but not between the digits and shank ($p = 0.069$). The energy change of the shank was significantly lower than that of the thigh ($p = 0.008$), but was not different from that of the tarsals ($p = 0.114$). The energy change of the thigh and tarsals were not statistically different either ($p = 0.280$).

The sum of powers of all joint forces and muscle moments applied to a body segment ($\dot{E}_s$, Eq. 3) should be equal to the rate of change of the total energy of the segment ($\dot{E}_s^{'}$, Eq. 4). This was

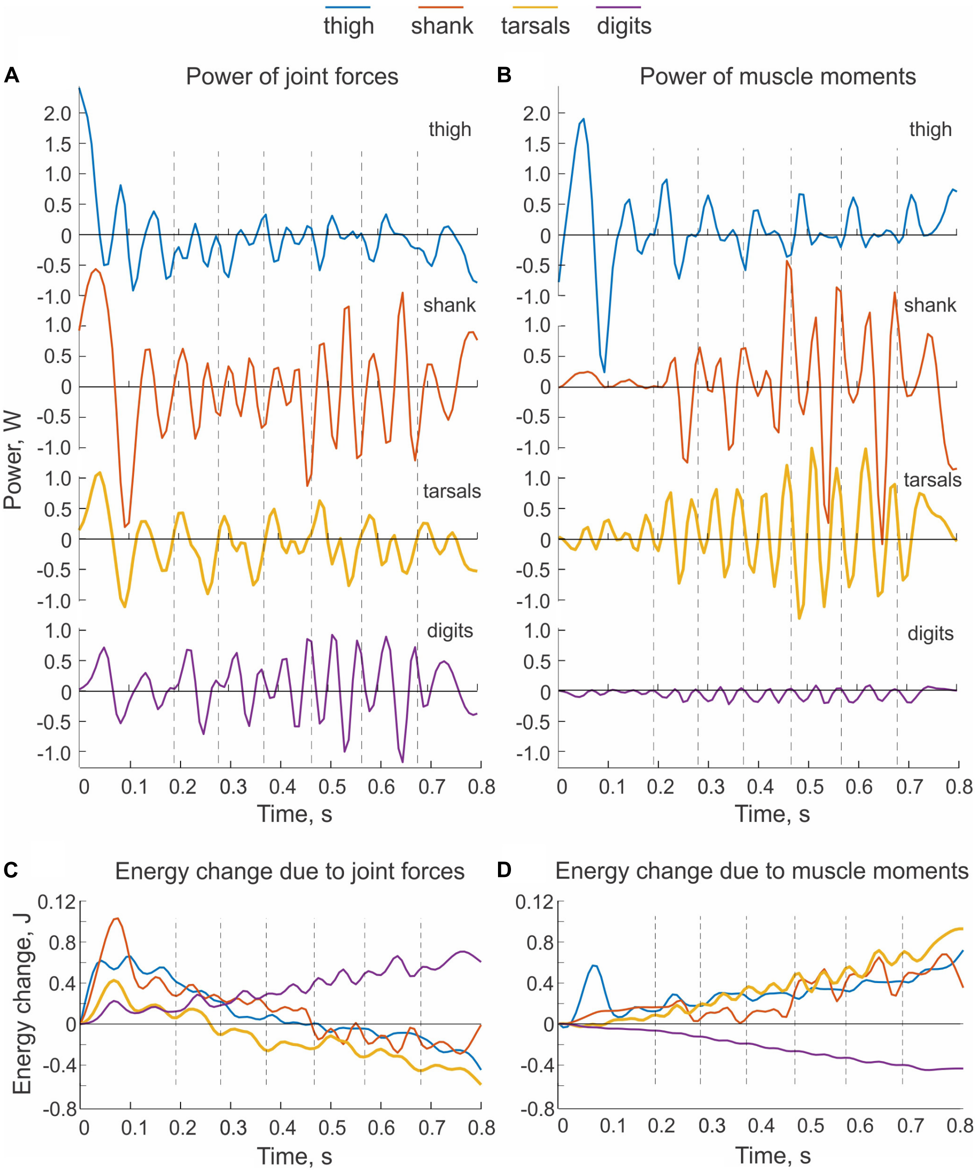

FIGURE 4 | Examples of power of sources of mechanical energy applied to hindlimb segments and the corresponding changes in total energy of the segments during real paw shaking. Cat BL. **(A)** Total power of joint forces applied to each body segment. **(B)** Total power of muscle moments applied to each body segment. **(C)** Changes of total energy of each body segment due to the action of joint forces. Energy changes were computed by integration of the corresponding total power **(A)** over time. **(D)** Changes of total energy of each body segment due to the action of muscle moments. Energy changes were computed by integration of the corresponding total power **(B)** over time.

not the case in the example shown in **Figure 6A**, although the similarity of the two patterns was apparent. Possible reasons for the observed differences will be considered in Discussion.

Simulated Paw Shaking

General Characteristics of Simulated Paw Shaking

An example of paw shake simulation results is shown in **Figure 2B**. The ranges of joint motion and the peaks of joint velocities were smaller than during real paw shaking for the knee and ankle and similar for the hip and MPT joints. Correspondingly, the hip flexion and extension moments and the knee flexion moment had peak magnitudes similar to those in real paw shaking. The model produced a very small knee extension moment (below 0.03 Nm). The simulated ankle flexion and extension moments were much lower than observed in the experiments. There were differences in joint movement phases between simulated and experimental paw shaking. Although simulated muscle moments demonstrated the experimentally observed muscle moment combinations in the first and second half of the cycle (hip flexion-knee extension-ankle flexion and hip extension-knee flexion-ankle extension, respectively), some

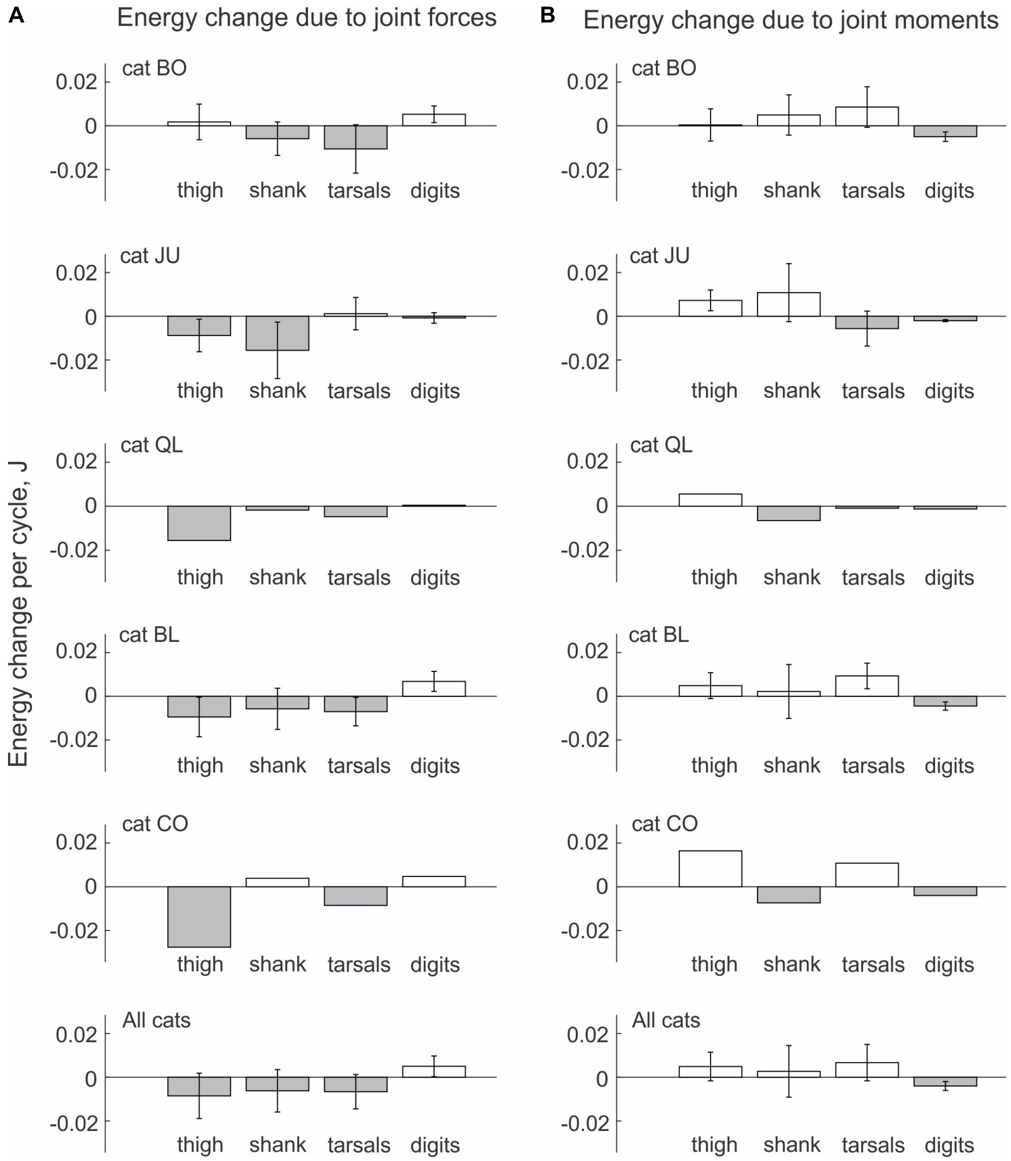

FIGURE 5 | Mean (± SD) energy change of each hindlimb segment per cycle of real paw shaking due to the action of joint forces **(A)** and muscle moments **(B)** computed across paw-shake cycles of individual cats and all cats together. Standard deviations (SD) for cats QL and CO were not computed because of the small number of cycles analyzed (see **Table 1** for the number of analyzed cycles).

phase shifts of angular displacements and velocities between joints in simulated paw shaking were different compared to the real one. For example, the peak of MTP flexion angle coincided with the peak of ankle extension angle in simulations (**Figure 2B**), whereas these events were separated by about 25% of the cycle time in real paw shaking (**Figure 2A**). In addition, changes in hip extension and flexion angles coincided perfectly with changes in knee flexion and extension angles in simulations, whereas in real paw shaking these angle changes were shifted in time by a half of the cycle. Nevertheless, the model demonstrated a clear proximal-to-distal gradient of the segmental angular velocities and accelerations with peak values for the hip and MPT joints closely matching the experimental values (compare **Figures 7A,B**, nominal model with **Figures 3A,B**, all cats). The simulated muscle moment peaks likewise demonstrated the distal-to-proximal gradient (compare **Figure 2B** with **Figure 2A**).

Energy Generation and Transfer by Muscle Moments and Joint Forces in Simulated Paw Shaking

Since the hindlimb model was designed to generate energy by one-joint hip muscles only, we expected that muscle moments would increase energy of the thigh only and that this energy would be transmitted to the shank by the knee joint force, that is, the thigh would lose energy through the action of the joint forces applied to the thigh. This is exactly what we observed (**Figure 8A**). Energy delivered to the thigh by muscle moments

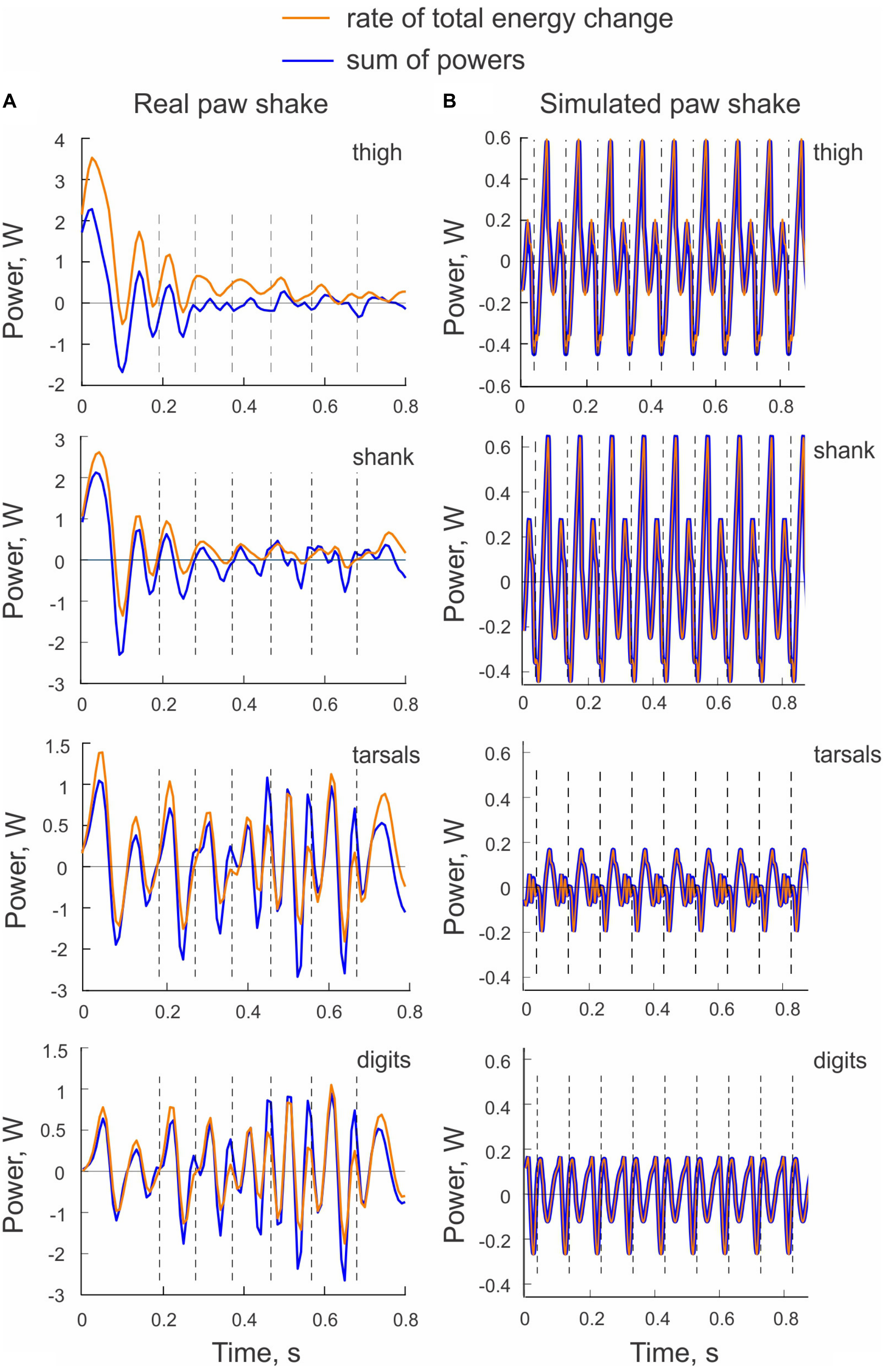

FIGURE 6 | Examples of the rate of total energy change and the sum of powers of all sources of energy for each hindlimb segment computed for a real paw shaking episode of cat BL **(A)** and for simulated paw shaking **(B)**.

increased throughout the simulated paw shake episode and matched approximately the thigh energy loss due to the action of the knee joint force (power of the hip joint force was zero because the hip was fixed in place)—compare energy values in the left and right panels at 0.7 s in **Figure 8A**. All other muscles of the hindlimb model were passive and thus could not generate

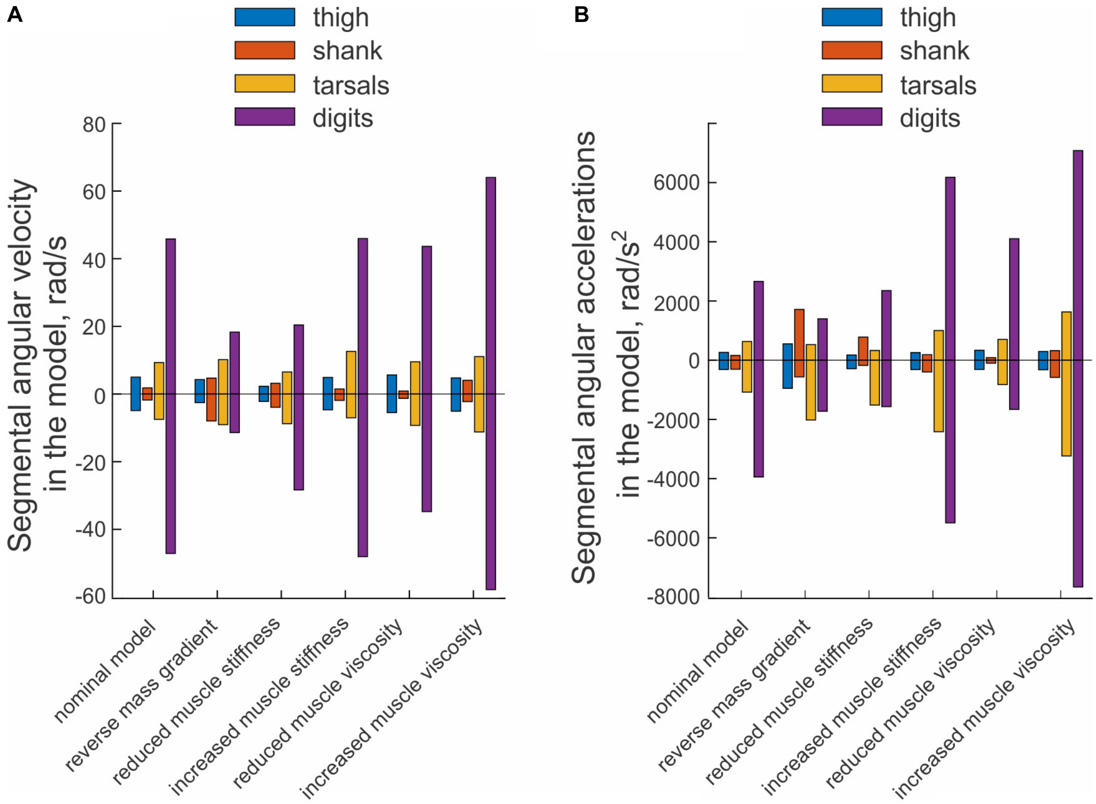

FIGURE 7 | Mean peaks of segmental angular velocity **(A)** and acceleration **(B)** computed across 10 simulated paw-shake cycles for different versions of the model. Nominal parameters of the model are listed in **Tables 3**, **4**. In model with reverse mass gradient, segmental masses were changed so that mass of hindlimb segments decreased in the distal-to-proximal direction (see **Table 2**). In model with reduced and increased muscle stiffness, stiffness of muscle parallel and series elements was reduced and increased by 20% from the nominal values, respectively (see **Table 4**). In model with reduced and increased muscle viscosity, viscocity of muscle contractile element was reduced and increased from the nominal values by 90%, respectively (see **Table 4**).

energy by themselves. However, these muscles produced passive forces as a function of muscle length and stretch velocity. As seen in **Figure 8A** (right panel), muscle moments applied to the shank, tarsals and digits absorbed energy and thus decreased energy of these segments. The joint forces applied to the shank, tarsals and digits increase their energy (**Figure 8A**, left panel). In fact, the total energy gain of these segments corresponded to the energy loss of the thigh through the action of the joint forces since the muscle moments did not generate energy. The increase of shank energy was relatively small because most of energy received by the shank from the thigh was delivered to the tarsals through the ankle joint force. The tarsals in turn transferred about half of energy received from the shank to the digits (**Figure 8A**, left panel).

The energy changes of hindlimb segments per cycle of simulated paw shaking likewise show that energy of the thigh was increased by muscle moments at the hip (11.5 mJ), while muscle moments decreased energy of the more distal tarsals (−5.7 mJ) and digits (−4.6 mJ); energy of the shank did not change substantially (–0.5 mJ; **Figure 9A**, right panel). Energy loss in the thigh and energy gain in the tarsals and digits due to joint forces were opposite to the energy gain and loss due to muscle moments. Correspondingly, energy of the shank increased little (1.0 mJ) because almost all energy it received from the thigh (11.4 mJ) was transferred to the tarsals (5.9 mJ) and digits (4.8 mJ); **Figure 9A**, left panel; see also **Data Sheet 2** in **Supplementary Material**.

Comparisons between the sum of all powers delivered to each segment by the joint forces and muscle moments ($\dot{E}_s$, Eq. 3) and the rate of change of the total energy of each segment ($\dot{E}_s'$, Eq. 4) demonstrated a perfect match (**Figure 6B**). This verifies the correctness of our segmental energy analysis.

Effects of Hindlimb Inertia Distribution and Muscle Viscoelastic Properties on Simulated Energy Transfer

The change in hindlimb mass distribution altered energy exchange among hindlimb segments. Energy generated by muscle moments applied to the thigh (**Figure 8B**, right panel) was transferred by the joint knee moment to the shank (the decrease in the thigh energy due to the knee joint force led to the increase in shank energy; **Figure 8B**, left panel). However, little energy was transferred from the shank to the tarsals and especially to the digits. For example, the digits received only 0.059 mJ of energy in the paw shake cycle out of 7.8 mJ transferred from the thigh (**Figure 9B**, left panel). The tarsals received slightly more energy per cycle (1.381 mJ; **Figures 8B**, **9B**, left panels). As a result,

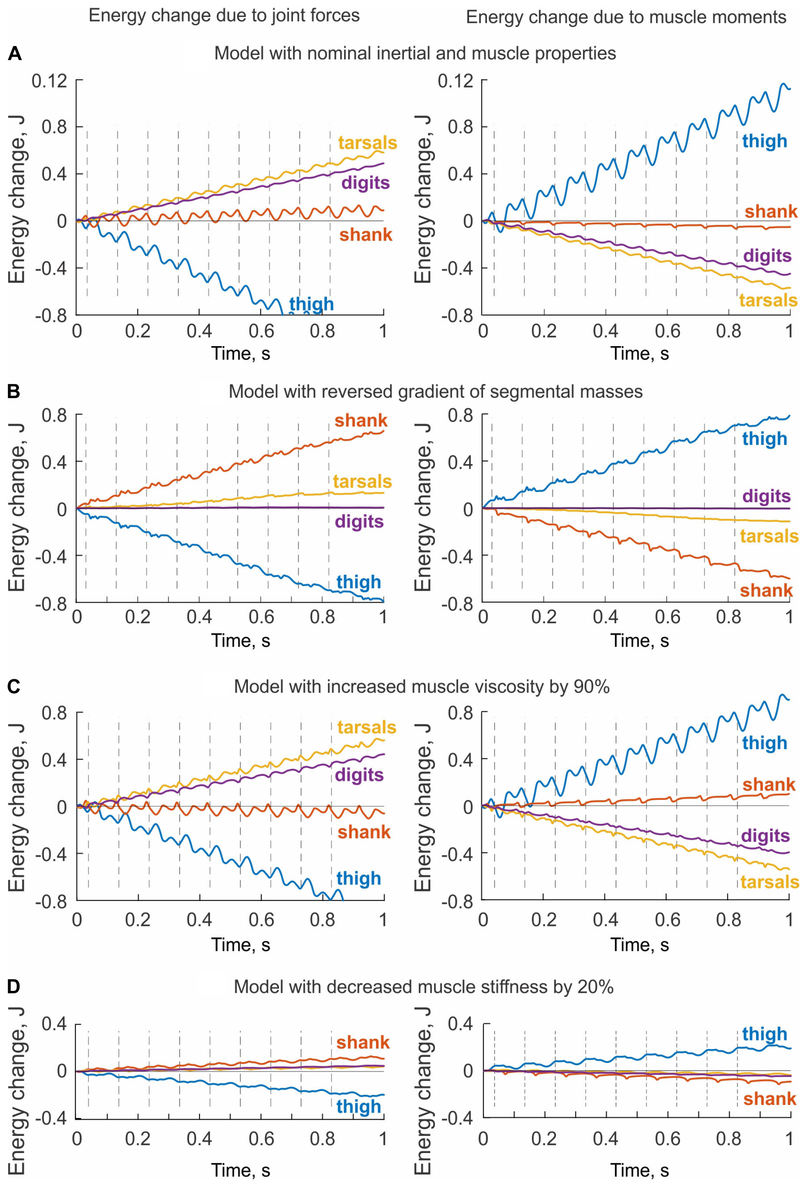

FIGURE 8 | Changes of total energy of each body segment due to the action of joint forces (left panels) and muscle moments (right panels) computed for simulated paw shaking of different versions of the model. **(A)** Model with nominal inertial and muscle properties. **(B)** Model with reverse gradient of segmental masses (**Table 3**). **(C)** Model with increased muscle viscosity by 90% (**Table 4**). **(D)** Model with decreased muscle stiffness by 20% (**Table 4**).

there was a substantial decrease in peaks of angular velocity (by 3–4 times) and acceleration (by over 2 times) of the digits compared to simulations with the nominal segmental masses, and the proximal-to-distal gradient almost disappeared, especially for accelerations (**Figure 7**).

We also investigated the effect of muscle elastic properties (stiffness of the parallel and series elastic elements, **Table 4**) on the whip-like mechanism in the model because elasticity was shown to play a role in transmission of whip waves (McMillen and Goriely, 2003) and because in our model, distal hindlimb muscles develop passive length-dependent forces. We changed the nominal stiffness values of all muscles in the model by ± 20% and conducted simulations with the same neural inputs to motoneurons of hip muscles IP and BFA. The decrease in stiffness increased the joint angle magnitudes and led to a slight overextension at the knee by about 20°. Simulations with increased muscle stiffness demonstrated anatomically realistic ranges of motion, i.e., without knee overextension. We did not increase the range of stiffness changes further to keep the changes symmetric and simulations anatomically realistic. Examples of segmental energy changes with decreased muscle stiffness are shown in **Figure 8D**). Energy delivered to the thigh by muscle moments during simulated paw shaking were much smaller than in the model with nominal stiffness. This was caused by

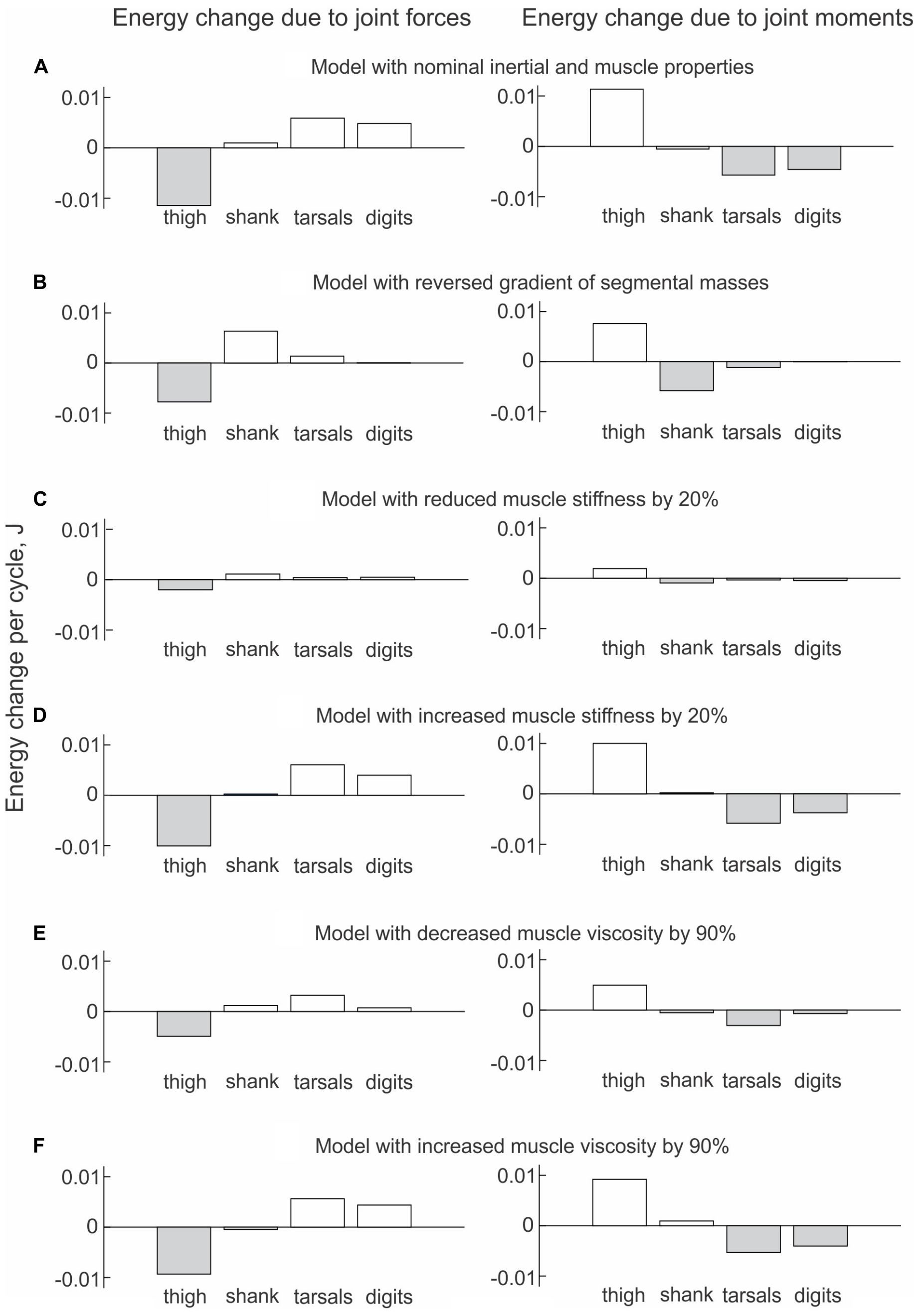

FIGURE 9 | Mean energy change of each hindlimb segment per cycle of simulated paw shaking due to the action of joint forces (left panels) and muscle moments (right panels) computed across 10 cycles of paw-shake simulations performed for different versions of the model. **(A)** Model with nominal inertial and muscle properties. **(B)** Model with reversed gradient of segmental masses. **(C)** Model with reduced stiffness of the parallel and series elastic elements of each muscle by 20%. **(D)** Model with increased stiffness of the parallel and series elastic elements of each muscle by 20%. **(E)** Model with reduced viscosity of the contractile element of each muscle by 90%. **(F)** Model with increased viscosity of the contractile element of each muscle by 90%.

smaller tendon forces due to much more compliant tendon of the hip muscles (not shown). Energy transfer from the thigh to the distal segments were minimal (2 mJ; **Figures 8D**, **9C**, left panels) due to low forces of the distal muscles. The changes in energy generation and transfer with reduced stiffness were also reflected in a reduced angular velocity and acceleration of the digits compared to the nominal model (**Figure 7**). The increase in muscle stiffness by 20% resulted in paw shake simulations similar to those of the nominal model. Specifically, there was comparable supply and absorption of segmental energy per cycle by the muscle moments and energy transfer from the thigh to the tarsals and digits by the joint forces in the two simulations

(**Figure 9D**). In addition, the two simulations had comparable proximal-to-distal gradients of segmental angular velocities and accelerations (**Figure 7**).

Since muscle force development and energy absorption in the model depend on muscle viscosity, we also investigated effects of muscle viscosity on the whip-like mechanism. The model was less sensitive to changes in muscle viscosity, so we conducted simulations with viscosity changed by ± 90% from its nominal values in all muscles (**Table 4**). Segmental energy changes in simulated paw shaking with increased muscle viscosity by 90% (**Figure 8C**) were comparable to the changes in the model with nominal parameters (**Figure 8A**). For example, the difference in energy changes due to joint forces in the thigh, shank, tarsals and digits were 2.1 mJ (18% of the nominal model), 0.51 mJ (52%), 0.20 mJ (3%), and 0.43 mJ (9%), respectively. The corresponding values for segmental energy changes due to joint moments were 2.15 mJ (19%), 0.42 mJ (44%), 0.40 mJ (7%), and 0.53 mJ (12%), respectively. One noticeable difference was that muscle moments supplied small amount of energy to the shank (the change of energy per cycle is positive compared with a negative change in the nominal simulations; compare **Figure 8A** with **Figure 8C**, **Figure 9A** with **Figure 9F**). This was caused by a slightly greater stretch velocity-depended muscle moments (quantified as the mean of moment peaks) of the knee extensors (0.035 Nm vs. 0.026 Nm) and flexors (–0.302 Nm vs. –0.249 Nm). Energy transferred by the joint forces from the thigh and shank to the tarsals and digits was about the same as in the nominal model (**Figures 8C**, **9F**). The proximal-to-distal gradient of segmental velocities and accelerations was preserved in this case with higher digits velocity and acceleration than in the nominal model (**Figure 7**). The decrease in muscle viscosity by 90% resulted in very small muscle forces, in paw shaking that was very different from the natural one, and in small energy generation, absorption and transfer per cycle (**Figure 9E**). The velocity and acceleration gradients were, however, generally preserved (**Figure 7**).

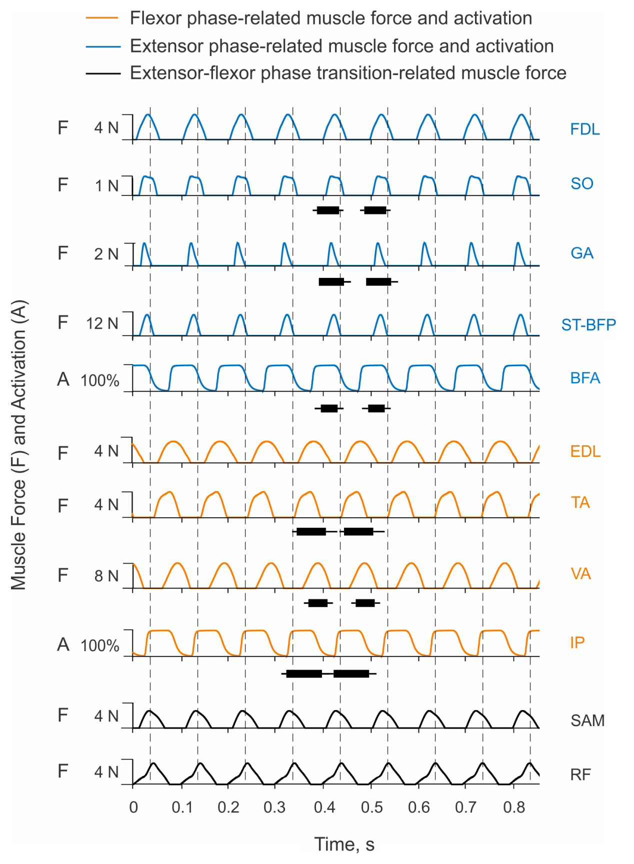

FIGURE 10 | Activation patterns of one-joint hip muscles and passive motion-depended forces of more distal hindlimb muscles during simulated paw shaking. One-joint hip flexor iliopsoas (IP) and one-joint hip extensor biceps femoris anterior (BFA) receive excitatory input from the CPG in the flexor and extensor phases, respectively; their activation (A) is shown in % of maximum activation. Passive motion-depended forces of the remaining muscles (F) are shown in N. Vertical dashed lines separate paw-shake cycles. The cycle onset is defined as the onset of the hip flexion moment (see **Figure 2**). The EMG burst durations for selected muscles are shown for 2 cycles as horizontal bars connecting the EMG burst onset and offset times measured in real paw shaking (mean ± SD, **Table 2**). To compare the simulated muscle activation and forces with the measured EMG burst durations, IP EMG burst onset was aligned with the IP simulated activation onset in a cycle. The horizontal black bars shown in two cycles are identical. For muscle abbreviation (see **Figure 1** and **Table 4**).

Muscle Coordination in Simulated Paw Shaking

Only two muscles in the model received excitatory input from the CPG, hip flexor IP and hip extensor BFA. Their simulated activation was reciprocal with little overlap at the cycle onset (the extensor-flexor phase transition at the onset of hip flexion moment) and at mid-cycle (the flexor-extensor phase transition at the onset of hip extensor moment; **Figure 10**). Onset of the simulated hip flexion moment (paw shake cycle onset, indicated by vertical dashed lines in **Figure 10**) occurred with a delay of 14 ms after onset of simulated IP activation. Onset of the hip extension moment occurred in the middle of the cycle, 16 ms after BFA activation onset. By model design (see section "Materials and Methods"), the other hindlimb muscles did not receive neural input. They produced passive viscoelastic force (**Figure 10**) as a function of the muscle length and stretch velocity (not shown but can be inferred from the joint angles and velocities in **Figure 2B**). For example, the ankle flexor TA developed passive force in the first half of the cycle (**Figure 10**) when the hip moment is flexion and ankle is extending (**Figure 2B**), i.e., when TA is lengthening. The MTP flexor EDL likewise produced force in the first half of the cycle, although its force production lasted slightly longer since the maximal length of this muscle (or MTP extension angle) in the cycle was reached slightly later than in TA (the TA peak length occurs at peak of the ankle extension; **Figure 2B**). The knee extensor VA produced force almost in phase with the MPT flexor EDL and ankle flexor TA, although the onset of VA force production was delayed compared to all other flexors (by 10–17 ms, **Figure 10**). The VA passive force production coincided with the knee flexion phase (**Figure 2B**), during which VA was lengthening. In simulations, the hip extensor BFA was activated in the second half of the paw-shake cycle (**Figure 10**). The force development of the MTP and ankle extensors (FDL, SO, GA) and of a two-joint hip extensor-knee flexor ST-BFP occurred in the last 30–40% of the cycle (**Figure 10**) in phase with lengthening of these muscles (or extension of the knee and flexion of the ankle and MTP joints; **Figure 2B**). Proximal two-joint muscles SAM (hip and knee flexor) and RF (hip flexor and knee extensor) produced their peak forces close to the extensor-flexor phase transition (**Figure 10**) when the hip and knee joints were extending and their angular velocities reached the maximum values (**Figure 2B**).

Despite simplicity of the hindlimb neuromechanical model, in which only hip one-joint muscles produced active muscle force and generated mechanical energy while the other muscles produced passive length- and stretch velocity-depended forces, the time of simulated force development was generally consistent with periods of EMG bursts recorded in selected muscles during real paw shaking. For example, anterior hindlimb muscles that accelerate the hindlimb forward (flexors IP, TA, EDL and extensor VA) produced force in the first half of the cycle when the EMG bursts of IP, TA and VA occurred in real paw shaking (**Figure 10** and **Table 2**). Ankle extensors (SO and GA) and hip extensor BFA produced their EMG bursts in the second half of the cycle in phase with the simulated forces or activation of these muscles. These muscles also demonstrated reciprocal EMG activity with and shorter EMG burst durations than the corresponding ankle and hip flexors (TA and IP; **Figure 10** and **Table 2**). Specifically, the EMG burst durations of extensors SO, GA and BFA were 46.3 ± 13.9 ms, 52.8 ± 14.6 ms and 35.1 ± 17.1 ms, respectively. These values were significantly shorter than the EMG burst durations of flexors TA (61.7 ± 16.5 ms) and IP (74.8 ± 16.1 ms); [$F(5, 305) = 33.8$, $p < 0.014$]. The durations of the simulated force development by extensors FDL, SO, GA and ST-BFP and flexors EDL and TA had similar trends (24 ms–38 ms vs. 55 ms–69 ms, respectively, **Figure 10**). Interestingly, the knee extensor VA demonstrated a greater co-activation with flexors TA and IP (EMG burst overlaps were 42 and 34 ms, respectively) than with extensors SO, GA and BFA (overlap between 8 and 12 ms), resembling the corresponding simulated force patterns (**Figure 10**).

DISCUSSION

Study Goals and Hypotheses

One goal of the study was to examine if paw shaking in cats is organized as a whip-like movement, in which energy generated by larger proximal muscles is transferred to distal segments by joint forces; for review see Zatsiorsky (2002). This whip-like mechanism has been suggested to contribute to developing high velocities of the distal segments of the arm and leg during fast throwing and kicking movements in humans (Putnam, 1991; Hirashima et al., 2003) and knee extension during the swing phase of locomotion in cats and humans (Chapman and Caldwell, 1983; Martin and Cavanagh, 1990; Wisleder et al., 1990). We confirmed and expended to the digits previous reports (Hoy et al., 1985; Hoy and Zernicke, 1986) demonstrating the proximal-to-distal gradient of segmental angular velocities and accelerations during cat paw shaking. We showed for the first time that during paw shaking, energy delivered to hindlimb segments proximal to the digits by muscle moments was transferred to the digits by the joint forces.

The second goal was to develop a simplified neuromechanical model of a cat hindlimb with a half-center CPG, activating hip flexor and extensor muscles, and passive viscoelastic distal muscles. We also investigated if this model could reproduce whip-like paw shake movements, i.e., the proximal-to-distal gradient of segmental angular velocities and accelerations, as well as energy generation and absorption by muscle moments and energy transfer in the proximal-to-distal direction by the joint forces. We found that this model was able to reproduce the above features of the whip-like motion. In addition, we demonstrated that the mass distribution along the hindlimb and muscle stiffness had major effects on the generation of high angular velocity and acceleration of the digits during paw shaking and on the transfer of energy to the digits.

Whip-Like Mechanism

The term whip-like motion has been used in biomechanics and neural control of movement to describe motion of multi-segmented open kinematic chains of upper and lower extremities, the goal of which is to develop a high linear or angular velocity of the last segment of the kinematic chain; see for example (Zatsiorsky, 2002). The progressively increasing angular velocity of more distal segments in this motion has been explained in part by the action of joint force applied at the proximal joint of distal segments that creates a moment of force with respect to the center of mass of the distal segment and increases its the angular acceleration and velocity (Chapman and Caldwell, 1983; Martin and Cavanagh, 1990; Putnam, 1993; Zatsiorsky, 2002).

Experimental studies and theoretical analyses of propagation of whip waves along real whips demonstrated that the reduction of the cross-sectional area and mass of the whip in the proximal-to-distal direction is an important factor in increasing the whip tip velocity above the speed barrier and achieving translational accelerations of 50,000 times greater than the acceleration of gravity (Krehl et al., 1998; McMillen and Goriely, 2003). This result is explained by the laws of conservation of energy and momentum. The energy and momentum imparted to the whip at the handle travels as a whip wave along the whip, and the decrease in mass along the whip must increase the speed of the traveling wave, given constancy of the momentum. Although the mechanism of velocity enhancement along a real whip is likely different from the whip-like mechanism of energy transfer in kinematic chains, these two mechanisms appear to shear some common features. Efficiency of energy transfer and enhancement of velocity in the whip and in the cat hindlimb model depends on mass distribution along the length of the two systems and on their elastic properties.

The cat hindlimb inertia and muscle mass and volume also decrease in the proximal-to-distal direction (Sacks and Roy, 1982; Hoy and Zernicke, 1985), as reflected in mass of body segments of our model (**Table 3**). This mass distribution in the hindlimb not only enhances angular velocity and acceleration of the digits in our simulated paw shaking, it also decreases hindlimb inertia with respect to the hip joint and thus reduces energy expenditure during the swing phase of locomotion (e.g., Martin, 1985). This cat hindlimb inertia and muscle volume distribution is also observed in the forelimbs of cats (Hoy and Zernicke, 1985; Martin et al., 2010) and in human arms (Zatsiorsky, 2002; Holzbaur et al., 2007). The greater ability of larger proximal muscles to generate mechanical energy for movement may also explain a typical organization of arm reaching movements. Largest muscles around proximal (leading) joints generate muscle moments that drive the arm toward the target, while muscle moments at the distal (trailing) joints counter the interaction motion-dependent moments (Sainburg et al., 1999; Dounskaia, 2010). This joint coordination strategy was suggested to reduce the number of control variables, simplify neural control of reaching and minimize neural effort for joint coordination (Dounskaia and Shimansky, 2016).

Our paw-shake simulations with changed muscle viscoelasticity of distal hindlimb muscles suggested an important role of this muscle property in muscle and inter-joint coordination and efficient energy transfer along the hindlimb. This result is consistent with previous studies demonstrating the importance of limb stiffness regulation in various postural and movement tasks (Mussa-Ivaldi et al., 1985; Nichols et al., 1999; Frolov et al., 2006). This regulation is primarily mediated by muscle length and force-depended spinal reflexes (Eccles et al., 1957a,b; Fritz et al., 1989; Nichols, 2018). The length and stretch-velocity sensitive muscle spindle group Ia afferents from the triceps surae and hamstrings muscles demonstrate extremely high firing rates during cat paw shaking (Prochazka et al., 1989). This afferent activity occurs in phase with stretch and EMG burst of these muscles, indicating that these muscles absorb energy of the flexing tarsals and extending shank and slow them down, as we observed in our simulations (**Figures 8A**, **9A**). In real paw shaking, we observed energy absorption by muscle moments of only the most distal segment, the tarsals (**Figures 4D**, **5B**). This is because energy received by the shank and tarsals from the action of joint forces and muscle moments exceeded energy transported from them to the digits. Thus, it appears that length- and stretch velocity-depended feedback from distal segments help regulate the proper timing of muscle activity to coordinate inter-joint coordination that allows for efficient energy transfer and absorption. The role of this motion-depended feedback in distal muscles of our simulation model played their passive viscoelastic properties, i.e., the dependence of muscle force on muscle length and stretch velocity. In fact, timing of forces produced by the passive muscles during simulated paw shaking were remarkably similar to the periods of EMG bursts of selected muscles during real paw shaking in this (**Figures 2A**, **10**) and other studies (Smith et al., 1985). This similarity includes the atypical co-activation between ankle and hip flexors TA and IP and knee extensor VA. In the model, the VA force generation is caused by VA elongation during limb forward acceleration due to activation of IP. During real paw shaking, length-depended feedback from elongating VA can also contribute to the VA EMG burst in phase with flexors, although other factors including central commands are also likely to contribute. EMG bursts of VA during real paw shaking is more variable than in other muscles, with bursts missing occasionally or consisting of two parts—in phase with flexors and in phase with extensors (see Figure 3 in Smith et al., 1985). Double activity bursts in the VA nerve spanning the flexor and extensor phases were also reported in fictive paw-shake-like activity, i.e., without motion-depended feedback (Pearson and Rossignol, 1991). This suggests that central inputs from spinal CPG contribute to EMG activity of VA in real paw shaking. CPG is likely to contribute substantially to EMG activity of other hindlimb flexors and extensors, since they produce activity bursts in the corresponding flexor and extensor phases defined by the direction of the flexion and extension muscle moments (**Figures 2A**, **10**). Additional evidence for substantial contributions of central inputs to the EMG magnitude of ankle extensors was provided in Mehta and Prilutsky (2014); in that study removal of stretch reflex from these muscles by muscle self-reinnervation had no effect on their EMG burst timing and relative magnitude.

Possible Organization of Neural Control of Paw Shaking

Since joint kinematics and kinetics, inter-joint coordination, and EMG activity patterns (with co-activation of TA and VA) of cat paw shaking appeared drastically different from those of cat locomotion (Hoy et al., 1985; Smith et al., 1985, 1998; Carter and Smith, 1986; Hoy and Zernicke, 1986; Koshland and Smith, 1989; Prochazka et al., 1989), it has been suggested that paw shaking is controlled by a substantially reconfigured locomotor unit-burst CPG (Carter and Smith, 1986). In addition, motion-depended sensory feedback was suggested to affect primarily EMG activity of the knee extensor VA and ankle flexor TA, but not other muscles, because hindlimb deafferentation or limb casting led to changes in their EMG burst onsets and offsets (Smith and Zernicke, 1987; Koshland and Smith, 1989). The organization of the mammalian CPG controlling rhythmic behaviors, such as different forms of locomotion, scratching, and paw shaking, is not fully understood. Although many researchers agree that some common elements of the CPG network can be used to control different rhythmic movements, there is an ongoing debate about whether the spinal CPG has a single-level or a multi-level architecture (McCrea and Rybak, 2008; McLean and Dougherty, 2015; Ausborn et al., 2021; Grillner and Kozlov, 2021; Klishko et al., 2021). In the former, unit-bursts generators do not receive common flexor- and extensor-related rhythmic inputs and can be flexibly reorganized by sensory and/or central inputs to meet mechanical demands of various motor behaviors (Grillner, 1981; Carter and Smith, 1986; Grillner and Kozlov, 2021). In the latter, a top half-center CPG layer sets a common rhythm and phase for all flexor and extensor last order interneurons controlling motoneuronal activities of flexors and extensors, and a lower CPG layer can adjust the duration and magnitude of flexor and extensor activity of the corresponding motoneurons based on sensory and/or central inputs without necessarily changing the rhythm, the so-called non-resetting effects (McCrea and Rybak, 2008). Our previous study (Bondy et al., 2016) demonstrated that even a classic single-level half-center CPG organization (Brown, 1911, 1914) in combination with specifically organized motion-dependent feedback could reasonably predict basic features of mechanics and muscle activity of walking and paw shaking. The current study extended previous results to demonstrate that a simple half-center CPG, controlling activity of hip flexors and extensors, with autogenic length and stretch-velocity feedback controlling force production in more distal muscles, can provide a proper inter-joint and muscle coordination for energy generation and transfer to the digits and for providing the proximal-to-distal gradient of segmental angular velocities and accelerations during paw shaking. The proper coordination appears to emerge from interactions between the half-center CPG, inertial properties of hindlimb segments, and muscle length and stretch-velocity feedback. The neural control of paw shaking seems well adjusted to the natural passive dynamics of the hindlimb and thus requires minimal intervention. Similar well-adjusted interactions between natural dynamics of the musculoskeletal system and neural control have been proposed based on demonstrations of human-like walking in a passive physical model (McGeer, 1990) and swimming of a dead fish against the flow (Beal et al., 2006). Future studies will need to reconcile the current and previous findings suggesting the importance of length feedback for regulation of activity of ankle and knee muscles during paw shaking (Koshland and Smith, 1989; Prochazka et al., 1989; Bondy et al., 2016) with the fact that removal of monosynaptic length feedback from ankle extensors by muscle self-reinnervation does not affect their activity patterns in paw shaking (Mehta and Prilutsky, 2014).

Limitations of the Study

We noticed substantial differences between the rate of the total energy of hindlimb segments (Eq. 4) and the sum of powers of the joint forces and muscle moments applied to these segments (Eq. 3); **Figure 6A**. These mechanical variables must be identical in accordance with the law of conservation of energy. Our inverse dynamics analysis and computer code were correct since we used the same code to compute these variables for the model and obtained a perfect match (**Figure 6B**). The differences between the real and simulated paw shaking are that the latter is strictly planar and produced by a model composed of ideal rigid segments interconnected by frictionless hinge joints with fixed location and orientation of joint axes. To perform inverse dynamics analysis of real paw shaking we assumed constant segment lengths and inertial properties and constant position and orientation of the rotation axis at each joint. These assumptions seem justified for the cat as the body COM acceleration computed from kinematics of a walking cat was similar to the COM acceleration obtained from the recorded ground reaction forces (Manter, 1938). However, real paw shaking was not fully planar. As explained in Methods, we discarded paw shakes in which the thigh was abducted-adducted by more than ∼25°. Still, in the retained cycles, there were instantaneous deviations from the sagittal plane, which could potentially explain the observed differences between the rate of total energy changes and the total power for the segments, although the exact reason for this offset is unclear. Another source of observed differences, especially in the ranges between maximal and minimal values of the two variables, could be small random errors in digitized marker coordinates magnified by the numerical differentiation, e.g., Winter (2004). This explanation is consistent with greater peak values of the total segmental total power, which requires more numerical differentiation (e.g., computing second time derivatives of linear and angular accelerations for obtaining joint forces and muscle moments) than for computations of the rate of energy change. Given the similar proximal-to-distal direction of energy flow in the real and simulated paw shakes (**Figures 4**, **5**, **8A**, **9A**), the described discrepancies do not appear to affect our major conclusions.

Another limitation of the study was that our paw-shake simulations did not fully match the real paw shaking. The largest discrepancies of simulated paw shaking were in the in-phase changes of knee and hip angles and velocities and in the small knee extension moment (**Figure 2**). We expected that our simplified version of a more complex previous model (Bondy et al., 2016) would not reproduce precisely all aspects of real paw shaking. In the simplified model, we removed CPG input to all but two hip muscles and eliminated muscle spindle length-depended excitation to all hindlimb muscle motoneurons, except for IP and BFA. The force production in the passive viscoelastic distal muscles of this model depended on muscle length and stretch velocity. This was done to make the hindlimb model and paw-shake simulations more similar to a whip and to the process of energy generation at the proximal end of the whip and to the velocity enhancement along the whip length. Despite the mentioned discrepancies, the model clearly reproduced the energy generation, transfer and absorption (compare **Figures 4C,D**, **5** with **Figures 8A**, **9A**), the proximal-to-distal gradient of segmental angular velocity and acceleration (compare **Figure 3** with **Figure 7**), and timing of muscle force production in selected muscles (**Figures 2**, **10**).

DATA AVAILABILITY STATEMENT

The original contributions presented in the study are included in the article/**Supplementary Material**, further inquiries can be directed to the corresponding author.

ETHICS STATEMENT

The animal study was reviewed and approved by the Institutional Animal Care and Use Committee of Georgia Institute of Technology.

AUTHOR CONTRIBUTIONS

BP conceived and designed the study, carried out the experiments, data analysis and model development, and drafted the manuscript. JP helped with data analysis and model development, and critically revised the manuscript. GC helped with conceiving and designing the study, carried out model development, and critically revised the manuscript. AK helped with conceiving and designing the study, carried out the experiments, data analysis and model development, and critically revised the manuscript. All authors contributed to the article and approved the submitted version.

FUNDING

This work was supported by the NIH (grants NS110550 and NS100928) to BP, NIH (grant NS111355) to GC, and the Georgia State University Brains and Behavior Fellowship to JP.

ACKNOWLEDGMENTS

We would like to thank Ricky Mehta-Desai for help with data collection.

SUPPLEMENTARY MATERIAL

The Supplementary Material for this article can be found online at: https://www.frontiersin.org/articles/10.3389/fnint.2022.810139/full#supplementary-material

REFERENCES

Abraham, L. D., and Loeb, G. E. (1985). The distal hindlimb musculature of the cat. Patterns of normal use. *Exp. Brain Res.* 58, 583–593.

Aleshinsky, S. Y. (1986). An energy 'sources' and 'fractions' approach to the mechanical energy expenditure problem–I. Basic concepts, description of the model, analysis of a one-link system movement. *J. Biomech.* 19, 287–293. doi: 10.1016/0021-9290(86)90003-5

Ausborn, J., Shevtsova, N. A., and Danner, S. M. (2021). Computational Modeling of spinal locomotor circuitry in the age of molecular genetics. *Int. J. Mol. Sci.* 22:6835. doi: 10.3390/ijms22136835

Baratta, R. V., Solomonow, M., Best, R., Zembo, M., and D'Ambrosia, R. (1995). Architecture-based force-velocity models of load-moving skeletal muscles. *Clin. Biomech. (Bristol, Avon)* 10, 149–155. doi: 10.1016/0268-0033(95)93705-x

Beal, D. N., Hover, F. S., Triantafyllou, M. S., Liao, J. C., and Lauder, G. V. (2006). Passive propulsion in vortex wakes. *J. Fluid Mech.* 549, 385–402.

Bernstein, N. A. (1940). *Studies of the Biodynamics of Walking, Running and Jumping*. Moscow: Central Research Institute of Physical Culture.

Bondy, B., Klishko, A. N., Edwards, D. H., Prilutsky, B. I., and Cymbalyuk, G. (2016). "Control of cat walking and paw-shake by a multifunctional central pattern generator," in *Neuromechanical Modeling of Posture and Locomotion*, eds B. I. Prilutsky and D. H. Edwards (New York, NY: Springer), 333–359.

Boyd, S. K., and Ronsky, J. L. (1998). Instantaneous moment arm determination of the cat knee. *J. Biomech.* 31, 279–283. doi: 10.1016/s0021-9290(97)00135-8

Brown, I. E., Liinamaa, T. L., and Loeb, G. E. (1996). Relationships between range of motion, lo, and passive force in five strap-like muscles of the feline hind limb. *J. Morphol.* 230, 69–77. doi: 10.1002/(SICI)1097-4687(199610)230:1<69::AID-JMOR6>3.0.CO;2-I

Brown, T. G. (1911). The intrinsic factors in the act of progression in the mammal. *Proc. R. Soc. B* 84, 308–319. doi: 10.1016/0301-0082(96)00028-7

Brown, T. G. (1914). On the nature of the fundamental activity of the nervous centres; together with an analysis of the conditioning of rhythmic activity in progression, and a theory of the evolution of function in the nervous system. *J. Physiol.* 48, 18–46. doi: 10.1113/jphysiol.1914.sp001646

Burkholder, T. J., and Nichols, T. R. (2004). Three-dimensional model of the feline hindlimb. *J. Morphol.* 261, 118–129. doi: 10.1002/jmor.10233

Carter, M. C., and Smith, J. L. (1986). Simultaneous control of two rhythmical behaviors. II. Hindlimb walking with paw-shake response in spinal cat. *J. Neurophysiol.* 56, 184–195. doi: 10.1152/jn.1986.56.1.184

Chapman, A. E., and Caldwell, G. E. (1983). Factors determining changes in lower limb energy during swing in treadmill running. *J. Biomech.* 16, 69–77. doi: 10.1016/0021-9290(83)90047-7

Cofer, D., Cymbalyuk, G., Reid, J., Zhu, Y., Heitler, W. J., and Edwards, D. H. (2010). AnimatLab: a 3D graphics environment for neuromechanical simulations. *J. Neurosci. Methods* 187, 280–288. doi: 10.1016/j.jneumeth.2010.01.005

Dounskaia, N. (2010). Control of human limb movements: the leading joint hypothesis and its practical applications. *Exerc. Sport Sci. Rev.* 38, 201–208. doi: 10.1097/JES.0b013e3181f45194

Dounskaia, N., and Shimansky, Y. (2016). Strategy of arm movement control is determined by minimization of neural effort for joint coordination. *Exp. Brain Res.* 234, 1335–1350. doi: 10.1007/s00221-016-4610-z

Eccles, J. C., Eccles, R. M., and Lundberg, A. (1957a). The convergence of monosynaptic excitatory afferents on to many different species of alpha motoneurones. *J. Physiol.* 137, 22–50. doi: 10.1113/jphysiol.1957.sp005794

Eccles, J. C., Eccles, R. M., and Lundberg, A. (1957b). Synaptic actions on motoneurones caused by impulses in Golgi tendon organ afferents. *J. Physiol.* 138, 227–252. doi: 10.1113/jphysiol.1957.sp005849

Farrell, B. J., Bulgakova, M. A., Beloozerova, I. N., Sirota, M. G., and Prilutsky, B. I. (2014). Body stability and muscle and motor cortex activity during walking with wide stance. *J. Neurophysiol.* 112, 504–524. doi: 10.1152/jn.00064.2014

Fowler, E. G., Gregor, R. J., and Roy, R. R. (1988). Differential kinetics of fast and slow ankle extensors during the paw-shake in the cat. *Exp. Neurol.* 99, 219–224. doi: 10.1016/0014-4886(88)90141-0

Fritz, N., Illert, M., De La Motte, S., Reeh, P., and Saggau, P. (1989). Pattern of monosynaptic Ia connections in the cat forelimb. *J. Physiol.* 419, 321–351. doi: 10.1113/jphysiol.1989.sp017875

Frolov, A. A., Prokopenko, R. A., Dufosse, M., and Ouezdou, F. B. (2006). Adjustment of the human arm viscoelastic properties to the direction of reaching. *Biol. Cybern.* 94, 97–109. doi: 10.1007/s00422-005-0018-8

Goslow, G. E. Jr., Cameron, W. E., and Stuart, D. G. (1977). Ankle flexor muscles in the cat: length-active tension and muscle unit properties as related to locomotion. *J. Morphol.* 153, 23–37. doi: 10.1002/jmor.1051530103

Goslow, G. E. Jr., Reinking, R. M., and Stuart, D. G. (1973). The cat step cycle: hind limb joint angles and muscle lengths during unrestrained locomotion. *J. Morphol.* 141, 1–41. doi: 10.1002/jmor.1051410102

Gregor, R. J., Maas, H., Bulgakova, M. A., Oliver, A., English, A. W., and Prilutsky, B. I. (2018). Time course of functional recovery during the first 3 mo after surgical transection and repair of nerves to the feline soleus and lateral gastrocnemius muscles. *J. Neurophysiol.* 119, 1166–1185. doi: 10.1152/jn.00661.2017

Grillner, S. (1981). "Control of locomotion in bipeds, tetrapods, and fish," in *Handbook of Physiology. Section I. The Nervous System*, ed. V. Brooks (Bethesda, MD: American Physiological Society), 1179–1236. doi: 10.1126/science.1245629

Grillner, S., and Kozlov, A. (2021). The CPGs for limbed locomotion-facts and fiction. *Int. J. Mol. Sci.* 22:5882. doi: 10.3390/ijms22115882

Herzog, W., Leonard, T. R., Renaud, J. M., Wallace, J., Chaki, G., and Bornemisza, S. (1992). Force-length properties and functional demands of cat gastrocnemius, soleus and plantaris muscles. *J. Biomech.* 25, 1329–1335. doi: 10.1016/0021-9290(92)90288-c

Hirashima, M., Kudo, K., and Ohtsuki, T. (2003). Utilization and compensation of interaction torques during ball-throwing movements. *J. Neurophysiol.* 89, 1784–1796. doi: 10.1152/jn.00674.2002

Hodson-Tole, E. F., Pantall, A. L., Maas, H., Farrell, B. J., Gregor, R. J., and Prilutsky, B. I. (2012). Task dependent activity of motor unit populations in feline ankle extensor muscles. *J. Exp. Biol.* 215, 3711–3722. doi: 10.1242/jeb.068601

Holzbaur, K. R., Murray, W. M., Gold, G. E., and Delp, S. L. (2007). Upper limb muscle volumes in adult subjects. *J. Biomech.* 40, 742–749. doi: 10.1016/j.jbiomech.2006.11.011

Hoy, M. G., and Zernicke, R. F. (1985). Modulation of limb dynamics in the swing phase of locomotion. *J. Biomech.* 18, 49–60. doi: 10.1016/0021-9290(85)90044-2

Hoy, M. G., and Zernicke, R. F. (1986). The role of intersegmental dynamics during rapid limb oscillations. *J. Biomech.* 19, 867–877. doi: 10.1016/0021-9290(86)90137-5

Hoy, M. G., Zernicke, R. F., and Smith, J. L. (1985). Contrasting roles of inertial and muscle moments at knee and ankle during paw-shake response. *J. Neurophysiol.* 54, 1282–1294. doi: 10.1152/jn.1985.54.5.1282

Klishko, A. N., Akyildiz, A., Mehta-Desai, R., and Prilutsky, B. I. (2021). Common and distinct muscle synergies during level and slope locomotion in the cat. *J. Neurophysiol.* 126, 493–515. doi: 10.1152/jn.00310.2020

Koshland, G. F., and Smith, J. L. (1989). Mutable and immutable features of paw-shake responses after hindlimb deafferentation in the cat. *J. Neurophysiol.* 62, 162–173. doi: 10.1152/jn.1989.62.1.162

Krehl, P., Engemann, S., and Schwenkel, D. (1998). The puzzle of whip cracking – uncovered by a correlation of whip-tip kinematics with shock wave emission. *Shock Waves* 8, 1–9.

Maas, H., Gregor, R. J., Hodson-Tole, E. F., Farrell, B. J., English, A. W., and Prilutsky, B. I. (2010). Locomotor changes in length and EMG activity of feline medial gastrocnemius muscle following paralysis of two synergists. *Exp. Brain Res.* 203, 681–692. doi: 10.1007/s00221-010-2279-2

MacFadden, L. N., and Brown, N. A. (2007). Biarticular hip extensor and knee flexor muscle moment arms of the feline hindlimb. *J. Biomech.* 40, 3448–3457. doi: 10.1016/j.jbiomech.2007.05.021

Manter, J. T. (1938). The dynamics of quadrupedal walking. *J. Exp. Biol.* 15, 522–540. doi: 10.1242/jeb.15.4.522

Martin, P. E. (1985). Mechanical and physiological responses to lower extremity loading during running. *Med. Sci. Sports Exerc.* 17, 427–433. doi: 10.1249/00005768-198508000-00004

Martin, P. E., and Cavanagh, P. R. (1990). Segment interactions within the swing leg during unloaded and loaded running. *J. Biomech.* 23, 529–536. doi: 10.1016/0021-9290(90)90046-6

Martin, R., Tan, C., Burkholder, T. J., and Nichols, T. R. (2010). "Construction of a musculoskeletal model of the cat forelimb. Abstract 381.19," in *Proceedings of the Society for Neuroscience Meeting*. San Diego, CA: Society for Neuroscience. Online).

McCrea, D. A., and Rybak, I. A. (2008). Organization of mammalian locomotor rhythm and pattern generation. *Brain Res. Rev.* 57, 134–146. doi: 10.1016/j.brainresrev.2007.08.006

McGeer, T. (1990). Passive dynamic walking. *Intern. J. Robot. Res* 9, 62–82.

McLean, D. L., and Dougherty, K. J. (2015). Peeling back the layers of locomotor control in the spinal cord. *Curr. Opin. Neurobiol.* 33, 63–70. doi: 10.1016/j.conb.2015.03.001

McMillen, T., and Goriely, A. (2003). Whip waves. *Phys. D* 184, 192–225. doi: 10.1016/s0167-2789(03)00221-5

Mehta, R., and Prilutsky, B. I. (2014). Task-dependent inhibition of slow-twitch soleus and excitation of fast-twitch gastrocnemius do not require high movement speed and velocity-dependent sensory feedback. *Front. Physiol.* 5:410. doi: 10.3389/fphys.2014.00410

Mussa-Ivaldi, F. A., Hogan, N., and Bizzi, E. (1985). Neural, mechanical, and geometric factors subserving arm posture in humans. *J. Neurosci.* 5, 2732–2743. doi: 10.1523/JNEUROSCI.05-10-02732.1985

National Research Council of the National Academies. (2011). *Guide for the Care and Use of Laboratory Animals*. Washington, DC: National Academies Press.

Nichols, T. R. (2018). Distributed force feedback in the spinal cord and the regulation of limb mechanics. *J. Neurophysiol.* 119, 1186–1200. doi: 10.1152/jn.00216.2017

Nichols, T. R., Cope, T. C., and Abelew, T. A. (1999). Rapid spinal mechanisms of motor coordination. *Exerc. Sport Sci. Rev.* 27, 255–284.

Parker, J., Bondy, B., Prilutsky, B. I., and Cymbalyuk, G. (2018). Control of transitions between locomotor-like and paw shake-like rhythms in a model of a multistable central pattern generator. *J. Neurophysiol.* 120, 1074–1089. doi: 10.1152/jn.00696.2017

Parker, J. R., Klishko, A. N., Prilutsky, B. I., and Cymbalyuk, G. S. (2021). Asymmetric and transient properties of reciprocal activity of antagonists during the paw-shake response in the cat. *PLoS Comput. Biol.* 17:e1009677. doi: 10.1371/journal.pcbi.1009677

Pearson, K. G., and Rossignol, S. (1991). Fictive motor patterns in chronic spinal cats. *J. Neurophysiol.* 66, 1874–1887. doi: 10.1152/jn.1991.66.6.1874

Phillips, S. J., Roberts, E. M., and Huang, T. C. (1983). Quantification of intersegmental reactions during rapid swing motion. *J. Biomech.* 16, 411–417. doi: 10.1016/0021-9290(83)90073-8

Prilutsky, B. I., Herzog, W., Leonard, T. R., and Allinger, T. L. (1996). Role of the muscle belly and tendon of soleus, gastrocnemius, and plantaris in mechanical energy absorption and generation during cat locomotion. *J. Biomech.* 29, 417–434. doi: 10.1016/0021-9290(95)00085-2

Prilutsky, B. I., Sirota, M. G., Gregor, R. J., and Beloozerova, I. N. (2005). Quantification of motor cortex activity and full-body biomechanics during unconstrained locomotion. *J. Neurophysiol.* 94, 2959–2969. doi: 10.1152/jn.00704.2004

Prochazka, A., Hulliger, M., Trend, P., Llewellyn, M., and Durmuller, N. (1989). Muscle afferent contribution to control of paw shakes in normal cats. *J Neurophysiol.* 61, 550–562. doi: 10.1152/jn.1989.61.3.550

Prochazka, A., Westerman, R. A., and Ziccone, S. P. (1977). Ia afferent activity during a variety of voluntary movements in the cat. *J. Physiol.* 268, 423–448. doi: 10.1113/jphysiol.1977.sp011864

Putnam, C. A. (1991). A segment interaction analysis of proximal-to-distal sequential segment motion patterns. *Med. Sci. Sports Exerc.* 23, 130–144.

Putnam, C. A. (1993). Sequential motions of body segments in striking and throwing skills: descriptions and explanations. *J. Biomech.* 26(Suppl. 1), 125–135. doi: 10.1016/0021-9290(93)90084-r

Robertson, D. G. E., and Winter, D. A. (1980). Mechanical energy generation, absorption and transfer amongst segments during walking. *J. Biomech.* 13, 845–854. doi: 10.1016/0021-9290(80)90172-4

Sacks, R. D., and Roy, R. R. (1982). Architecture of the hind limb muscles of cats: functional significance. *J. Morphol.* 173, 185–195. doi: 10.1002/jmor.1051730206

Sainburg, R. L., Ghez, C., and Kalakanis, D. (1999). Intersegmental dynamics are controlled by sequential anticipatory, error correction, and postural mechanisms. *J. Neurophysiol.* 81, 1045–1056. doi: 10.1152/jn.1999.81.3.1045

Scott, S. H., and Loeb, G. E. (1995). Mechanical properties of aponeurosis and tendon of the cat soleus muscle during whole-muscle isometric contractions. *J. Morphol.* 224, 73–86. doi: 10.1002/jmor.1052240109

Smith, J. L., Betts, B., Edgerton, V. R., and Zernicke, R. F. (1980). Rapid ankle extension during paw shakes: selective recruitment of fast ankle extensors. *J. Neurophysiol.* 43, 612–620. doi: 10.1152/jn.1980.43.3.612

Smith, J. L., Carlson-Kuhta, P., and Trank, T. V. (1998). Motor patterns for different forms of walking: cues for the locomotor central pattern generator. *Ann. N. Y. Acad. Sci.* 860, 452–455. doi: 10.1111/j.1749-6632.1998.tb09073.x

Smith, J. L., Hoy, M. G., Koshland, G. F., Phillips, D. M., and Zernicke, R. F. (1985). Intralimb coordination of the paw-shake response: a novel mixed synergy. *J. Neurophysiol.* 54, 1271–1281. doi: 10.1152/jn.1985.54.5.1271

Smith, J. L., and Zernicke, R. F. (1987). Predictions for neural control based on limb dynamics. *Trends Neurosci.* 10, 123–128.

Winter, D. A. (2004). *Biomechanics and Motor Control of Human Movement*, 3rd Edn. New York, NY: John Wiley & Sons.

Wisleder, D., Zernicke, R. F., and Smith, J. L. (1990). Speed-related changes in hindlimb intersegmental dynamics during the swing phase of cat locomotion. *Exp. Brain Res.* 79, 651–660. doi: 10.1007/BF00229333

Zatsiorsky, V. M. (2002). *Kinetics of Human Motion*. Champaign, IL: Human Kinetics.

Conflict of Interest: The authors declare that the research was conducted in the absence of any commercial or financial relationships that could be construed as a potential conflict of interest.

frontiers | Frontiers in Integrative Neuroscience

ORIGINAL RESEARCH
published: 26 April 2022
doi: 10.3389/fnint.2022.836757

Motor Unit Discharge Patterns in Response to Focal Tendon Vibration of the Lower Limb in Cats and Humans

*Christopher K. Thompson[1], Michael D. Johnson[2], Francesco Negro[3], Dario Farina[4] and C. J. Heckman[2]**

[1] *Department of Health and Rehabilitation Sciences, Temple University, Philadelphia, PA, United States,* [2] *Department of Physiology, Northwestern University, Chicago, IL, United States,* [3] *Department of Clinical and Experimental Sciences, Università degli Studi di Brescia, Brescia, Italy,* [4] *Department of Bioengineering, Imperial College London, London, United Kingdom*

High-frequency vibration of the tendon provides potent activation of Ia afferents time-locked to the stimulation frequency and provides excitatory ionotropic activation of homonymous motor pools. In cats, the evoked motor unit discharge is constrained to discharge at integer multiples of the vibration frequency, resulting in a probability of discharge that is highly punctuated. Here we quantify the robustness of this punctuated response in the cat and evaluate whether it is present in the human. Soleus electromyography (EMG) was collected from eight cats using 64 channel electrodes during three modes of motoneuron activation. First, tendon vibration parameters were modified. Second, secondary reflex inputs are applied concurrently with tendon vibration. Third, the state of the spinal cord was altered through pharmacological or surgical manipulations. Analogous surface high-density EMG was collected from the lower leg of six humans during both vibration evoked and matched volitional contractions. Array EMG signals from both the cat and human were decomposed into corresponding motor unit action potential spike trains, and the punctuation in discharge was quantified. In the cat, regardless of vibration parameters, secondary synaptic drive, and state of spinal circuitry, focal tendon vibration evoked punctuated motor unit discharge. However, in the human lower limb, the vibration-evoked contractions do not produce punctuated motor unit discharge.

Keywords: motor unit, tendon vibration, electromyogram (EMG), reflex, cat, human

OPEN ACCESS

Edited by:
Richard Nichols,
Georgia Institute of Technology, United States

Reviewed by:
Ken Muramatsu,
Kyorin University, Japan
Leonardo Gizzi,
Fraunhofer Institute for Manufacturing Engineering and Automation, Germany

****Correspondence:***
C. J. Heckman
c-heckman@northwestern.edu

Received: *15 December 2021*
Accepted: *31 March 2022*
Published: *26 April 2022*

Citation:
Thompson CK, Johnson MD, Negro F, Farina D and Heckman CJ (2022) Motor Unit Discharge Patterns in Response to Focal Tendon Vibration of the Lower Limb in Cats and Humans.
Front. Integr. Neurosci. 16:836757.
doi: 10.3389/fnint.2022.836757

INTRODUCTION

Focal vibration of the tendon is used to activate the homonymous motor pool in both animals and humans, and it results in potent activation of the muscle spindles (Brown et al., 1967). Spindles respond to vibration with a stereotypical Ia discharge, which is one-to-one with the period of the vibration frequency. For example, in the cat, vibration up to 500 Hz results in Ia afferents to discharging time-locked to the vibration frequency (Granit and Henatsch, 1956; Brown et al., 1967). In humans, Ia afferent discharge may be locked to either the vibration frequency or its subharmonics (Burke et al., 1976; Houk, 1976). These afferents activate the motoneuron pool in a one-to-all pattern, where a single Ia afferent provides excitatory monosynaptic input to nearly every motoneuron in the pool (Mendell and Henneman, 1968). At the level of the motoneuron, this induces membrane depolarization at the vibration frequency (Westbury, 1972) and can activate persistent inward currents (PIC; Lee and Heckman, 1996). As such, tendon vibration can evoke a tendon vibration reflex (TVR), where the vibration of the distal tendon can evoke motor output through activation of monosynaptic Ia afferents.

Recordings from the afferents, the motoneuron, and the muscle are routinely made during these vibration evoked contractions, however, the resulting discharge patterns of individual motoneurons or motor units are less commonly reported. In the cat, there is evidence that tendon vibration produces motor output by inducing highly synchronous discharge at integer multiples of the vibration frequency, resulting in a probability of discharge that is highly punctuated (Matthews, 1966; Homma et al., 1971; Thompson et al., 2018). Though this result is strikingly apparent in the cat in response to tendon vibration, it remains unclear how or if this rule-like motor unit response to tendon vibration can be modified.

Observations in humans are less uniform. In fact, frequency-locked discharges have been observed occasionally in the arm (Romaiguere et al., 1991), leg (Homma et al., 1971; Burke and Schiller, 1976), and jaw muscles (Desmedt and Godaux, 1975; Hagbarth et al., 1976) of humans. Nevertheless, the majority of human investigations of motor unit activity during TVR of limb muscles do not observe (Godaux et al., 1975; Hagbarth et al., 1976) or report (Bongiovanni et al., 1990; Bongiovanni and Hagbarth, 1990; Romaiguere et al., 1993; Kiehn and Eken, 1997; Griffin et al., 2001; Gorassini et al., 2002, 2004; Grande and Cafarelli, 2003; MacDonell et al., 2010; Fuglevand et al., 2015; Mosier et al., 2017) rigid time-locked motor unit discharge.

Motor unit discharge patterns provide one of the most detailed measures of the mammalian motor system. Given our initial observations of punctuated discharge in the cat (Thompson et al., 2018), we first sought to test how rigid this punctuated discharge is in the cat. We did so by varying the vibration parameters, adding secondary reflex drive, and altering the state of spinal circuitry. In the cat, in all cases and in all units, punctuated discharge in response to tendon vibration was observed. We then sought to quantify motor unit discharge in response to tendon vibration in the human using high density EMG approaches. In the human, TVR evoked motor unit discharge is not punctuated.

MATERIALS AND METHODS

Cat

Ethical Approval

Data presented here are from eight adult cats of either sex weighing 2.5–4 kg. All animals were obtained from a designated scientific research breeding establishment. Animals were housed at Northwestern University's Center for Comparative Medicine, an AAALAC accredited animal research program. All procedures were approved by the Institutional Animal Care and Use Committee at Northwestern University.

Terminal Surgery

Anesthesia was induced with 4% isoflurane and a 1:3 mixture of N_2O and O_2. A permanent tracheal tube was placed through which isoflurane (0.5–2.5%) and gasses were delivered for the duration of the procedures. The animal was immobilized using a stereotaxic frame by a head clamp, a spinal clamp on the L2 dorsal vertebral process, and bilateral hip pins at the iliac crest. The left hindlimb was secured through pins at the knee and clamps at the ankle, and the right hindlimb was secured using a clamp distal to the ankle. The left soleus was dissected, isolated, and its distal tendon was attached to a load cell via a calcaneus bone chip in series with a linear variable differential transformer and customized voice coil. A distal, cutaneous branch of the right superficial peroneal nerve was dissected, and a cuff electrode was secured around the nerve. Likewise, in one experiment, the left common peroneal nerve was dissected and secured with a cuff electrode proximal to the innervation of the left TA. On select experiments, a L4-S1 laminectomy was provided for intrathecal drug administration via subdural catheter. The dorsal and ventral roots were left intact. In all experiments, following a craniotomy, a precollicular decerebration was performed. At this point, the animals are considered to have a complete lack of sentience, and anesthesia was discontinued (Silverman et al., 2005). An esophageal thermistor assisted in the maintenance of heat lamps and hot pads to maintain a core temperature of 35–37°C. At the end of the experiment animals were euthanized using a 2 mM/kg solution of KCl in addition to a bilateral thoracotomy.

Electromyography and Force Recordings

Differential EMG recordings were collected using a custom 64-channel array electrode (5 × 13; 2.54 mm interelectrode distance) placed on the surface of the exposed soleus muscle. A ground electrode was placed on the back. Array data were filtered (100–900 Hz), amplified (0.5–2k), and sampled at 5,120 Hz by a 12-bit A/D converter simultaneously with soleus force data (EMG-USB 2, OT Bioelettronica, Torino, Italy).

Sensory Inputs

Vibration was delivered at high frequencies (∼130 Hz) and small amplitude (∼80 μm) through the voice coil. This device was fit with a linear variable differential transformer to directly measure linear position of the voice coil. In one experiment, a child size electric toothbrush (Colgate) was manually applied to the distal tendon of the soleus. Such manual application that is perpendicular to the tendon is similar to the approach used in humans.

The role of additional synaptic inputs on the punctuated discharge of motor units during tendon vibration was assessed using three forms of inputs in three separate animals. First, muscle stretch was delivered during tendon vibration through the same voice coil using a low frequency (1 Hz), and large amplitude (1 cm) imposed sin wave change in muscle length.

Second, crossed extension reflex was evoked through stimulation (20–50 Hz; 1-ms biphasic; 2× reflex threshold) delivered to the contralateral superficial peroneal nerve through the cuff electrode using a Grass S88 stimulator and isolation unit. Third, reciprocal inhibition was evoked through stimulation (20–50 Hz; 1-ms biphasic; 1.2× reflex threshold) delivered to the ipsilateral common peroneal nerve through the cuff electrode using a Grass S88 stimulator and isolation unit.

State of the Spinal Cord

The motor unit response to tendon vibration was assessed under three different states of the spinal cord: high levels of neuromodulation, acute spinal lesion, and chronic spinal lesion. To increase the activity of lumbar spinal neurons, during one experiment, 50 μL of 100 mM Methoxamine, a norepinephrine α1 agonist, was applied to the spinal cord through the intrathecal catheter. Methoxamine has been shown previously to increase the excitability of spinal motoneurons through an increased magnitude of persistent inward currents (Lee and Heckman, 1999).

In one experiment, a laminectomy was performed from T12 to L1 during the initial surgery. This was packed with saline-soaked gauze, and the incision was held in opposition. Hours after decerebration, the animal was placed back on isoflurane (0.5%), the spine was re-exposed, the dura was cut, and a dorsal hemisection was provided by lesioning the dorsal portion of the cord to the central canal bilaterally. The isoflurane was removed, and the animal was allowed 30 mins to recover.

In one animal, a dorsal hemisection was provided at T13 1 month prior to the terminal experiment. Prior to surgery, cats were sedated (butorphanol, 0.4 mg/kg im; acepromazine, 0.05–0.1 mg/kg im; glycopyrrolate, 0.01 mg/kg sc) and induction was done with propofol (2–3 mg/kg iv). The animal was intubated, and anesthesia was maintained by adjusting isoflurane concentration as needed (1.5–3%). The fur overlying the back and forelimb was shaved with electric clippers. An intravenous line was placed in a cephalic vein to deliver intravenously saline with 2.5% dextrose at a rate of 5–10 ml/kg/h. Under aseptic conditions, a small lower thoracic laminectomy was performed, the dura was removed, and a dorsal hemisection was provided by lesioning the dorsal portion of the cord to the central canal bilaterally. Hemostatic material (Surgicel) was inserted within the gap, and muscles and skin were sutured in anatomic layers. A transdermal fentanyl patch (25 μg/h) was taped to the base of the tail. During surgery and ∼6 h later, an analgesic (buprenorphine, 0.01 mg/kg) was administered subcutaneously. An oral antibiotic (Baytril, 5 mg/kg) was given once a day for 5 days after surgery. The animals were monitored daily by experienced personnel and veterinarians and included manual bladder expressions 1–2 times per day and warm soapy baths as needed.

The TVR data from the cat were compared to a normative dataset of soleus motor unit discharge in the cat (Thompson et al., 2019). This dataset consisted of 297 bouts of self-sustained discharge across 20 animals. These EMG and force data were collected in a similar manner and periods of self-sustained discharge were defined as motor output remaining more than 5 s following the cessation of a specific input.

Human

Ethical Approval

The human data presented here was collected from six adults recruited from the university population. Subjects signed an informed consent approved by the Institutional Review Board of Temple University (protocol #23971).

Electromyography and Torque Recordings

Subjects are seated comfortably in an isokinetic dynamometer (Biodex System 4; Shirley, NY, United States) with hips at 45–90 degrees of flexion, the right knee fully extended, and the ankle between 0 and 30 degrees of plantarflexion. The ankle was securely attached to a footplate and which was coupled to a six-degree of freedom load cell (JR3 75E20; Woodland, CA, United States) with the axis of rotation aligned to the center of the ankle joint. EMG signals are collected from the Tibialis Anterior (TA), Soleus (Sol), Medial Gastrocnemious (MG), or Lateral Gastrocnemious (LG) using 64 channel electrodes grids placed on the belly of the muscle.

The output of a single 8.9 mm differential channel (channel 27) of the array was collected through a secondary data acquisition system. Feedback of the rectified and smoothed (500 ms RMS) EMG signal for TA or Sol was provided to the subjects during dorsiflexion or plantarflexion, respectively, on a 42-inch monitor placed ∼1.5 m in front of the subject at eye level.

Vibration

A commercially available personal massager (Lyork, Guangdong Sheng, China) was used to evoke TVR in humans by manually holding the vibrator perpendicular to the TA or triceps surae tendon. This consisted of a 3 cm silicone contact with the skin, vibrating at 78 Hz. Vibration frequency was clearly visible in the off-axis force component of the loadcell and used for this calculation. To both promote the TVR response and provide access to the tendon, the tested muscle was slightly lengthened by rotating the ankle joint – to assess the TVR of the TA, the ankle was put into 30 degrees of plantarflexion, whereas the ankle was held neutral when assessing plantarflexion.

Experimental Design

Our primary goal with the human data was to quantify the discharge of the same motor unit driven by vibration and by voluntary drive. To accomplish this, we evoked a relatively long TVR response over ∼40 s of vibration, the subject was then provided ∼20 s of rest, afterward the subjects were asked to either dorsiflex or plantarflex in an attempt to volitionally match the conditioned TA or Sol EMG feedback signal from the vibration period. Prior to each trial, the subjects were asked to relax during the vibration and not intervene; following each trial, subjects confirmed that they were relaxed during the vibration.

Analysis

In both the cat and human, the high-density EMG data was decomposed into the discharge of individual motor units through a well-validated algorithm (Negro et al., 2016). Only units with a silhouette value greater than 0.90 were isolated for further analysis. In the cat, these motor unit discharge times have been demonstrated to have a rate of agreement of 93% among the same motor unit decomposed from both the array and fine wire signal (Thompson et al., 2018).

To quantify the motor unit discharge response to tendon vibration, all the ISIs from all of the motor units are collapsed to form a composite interspike interval (cISI) histogram for each period of interest. This cISI histogram was normalized by dividing each bin by the total number to provide a percentage used for further analysis. For the cat data with a single input and all the human data, a 10–40 s segment of steady state activity was chosen for analysis; for the cat data with multiple inputs, segments of time with a single or combined inputs were calculated. Histogram parameters are relatively wide 20–800 ms range with 2-ms bin width allowing for standardization across trials.

In the cat, the punctuation of the cISI histogram was calculated in two manners. First, a within histogram metric of punctuation was defined as the absolute sum of the first derivative of the histogram (ASD). To calculate the ASD, sequential bin heights were subtracted from one another using the normalized cISI histogram, the absolute value was found and summated. Using this measure, a cISI distribution whose sequential values are relatively close in number, the ASD will be relatively small. In contrast, a cISI histogram that has a large bin-to-bin variance (as observed with the punctuated histograms) will have an increasingly large number. Second, the TVR data from the cat was compared to a normative data set of motor unit discharge patterns collected from the soleus during self-sustained motor unit discharge of the *in vivo* cat. Each of the current cISI histograms was compared to each of the 297 cISI histograms derived from 5,618 spike trains from control trials. To quantify the pairwise similarity between these histograms, each histogram was normalized and mean subtracted. The Euclidian distance between these two normalized, mean-subtracted histograms was calculated to provide a normalized measure of similarity from zero (identical) to one (dissimilar). The TVR trials were grouped as either TVR alone or TVR contaminated with secondary inputs or altered spinal circuitry. The ASD and distance measures were compared to the self-sustained discharge values using a one-way analysis of variance. Significant pairwise differences were assessed using Tukey's Honest Significant Difference *post hoc* test.

The human data allowed for a similar within and across trial analysis of the discharge characteristics. Normalized cISI histograms are constructed for each muscle within a trial. The ASD is calculated for both the vibration and volitional evoked contractions. Further, within each trial, the vibration and volitional induced motor output is compared by Euclidian distance between the normalized, mean subtracted vibratory and volitional histograms pairs. As we were able to get paired vibration and volitional contractions in the humans, average torque, EMG, and motor unit discharge rate were calculated during the last 5 s of each contraction; in addition, the recruitment threshold was calculated for each motor unit in each contraction. Paired t-tests were performed to assess for differences in torque and motor unit characteristics between each set of vibration and volitional contractions.

RESULTS

Cat

To assess the robustness of punctuated discharge of motor units in response to tendon vibration in the cat, we altered the vibration parameters, combined TVR with additional reflexive inputs and assessed TVR with spinal circuits in multiple states.

Tendon Vibration Reflex Parameters

Figure 1 shows a representative force and motor unit response to 40 s of tendon vibration. A gradual buildup of muscle force occurs via the recruitment of additional motor units, whereas minimal changes in discharge rate are observed following an initial acceleration of discharge at the onset. When the instantaneous discharge rates for each motor unit are overlaid onto one another, a clear banding of discharge rates is observed. This is further shown in the composite ISI histogram, where abrupt punctuations are observed. ISI histograms of two of the 18 motor units collected during this contraction are plotted on top of the cISI histogram and show individual motor units can be non-overlapping within the range of the cISI histogram.

The punctuation of the ISI histogram is quantified in two ways. First, we take the summation of the absolute sum of the sequential difference of the cISI histogram (ASD). The data in **Figure 2** demonstrates an ASD value of 1.54. The ASD value observed for this TVR trial is well outside of the range of ASD values derived from the control data (0.21 ± 0.09; mean ± SD). Second, we can compare the TVR evoked histogram to a normative dataset using the Euclidean distance between the normalized histograms. **Figure 2** demonstrates the distance from the vibration data to each of the control trials. The control trials demonstrate an average 0.31 ± 0.11 distance from one another, whereas this trial has a mean distance of 0.66 ± 0.06. Both the ASD and the distance measures demonstrate that motor unit discharge patterns in response to tendon vibration in the cat are highly punctuated. This punctuated activity is not observed in the control data, where is an absence of stimulus-evoked motor unit activity.

In one animal, the amplitude of the vibration was altered over a ∼100 μm range to quantify the occurrence of the punctuated discharge. **Figure 3** provides an example of motor unit response to changes in vibration amplitude. Across the 136 motor unit spike trains, punctuated discharge occurred under each of these amplitudes, with an ASD of 1.56 ± 0.14 and a distance of 0.59 ± 0.05. There was, however, a leftward shift in the ISI histogram with increasing vibration amplitudes.

To better understand the potential effect of the vibration stimulus itself and to better replicate approaches used in humans, a less precise vibrator (electric toothbrush), was manually applied perpendicular to the distal tendon. Such apparatus and setup are more akin to human approaches, as compared to precisely controlled vibration delivered parallel to the muscle typically performed in the cat. Such vibration stimuli produced results qualitatively and quantitatively similar to those evoked by more

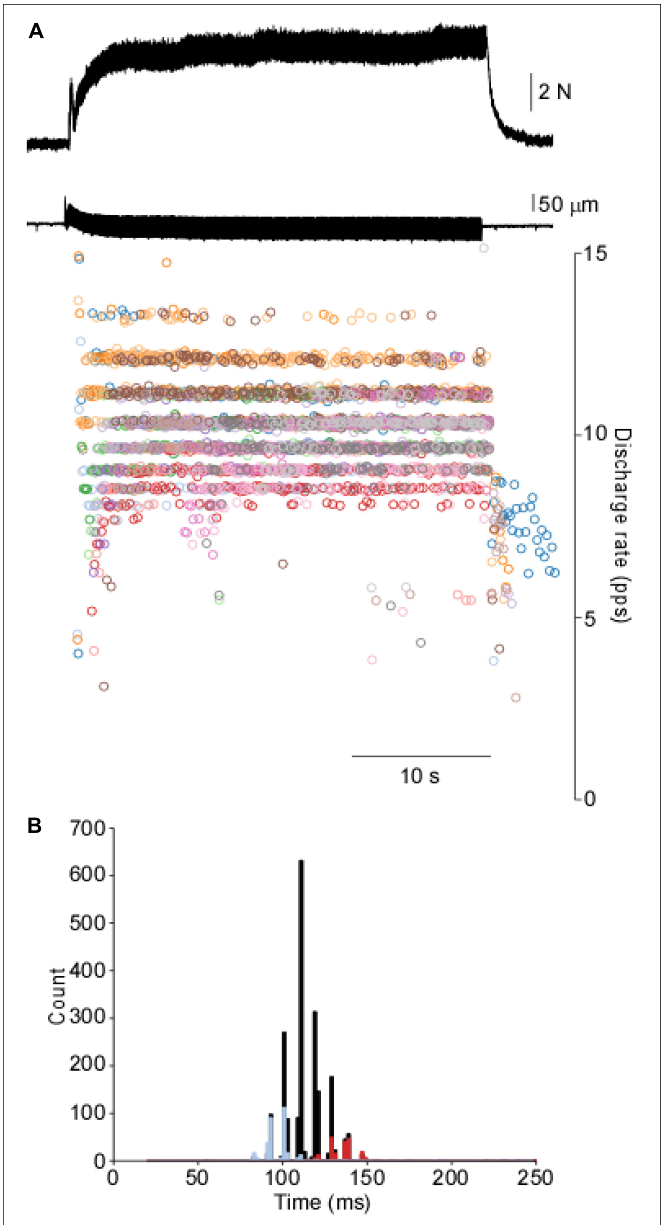

FIGURE 1 | Motor unit response to vibration in the cat's soleus. **(A)** Tendon vibration of the soleus muscle produces motor output through the punctuated discharge of motor units. **(B)**. The cISI histogram reveals a highly punctuated discharge across a range of intervals. Two motor units are overlaid on top of the cISI histogram to demonstrate a single unit is relatively constrained further from the population data.

traditional approaches used elsewhere. The response of 61 motor unit spike trains evoked in response to the manual application of the toothbrush perpendicular to the tendon contains an ASD of 1.18 ± 0.41 and a distance of 0.58 ± 0.04.

Tendon Vibration Reflex in Combination With Secondary Synaptic Drive

Next, we added other excitatory and inhibitory inputs in combination with tendon vibration in order to assess if such secondary inputs could serve to diminish the punctuated discharge observed with vibration alone. Electrical stimulation of select peripheral nerves or stretch of the agonist muscle were used to deliver three forms of secondary inputs.

Electrical stimulation of a distal branch of the contralateral superficial peroneal nerve was used to elicit a net excitatory stimulus to the soleus motor pool (XEX; **Figure 4**). During a prolonged bout of 20 Hz XEX stimulation, 5–10 s long bouts of tendon vibration are delivered. From 68 motor unit spike trains, the ISI histograms derived from the XEX alone portions showed no apparent punctuation in discharge with an ASD of 0.36 ± 0.07 and a distance of 0.30 ± 0.04. However, in the XEX + TVR periods, significant increases in punctuation were observed (ASD = 1.18 ± 0.19 and distance = 0.47 ± 0.08). Punctuation is observed in the XEX + TVR periods but not in the XEX alone epochs.

Next, during the vibration period, a 2 mm peak-to-peak change in muscle length is delivered at 1 Hz. Motor units are responsive to stretch, as demonstrated by their change in discharge with muscle length. However, very little difference is observed in the ASD (1.23 ± 0.06 and 1.21 ± 0.08) and distance (0.52 ± 0.04 and 0.58 ± 0.09) values between the TVR alone and Stretch + TVR conditions from 122 motor unit spike trains, with punctuation being demonstrated throughout.

Lastly, electrical stimulation of the nerve to TA was used to provide reciprocal inhibitory synaptic input to the soleus motor pool. As with the stretch condition, a long bout of TVR is interposed by ∼10 s train of electrical stimulation of the common peroneal nerve. This was observed to decrease ongoing force and EMG activity and was mediated by either motor unit derecruitment or a decreased discharge frequency of ongoing motor units. Therefore, during the inhibition + TVR periods, a decreased frequency of discharge is observed. However, data from 63 motor unit spike trains, there is little change between the punctuation observed in the TVR and inhibition + TVR conditions with ASD values of and 1.51 ± 0.07 and 1.50 ± 0.10 and distance values of 0.53 ± 0.05 and 0.67 ± 0.06, respectively.

Tendon Vibration Reflex in Altered States of the Spinal Cord

In our final attempt to quantify the robustness of motor unit response to TVR in the cat, we sought to quantify the TVR evoked motor unit responses to altered states of spinal circuitry through pharmacological and surgical approaches. First, exogenous neuromodulation of spinal neurons can profoundly alter the state of spinal circuitry. The NEa1 receptor agonist methoxamine has been shown to increase the excitability of spinal motoneurons (Lee and Heckman, 1996). In this state, the increased intrinsic currents and receptiveness to other inputs may serve to diminish the proportional role of the vibratory input. Despite this, motor units can respond to vibration, and this response maintains its punctuated discharge. From the 33 motor unit spike trains collected in this condition showed ASD and distance values of 1.08 ± 0.11 and 0.49 ± 0.09, respectively.

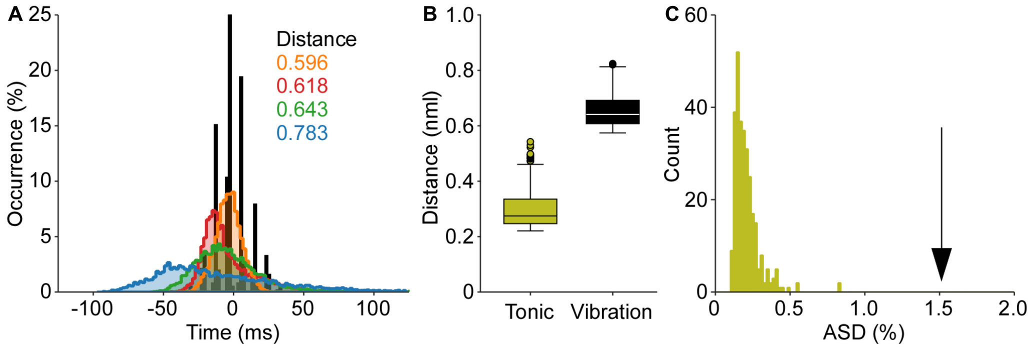

FIGURE 2 | Quantification of punctuated discharge in response to tendon vibration. The data from **Figure 1** is used to demonstrate both analyses of punctuated discharge. **(A)** First, the mean subtracted, normalized cISI histogram is compared to a normative dataset of self-sustained discharge. The Euclidian distance is calculated between these histograms. **(B)** The distance between the TVR evoked cISI histogram is greater than the distance between cISI histograms derived from the self-sustained discharge. **(C)** Second, the absolute sum of the first derivative of the cISI histogram (ASD) during vibration is much greater than the ASD values found during self-sustained discharge. Both the distance and ASD measures suggest the TVR cISI histogram is more punctuated than the cISI histogram derived from a control dataset of self-sustained motor unit discharge.

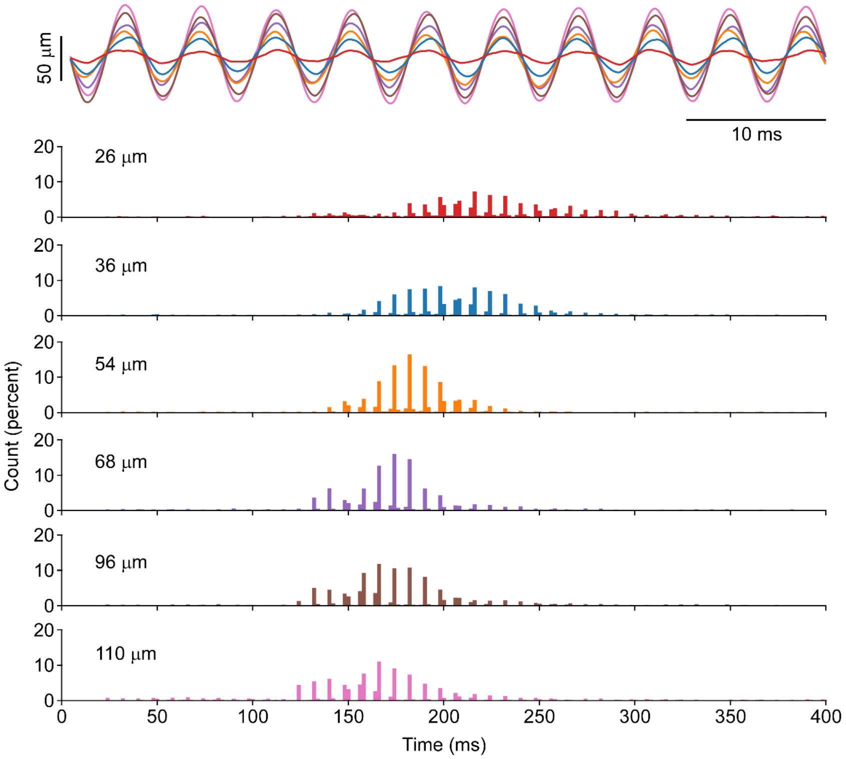

FIGURE 3 | Motor unit response to vibration of different amplitudes in the cat's soleus. A segment of position recording of vibration excursion overlapped across a range of amplitudes is shown for six different amplitudes at the same vibration frequency in one animal. The corresponding cISI of evoked at each length shown increased vibration amplitude will produce a leftward shift in the ISI, whereas the punctuation remains evident at all vibration amplitudes.

Additionally, spinal lesions in both the acute and chronic stages will have a profound impact on the state of spinal circuitry. Though motor unit discharge rates and force were substantially lower, an acute dorsal hemisection had little effect on the punctuated discharge (ASD = 1.35 ± 0.07 and distance = 0.75 ± 0.18) across 82 motor unit spike trains. In an animal with a chronic dorsal hemisection, punctuation remained strong (ASD = 0.96 ± 0.28 and distance = 0.57 ± 0.10) across 53 motor unit spike trains.

Overall Comparison in the Cat

In the cat, every application of vibration to the soleus tendon resulted in motor output that was highly punctuated. Such punctuation was never observed during self-sustained discharge.

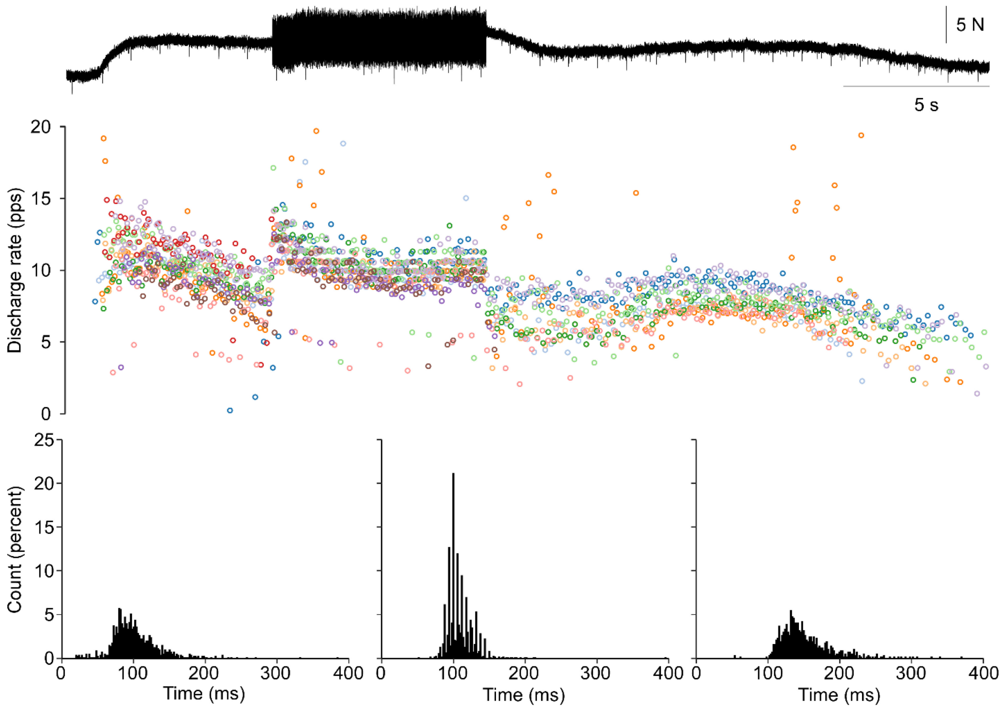

FIGURE 4 | Punctuated discharge remains with the addition of crossed extension. A single trial of relatively brief train of vibration is applied during a longer bout of crossed extension (XEX) stimulation. During XEX alone, no punctuation is observed. Concurrent vibration elicits an increase in both soleus torque and motor unit discharge rates. Furthermore, the discharge during TVR + XEX shows robust punctuation. This is observed in the representative data and the cISI histograms for the XEX alone (sides) and TVR + XEX (middle).

Across all 24 epochs of TVR alone from four animals, the average ASD was 1.44 ± 0.15 and the average distance was 0.56 ± 0.05. Across the 18 epochs of TVR contaminated with either secondary inputs or altered spinal circuitry from six animals, the average ASD was slightly smaller (1.21 ± 0.23) and the average distance was slightly larger (0.59 ± 0.14). When the TVR alone and contaminated TVR groups were compared to the 297 self-sustained discharge trials, both the ASD and distance measure revealed a similar trend. Separate one-way ANOVAs revealed self-sustained discharge has a significantly lower ASD and distance compared to both TVR alone and the corrupted TVR (all $p < 0.0001$). Significant differences were observed between TVR alone and the corrupted TVR for ASD ($p < 0.0001$) but not distance ($p = 0.77$). Though significant, the difference between the TVR alone and contaminated TVR on the ASD measure was much smaller (0.23) than the difference between these data and the self-sustained discharge (1.23 and 1.00, respectively).

Human

Six individuals (two female) with an average age of 22.8 ± 5.2 years, height of 171.6 ± 10.3 cm, and weight of 68.9 ± 10.9 kg participated in the experiment. The human data was collected and analyzed in a manner akin to both previous human investigations and the above cat experiments, however, the human data provided us with the ability to have the participants volitionally match the EMG evoked during the prior tendon vibration.

The mean EMG amplitude was not different between vibration and volitional contractions (26.2 ± 40.3 versus 25.8 ± 40.3 μV; $p = 0.822$). However, this matched EMG resulted in greater ankle torque in the voluntary (5.27 ± 6.84 Nm) as compared to the vibration (3.78 ± 5.86) contractions ($p = 0.012$).

From the surface EMG arrays, 67 motor unit spike trains were matched across both the vibration and volitional conditions. This represented 44 TA motor units across 10 dorsiflexion trials from four individuals and 8 Sol, 6 LG, and 9 MG motor units across 8 trials in two individuals. On average, across all motor units the discharge rates (9.5 ± 2.7 versus 9.5 ± 3.2 pps) and recruitment thresholds (2.22 ± 3.99 vs. 2.01 ± 2.29 Nm) were not different between vibration and volitional activation ($p = 0.953$ and $p = 0.586$, respectively).

Moreover, punctuated motor unit discharges evoked through tendon vibration were not observed in the human lower limb. **Figure 5** shows ankle torque, MG EMG, and four MG motor units during vibration evoked contraction of the triceps surae followed by a volitional match of the EMG produced during the vibration period. A lack of punctuated discharge is observed in the TVR evoked motor unit discharge.

This lack of punctuated discharge is consistently observed in the lower limb of subjects. Data from these six subjects

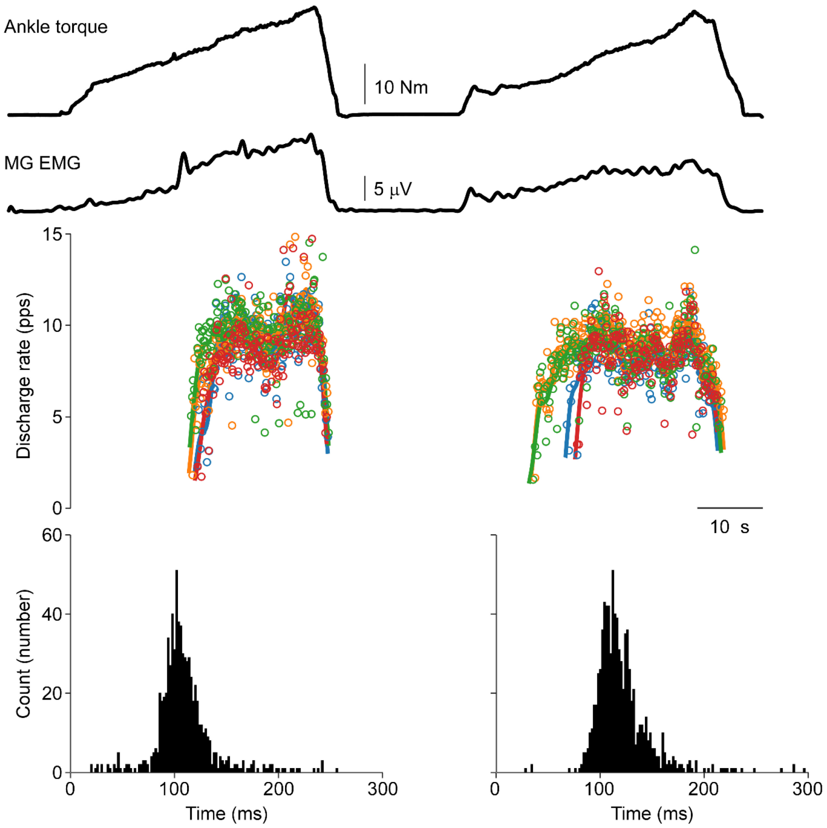

FIGURE 5 | Vibration evoked and matched volitional contractions in the human. Representative data from a single human participant. The first contraction is elicited by vibration of the triceps surae tendon, whereas the second contraction is a volitional contraction set to match the EMG profile of the vibration evoked contraction. Similar motor unit discharge patterns are observed in both contractions. No punctuation is observed during the vibration evoked contraction with ASD values of 0.36 and 0.32 during vibration-evoked and volitional contractions, respectively. A distance of 0.28 is observed between these cISI histograms.

consistently demonstrates this lack of punctuated discharge in response to focal TVR at the ankle. ASD values were nearly identical between the vibration (0.25 ± 0.08) and volitional (0.25 ± 0.06) histograms ($p = 0.93$). The average distance between the vibration and volitional contraction is 0.27 ± 0.14, slightly below the distance between the self-sustained discharge condition in the cat.

Despite this lack of punctuated discharge, the neural representation of the vibration frequency was not fully absent in humans. **Figure 6** shows the coherence between the CST and the unfiltered force or torque output for one representative example of the cat and human data. As expected, the CST extracted from all cat recordings is highly coherent with the vibration frequency (>0.8). On the other hand, human data show a much lower amplitude, though not absent, coherence at the vibration frequency (<0.2).

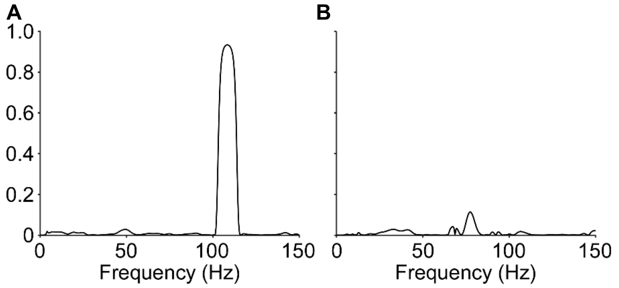

FIGURE 6 | Coherence between the neural drive to muscle and the vibration frequency. Representative data showing the coherence between the composite spike train and the vibration frequency, determined through the force signal, are shown for the cat **(A)** and human **(B)**. The data from the cat show relatively large coherence (0.93) at the vibration frequency, however, data from the human shows a stark reduction, but not complete abolishment, of the observed coherence (0.11) at the vibration frequency.

DISCUSSION

The punctuated motor unit discharge in response to tendon vibration is a robust occurrence in the cat. However, in humans, such punctuated discharge is not readily apparent.

Tendon Vibration in the Cat

The TVR has been thoroughly investigated in the cat. Spindle afferents are highly sensitive to vibration and result in afferent action potentials time locked to the vibration period

(Brown et al., 1967). This afferent drive provides distributed monosynaptic input to each of the motoneurons of the motor pool (Mendell and Henneman, 1968) and steady-state activation of the Ia afferents will produce a relatively stable depolarization of the spinal motoneuron (Lee and Heckman, 1996). Previous data has shown spinal motoneurons in the cat discharge at integer multiples of the vibration frequency. Here we demonstrate this is a common occurrence for the soleus muscle across a wide range of conditions.

It is possible that our vibration was not fully selective for Ia afferents. Group II afferents may be activated by tendon vibration in the cat, however, it is expected that the discharge of these afferents would be proportional to the amplitude, rather than frequency, of vibration (Brown et al., 1967). As the muscle was surgically isolated from the surrounding tissue, it is likely that potential heteronymous and cutaneous activation is diminished but cannot be excluded. Given the strict rule-like nature of the motoneuron discharge, it may be expected that recurrent inhibition would be patterned in a similar manner. Lastly, Ib fibers may be activated by the stimulus, but would also be activated in a manner that is proportional to the active muscle force generation. While it is clear that the activation of these other pathways does not fully interfere with the punctuated discharge of motoneurons, it remains unclear what role they may have in modulating, or even promoting, this pattern of discharge.

To further explore this idea, we augmented non-Ia sources of synaptic drive to these spinal motoneurons by providing specific afferent drive in conjunction with the tendon vibration. The addition of stretch, crossed extension, and reciprocal inhibitory inputs had clear effects on the mean discharge frequency, however, minimal effects were observed on the punctuated discharges. Similarly, concurrent electrical activation of the nerve to TA (the antagonist muscle) did not alter the discharge pattern in response to tendon vibration of the soleus muscle. Lastly, both pharmacological and surgical attempts to alter the state of the spinal cord failed to significantly diminish the presence of punctuated TVR evoked discharge in the cat.

Tendon Vibration in the Human

Focal tendon vibration failed to produce punctuated discharge patterns in human lower leg motor units. When quantifying the discharge of the same motor unit across conditions, the TVR evoked contraction, and the volitional contraction produced nearly identical patterns of motor output. This was consistently observed in all units detected in the lower limb in each of the human subjects assessed.

Though researchers have observed some level of phase-locking (Homma et al., 1971; Desmedt and Godaux, 1975; Burke and Schiller, 1976; Hagbarth et al., 1976; Romaiguere et al., 1991) of, numerous other descriptions of human motor unit discharge during focal tendon vibration either did not observe this discharge pattern or did not report it. In the latter group, it may be expected that these investigators would have noted such patterns, as it is quite striking when observing the discharge rate overtime or the ISI histogram. Additionally, a visual assessment of the discharge patterns in these manuscripts does not demonstrate punctuated discharge (Bongiovanni et al., 1990; Bongiovanni and Hagbarth, 1990; Romaiguere et al., 1993; Kiehn and Eken, 1997; Gorassini et al., 2002, 2004; Grande and Cafarelli, 2003; MacDonell et al., 2010; Fuglevand et al., 2015; Mosier et al., 2017). The primary finding from the human data is that the punctuation of motor unit discharge is much less robust than in the cat.

Potential Mechanisms

Several potential mechanisms may underlie this discrepancy in motor unit discharge patterns in leg muscles in both the cat and human. The discharge of spindle afferents is phase locked to the primary or subharmonic frequency of vibration in both the cat and humans. At sub motor threshold levels, human spinal afferents may not discharge in a non-time locked manner (Fallon and Macefield, 2007), however, at higher vibration amplitudes, this discharge is locked to the vibratory stimulus (Burke et al., 1976; Houk, 1976). If such afferent discharge is phase locked to the vibratory input and if the one-to-all distribution of Ia afferents to spinal motoneuron also holds true, the discrepancy between the cat and human may be due to either activation of non-monosynaptic pathways or length of the reflex arc.

The gradual build-up of force generation during constant vibratory input was initially taken as evidence of the slow activation of polysynaptic circuits through collaterals from the Ia afferents, which are thought to be "more insecure and less straightforward in nature than the monosynaptic excitation" (Godaux and Desmedt, 1975). Though such collaterals exist (Scheibel and Scheibel, 1969; Brown and Fyffe, 1978; Ishizuka et al., 1979; Vincent et al., 2017; Lucas-Osma et al., 2018) and activation of the motoneuron through Ia mediated polysynaptic circuits likely does occur (Jankowska et al., 1981; Burke et al., 1984), the role of the persistent inward currents, intrinsic to the motoneuron, seems highly plausible. Rather than the gradual buildup of polysynaptic circuit activity, the gradual warm-up of PIC activity may underlie this recruitment of additional motoneurons (Heckman and Lee, 2001). In addition to promoting a recruitment-based strategy for increasing torque generation, this secondary form of input, whether extrinsic or intrinsic, may diminish the punctuated discharge of motor units. The motor unit data from the cat presented here demonstrate that secondary forms of input do little to alter the punctuated discharge of spinal motoneurons. Instead, the TVR evoked punctuated discharge remains robust across either patterned afferent drive or alterations in the state of the spinal cord.

Small changes in the dispersion of axonal conduction velocity can affect the transmission of oscillations over longer pathways. If the range of the latency jitter delays of Ia afferents exceeds the vibration period, the motoneurons may receive a smoothed and relatively more uniform synaptic input. Such phenomenon is consistent with the substantial decrease of the correlation between neural drive and vibration oscillations in humans. In humans, the TVR evoked synchronization of motor units may be less readily observed in more distal muscles (Hagbarth et al., 1976). Such findings are consistent with both the cat and human data presented here. However, this is contrary to the patterns of motor unit synchronization during volitional contractions. During voluntary contractions, more distal motor pools are observed to have a greater amount of synchronization (Keen et al., 2012) and shared oscillations in alpha and beta frequency bands (Negro and Farina, 2012; Castronovo et al., 2015). Therefore, it is unclear if the same results will be observed during a stochastic/non-periodic, lower frequency physiological activation of spinal motoneurons.

There are several limitations to these results. First, the cat data were obtained from a single muscle following decerebration. An ideal model would be test this in a variety of muscles in the awake behaving cat, like what was reported here for the human lower limb. Future investigations should work toward developing technical and behavioral approaches to investigate motor unit activity during tonic sensory drive in the awake behaving animal. Additionally, vibration was delivered at different frequencies, however, previous work from the cat has shown that motor unit discharge remains highly punctuated across a range of frequencies (Thompson et al., 2018) and it does not appear that there is a dramatic shift toward punctuated discharge across a range of vibration frequencies in human lower limb muscles (Mildren et al., 2019). Lastly, we may be recording from a biased sample of motor units, particularly in the human. The high-density EMG approach is selective to superficial motor unit and it may be that larger motor units are positioned more superficially (Knight and Kamen, 2005). It would be of great interest to see if there is a subpopulation of motor units which does demonstrate punctuated discharge in response to tendon vibration, however, none of the 67 motor unit spike trains collected from the human lower limb demonstrated this behavior.

Here we observe that focal tendon vibration in the cat produces highly punctuated motor unit discharge. This occurs across various vibration parameters, with the addition of secondary inputs, and with altered states of the spinal cord. This rule-like response to tendon vibration is observed in every unit of every animal. The addition of non-monosynaptic inputs does little to distort the punctuated discharge of spinal motoneurons in response to tendon vibration in the decerebrate cat. Such punctuated discharge is not observed in the human limb. Taken together, these data suggest the lack of punctuated discharge in humans may be due to phenomena other than non-monosynaptic inputs. It may be the case that the dispersion of the coherence between the neural drive and the vibration oscillations is influenced by the long conductance distance between the vibrated tendon and its motoneuron pool.

DATA AVAILABILITY STATEMENT

The raw data supporting the conclusions of this article will be made available by the authors, without undue reservation.

ETHICS STATEMENT

The studies involving human participants were reviewed and approved by Temple University's Human Research Protection Program (HRPP). The patients/participants provided their written informed consent to participate in this study. The animal study was reviewed and approved by Institutional Animal Care and Use Committee (IACUC).

AUTHOR CONTRIBUTIONS

CT, MJ, DF, CH, and FN contributed to conception and design of the study. CT and MJ performed the experiments. CT and FN performed the analyses. CT wrote the first draft of the manuscript. All authors contributed to manuscript revision, read, and approved the submitted version.

FUNDING

This work was supported in part by a Craig H. Neilsen Foundation Postdoctoral Fellowship (CT), National Institutes of Health (NIH) grants T32HD007418 (CT and MJ), R01NS098509 (CH), and R01NS089313 (CH), and the European Research Council (ERC) under the European Union's Horizon 2020 Research and Innovation Program (grant agreement No. 810346, ERC Synergy project Natural BionicS; DF).

REFERENCES

Bongiovanni, L. G., and Hagbarth, K. E. (1990). Tonic vibration reflexes elicited during fatigue from maximal voluntary contractions in man. *J. Physiol.* 423, 1–14. doi: 10.1113/jphysiol.1990.sp018007

Bongiovanni, L. G., Hagbarth, K. E., and Stjernberg, L. (1990). Prolonged muscle vibration reducing motor output in maximal voluntary contractions in man. *J. Physiol.* 423, 15–26. doi: 10.1113/jphysiol.1990.sp018008

Brown, A. G., and Fyffe, R. E. (1978). The morphology of group Ia afferent fibre collaterals in the spinal cord of the cat. *J. Physiol.* 274, 111–127. doi: 10.1113/jphysiol.1978.sp012137

Brown, M. C., Engberg, I., and Matthews, P. B. (1967). The relative sensitivity to vibration of muscle receptors of the cat. *J. Physiol.* 192, 773–800. doi: 10.1113/jphysiol.1967.sp008330

Burke, D., Gandevia, S. C., and McKeon, B. (1984). Monosynaptic and oligosynaptic contributions to human ankle jerk and H-reflex. *J. Neurophysiol.* 52, 435–448. doi: 10.1152/jn.1984.52.3.435

Burke, D., Hagbarth, K. E., Lofstedt, L., and Wallin, B. G. (1976). The responses of human muscle spindle endings to vibration during isometric contraction. *J. Physiol.* 261, 695–711. doi: 10.1113/jphysiol.1976.sp011581

Burke, D., and Schiller, H. H. (1976). Discharge pattern of single motor units in the tonic vibration reflex of human triceps surae. *J. Neurol. Neurosurg. Psychiatry* 39, 729–741. doi: 10.1136/jnnp.39.8.729

Castronovo, A. M., Negro, F., and Farina, D. (2015). Theoretical model and experimental validation of the estimated proportions of common and independent input to motor neurons. *Conf. Proc. IEEE Eng. Med. Biol. Soc.* 2015, 254–257. doi: 10.1109/EMBC.2015.7318348

Desmedt, J. E., and Godaux, E. (1975). Vibration-induced discharge patterns of single motor units in the masseter muscle in man. *J. Physiol.* 253, 429–442. doi: 10.1113/jphysiol.1975.sp011198

Fallon, J. B., and Macefield, V. G. (2007). Vibration sensitivity of human muscle spindles and Golgi tendon organs. *Muscle Nerve* 36, 21–29. doi: 10.1002/mus.20796

Fuglevand, A. J., Lester, R. A., and Johns, R. K. (2015). Distinguishing intrinsic from extrinsic factors underlying firing rate saturation in human motor units. *J. Neurophysiol.* 113, 1310–1322. doi: 10.1152/jn.00777.2014

Godaux, E., and Desmedt, J. E. (1975). Evidence for a monosynaptic mechanism in the tonic vibration reflex of the human masseter muscle. *J. Neurol. Neurosurg. Psychiatry* 38, 161–168. doi: 10.1136/jnnp.38.2.161

Godaux, E., Desmedt, J. E., and Demaret, P. (1975). Vibration of human limb muscles: the alleged phase-locking of motor unit spikes. *Brain Res.* 100, 175–177. doi: 10.1016/0006-8993(75)90255-3

Gorassini, M., Yang, J. F., Siu, M., and Bennett, D. J. (2002). Intrinsic activation of human motoneurons: possible contribution to motor unit excitation. *J. Neurophysiol.* 87, 1850–1858. doi: 10.1152/jn.00024.2001

Gorassini, M. A., Knash, M. E., Harvey, P. J., Bennett, D. J., and Yang, J. F. (2004). Role of motoneurons in the generation of muscle spasms after spinal cord injury. *Brain* 127(Pt 10), 2247–2258. doi: 10.1093/brain/awh243

Grande, G., and Cafarelli, E. (2003). Ia Afferent input alters the recruitment thresholds and firing rates of single human motor units. *Exp. Brain Res.* 150, 449–457. doi: 10.1007/s00221-003-1463-z

Granit, R., and Henatsch, H. D. (1956). Gamma control of dynamic properties of muscle spindles. *J. Neurophysiol.* 19, 356–366. doi: 10.1152/jn.1956.19.4.356

Griffin, L., Garland, S. J., Ivanova, T., and Gossen, E. R. (2001). Muscle vibration sustains motor unit firing rate during submaximal isometric fatigue in humans. *J. Physiol.* 535(Pt 3), 929–936. doi: 10.1111/j.1469-7793.2001.00929.x

Hagbarth, K. E., Hellsing, G., and Lofstedt, L. (1976). TVR and vibration-induced timing of motor impulses in the human jaw elevator muscles. *J. Neurol. Neurosurg. Psychiatry* 39, 719–728. doi: 10.1136/jnnp.39.8.719

Heckman, C., and Lee, R. H. (2001). "Advances in measuring active dendritic currents in spinal motoneurons in vivo," in *Motor Neurobiology of the Spinal Cord*, ed. T. C. Cope (London: CRC Press), 89–106.

Homma, S., Kanda, K., and Watanabe, S. (1971). Monosynaptic coding of group Ia afferent discharges during vibratory stimulation of muscles. *Jpn. J. Physiol.* 21, 405–417. doi: 10.2170/jjphysiol.21.405

Houk, J. C. (1976). Single unit spindle responses to muscle vibration in man. *Prog. Brain Res.* 44, 281–289. doi: 10.1016/s0079-6123(08)60739-6

Ishizuka, N., Mannen, H., Hongo, T., and Sasaki, S. (1979). Trajectory of group Ia afferent fibers stained with horseradish peroxidase in the lumbosacral spinal cord of the cat: three dimensional reconstructions from serial sections. *J. Comp. Neurol.* 186, 189–211. doi: 10.1002/cne.901860206

Jankowska, E., Johannisson, T., and Lipski, J. (1981). Common interneurones in reflex pathways from group 1a and 1b afferents of ankle extensors in the cat. *J. Physiol.* 310, 381–402. doi: 10.1113/jphysiol.1981.sp013556

Keen, D. A., Chou, L. W., Nordstrom, M. A., and Fuglevand, A. J. (2012). Short-term synchrony in diverse motor nuclei presumed to receive different extents of direct cortical input. *J. Neurophysiol.* 108, 3264–3275. doi: 10.1152/jn.01154.2011

Kiehn, O., and Eken, T. (1997). Prolonged firing in motor units: evidence of plateau potentials in human motoneurons? *J. Neurophysiol.* 78, 3061–3068. doi: 10.1152/jn.1997.78.6.3061

Knight, C. A., and Kamen, G. (2005). Superficial motor units are larger than deeper motor units in human vastus lateralis muscle. *Muscle Nerve* 31, 475–480. doi: 10.1002/mus.20265

Lee, R. H., and Heckman, C. J. (1996). Influence of voltage-sensitive dendritic conductances on bistable firing and effective synaptic current in cat spinal motoneurons in vivo. *J. Neurophysiol.* 76, 2107–2110. doi: 10.1152/jn.1996.76.3.2107

Lee, R. H., and Heckman, C. J. (1999). Enhancement of bistability in spinal motoneurons in vivo by the noradrenergic alpha1 agonist methoxamine. *J. Neurophysiol.* 81, 2164–2174. doi: 10.1152/jn.1999.81.5.2164

Lucas-Osma, A. M., Li, Y., Lin, S., Black, S., Singla, R., Fouad, K., et al. (2018). Extrasynaptic alpha5GABAA receptors on proprioceptive afferents produce a tonic depolarization that modulates sodium channel function in the rat spinal cord. *J. Neurophysiol.* 120, 2953–2974. doi: 10.1152/jn.00499.2018

MacDonell, C. W., Ivanova, T. D., and Garland, S. J. (2010). Changes in the estimated time course of the motoneuron after hyperpolarization induced by tendon vibration. *J. Neurophysiol.* 104, 3240–3249. doi: 10.1152/jn.00941.2009

Matthews, P. B. (1966). The reflex excitation of the soleus muscle of the decerebrate cat caused by vibbration applied to its tendon. *J. Physiol.* 184, 450–472. doi: 10.1113/jphysiol.1966.sp007926

Mendell, L. M., and Henneman, E. (1968). Terminals of single Ia fibers: distribution within a pool of 300 homonymous motor neurons. *Science* 160, 96–98. doi: 10.1126/science.160.3823.96

Mildren, R. L., Peters, R. M., Carpenter, M. G., Blouin, J. S., and Inglis, J. T. (2019). Soleus single motor units show stronger coherence with Achilles tendon vibration across a broad bandwidth relative to medial gastrocnemius units while standing. *J. Neurophysiol.* 122, 2119–2129. doi: 10.1152/jn.00352.2019

Mosier, E. M., Herda, T. J., Trevino, M. A., and Miller, J. D. (2017). The influence of prolonged vibration on motor unit behavior. *Muscle Nerve* 55, 500–507. doi: 10.1002/mus.25270

Negro, F., and Farina, D. (2012). Factors influencing the estimates of correlation between motor unit activities in humans. *PLoS One* 7:e44894. doi: 10.1371/journal.pone.0044894

Negro, F., Muceli, S., Castronovo, A. M., Holobar, A., and Farina, D. (2016). Multi-channel intramuscular and surface EMG decomposition by convolutive blind source separation. *J. Neural Eng.* 13:026027. doi: 10.1088/1741-2560/13/2/026027

Romaiguere, P., Vedel, J. P., Azulay, J. P., and Pagni, S. (1991). Differential activation of motor units in the wrist extensor muscles during the tonic vibration reflex in man. *J. Physiol.* 444, 645–667. doi: 10.1113/jphysiol.1991.sp018899

Romaiguere, P., Vedel, J. P., and Pagni, S. (1993). Effects of tonic vibration reflex on motor unit recruitment in human wrist extensor muscles. *Brain Res.* 602, 32–40. doi: 10.1016/0006-8993(93)90237-h

Scheibel, M. E., and Scheibel, A. B. (1969). Terminal patterns in cat spinal cord. 3. Primary afferent collaterals. *Brain Res.* 13, 417–443. doi: 10.1016/0006-8993(69)90258-3

Silverman, J., Garnett, N. L., Giszter, S. F., Heckman, C. J. II, Kulpa-Eddy, J. A., Lemay, M. A., et al. (2005). Decerebrate mammalian preparations: unalleviated or fully alleviated pain? A review and opinion. *Contemp. Top. Lab. Anim. Sci.* 44, 34–36.

Thompson, C. K., Johnson, M. D., Negro, F., McPherson, L. M., Farina, D., and Heckman, C. J. (2019). Exogenous neuromodulation of spinal neurons induces beta-band coherence during self-sustained discharge of hind limb motor unit populations. *J. Appl. Physiol.* 127, 1034–1041. doi: 10.1152/japplphysiol.00110.2019

Thompson, C. K., Negro, F., Johnson, M. D., Holmes, M. R., McPherson, L. M., Powers, R. K., et al. (2018). Robust and accurate decoding of motoneuron behaviour and prediction of the resulting force output. *J. Physiol.* 596, 2643–2659. doi: 10.1113/JP276153

Vincent, J. A., Gabriel, H. M., Deardorff, A. S., Nardelli, P., Fyffe, R. E. W., Burkholder, T., et al. (2017). Muscle proprioceptors in adult rat: mechanosensory signaling and synapse distribution in spinal cord. *J. Neurophysiol.* 118, 2687–2701. doi: 10.1152/jn.00497.2017

Westbury, D. R. (1972). A study of stretch and vibration reflexes of the cat by intracellular recording from motoneurones. *J. Physiol.* 226, 37–56. doi: 10.1113/jphysiol.1972.sp009972

Conflict of Interest: The authors declare that the research was conducted in the absence of any commercial or financial relationships that could be construed as a potential conflict of interest.

frontiers | Frontiers in Integrative Neuroscience

ORIGINAL RESEARCH
published: 06 May 2022
doi: 10.3389/fnint.2022.815750

Neural Correlates of Multisensory Integration for Feedback Stabilization of the Wrist

Aaron J. Suminski[1,2,3], *Raymond C. Doudlah*[4] *and Robert A. Scheidt*[1]

[1] Department of Biomedical Engineering, Marquette University, Milwaukee, WI, United States, [2] Department of Neurological Surgery, University of Wisconsin-Madison, Madison, WI, United States, [3] Department of Biomedical Engineering, University of Wisconsin-Madison, Madison, WI, United States, [4] Department of Neuroscience, University of Wisconsin-Madison, Madison, WI, United States

Robust control of action relies on the ability to perceive, integrate, and act on information from multiple sensory modalities including vision and proprioception. How does the brain combine sensory information to regulate ongoing mechanical interactions between the body and its physical environment? Some behavioral studies suggest that the rules governing multisensory integration for action may differ from the maximum likelihood estimation rules that appear to govern multisensory integration for many perceptual tasks. We used functional magnetic resonance (MR) imaging techniques, a MR-compatible robot, and a multisensory feedback control task to test that hypothesis by investigating how neural mechanisms involved in regulating hand position against mechanical perturbation respond to the presence and fidelity of visual and proprioceptive information. Healthy human subjects rested supine in a MR scanner and stabilized their wrist against constant or pseudo-random torque perturbations imposed by the robot. These two stabilization tasks were performed under three visual feedback conditions: "No-vision": Subjects had to rely solely on proprioceptive feedback; "true-vision": visual cursor and hand motions were congruent; and "random-vision": cursor and hand motions were uncorrelated in time. Behaviorally, performance errors accumulated more quickly during trials wherein visual feedback was absent or incongruous. We analyzed blood-oxygenation level-dependent (BOLD) signal fluctuations to compare task-related activations in a cerebello-thalamo-cortical neural circuit previously linked with feedback stabilization of the hand. Activation in this network varied systematically depending on the presence and fidelity of visual feedback of task performance. Addition of task related visual information caused activations in the cerebello-thalamo-cortical network to expand into neighboring brain regions. Specific loci and intensity of expanded activity depended on the fidelity of visual feedback. Remarkably, BOLD signal fluctuations within these regions correlated strongly with the time series of proprioceptive errors—but not visual errors—when the fidelity of visual feedback was poor, even though visual and hand motions had similar variability characteristics. These results provide insight into the neural control of the body's physical interactions with its environment, rejecting the standard Gaussian cue combination model of multisensory integration in favor of models that account for causal structure in the sensory feedback.

Keywords: fMRI, motor control, vision, proprioception, error correction (EC)

Edited by:
Richard Nichols,
Georgia Institute of Technology,
United States

Reviewed by:
Herbert Heuer,
Leibniz Research Centre for Working Environment and Human Factors (IfADo), Germany
J. C. Mizelle,
East Carolina University, United States

***Correspondence:**
Robert A. Scheidt
scheidt@ieee.org

Received: *15 November 2021*
Accepted: *25 March 2022*
Published: *06 May 2022*

Citation:
Suminski AJ, Doudlah RC and Scheidt RA (2022) Neural Correlates of Multisensory Integration for Feedback Stabilization of the Wrist. Front. Integr. Neurosci. 16:815750. doi: 10.3389/fnint.2022.815750

INTRODUCTION

Stabilizing hand-held objects is an important behavior in everyday life. Despite decades of study, it remains unclear how the brain uses sensory information to control manual interactions with physical objects. Stabilizing a hand-held object like a glass of water relies heavily on visual feedback to determine, for example, the tilt of the water relative to the rim. Other actions like stabilizing a car's steering wheel are dominated by proprioceptive feedback because maneuvering through traffic requires visual attention to be focused on other vehicles. Still other activities require flexible patterns of multisensory control, where the relative importance of visual and proprioceptive feedback varies as the dynamic demands of the task change. For example, a restaurant server uses visual and proprioceptive cues to stabilize a hand-held serving tray when removing one of several dishes to be served, but likely uses proprioception alone to stabilize the tray when delivering a plate to table because visual attention is required to avoid table-top obstacles such as glasses and silverware. How does the brain combine multiple sources of sensory information for ongoing limb stabilization? This paper addresses that question within the context of a limb stabilization task we previously used to study electromyographic and neural correlates of proprioceptive feedback control (Suminski et al., 2007a). We now ask how the presence and fidelity of visual feedback impacts the neural processing of proprioceptive and visual signals related to feedback stabilization of the wrist against uncertain environmental loads.

For decades, there has been debate about how the brain integrates information from the different senses to estimate limb state for perception (Tillery et al., 1991; Ernst and Banks, 2002; van Beers et al., 2002; Ernst, 2006; Reuschel et al., 2010) and action (Soechting and Flanders, 1989; Henriques and Crawford, 2002; Körding and Wolpert, 2004; Scheidt et al., 2005; Bagesteiro et al., 2006; Judkins and Scheidt, 2014; Crevecoeur et al., 2016). As one example, Ernst and Banks (2002) presented human subjects with sequential pairs of "raised ridge" stimuli that they could view binocularly and/or grasp with the index finger and thumb (Ernst and Banks, 2002). Each presentation of visual and/or mechanical stimuli lasted for 1 s and could vary in height. Noise was sometimes added to the visual display to vary its reliability. The subject's task was to indicate which of the paired stimuli (first or second) was apparently taller. The resulting data suggested that the combination of sensory cues in the presence of noise was well-described by an integration rule based on *Maximum Likelihood Estimation* (MLE), which proposes that the brain combines information from each sensory modality in a way that minimizes uncertainty (variance) in a unified multisensory state estimate:

$$S_{MS}(t) = \sum\nolimits_i w_i S_i(t), \text{ with } w_i = \frac{\sigma_i^{-2}}{\sum_j \sigma_j^{-2}}. \tag{1}$$

In this model, the multisensory percept $S_{MS}(t)$ is a combination of evidence provided by sensory cues $S_i(t)$ weighted in inverse proportion to the cues' uncertainties σ_i^{-2}. The more reliable the signal, the more it contributes to the multisensory estimate of the state. By contrast, others have suggested that the brain combines sensory cues for generating actions using context-specific weighting schemes that may not strictly adhere to the "static" integration rule described by Equation 1. For example, in one study of goal-directed reaching, Sober and Sabes (2003) reported evidence that multisensory integration rules vary depending on what aspect of movement is being planned. Limb position estimation for planning the direction and extent of a goal-directed reach appears to rely mostly on visual feedback, whereas limb position estimation for computing requisite motor commands appears to be biased toward proprioceptive information (Sober and Sabes, 2003). While such findings do not outright contradict the conclusions of Ernst and Banks (2002), they do suggest that multisensory integration in the estimation of limb state for action may well be context-dependent, adjusting dynamically even within the early stages of planning and executing a single goal-directed action.

In another relevant study, Judkins and Scheidt (2014) used a simple virtual reality display and a hand-held robotic handle to examine sensorimotor adaptation of goal-directed reaching in response to robotic (physical) and/or virtual (visual) spring-like loads that varied randomly from one trial to the next. The virtual load was driven by forces applied to the robot's handle and thus, the cursor's motion could differ from that of the physical load (i.e., the handle) if the simulated spring constants differed. This decoupling of the physical and virtual responses to perturbation allowed independent assessment of the influence of visually and proprioceptively perceived performance errors on subsequent movements. Surprisingly, the authors observed complete visual capture in the trial-by-trial updating of goal-directed reaches despite the presence of substantial uncertainty in both the visual and proprioceptive percepts. Based on the experimental data, the authors concluded that multisensory integration for the adaptive control of reaching did not conform to predictions of a MLE model, which instead predicted incomplete visual capture (i.e., proprioceptive contributions in the presence of a moderate visual bias) (Judkins and Scheidt, 2014). One possible explanation for why a MLE of sensory integration might fail to describe multisensory integration for the trial-by-trial correction of movement errors is that the movements in that study were fast and performance feedback was fleeting at the moment of target capture. By contrast, subjects in perceptual tasks typically have much more time to explore the stimuli and to make a perceptual decision. Severe limitations in the amount of time available for multisensory integration could constrain the neural computations responsible for integrating sensory feedback for the control of action, forcing the brain to choose one modality over the other based on factors other than just the relative reliability of the sensory cues (cf., a summary of Crevecoeur et al., 2016 in "DISCUSSION"). Another possibility is that unimodal sensory capture arises when the several feedback sources differ to such an extent that they no longer are interpreted as deriving from a common source, again forcing the brain to choose one modality over the other to drive goal-directed actions. The absence of integration is predicted by *Bayesian Causal Inference* (BCI) models of perception (e.g., Körding et al., 2007; Debats et al., 2017), which only integrate multimodal sensory cues as in Equation 1 if they have a common cause but keeps them segregated if they have independent causes.

Here, we probe the neural mechanisms of multimodal sensorimotor control in a task (wrist position stabilization) that allows prolonged time-on-task while also permitting independent manipulation of visual and proprioceptive feedback of task performance. Subjects reclined in a magnetic resonance (MR) scanner and underwent functional MR imaging (fMRI) while stabilizing their hand against two forms of robotic perturbations—constant and random wrist torques—using three different forms of real-time sensory feedback: no visual feedback (i.e., proprioception only), veridical visual feedback wherein a visual cursor tracked hand motion faithfully, and a random vision condition wherein cursor motion was uncorrelated with actual hand motion. We analyzed correlations between blood-oxygenation level-dependent (BOLD) signal fluctuations and time series of visual and proprioceptive performance feedback to probe how the presence and fidelity of visual feedback of task performance impacts task-related activations in a cerebello-thalamo-cortical neural circuit previously associated with mechanical stabilization of the upper extremity (cf, Suminski et al., 2007a). We examined the extent to which the neural correlates of multisensory integration for control align with predictions of the MLE and BCI models of perception. The results advance a fundamental understanding of how sensory context impacts information processing in the neural circuits responsible for feedback stabilization of the hand against unpredictable environmental perturbations.

MATERIALS AND METHODS

Twelve right-handed adults (4 female) participated in this study. Subjects were between the ages of 19 and 48 years (27.5 ± 8.4 year; mean ± 1 SD, here and elsewhere). All subjects were strongly right-handed according to the Edinburgh Handedness Inventory (Oldfield, 1971). Exclusion criteria included: Significant neurological, psychiatric or other medical history, currently taking psychoactive medications, and additional exclusion criteria specific to MR scanning: Ferrous objects within the body, weight inappropriate for height, pregnancy, low visual acuity, or a history of claustrophobia. No participants were excluded from this study based on these criteria. Written informed consent was obtained from each subject in accord with the Declaration of Helsinki and with the institutional guidelines of Marquette University and the Medical College of Wisconsin.

Experimental Procedure

Subjects rested supine in a 1.5T General Electric Signa scanner (General Electric Healthcare, Milwaukee, WI) at Froedtert Memorial Lutheran Hospital in Milwaukee, Wisconsin. The scanner was equipped with a 3-axis local gradient head coil and an elliptical endcapped quadrature radiofrequency coil. The subjects' heads were constrained by foam padding to reduce motion inside the head coil. With arms at their sides, subjects grasped the handle of a MR-compatible, 1 degree-of-freedom robotic manipulandum with their right hands (**Figure 1A**). The handle's axis of rotation was aligned with that of the wrist. The frame of the device was secured to both the subject's forearm and the inner wall of the scanner bore for support. The robot includes a pneumatic actuator that exerts computer-controlled torques about the wrist. Analog measurements of pressure within the actuator were amplified and low-pass filtered with a cutoff frequency of 20 Hz. The torque applied at the wrist joint was computed based on the pressure in the actuator and the moment arm of the device. Robotic signal processing and control was performed at a rate of 1,000 samples per second. Additional details of the robotic system's design, performance and MR-compatibility are described elsewhere (Suminski et al., 2007b).

Each subject performed a series of wrist stabilization tasks while simultaneously undergoing fMRI scanning. A single stabilization trial was conducted in 5 phases (**Figure 1B**). Phase 1: During the 30 s prior to stabilization onset, the subject was instructed to relax while the robot held the hand in a comfortable resting posture θ_r (40° flexion). Phase 2: 3 s prior to the start of stabilization, the robot moved the relaxed hand to the target posture (20° flexion) and held it there until stabilization onset. Phase 3: During the stabilization period itself (30 s in duration), subjects were instructed to maintain wrist position against one of two types of extensor torque loads. In one, the robot was programmed to apply a predictable, *constant torque* (***CT***, mean = 1.2 Nm). In the other, the device applied *pseudo-random torques* (***RT***) consisting of band-limited, Gaussian, "white" noise (1.2 ± 1.1 Nm) having the same average extensor torque as the constant perturbation and a low-pass cutoff frequency of 1.6 Hz. Phase 4: At the end of the stabilization period, the subject was instructed to relax as the robot moved the passive hand back to its resting position at 40° flexion. Phase 5: the subject rested until the start of the next trial.

Although direct view of the wrist was precluded, a wedge-shaped cursor (**Figure 1C**) was sometimes projected onto a screen at the subject's feet using a back-projection LCD projector. This cursor represented error between current and desired wrist angles. Subjects viewed the screen using prism glasses, which allowed them to see the visual feedback while lying on their back as if it were displayed on a screen placed directly in front of them. Subjects were provided with one of three types of visual feedback during stabilization: *true vision* (***TV***), *pseudo-random vision* (***RV***), and *no vision* (***NV***). Accurate real-time feedback of wrist angle relative to the target angle was provided in the ***TV*** condition. In the ***RV*** condition, a "surrogate" band-limited Gaussian noise signal replaced the actual wrist angle for computing real-time location of cursor feedback. Surrogate visual feedback was matched to the hand displacement profiles under ***RT*** perturbation both in range and spectral content, but was constructed to include no significant temporal correlation with the pseudo-random torque perturbation sequence. This construction ultimately allowed for independent assessment of neural correlates of physical (proprioceptive) and visual feedback of performance errors. In the ***NV*** condition, no cursor wedge was displayed. In all cases however, a thin, stationary fixation target was displayed in the center of the display screen in an attempt to minimize extraneous eye movements.

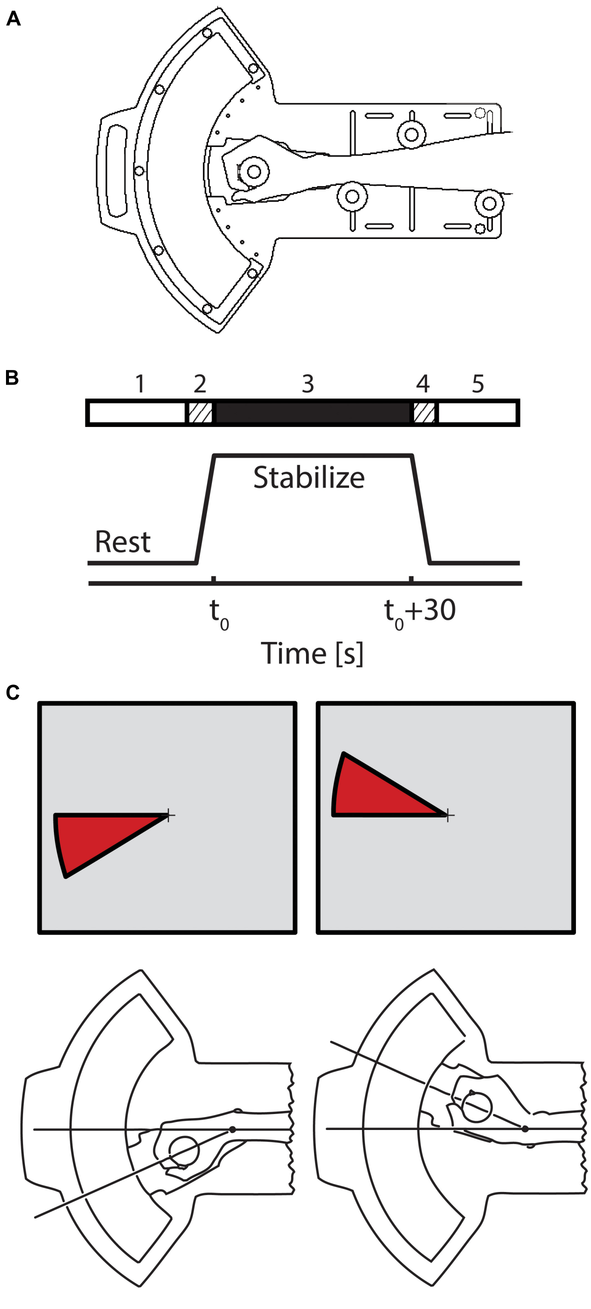

FIGURE 1 | (A) Schematic representation of the 1 degree of freedom pneumatic manipulandum illustrating how the subject interfaces to the device. **(B)** A single trial was conducted in 5 phases. During the 30 s prior to stabilization (phase 1), the subject was instructed to relax while the robot held the hand in a comfortable posture of 40° flexion. Three seconds prior to the start of stabilization (phase 2), the robot moved the relaxed hand to the target posture (20° flexion) and held it there until the onset of the stabilization period. During stabilization periods (phase 3), subjects were instructed to maintain their wrist position at 20° flexion. At the end of the stabilization period, the subject was instructed to relax, and the robot moved the passive hand to its resting position at 40° flexion (phase 4) after which the subject rested (phase 5) in preparation for the next trial. **(C)** On select trials, visual feedback of wrist angle was provided *via* a wedge-shaped cursor projected onto a vertical display screen. A small fixation point (cross hairs) was visible in the middle of the screen throughout the entire experiment.

Each subject participated in a single, blocked-design experiment requiring alternating periods of rest and active stabilization. Each subject performed 10 functional imaging "runs," which included each of the 6 trial types (2 torque × 3 visual conditions) presented one time per run in pseudo-random order. During each run, whole-brain images were acquired using a single-shot, blipped gradient-echo echo-planar pulse sequence (19 contiguous sagittal 7-mm slices, TE = 40 ms, TR = 2.5 s, 90° flip angle, FOV = 24 cm, 64 × 64 matrix, 3.75-mm in-plane resolution). Blood-oxygenation level-dependent (BOLD) signal contrast was used to image hemodynamic-related changes evoked by stabilization in the 6 trial conditions. High-resolution 3D spoiled gradient recalled at steady-state T1-weighted anatomic images also were collected prior to functional imaging for subsequent anatomic localization and co-registration of the functional images (TE = 5 ms, TR = 24 ms, 40° flip angle, slice thickness = 1.2 mm, FOV = 24 cm, 256 × 192 matrix).

Behavioral Data Analysis

Time series of wrist joint angle and joint angular velocity were low-pass filtered at a cutoff frequency of 10 Hz. Stabilization was evaluated using several kinematic performance measures. We computed *objective stabilization error* $\varepsilon_o(nT)$ as the difference between the actual and desired (target) hand positions:

$$\varepsilon_o(nT) \;=\; \theta(nT) - \theta_t \tag{2}$$

where θ_t is the targets wrist angle (20° flexion) and $\theta(nT)$ is the instantaneous wrist angle at sample instant nT. To compare objective performance across stabilization conditions, we then computed the root mean square (RMS) value of this objective error time series throughout each 30-s trial (i.e., $RMS(\varepsilon_o(nT))$).

We quantified *drift* in the instantaneous joint angle equilibrium position by fitting a first-order polynomial to the joint angle time series data over the final 20 s of each trial. We only considered the final portion of each trial to avoid start-up transients that were visible within the first 5 s on some trials. Drift was considered significant in those trials where the slope of the regression line was statistically different from zero. This polynomial defined the subjective wrist target angle $\theta_s(nT)$ as the instantaneous reference angle about which small corrections were observed. We used $\theta_s(nT)$ to estimate a *subjective stabilization error* $\varepsilon_s(nT)$ [i.e., the instantaneous deviations of the wrist about $\theta_s(nT)$]:

$$\varepsilon_s(nT) \;=\; \theta(nT) - \theta_s(nT)\,. \tag{3}$$

We compared subjective performance across stabilization conditions using the $RMS(\varepsilon_s(nT))$ value computed in each trial.

We constructed an estimate of subjective wrist *state estimation errors* $\varepsilon_q(nT)$ during phases 2 through 4 of each trial (i.e., during stabilization as well as during the preceding and following passive movement phases) under the assumptions that during trial phases 2 and 4, passive movement of the wrist induced a discrepancy between actual limb position and the angle expected given the recent history of motor output (resting angle $\theta_r = 40°$ flexion; target angle $\theta_t = 20°$ flexion), whereas during phase 3, state estimation errors would arise from load-induced deviations from the subjective target angle $\theta_s(nT)$. Specifically,

$$\varepsilon_q(nT) = \begin{cases} \theta(nT) - \theta_r; & phase\ 2 \\ \varepsilon_s(nT); & phase\ 3 \\ \theta(nT) - \theta_t; & phase\ 4 \end{cases} \tag{4}$$

The time series of $\varepsilon_q(nT)$ were used to compute RMS values of limb state estimation errors on a moment-by-moment basis [i.e., within each 2.5 s (2,500 sample) integration window, thereby emulating the temporal sampling of the functional imaging pulse sequence, TR], thus obtaining $RMS_{TR}(\varepsilon_q(m))$, where m is an index running from 1 to the total number of TR sampling intervals spanning phases 2 through 4 of the trial.

We quantified *visual stabilization error* $\varepsilon_v(nT)$ during trial phase 3 as the difference between the instantaneous visual representation of wrist angle and the target wrist angle (i.e., the angular size of the wedge-shaped cursor). Because visual feedback faithfully tracked wrist angle during trials with ***TV*** feedback and because visual feedback was absent during ***NV*** trials, $\varepsilon_v(nT)$ was quantifiably distinct from $\varepsilon_s(nT)$ only during ***RV*** trials. For subsequent use in functional neuroimage analysis, we computed the RMS value of $\varepsilon_v(nT)$ within 2.5 s integration windows to emulate the temporal sampling of the functional imaging pulse sequence, thus obtaining $RMS_{TR}(\varepsilon_v(m))$.

Statistical Inference for Behavioral Performance Measures

Objective RMS stabilization errors and the unsigned magnitude of positional drift were averaged within subject by trial type. Individual 2-way repeated measures ANOVA assessed differences in stabilization error and drift due to the two factors: Torque perturbation type (***RT***, ***CT***) and visual feedback type (***TV***, ***NV***, or ***RV***). *Post-hoc* Tukey *t*-tests were used to identify the source of significant main and interaction effects. Statistical testing was carried out within the Minitab computing environment (Minitab, Inc., State College, PA). Effects were considered statistically significant at the $\alpha = 0.05$ level.

Functional MR Imaging Data Analysis

Functional MR images were generated and analyzed within the Analysis of Functional NeuroImages (AFNI) software package (Cox, 1996). During each run, a total of 156 images were collected at each voxel yielding a total run duration of 6.5 min. The three images at the beginning and end of each run were discarded to allow for equilibration of the magnetic field. For each subject, the resulting 150 point time series from each of the 10 imaging runs were first concatenated into one large dataset. We then used an interactive, linear, least squares method to align the images in three-dimensional space to counteract the effects of head motion. Registration yielded 6 movement indices per functional imaging run. The across-subjects average head movement for the rotation indices were 0.63 ± 0.4°, 0.29 ± 0.16°, and 0.55 ± 0.44° (rotations in the superior-inferior, anterior-posterior, and left-right planes, respectively); average translational head movement were 0.95 ± 0.49 mm, 0.43 ± 0.28 mm, and 0.53 ± 0.24 mm (translation in the superior-inferior, anterior-posterior, and left-right direction, respectively). No subjects or trials were excluded from further analysis due to head motions because none were found to exceed $^1/_2$ the smallest voxel dimension.

In a previous study (Suminski et al., 2007a), we asked subjects to stabilize their wrists against robotic perturbations in the absence of ongoing visual feedback and used a hierarchical multilinear regression technique to identify BOLD signal correlates of error corrections that operate over longer (trial-by-trial) and shorter (TR-by-TR) time scales. Here, we extended that approach to determine how the neural mechanisms regulating hand position respond to the presence and fidelity of visual feedback of ongoing performance. To do so, we modeled BOLD signal fluctuations within each voxel as a combination of three independent sources of variability: (1) nuisance variables common to fMRI data collection (i.e., head motion and baseline BOLD signal drift); (2) factors generally related to the performance of the visuomotor stabilization task that do not change from one trial to the next; and (3) factors related to both visual and proprioceptive performances errors that changed from TR-to-TR. In our analysis, unmodeled signal variations that remained after an initial block-wise analysis (*Stage 1 Regression—Baseline Noise Model and Block-by-Block Effects*) became the input to a subsequent TR-by-TR analysis focusing on moment by moment changes in task performance (*Stage 2 Regression—TR-by-TR Effects*).

Stage 1 Regression—Baseline Noise Model and Block-by-Block Effects

We performed an initial voxel-wise multiple linear regression analysis that served two purposes: (1) To remove from the fMRI dataset all BOLD signal modulations correlated with nuisance cofactors such as head motion and baseline drift; and (2) to identify fMRI signal fluctuations that were related generally to execution of the wrist stabilization task under each testing condition but did not vary in a manner reflecting moment-by-moment task performance. The baseline noise model included the six time series of head motion indices obtained from the spatial registration process (sample interval = 1 TR). By including these subject- and run-specific nuisance factors in the multilinear regression, we reduced the likelihood of false positive results due to stimulus-correlated motion. Next, we defined an input reference function for each of the six stabilization conditions to model general task-dependent effects. These time series were assigned a value of 1 during their respective stabilization periods and 0 otherwise. Each of these reference functions was created separately for each run performed by each participant, reflecting the pseudo-randomized presentation order of task conditions across runs and participants. Each time series was then convolved with a γ-variate function to model the temporal filtering properties of the hemodynamic response.

Stage 2 Regression—TR-by-TR Effects

The purpose of the Stage 2 analysis was to identify BOLD signal variations that correlated significantly with the moment-by-moment (TR-by-TR) changes in wrist or cursor positioning errors [i.e., $RMS_{TR}(\varepsilon_q)$ and $RMS_{TR}(\varepsilon_v)$, respectively]. We restricted this event-related analysis to include trials only wherein subjects experienced persistent physical perturbations and subsequent error corrections (i.e., ***RT*** conditions) or visual feedback that varied moment by moment (i.e., ***TV*** and ***RV*** conditions). Therefore, ***CTTV*** and ***CTNV*** trials were not included in this analysis because performance errors were relatively constant throughout the trial. Note that in ***RTTV*** trials, proprioceptive and visual performance errors were perfectly correlated whereas in ***RTRV*** trials, proprioceptive and visual performance errors were minimally correlated.

We therefore created a total of four reference functions to explore the relationship between BOLD fluctuations and behavioral errors. Two of these time series were derived from the ***RTNV*** and ***RTRV*** conditions on a TR-by-TR basis; they quantified performance errors that could be sensed proprioceptively. The time series derived from the ***CTRV*** and ***RTRV*** conditions quantified TR-by-TR variations in visual errors that were distinct from proprioceptive errors. The last reference function was derived from the ***RTTV*** condition, and it jointly represented both proprioceptive and visual errors when they were highly correlated. The proprioceptive and visuomotor reference function values at each TR sampling instant were defined, respectively, by the $RMS_{TR}\left(\varepsilon_q\right)$ and $RMS_{TR}\left(\varepsilon_v\right)$ values computed during the corresponding 2.5 s TR sampling period. Each of these reference functions was created separately for each run performed by each participant, and then convolved with a γ-variate function to model the temporal filtering of the hemodynamic response.

Statistical Inference for Functional MR Imaging Data

Functional images resulting from the hierarchical multilinear regressions were interpolated to obtain a volumetric grid having 1 mm^3 voxel volumes, co-registered, and then converted into the Talairach stereotaxic coordinate space. To facilitate across-subjects analyses, the normalized functional images were spatially blurred using a 4-mm Gaussian, full-width half-maximum filter to compensate for inter-subject anatomical variability. In all across-subject analyses, a cluster-size and thresholding technique was used to correct for multiple comparisons in the group analysis to reduce type-I inference errors at the $\alpha = 0.05$ level. We performed a 10,000-iteration Monte-Carlo simulation using the *3dClustSim* tool within AFNI to identify cluster sizes and individual voxel *p*-values appropriate for the Stage 1 block-wise effects analysis (cluster size: 289 μl; individual voxel *p*-value: 0.001). A second 10,000-iteration Monte-Carlo simulation was performed to identify cluster sizes and individual voxel *p*-values appropriate for the Stage 2 event-related analysis (cluster size: 505 μl; individual voxel *p*-value: 0.005). The use of a less conservative individual voxel probability value in the TR-by-TR effects analysis was justified because the BOLD signal fluctuations of interest were small and embedded within the residuals of the Stage 1 analysis. The locations of activated regions in the group statistical parametric maps were obtained using the integrated atlas within AFNI. Surface based representations of cortical activations were visualized using CARET (Van Essen et al., 2001).

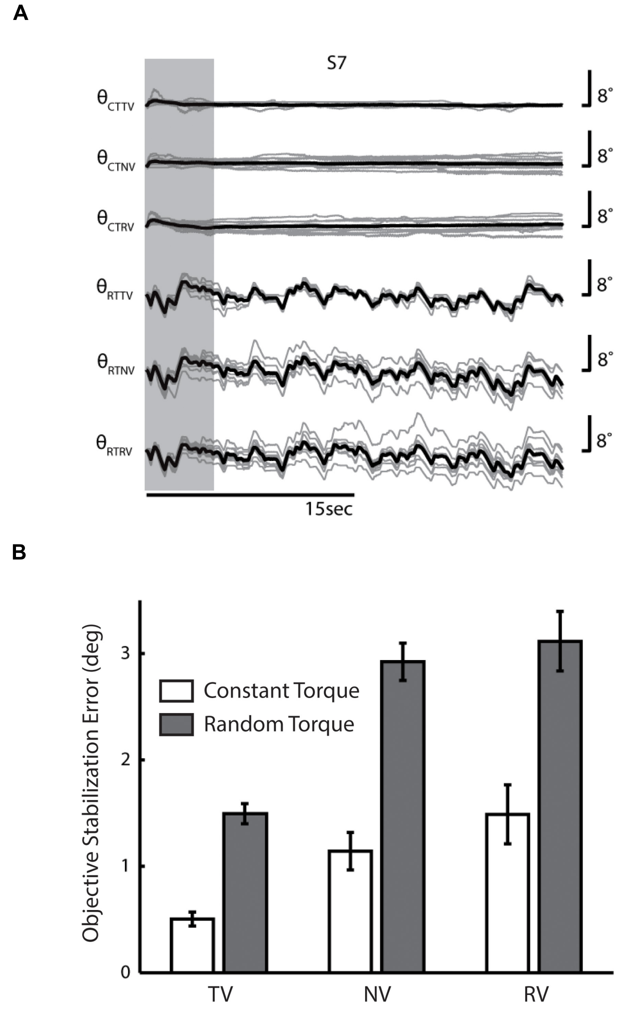

FIGURE 2 | (A) Wrist angle error θ for a representative single subject (S7) in each of the six combinations of two environmental loads (***CT***, constant torque; ***RT***, random torque) and three sensory feedback conditions (***TV,*** true vision; ***NV***, no vision; ***RV***, random vision). Light gray lines indicate the subject's performance on individual trials, whereas heavy black lines denote the mean performance of the subject across trials. Vertical gray band: initial portion of data where startup transients were frequently observed. **(B)** Population statistics—comparison of averaged RMS wrist angle errors across feedback conditions (***CT***, white bars; ***RT***, shaded bars). Error bars indicate the 95% confidence interval about the mean (i.e., ± 1.96 * standard error).

For the analysis of BOLD signal activations on a longer (block-by-block) time scale, we analyzed the functional neuroimaging data in a manner similar to our analysis of behavioral data: we used a 3-way, mixed-model, repeated measures ANOVA (treating subjects as a random factor) to identify voxel clusters exhibiting BOLD signal fluctuations that correlated systematically with variations in load type, visual feedback condition, and the interaction of these two factors. First, we used *post-hoc t*-tests to identify patterns of neural activity that were related—in a general sense—to the active compensation for wrist position

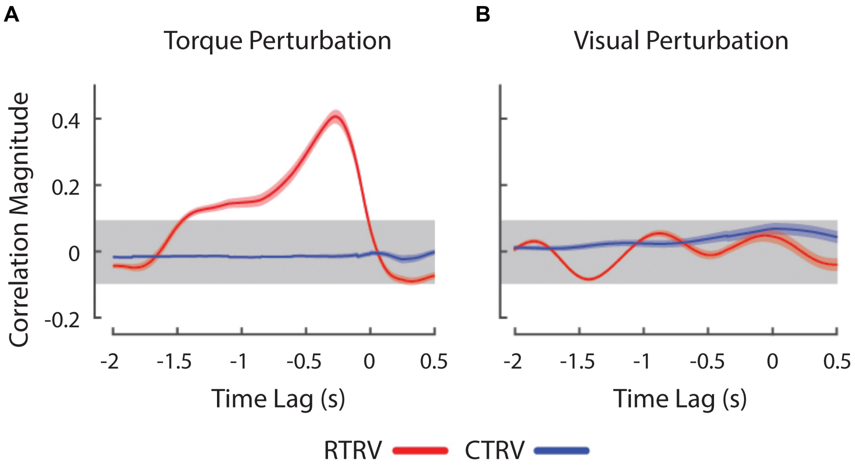

FIGURE 3 | Cross-correlation between wrist angle and experimental perturbations during ***RTRV*** (red lines) and ***CTRV*** (blue lines) trials. **(A)** Cross-correlation between wrist angle and the ***RT*** perturbation averaged across subjects. **(B)** Cross-correlation between the wrist angle and ***RV*** perturbation averaged across subjects. Peaks at negative lags denote conditions where changes in the perturbation precede movement of the wrist in time. The horizontal gray band represents an empirical estimation of the spurious correlation associated with the time series. Error envelopes indicate 1 standard error about the mean correlation.

errors (the "Error Correction" contrast). We did so by contrasting BOLD signal changes (relative to rest) across the task conditions requiring stabilization against random vs. constant torque perturbations (i.e., the three ***RT*** conditions vs. the three ***CT*** conditions). Second, we used the results of *post-hoc t*-tests to visualize the neural mechanisms responding to visual motion of the cursor during stabilization (the "Visual Motion" contrast). Here, we contrasted the {***RTTV***, ***RTRV***} conditions vs. the ***RTNV*** condition, ignoring all ***CT*** conditions wherein motion of the cursor was absent (***CTNV***), negligible (***CTTV***), or obviously discrepant (***CTRV***). Finally, we examined the interaction between the two factors by performing a set of three contrasts that explored how neural activities related to error correction are modulated by the presence and fidelity of real-time visual feedback (the "Visual Interaction Effect"). Here, we used three separate *t*-tests to contrast BOLD signal responses across ***RT*** vs. ***CT*** stabilization tasks during the three visual feedback conditions (i.e., ***RTNV-CTNV, RTTV-CTTV,*** and ***RTRV-CTRV***).

Next, motivated by our previous finding that BOLD signal contrast within brain regions involved in the proprioceptive control of wrist position are sensitive to performance errors on a moment-by-moment basis (Suminski et al., 2007a), we used a 2 way, mixed-model, repeated measures ANOVA (treating subjects as a random factor) to identify voxel clusters exhibiting BOLD signal fluctuations that correlated significantly with TR-by-TR changes in performance errors. This analysis of error corrections on a short, moment-by-moment time scale used the four separate and orthogonal reference functions that captured the TR-by-TR variations in hand and cursor motion as described earlier (*Stage 2 Regressions—TR-by-TR Effects*). For this analysis, we applied *post-hoc*, voxel-wise *t*-tests (against 0) to the regression coefficients for each reference function to identify BOLD signal correlates of TR-by-TR changes in performance errors sensed proprioceptively (***RTNV*** and ***RTRV***), visually (***CTRV*** and ***RTRV***), or jointly (***RTTV***). Finally, we planned two additional contrasts to explore how neural activities related to the TR-by-TR correction of proprioceptive errors are modulated by the presence and fidelity of real-time visual feedback (i.e., separate *t*-tests performing the ***RTTV-RTNV*** and ***RTRV-RTNV*** contrasts.

RESULTS

Behavioral Correlates of Sensorimotor Stabilization

We first sought to determine the extent to which the presence and fidelity of visual feedback and differences in load type might have elicited differences in performance during stabilization. Because torque perturbations were biased into wrist extension in all task conditions, subjects were required to actively engage in the task to perform with any degree of success. If they were to "give up," the wrist would be driven into the robot's mechanical limits at 30° extension. Because no wrist angle trajectories were observed to reach and remain at 30° extension, we infer that all of the participants performed in a task-appropriate manner on every trial. Nevertheless, wrist angle deviations from the target were variably compensated both within and between trials; subjects were able to recover the desired reference position only on average across many trials (**Figure 2A**).

Linear regression found significant drift in wrist angle as a function of time in the vast majority of trials (***RTTV:*** 79% of trials, with the absolute magnitude of drift averaging 0.05 ± 0.03°/s; ***RTNV:*** 98%, 0.14 ± 0.06°/s; ***RTRV:*** 98%, 0.14 ± 0.06°/s; ***CTTV:*** 76%, 0.01 ± 0.01°/s; ***CTNV:*** 77%, 0.03 ± 0.02°/s; ***CTRV:*** 79%, 0.03 ± 0.02°/s). In all cases, drift was evenly distributed about the target angle and varied randomly from one trial to the next. The magnitude of positional drift varied both by load type [$F_{(1,\ 60)} = 135.7$, $p < 0.0005$] and by visual feedback condition [$F_{(2,\ 60)} = 19.8$, $p < 0.0005$]. The interaction between these

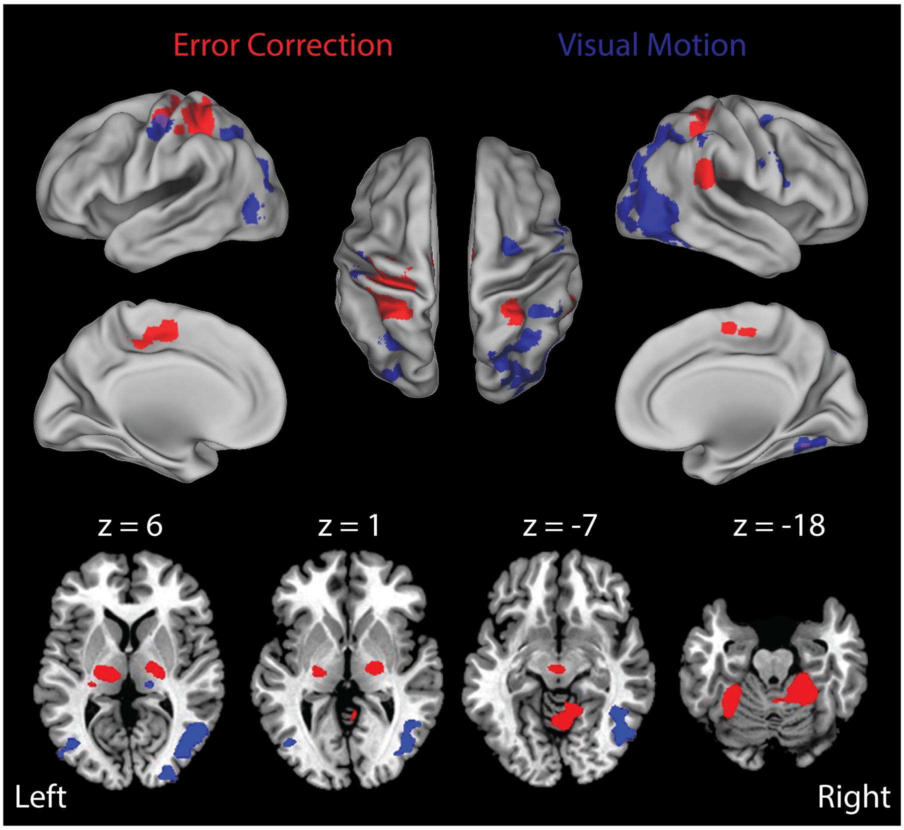

FIGURE 4 | Results of the Stage 1 voxel-wise multiple linear regression: block-by-block effects. BOLD signal correlates of ongoing error correction and visual motion are depicted in separate arbitrary colors that should not be interpreted as a "heat map" signal intensity. Red: functional activation maps for the study population showing the regions of interest (ROIs) that exhibited significantly enhanced activation during stabilization against random environmental torques relative to constant torques (***RT*** > ***CT***) (i.e., the "Error Correction" contrast). This contrast highlights activities related to ongoing error correction (***RT*** trials) above and beyond those related more generally to the wrist stabilization task (***CT*** trials). We observed prominent activation within a cerebello-thalamo-cortical network when stabilizing against unpredictable loads as opposed to predictable loads. Blue: ROIs that exhibited enhanced activation during stabilization in ***RT*** trials with visual motion (the ***RTTV*** and ***RTRV*** cases) relative to stabilization in ***RT*** trials with no visual motion (the ***RTNV*** case) (i.e., the "Visual Motion" contrast). We observed prominent activation within secondary- and higher-order visual processing areas including middle/inferior occipital gyrus, middle temporal gyrus, fusiform gyrus, inferior parietal lobule and premotor cortex. Colored areas indicate regions that were shown to be significantly active in these contrasts at the $p < 0.05$ level of significance (corrected for multiple comparisons). Top: activations mapped onto inflated representations of the cerebral hemispheres; bottom: subcortical activations in the basal ganglia and thalamus (left: $z = 6$; center-left: $z = 1$) and anterior cerebellar cortex (center-right: $z = -7$; right: $z = -18$).

factors was also significant [$F_{(2,\ 60)} = 8.9$, $p < 0.0005$]. *Post-hoc t*-tests found that the magnitude of drift was greatest when subjects were perturbed by pseudo-random torques without reliable visual performance feedback (***RTNV*** and ***RTRV*** **vs.** ***all other cases***; $p < 0.0005$). In the ***TV*** cases, drift was approximately one third that observed in the ***NV*** and ***RV*** cases, regardless of perturbation type. The magnitude of drift observed here is consistent with that reported in an earlier study of limb stabilization without concurrent visual feedback of performance (Suminski et al., 2007a).

Next, we investigated the effects of load type and visual feedback on the RMS objective stabilization performance. We found significant main effects of both load type and visual feedback condition on RMS objective stabilization performance as shown in **Figure 2B** [Load Type: $F_{(1,\ 60)} = 87.1$, $p < 0.0005$; Visual Feedback: $F_{(2,\ 60)} = 27.0$, $p < 0.0005$]. The interaction between load type and visual feedback condition failed to reach statistical significance. On average, subjects were less able to maintain steady hand posture while being perturbed by band-limited pseudo-random torques than by constant torques ($p < 0.0005$). Relative to the ***TV*** conditions, performance degraded markedly as visual feedback was made less reliable (***RV***: $p < 0.0005$) or was eliminated altogether (***NV***: $p < 0.0005$). We found no difference in performance between the ***NV*** and ***RV*** conditions, raising the possibility that subjects might have ignored the visual feedback provided during both ***RV*** conditions. To investigate this possibility, we computed the cross correlation between objective stabilization error and the torque or visual perturbation on ***CTRV*** and ***RTRV*** trials (**Figure 3**). As expected, we observed strong, positive cross-correlations between torque perturbation and stabilization error on ***RTRV*** trials at a time lag averaging −273 ms (i.e., with torque perturbations leading errors by about 1/4 s). In contrast, we found no evidence of correlation between objective stabilization errors and the visual perturbation on ***CTRV*** and ***RTRV*** trials. This supports the supposition that subjects severely discounted visual feedback on these two trial types, even though the magnitude and spectral content of the visual error signals were similar to those in the ***RTTV*** case, which exhibited much smaller performance errors.

Neural Correlates of Sensorimotor Stabilization

Stage 1 Analyses: Block-by-Block Effects

As noted above, participants never "gave up" and each engaged in active feedback stabilization of the wrist on every trial. **Figure 4** presents the results of our Stage 1 block-by-block analyses, wherein we separately examined the effects of load type and visual feedback conditions on the neural mechanisms engaged during wrist stabilization. Shown in red are regions of interest (ROIs) that exhibited enhanced BOLD signal activation in block conditions requiring active stabilization against ***RT*** perturbations that elicit richly persistent errors, relative to blocks requiring stabilization against ***CT*** loads that elicit significantly smaller errors (**Figure 4**, Error Correction contrast). Because the ***RT*** and ***CT*** perturbations had identical average extensor torque magnitudes (1.2 Nm in both cases), observed differences in this contrast were not due to differences in average torque applied in the two conditions. Consistent with our previous report (Suminski et al., 2007a), active compensation for kinematic performance errors elicits enhanced BOLD signal activation in the cerebello-thalamo-cortical pathways known to be engaged in the feedback control of upper limb movements. Shown in blue are ROIs that exhibited enhanced BOLD signal activation in block conditions having a moving visual cursor, relative to blocks where the cursor was stationary (**Figure 4**, Visual Motion contrast). As expected, the presence of a moving visual cursor elicited bilateral activations in areas known to process visual motion information and to coordinate movements of the eyes and hands. Broadly speaking, these ROIs include portions of the occipital, posterior parietal, and premotor cortices (**Table 1**).

Next, we investigated how the neural activities related to error correction were modulated by the presence and fidelity of real-time visual feedback (i.e., the interaction between load type and visual feedback condition). We did so by performing a more fine-grained block-wise analysis that involved three additional t-test contrasts to visualize how BOLD signal activations in the cerebello-thalamo-cortical pathway vary across the three visual feedback conditions (i.e., ***RTNV-CTNV, RTTV-CTTV,*** and ***RTRV-CTRV***; **Table 2**). As shown in **Figure 5**, active stabilization in the absence of visual feedback (i.e., the NV contrast ***RTNV-CTNV***; red ROIs) elicits activations that are largely restricted to regions in cerebello-thalamo-cortical pathways. While activations in this error correction network persist when visual feedback of cursor position is available regardless of fidelity (**Figure 5**, TV and NV and RV, cyan regions), we found that activations also expand into neighboring areas and appear in new brain regions when veridical visual feedback was available (**Figure 5**, TV: ***RTTV-CTTV***; blue ROIs). During ***TV*** conditions (relative to ***NV*** conditions), cortical activations in the left primary sensorimotor cortex, cerebellum and bilateral parietal cortex increase in volume encompassing areas traditionally associated with the processing of visuomotor information. Further, additional cortical activations appear in the right premotor cortex, bilateral inferior parietal lobule and left occipital/temporal cortex. Of particular interest are the subcortical activations related to error correction with veridical visual and somatosensory feedback. These areas include the left cerebellar cortex and bilateral ventral lateral nucleus of the thalamus. By contrast, providing incongruent visual feedback (**Figure 5**, RV: ***RTRV-CTRV;*** yellow ROIs) induced an anterior migration of the stabilization activation volume further into areas known to process somatosensory information, suggesting that subjects exerted additional attentional focus on proprioceptive rather than visual feedback when the two feedback sources were in conflict. This migration (from blue ROIs to the cyan, green, and yellow ROIs) is most prominently observed in the left parietal cortex and left thalamus ($z = 13$).

Stage 2 Analyses: Neural Correlates of Error Correction on a TR-by-TR Time Frame

As mentioned earlier, a previous neuroimaging study has identified distinct neural networks responsible for processing somatosensory-motor errors on long and short time scales during wrist stabilization (i.e., over the full duration of 30 s trials and from one moment to the next; Suminski et al., 2007a). We used a similar approach to probe how the presence and integrity of visual feedback impacts the processing of performance errors on a moment-by-moment basis. Here, residuals from the Stage 1 regression were used as inputs to the Stage 2 TR-by-TR regressions, which sought to identify BOLD signal changes that correlate significantly with performance errors felt proprioceptively [$RMS_{TR}\left(\varepsilon_q\right)$] or observed visually [$RMS_{TR}\left(\varepsilon_v\right)$]. In contrast to the Stage 1 analyses, the Stage 2 analyses examine neural correlates of information processing specifically related to visual and proprioceptive sensations of stabilization performance errors that fluctuate on a relatively short timescale (i.e., from one 2.5 s TR to the next).

Many regions exhibited BOLD signal changes that were correlated with the time series of somatosensory performance errors $RMS_{TR}\left(\varepsilon_q\right)$. **Figure 6** (and **Table 3**) presents ROIs exhibiting significant TR-by-TR correlations with $RMS_{TR}\left(\varepsilon_q\right)$ in each of the three ***RT*** trial conditions with rich, persistent, physical perturbations (***TV***: blue; ***NV***: red; ***RV***: yellow). Additional colors indicate regions of overlapping activations for the three feedback conditions. A comparison of BOLD signal correlations during the ***NV*** condition with the ***TV*** and ***RV*** conditions found that the addition of visual feedback generally caused marked changes in the overall network activity (a drop-out of prefrontal activation as well as dramatically increased activity in bilateral superior/inferior parietal lobule, right superior temporal/middle occipital cortex and left cerebellar cortex). This was particularly true when visual and proprioceptive feedback were congruent; the presence of veridical visual feedback and the neural activities it evoked enabled subjects to enhance wrist stability as shown in **Figure 2B**. In ***RV*** trials with visuo-proprioceptive conflict, representation of hand stabilization error information was greatly

TABLE 1 | Regions exhibiting significant activation in the Stage 1 (block-by-block) contrasts examining error correction and visual motion.

		Talairach coordinates				
	Hem	***X* (mm)**	***Y* (mm)**	***Z* (mm)**	**Volume (μl)**	**Mean T**
Error Correction						
Precentral gyrus (BA 4,6)	L	–30.2	27.9	51.8	6,798	5.11
Postcentral gyrus (BA 2,3,5)						
Inferior parietal lobule (BA 40)						
Cerebellar cortex (Lobule V, VI)	R	13.7	45.6	–13.1	5,171	5.33
Cerebellar vermis						
Thalamus (VPL, VL, MD, Pulvinar)	L	–16.7	19.3	9.9	3,541	5.07
Cerebellar cortex (Lobule VI)	L	–28.5	46.6	–19.2	1,986	5.73
Inferior parietal lobule (BA 40)	R	57.5	31.9	23.7	1,765	5.12
Thalamus (VPL, VL)	R	17.8	15.5	7.3	1,698	5.03
Medial frontal gyrus (BA 6)	L	–4.6	12.4	48.5	1,216	4.88
Postcentral gyrus (BA 3,40)	R	25.8	34.9	54.1	1,098	5.43
Inferior parietal lobule (BA 40)						
Red nucleus/thalamus	L	–2.2	20.1	–5.6	404	4.98
Visual motion						
Sup./Mid./Inf. Occipital Gyrus (BA 18,19)	R	35.4	66.4	14.1	13,268	5.26
Cuneus/precuneus						
Middle temporal gyrus (BA 39)						
Sup./Inf. parietal lobule (BA 7,40)						
Fusiform gyrus (BA 37)						
Superior parietal lobule (BA 7)	L	–28	55.5	45.3	938	5.02
Mid./Inf. occipital gyrus (BA 19,37)	L	–40.5	68.8	3.4	936	4.87
Inferior frontal gyrus (BA 9)	R	46.9	–2.5	25.9	834	4.99
Precentral gyrus (BA 4,6)	L	–40.4	12.7	46.8	797	5.21
Middle occipital gyrus (BA 19)	L	–29.3	80.5	21.6	619	5.08
Cuneus						
Middle frontal gyrus (BA 6)	R	23.9	5.5	45.9	518	4.81
Inferior parietal lobule (BA 40)	R	43.5	33.4	41.7	505	5.40
Pulvinar	R	18	27.6	8.7	382	4.96

BA, Broadman's Area; Sup., Superior; Mid., Middle; Inf., Inferior.

expanded in right hemispheric and left cerebellar regions known to respond preferentially to visual stimuli, but this did not enhance wrist stabilization performance as shown in **Figure 2B**.

By contrast, analysis of the Stage 2 multilinear regression identified no significant correlations with the time series of visuomotor errors [i.e., $RMS_{TR}(\varepsilon_v)$] in either ***RV*** condition. Subjects effectively discounted (or ignored) real-time visual feedback of wrist stabilization errors when visual and somatosensory feedback were in conflict, despite the fact that the mechanical and visual error signals varied in time in similar ways, both in range and spectral content. Taken together, these results suggest that our stabilization task elicited a pattern of interaction between visual and proprioceptive feedback sources that did not conform to the predictions of a MLE model of sensory integration, which given the similar variability of the two feedback signals, would instead predict a more balanced contribution of visual and proprioceptive sources.

Finally, we examined how the presence and fidelity of visual feedback impacted the processing of somatosensory performance errors by directly comparing Stage 2 analysis BOLD signal correlations in the ***TV*** and ***RV*** conditions to those in the ***NV*** condition (**Figure 7**). In ***NV*** trials, Stage 2 BOLD signal correlates of right-hand wrist angle errors were strongest in left intermediate cerebellum, and in the right posterior parietal, insula, and frontal cortices (**Figure 7**, NV > 0, green areas). Adding veridical visual resulted in a dramatic increase in the representation of wrist angle error information in the left primary sensorimotor, premotor, superior/inferior parietal cortices, in the right inferior parietal lobule, and in the left thalamus (ventral lateral, ventral posterior lateral and medial dorsal nucleus) (**Figure 7**, TV > NV, orange areas). By contrast, somatosensory-error processing in the presence of incongruent random visual feedback yielded an expansion of the representation of wrist angle error information into the bilateral putamen, exterior segment of the globus pallidus, and the right medial dorsal nucleus of the thalamus (**Figure 7**, RV > NV, purple areas). Activations in these regions suggest their involvement in the context-dependent evaluation of the disparate somatosensory-motor and visuomotor signals and/or the selection of the sensory information feedback channel more

TABLE 2 | Regions exhibiting significant activation in the Stage 1 (block-by-block) analysis of proprioceptive errors during wrist stabilization under three different sensory contexts.

		Talairach coordinates				
	Hem	***X* (mm)**	***Y* (mm)**	***Z* (mm)**	**Volume (μl)**	**Mean T**
RTTV v CTTV						
Postcentral gryus (BA 3)	L	–30.1	31.5	51.8	7,545	5.23
Precentral gyrus (BA 3, 4)						
Inf. parietal lobule						
Sup. parietal lobule (BA 7)						
Precuneus (BA 7)						
Culmen	R	12.2	47.6	–15.1	7,396	5.20
Declive						
Cerebellar lingual						
Nodule						
Culmen	L	–25.8	46.9	–19.8	4,762	5.62
Declive						
Inf. parietal lobule (BA 40)	R	57	31.8	22.9	1,862	5.25
Medial frontal gyrus (BA 6)	L	–2.4	12.2	49	1,846	4.91
Postcentral gryus (BA 40)	R	24.9	36.5	54.2	1,217	5.24
Paracentral lobule (BA 40)						
Thalamus	R	15.7	13.6	9.4	1,049	4.73
Ventral lateral nucleus						
Thalamus	L	–17	17.1	10.7	874	4.62
Ventral lateral nucleus						
Lentiform nucleus						
Inf. parietal lobule (BA 40)	L	–46.3	29.6	24.2	521	4.92
Precentral gyrus (BA 6)	R	30.9	8.4	55.5	429	4.64
Mid. frontal gyrus						
Cerebellar tonsil	L	–23.4	35.9	–44.6	427	5.41
Cerebellar tonsil	R	13.7	48.7	–42.5	422	4.88
Mid. occipital gyrus	L	–37.1	67.5	5.9	396	4.79
Mid. temporal gyrus						
Sup. temporal gyrus (BA 22)	R	53.8	–12.9	–3.8	346	5.49
RTNV v CTNV						
Precentral gyrus (BA 4)	L	–29.8	25.4	52.5	4,096	5.02
Postcentral gyrus (BA 3)						
Culmen	R	16.3	44.8	–13.7	2,192	5.29
Mid. occipital gyrus	R	36.7	72.5	12.6	721	5.21
Medial frontal gyrus (BA 6)	L	–5.5	13.1	47.9	556	4.81
Postcentral gyrus	R	26.5	33.9	54.5	362	5.27
Claustrum	L	–24.2	24	14.2	341	4.92
Insula						
Thalamus						
Thalamus	L	–14.5	18.3	6.8	308	4.78
Ventral posterior med. nucleus						
RTRV v CTRV						
Precentral gyrus (BA 4)	L	–30.3	29	51.7	3,932	5.20
Inf. parietal lobule						
Postcentral gyrus (BA 40)						
Culmen	R	13.7	42.5	-12.2	3,488	5.38
Thalamus	L	–15.1	18	10.1	911	5.28
Lateral posterior nucleus						
Ventral posterior lateral nucleus						
Paracentral lobule (BA 31)	L	–5.8	12	47.2	373	5.02
Cingulate gyrus (BA 31)						
Paracentral lobule	L	–6.8	23.7	42.9	366	4.96
Cingulate gyrus						

BA, Broadman's Area; Sup., Superior; Mid., Middle; Inf., Inferior; Med., Medial.

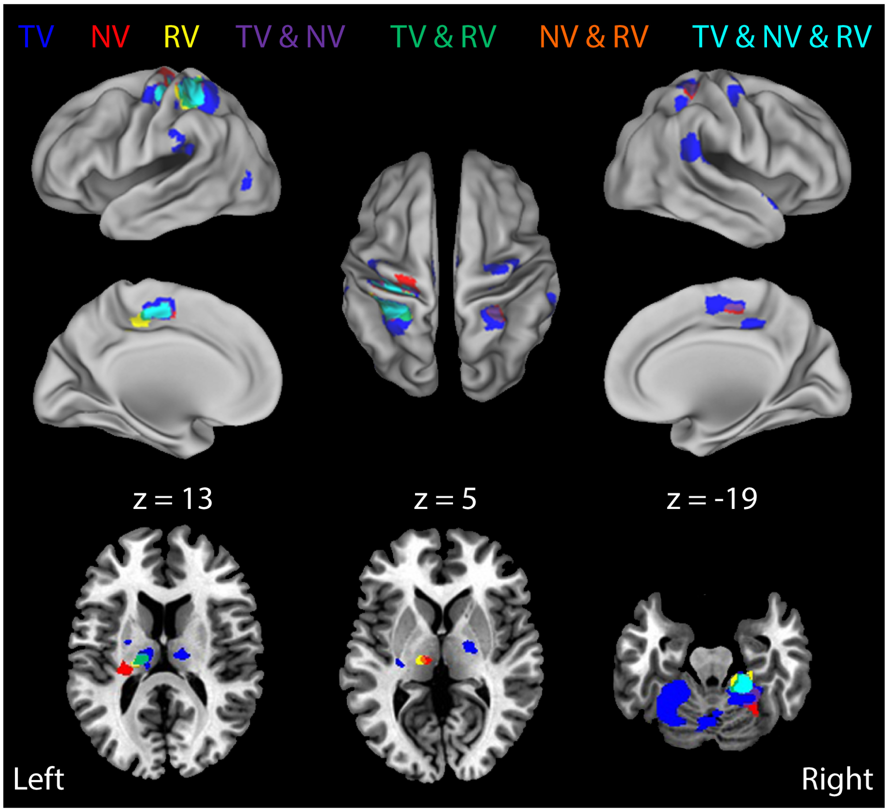

FIGURE 5 | Block-by-block analysis: BOLD signal correlates of ongoing error correction under each of the three visual feedback conditions. Colored regions depict functional activation maps for the study population showing ROIs that exhibited enhanced activation during stabilization against random environmental torques (***RT***) relative to constant torques (i.e., the ***RT*** > ***CT*** contrast) for each of the three different feedback conditions (***TV***: blue; ***NV***: red; ***RV***: yellow). Additional colors indicate regions of overlapping activations (conjunctions) for the three feedback conditions. Neural activities related to error correction are modulated by the presence and fidelity of real-time visual feedback. The results indicate some overlap, but also some differentiation, in regions of activation under the three different feedback conditions.

likely to facilitate success in the context of the current task. In any case, our analyses reveal an absence of Stage 2 correlates with $RMS_{TR}\ (\varepsilon_v)$ and an abundance of Stage 2 correlates with $RMS_{TR}\left(\varepsilon_q\right)$ in each of the three ***RT*** trial conditions. This pattern of results argues against the static MLE model of Eq. 1 as a sufficient description of sensorimotor integration for feedback stabilization of the wrist. Instead, the lack of Stage 2 BOLD correlates with visuomotor errors in the ***RV*** conditions is consistent with a model of sensory integration that also performs causal inference (cf. Debats et al., 2017), i.e., where a lack of kinematic correlation between hand and cursor motion operationally segregates the two sources of feedback prior to integration, with only one of them used subsequently for online limb position control.

DISCUSSION

The primary goal of this study was to examine how the presence and fidelity of visual and proprioceptive feedback impact the neural mechanisms mediating limb stabilization—an important form of mechanical interaction between the body and the environment. To do so, we used a pneumatic robot (Suminski et al., 2007b), functional MR imaging, a long duration wrist stabilization task, and event-related BOLD signal analysis techniques (cf., Suminski et al., 2007a) to elucidate the neural circuits that integrate sensory information from visual and proprioceptive sources to stabilize the wrist against environmental perturbations. In our study, the presence and relative reliability of visual feedback was manipulated, allowing to test whether rules governing integration of visual and proprioceptive information for limb stabilization might conform to models of how the brain uses multisensory feedback for perception (Tillery et al., 1991; Ernst and Banks, 2002; van Beers et al., 2002; Ernst, 2006; Körding et al., 2007; Reuschel et al., 2010; Seilheimer et al., 2014; Debats et al., 2017). In corroboration with a prior neuroimaging study of wrist stabilization in the absence of concurrent visual feedback (Suminski et al., 2007a), we found that wrist stabilization elicited activation in a cerebello-thalamo-cortical circuit known to be engaged in the active feedback control of the upper limb. Relative to a no-vision stabilization condition, the addition of veridical, task-related visual feedback caused activations in the cerebello-thalamo-cortical network to expand (**Figures 5–7**), ultimately yielding a

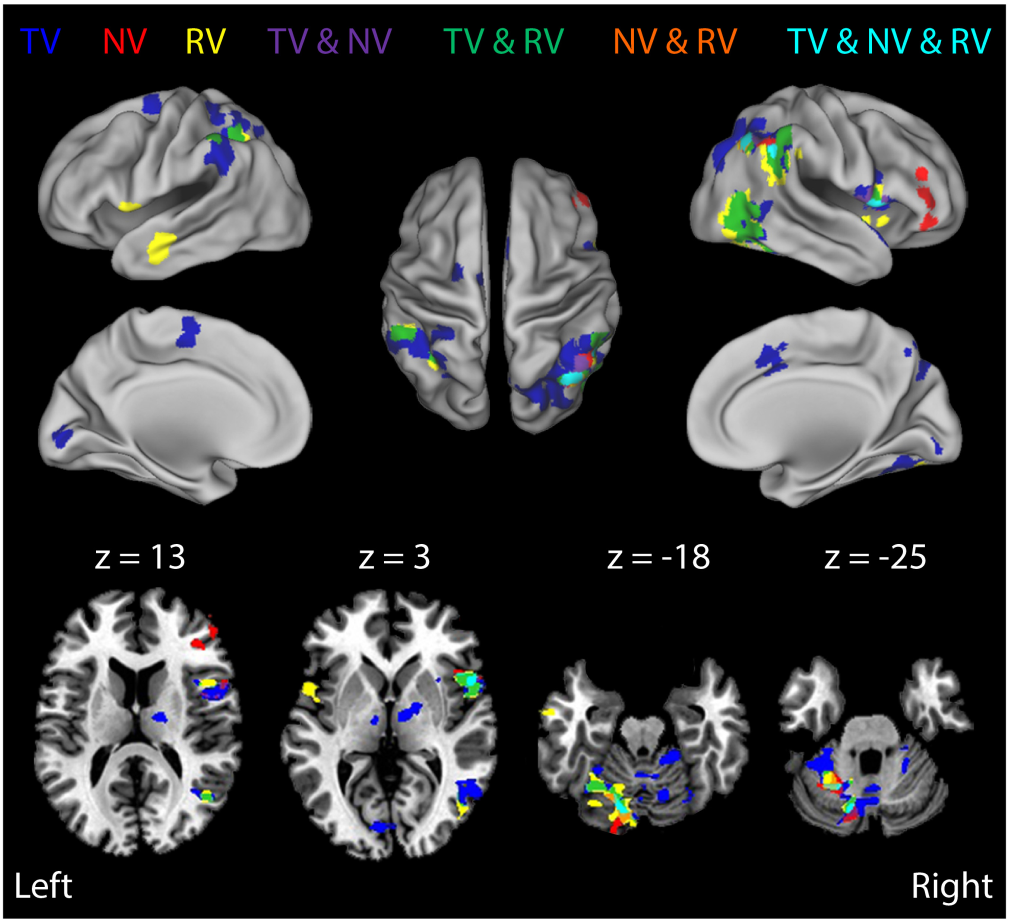

FIGURE 6 | Results of a Stage 2 event-related analysis performed on the BOLD signal residuals from the Stage 1 regressions: TR-by-TR analysis of BOLD signal correlations with wrist angle error RMS_{TR} (ε_q) for each of the three visual feedback conditions. Color coding of functional activation maps is the same as for **Figure 5**. BOLD signal fluctuations related to TR-by-TR variations in wrist angle error were broadly distributed in sensorimotor areas previously implicated in feedback control of the wrist, including lateral cerebellum, thalamus, posterior parietal cortex, and the supplementary motor area (SMA). Note also the robust activity related to wrist angle error within secondary visual processing areas, even in ***RV*** trials (green- and yellow-shaded regions). By contrast, we observed no significant Stage-2 BOLD signal correlations with visual cursor motion in ***RV*** trials, suggesting that proprioceptive feedback dominated performance in this task, at least during trials with visuo-proprioceptive conflict.

marked enhancement in behavioral performance (**Figure 2B**). The intensity and specific loci of expanded activity depended on the fidelity of visual feedback. When incongruous visual feedback was added, additional subcortical activations were observed in areas including the putamen, and thalamus (**Figure 7**), regions thought to be involved in context dependent action selection and multisensory integration amidst situational uncertainty (Reig and Silberberg, 2014; Wilson, 2014; Robbe, 2018; see also Houk and Wise, 1995). Upon further examination of the correlations between BOLD signal fluctuations and the time series of visual and proprioceptive errors, we found that subjects appeared to rely exclusively on proprioceptive feedback to stabilize the wrist when the fidelity of visual feedback was degraded, even though the mechanical and visual error signals varied similarly in range and spectral content, and despite the fact that objective measures of limb position drifted substantially in many trials without veridical visual feedback. Taken together, these results do not support a model of multisensory integration for action that is governed solely by the MLE rules commonly found to apply to perception. Instead, they likely reflect the action of an early process of causal inference (cf. Körding et al., 2007; Debats et al., 2017), wherein lack of kinematic correlation between hand and cursor motion in the ***RV*** conditions precludes binding of the hand and cursor into a unified object to be manipulated, thereby causing subjects to use just one of the feedback sources (proprioceptive feedback from the hand) for online limb position control.

Neural Integration of Visual and Proprioceptive Information for Feedback Stabilization of the Wrist

How does the brain integrate the different senses to estimate limb state for the control of stabilization behaviors? The neuromuscular response to perturbation is complex and known to involve at least three primary components: the segmental

TABLE 3 | Regions exhibiting significant activation in the Stage 2 (TR-by-TR) analysis of proprioceptive errors during wrist stabilization under three different sensory contexts.

		Talairach coordinates				
	Hem	***X* (mm)**	***Y* (mm)**	***Z* (mm)**	**Volume (µl)**	**Mean T**
TV						
Fastigium	L	–5.8	52.8	–21.6	8,999	3.78
Denate						
Culmen						
Declive						
Pyramis						
Inf. parietal lobule (BA 40)	R	34.9	52.4	39.1	8,690	3.81
Sup. parietal lobule						
Angular gyrus						
Precuneus						
Inf. parietal lobule (BA 40)	L	–39.7	40.6	40.5	4,498	3.78
Precuneus						
Postcentral gyrus						
Mid. temporal gyrus (BA 37)	R	43.7	57.5	–1.4	4,314	3.76
Inf. temporal gyrus (BA 37)						
Mid. occipital gyrus						
Precentral gyrus	R	47.1	–7.4	8.6	3,824	3.77
Insula						
Inf. frontal gyrus						
Sup. temporal gyrus						
Thalamus	R	6.9	11.1	2.7	1,787	3.77
Cingulate gyrus (BA 32)	R	4.8	–12.7	39.2	774	3.70
Med. frontal gyrus	L	–15.1	4.4	56.1	767	3.77
Cerebellar tonsil	R	23.6	35.1	–41.1	667	3.76
Lingual gyrus	L	–1	77.9	–0.8	651	3.79
NV						
Inf. frontal gyrus (BA 46)	R	42.9	–40.4	8.3	1,249	3.72
Declive	L	–14.1	71.6	–21.3	1,129	3.75
Precentral gyrus	R	47.8	–6.5	9.4	1,087	3.75
Inf. parietal lobule (BA 40)	R	42.8	51.2	41.1	911	3.66
Culmen	L	–22.4	53.4	–25.2	542	3.76
Dentate						
RV						
Declive	L	–17.3	61.5	–18.9	4,087	3.77
Culmen						
Dentate						
Mid. temporal gyrus (BA 37)	R	45.8	60	0.2	2,707	3.76
Mid. occipital gyrus (BA 37)						
Supramarginal gyrus	R	52.9	39.8	31.1	1,497	3.71
Sup. temporal gyrus						
Inf. parietal lobule (BA 40)						
Insula (BA 13)	R	46.6	–8.5	4.4	1,293	3.76
Sup. temporal gyrus						
Inf. parietal lobule	L	–29.1	46.7	40.5	698	3.73
Angular gyrus	R	35.7	54.3	36.6	681	3.71
Inf. parietal lobule						
Cerebellar tonsil	R	25	31.1	-37.8	617	3.74
Sup. temporal gyrus	L	–47.4	–5.2	1.4	596	3.79
Insula (BA 13)						
Inf. parietal lobule	L	–47.9	34.7	38	571	3.66
Mid. temporal gyrus (BA 21)	L	–54.5	9.9	–14.2	538	3.82

BA, Broadman's Area; Sup., Superior; Mid., Middle; Inf., Inferior; Med., Medial.

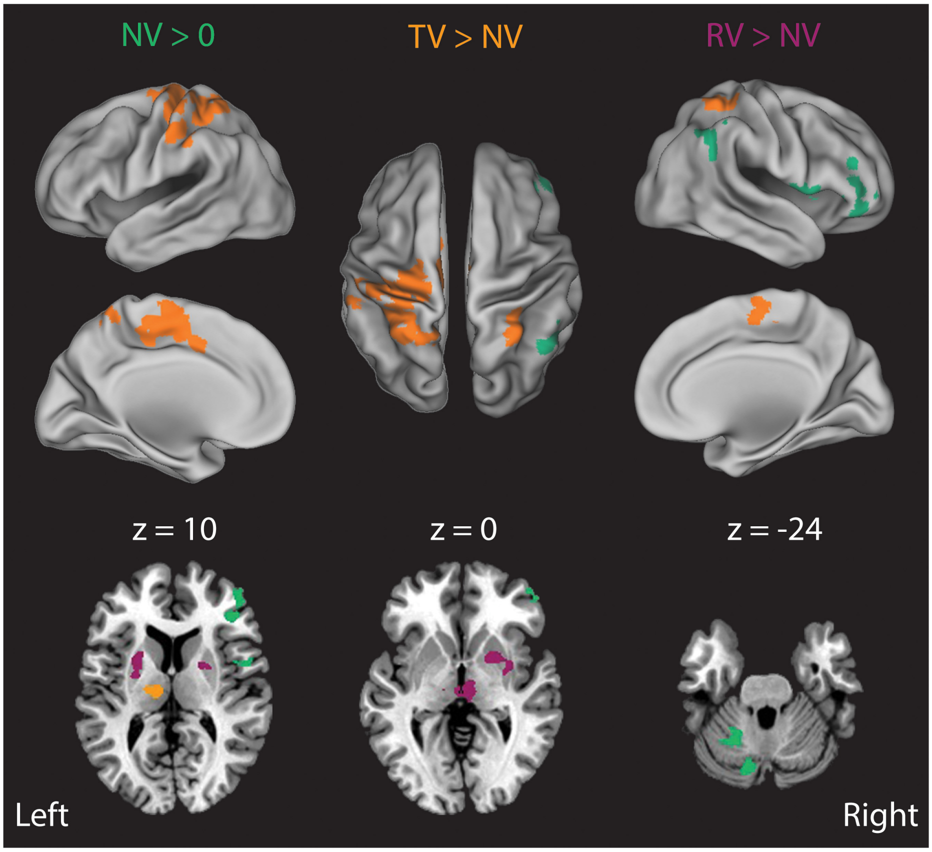

FIGURE 7 | Results of a Stage 2 event-related analysis of how the presence and fidelity of real-time visual feedback influences the moment-by-moment neural processing of proprioceptively-sensed wrist angle errors. In ***NV*** trials (***NV*** > 0, green), BOLD signal correlates of right-hand wrist angle errors were strongest in the left intermediate cerebellum, right posterior parietal cortex, insula and right frontal cortex. Addition of veridical visual feedback (***TV*** > ***NV***, orange) gave rise to a large increase in BOLD signal correlates of proprioceptive errors in the left thalamus, lateral cerebellum, as well as primary sensorimotor, premotor, cingulate motor, and posterior parietal cortices. By contrast, addition of incongruent visual feedback (***RV*** > ***NV***, purple) that was matched in amplitude and bandwidth to actual wrist displacements—but otherwise uncorrelated with them—induced an increase in BOLD signal correlates of actual wrist angle error in the putamen, thalamus and in the red nucleus/ventral tegmental area.

stretch reflex, long-loop reflex and voluntary responses (Phillips, 1969; Marsden et al., 1972). Our focus here is on the long-loop reflex mechanisms, which consist of neural circuits linking the motor cortex and anterior cerebellum, and which are known to be intimately involved in the closed loop control of limb position (Evarts and Tanji, 1976; Thach, 1978; Evarts and Fromm, 1981; Strick, 1983; Horne and Butler, 1995). In closed loop feedback control, the brain must compare the wrist's desired position with an estimate of its current state on an ongoing basis, and generate appropriate neuromotor responses to restore the wrist back to its desired position when errors are sensed. How does the brain compose an estimate of the current limb state for use in ongoing feedback control? Previously, we showed that the long-loop pathways involved in feedback control are heavily recruited in the no-vision version of our task when subjects stabilize against random torque perturbations to the wrist, and that it is possible to identify BOLD signal correlates of moment-by-moment changes in performance error using the hierarchical regression technique also employed in the present study (cf. Suminski et al., 2007a). The current results confirm those prior results, and they extend them into two additional sensory contexts involving veridical and incongruent visual feedback conditions (c.f., **Figures 5–7**). The results demonstrate that the neural processing of somatosensory performance errors depends strongly on the sensory context of the task. These results align well with recent behavioral and electromyographic evidence demonstrating that the long-loop reflex is a flexible, context-dependent mechanism that enables precise feedback control of the limb (Pruszynski et al., 2008, 2011; Nashed et al., 2012; Cluff et al., 2015; Crevecoeur et al., 2016; Ito and Gomi, 2020).

More specifically, results of the Stage 1 analyses show that providing veridical visual information about the position of the hand with respect to the target in our study increased activation in neural circuits typically implicated in visuomotor control (c.f., Vaillancourt, 2003; Vaillancourt et al., 2006) and enabled subjects to reduce the magnitude of stabilization errors relative to the no-vision condition. Improvement in the ability to correct positioning errors using visual feedback, over the course of the 30 s stabilization trial, was mediated by an increase in the volume of activated brain regions in the cerebello-thalamo-cortical pathway (**Figure 5**; TV) and expansion into other regions supporting visuomotor information processing including the left superior parietal lobule, inferior parietal lobule, cerebellar cortex (lobule IV–VI), right premotor cortex and inferior parietal lobule. By contrast, correcting persistent position errors when visual feedback was unreliable (***RV***) resulted in stabilization performance that was not very different than the no-visual feedback conditions (**Figure 2B**). This was so even though the condition with unreliable visual feedback still engaged neural activity in the cerebello-thalamo-cortical pathway, albeit to a reduced extent compared to both the veridical and no visual feedback conditions (**Figure 5**, RV; **Table 2**). Interestingly, we found that cortical activations in the right premotor/parietal cortex and left cerebellum, which were observed during stabilization with either veridical or no visual feedback, were absent when visual feedback was unreliable. Thus, degrading the reliability of visual information markedly alters the engagement of neural networks normally recruited in visuomotor tasks. These results both support and extend a prior report by Vaillancourt et al. (2006), which examined the effect of intermittent visual feedback on the neural mechanisms of visuomotor control (Vaillancourt et al., 2006). In a grip force control task, they showed that modulating the reliability of visual feedback by reducing its refresh rate reduced the magnitude of BOLD activity in the right premotor and parietal cortex and fully eliminated activity in the cerebellar cortex. This alteration of the neural circuits responsible for correcting persistent errors during periods of reduced sensory fidelity indicates a context-dependent change in control strategy used to integrate sensory information during action (e.g., a switch from one sensory modality to another).

We found further evidence of the context sensitivity of multisensory integration for action in the results of the Stage 2 analyses of BOLD signal correlations with the time series of visual and somatosensory performance errors under the three different sensory feedback conditions. In all cases, we observed BOLD responses related to the TR-by-TR variations in somatosensory performance errors $RMS_{TR}\left(\varepsilon_q\right)$ to be strongly represented throughout the brain, especially in areas known to process and integrate information from multiple sensory modalities: inferior parietal, superior temporal and lateral occipital cortices (c.f., Beauchamp, 2005; Macaluso, 2006). We found multiple overlapping activations in the right inferior parietal/superior temporal and lateral occipital cortices, where conditions with conflicting sensory feedback (***RV***) were represented more posterior to conditions with veridical information (***TV***). This patchy pattern of activity is similar to previous reports of activity in the superior temporal sulcus during a visual/auditory integration task (Beauchamp et al., 2004). By contrast, we found no activations related to visuomotor errors $RMS_{TR}\left(\varepsilon_v\right)$ when vision and somatosensation were in conflict, implying that subjects severely discounted (or ignored) visual information in the ***RV*** condition. On the one hand, this outcome was surprising given the similarity in the range and spectral content of the surrogate visual feedback and the applied torque perturbation sequence. Under the assumptions of MLE for multisensory integration (i.e., Eq. 1), we should have expected approximately equal contributions of vision and somatosensation to the feedback stabilization of the wrist given approximately equal amounts of variability in the different feedback signals. On the other hand, the absence of objective kinematic correlation between hand and cursor motions in our task likely weakened any belief that the visual and proprioceptive feedback signals originated from a common source (c.f., Körding et al., 2007; Debats et al., 2017). It is possible that the exclusive selection of proprioception as the preferred source of sensory information may be mediated by neural populations in the striatum, as shown by their increased activity during periods of sensory conflict (**Figure 7**, purple). These results are consistent with experimental evidence demonstrating multisensory integration in the striatum (Nagy et al., 2006; Reig and Silberberg, 2014; see also Wilson, 2014; Robbe, 2018) and with theoretical work describing the putative role of the basal ganglia as a context detector (Houk and Wise, 1995). Although elucidating the specific mechanism of multisensory integration for limb stabilization would require further refinement of the experimental approach described here (see section "*Limitations and Future Directions*" below), our results nevertheless provide strong support for the idea that the rules governing multisensory integration for action need to account for contextual factors such as the availability of—and kinematic correlation between—the different sensory feedback signals available before and during the task.

Factors Influencing Sensory Integration for Action

In the INTRODUCTION, we also raised the possibility that the standard MLE model might fail to describe limb state estimation for sensorimotor control in part because the real-time control of action places severe time constraints on the processing of sensory feedback signals that are quite unlike the timing constraints typically imposed in tasks of perceptual decision making. One constraint in tasks requiring fast and accurate movement derives from the fact that sensory feedback of ongoing performance is fleeting; unless feedback is acted on promptly, responses to evolving environmental perturbations can soon become outdated (i.e., unreliable), leading to potential instability in the coupled hand/handle system. Compounding this problem, sensory feedback signals are subject to neural transduction, transmission and processing delays that vary across the different senses: delays in proprioceptive pathways (∼60 ms) are approximately half those in visual pathways (∼120 ms; cf., Cameron et al., 2014).

To address this problem, Crevecoeur et al. (2016) recently proposed a dynamic Bayesian limb state estimation approach that augments the static approach of Eq. 1 with the ability to account for neural information processing delays and noises in the visual and proprioceptive feedback responses. Their model extends a Kalman filter design and yields an optimal state estimate by integrating (delayed) sensory feedback with corresponding prior state estimates for each sensory input. Remarkably, the model predicts that for system with visual delays approaching 100 ms and proprioceptive delays ∼50 ms, the reduction in posterior variance obtained when both vision and proprioception were available was $< 10\%$ of the variance obtained with proprioception only. This is much smaller than the reduction expected if the signals were combined based on their variance alone as implied by the model of Eq. 1. As a consequence, simulated kinematic responses to a step-wise mechanical perturbation to the elbow were similar with or without concurrent veridical visual feedback, suggesting that *"when dealing with unpredictable events such as external disturbances, vision plays a secondary role to proprioceptive feedback"* (Crevecoeur et al., 2016). The authors tested the predictions of their model in a series of experiments wherein subjects stabilized their arm against brief elbow torque perturbations presented with and without veridical visual feedback of hand position (as shown by a cursor on a horizontal display screen). Subjects were instructed to follow their hand (or the cursor representing it) with their eyes as they corrected for the perturbation. The authors monitored eye movements as an objective estimate of the subject's internal estimate of hand location. In agreement with their model, visual feedback-related reductions in arm movement variability were evident toward the later portion of error corrections (relative to their no-vision condition), and the variability of saccadic eye movement endpoints was reduced when visual feedback was also provided. However, the model did not account for the observation that saccade endpoint variability was lowest in a vision-only task that required subjects to track the playback of their prior recorded hand motions. In theory, the variability of a multisensory estimate should be better than that of any unimodal estimate for both the dynamic and static models, suggesting that the visual process *"was not fully contributing following the mechanical perturbations."* The model also predicted greater actual arm motions in response to the vision-only trials than were observed, prompting the authors to suggest that *"comparing motor responses to visual or mechanical perturbations during reaching may provide additional insight into dynamic multisensory integration."*

Building on that prior work, we used a long-duration wrist stabilization task and functional MR imaging techniques to infer neural correlates of internal state estimates and the visual and proprioceptive signals that contribute to them on a moment-by-moment (TR-by-TR) basis. If the difference in feedback delays were a primary factor influencing the preferential utilization of somatosensory feedback over visual feedback in our study, as would be suggested by the dynamic Bayesian estimation model, somatosensory feedback should have dominated kinematic performance regardless of whether or not visual feedback were available and veridical. This proposition can be rejected because subjects did in fact leverage veridical visual feedback to improve stabilization performance relative to the NV condition (**Figure 2B**), and they did so while increasing task-related activity in the cerebello-thalamo-cortical pathway and other visuomotor support areas (**Figures 5–7**). Instead, it is probable that additional important factors influencing multisensory integration pertain to the coherence between the available sensory signals (cf., Debats et al., 2017) and prior expectations as to whether the hand and cursor move together as a common controlled object (c.f., Körding et al., 2007). Because the robot's physical perturbations stimulated a rich set of proprioceptors sensitive to mechanical stimuli (including stretch receptors embedded in muscle bodies, force-sensitive Golgi tendon organs, and pressure-sensitive mechanoreceptors in the glabrous skin of the hand), $RMS_{TR}\left(\varepsilon_q\right)$ was bound to be highly correlated with each of these afferent signals regardless of sensory context in this study. By contrast, the visual feedback signal $RMS_{TR}(\varepsilon_v)$ had high coherence with the somatosensory signals in the ***TV*** condition and low coherence with those signals in the ***RV*** condition. A lack of cross modal sensory coherence in the ***RV*** conditions could have been a trigger that caused subjects to discount the cursor feedback as irrelevant to the task at hand: i.e., physically stabilizing the wrist. A neural mechanism for such context-dependent gating is suggested by the BOLD signal activations observed in the basal ganglia and thalamus in the ***RV*** > ***NV*** contrast shown in **Figure 7**.

Limitations and Future Directions

This study has several limitations. One limitation derives from our experimental design, which only included the two extreme visual feedback conditions (***TV*** and ***RV***) in addition to the ***NV*** control condition. Our design did not include intermediate blends of congruent and incongruent visual feedback, which would have allowed to test whether the lack of BOLD signal correlation with $RMS_{TR}(\varepsilon_v)$ in the current study was due to the fact that this signal was uncorrelated with the physical consequences of perturbation, as shown in **Figure 3**. A future study could address this limitation by requiring wrist stabilization in the presence of visual feedback $\theta_{vision}(t)$ that could be variably masked by bandlimited Gaussian noise $\theta_{surrogate}(t)$ as in:

$$\theta_{vision}(t) = \lambda\, \theta_{hand}(t) + (1-\lambda)\, \theta_{surrogate}(t). \qquad (5)$$

Here, λ is a weighting factor determining the extent to which visual cursor motion corresponds to actual motion of the wrist $\theta_{hand}(t)$ vs. bandlimited noise. Under the hypothesis that visual stimuli are discounted below some threshold of cross-modal coherence, one might expect to observe BOLD signal correlates with $\theta_{surrogate}(t)$ in brain regions involved in the low-level processing of moving visual stimuli when λ takes on moderate values, but to not observe such correlates when λ approaches extreme values of 0 or 1. However, other hypotheses are possible; if slow visual feedback is not really involved in the moment-by-moment formation of feedback responses to performance errors but is instead used to calibrate (or center) the faster proprioceptive feedback corrections about the desired goal posture, then one might expect to observe no BOLD signal correlates with $\theta_{surrogate}(t)$ for any value of λ.

Another limitation derives from the fact that the data we present were collected on a 1.5T MR scanner, which limited our image resolution and whole brain image capture rate. A significant benefit of using functional MR imaging in this study (rather than some other imaging technique such as electroencephalography, EEG) includes the ability to image the whole brain for neural correlates of signals of interest such as somatosensory and visual performance errors. If it were possible to repeat the study on a higher resolution scanner, the resulting data would undoubtedly have improved spatial and temporal resolution relative to those presented here. However, it is unlikely that any of our main conclusions would change, in part because the neural events of interest in functional MR imaging studies are commonly low-pass filtered both in space (with a blurring filter to accommodate inter-subject anatomical differences in across-subjects analyses) and in time (with a γ-variate or related hemodynamic response function to account for the sluggish physiological hemodynamic response). As shown above, our data have sufficient resolution to detect changes in the Stage 1 block-wise analyses of BOLD signals related to the different environmental load and sensory feedback conditions (**Table 1** and **Figures 4**, **5**). The data show that relative to the ***NV*** control condition, wrist-angle error-related BOLD signals expand in the cerebello-thalamo-cortical pathways known to contribute to feedback stabilization when veridical visual feedback is added, and they shift to include brain regions involved in context detection and action selection when incongruent visual feedback is added. Our data also suffice to identify Stage 2 BOLD signal correlates of wrist angle errors over a much shorter, TR-by-TR time frame (**Table 2** and **Figures 6**, **7**) riding on top of the signals described in the Stage 1 analysis. Improved temporal resolution would undoubtedly improve the statistical power of the Stage 2, TR-by-TR regressions, which could in turn improve sensitivity to BOLD signal correlates of RMS_{TR} (ε_v), the ***RV*** errors sensed visually. However, no degree of improved spatial or temporal resolution would change the observation that BOLD signal correlates of error signals sensed proprioceptively far outpower BOLD correlates of ***RV*** errors sensed visually; this degenerate outcome was rather unexpected because the magnitude and spectral characteristics of the visual feedback was similar in the ***TV*** and ***RV*** conditions. The fact that visual errors elicit no measurable BOLD signal correlates during wrist stabilization in the ***RV*** case argues against the idea that multisensory integration for limb stabilization is adequately described by the form of MLE model often posed for multisensory integration for perceptual decision making tasks, even as updated to account for differing sensory feedback delays. Instead, our findings bolster the idea that an early stage of sensorimotor control—prior to integration—involves discrete decisions: the binding of kinematically correlated feedback signals into a unified object to be controlled and the segregation/suppression of uncorrelated signals that are assumed to be task irrelevant. Further research is needed to clarify which contextual factors impact causal inference and multisensory integration for perception, cognition, and action.

DATA AVAILABILITY STATEMENT

The raw data supporting the conclusions of this article will be made available by the authors, without undue reservation.

ETHICS STATEMENT

The studies involving human participants were reviewed and approved by the Marquette University IRB Medical College of Wisconsin IRB. The patients/participants provided their written informed consent to participate in this study.

AUTHOR CONTRIBUTIONS

AS and RS contributed to conception and design of the study, wrote the first draft of the manuscript, and wrote sections of the manuscript. AS collected the data. AS and RD performed the statistical analysis. All authors contributed to manuscript revision, read, and approved the submitted version.

FUNDING

This work was supported by grants from the National Science Foundation (award number 0238442), the National Institute of Neurological Disorders and Stroke, and the National Institute of Child Health and Human Development (NIH) (R01HD53727 and R15HD093086).

ACKNOWLEDGMENTS

We thank Jared Koser for assistance with data processing and Steve Rao and Kristine Mosier for insightful discussions on a previous version of this manuscript.

REFERENCES

Bagesteiro, L. B., Sarlegna, F. R., and Sainburg, R. L. (2006). Differential influence of vision and proprioception on control of movement distance. *Exp. Brain Res.* 171, 358–370. doi: 10.1007/s00221-005-0272-y

Beauchamp, M. S. (2005). See me, hear me, touch me: multisensory integration in lateral occipital-temporal cortex. *Curr. Opin. Neurobiol.* 15, 145–153. doi: 10.1016/j.conb.2005.03.011

Beauchamp, M. S., Argall, B. D., Bodurka, J., Duyn, J. H., and Martin, A. (2004). Unraveling multisensory integration: patchy organization within human STS multisensory cortex. *Nat. Neurosci.* 7, 1190–1192. doi: 10.1038/nn1333

Cameron, B. D., de la Malla, C., and Lopez-Moliner, J. (2014). The role of differential delays in integrating transient visual and proprioceptive information. *Front. Psychol.* 5:50. doi: 10.3389/fpsyg.2014.00050

Cluff, T., Crevecoeur, F., and Scott, S. H. (2015). A perspective on multisensory integration and rapid perturbation responses. *Vision Res.* 110, 215–222. doi: 10.1016/j.visres.2014.06.011

Cox, R. W. (1996). AFNI: software for analysis and visualization of functional magnetic resonance neuroimages. *Comput. Biomed. Res.* 29, 162–173. doi: 10.1006/cbmr.1996.0014

Crevecoeur, F., Munoz, D. P., and Scott, S. H. (2016). Dynamic multisensory integration: somatosensory speed trumps visual accuracy during feedback control. *J. Neurosci.* 36, 8598–8611. doi: 10.1523/JNEUROSCI.0184-16.2016

Debats, N. B., Ernst, M. O., and Heuer, H. (2017). Kinematic cross-correlation induces sensory integration across separate objects. *Eur. J. Neurosci.* 46, 2826–2834. doi: 10.1111/ejn.13758

Ernst, M. O. (2006). *A Bayesian View on Multimodal Cue Integration. in Human body perception from the inside out: Advances in visual cognition*. New York, NY: Oxford University Press, 105–131.

Ernst, M. O., and Banks, M. S. (2002). Humans integrate visual and haptic information in a statistically optimal fashion. *Nature* 415, 429–433. doi: 10.1038/415429a

Evarts, E. V., and Fromm, C. (1981). Transcortical reflexes and servo control of movement. *Can. J. Physiol. Pharmacol.* 59, 757–775. doi: 10.1139/y81-112

Evarts, E. V., and Tanji, J. (1976). Reflex and intended responses in motor cortex pyramidal tract neurons of monkey. *J. Neurophysiol.* 39, 1069–1080. doi: 10.1152/jn.1976.39.5.1069

Henriques, D. Y. P., and Crawford, J. D. (2002). Role of eye, head, and shoulder geometry in the planning of accurate arm movements. *J. Neurophysiol.* 87, 1677–1685. doi: 10.1152/jn.00509.2001

Horne, M. K., and Butler, E. G. (1995). The role of the cerebello-thalamo-cortical pathway in skilled movement. *Prog. Neurobiol.* 46, 199–213. doi: 10.1016/0301-0082(95)80011-v

Houk, J. C., and Wise, S. P. (1995). Distributed modular architectures linking basal ganglia, cerebellum, and cerebral cortex: their role in planning and controlling action. *Cereb. Cortex. N Y N* 5, 95–110. doi: 10.1093/cercor/5.2.95

Ito, S., and Gomi, H. (2020). Visually-updated hand state estimates modulate the proprioceptive reflex independently of motor task requirements. *Elife* 9:e52380. doi: 10.7554/eLife.52380

Judkins, T., and Scheidt, R. A. (2014). Visuo-proprioceptive interactions during adaptation of the human reach. *J. Neurophysiol.* 111, 868–887. doi: 10.1152/jn.00314.2012

Körding, K. P., and Wolpert, D. M. (2004). Bayesian integration in sensorimotor learning. *Nature* 427, 244–247. doi: 10.1038/nature02169

Körding, K. P., Beierholm, U., Ma, W. J., Quartz, S., Tenenbaum, J. B., and Shams, L. (2007). Causal inference in multisensory perception. *PLoS One* 2:e943. doi: 10.1371/journal.pone.0000943

Macaluso, E. (2006). Multisensory processing in sensory-specific cortical areas. *Neurosci. Rev. J. Bring. Neurobiol. Neurol. Psychiatry* 12, 327–338. doi: 10.1177/1073858406287908

Marsden, C. D., Merton, P. A., and Morton, H. B. (1972). Servo action in human voluntary movement. *Nature* 238, 140–143. doi: 10.1038/238140a0

Nagy, A., Eördegh, G., Paróczy, Z., Márkus, Z., and Benedek, G. (2006). Multisensory integration in the basal ganglia. *Eur. J. Neurosci.* 24, 917–924. doi: 10.1111/j.1460-9568.2006.04942.x

Nashed, J. Y., Crevecoeur, F., and Scott, S. H. (2012). Influence of the behavioral goal and environmental obstacles on rapid feedback responses. *J. Neurophysiol.* 108, 999–1009. doi: 10.1152/jn.01089.2011

Oldfield, R. C. (1971). The assessment and analysis of handedness: the Edinburgh inventory. *Neuropsychologia* 9, 97–113. doi: 10.1016/0028-3932(71)90067-4

Phillips, C. G. (1969). The Ferrier lecture, 1968. Motor apparatus of the baboon's hand. *Proc. R Soc. Lond. B Biol. Sci.* 173, 141–174. doi: 10.1098/rspb.1969.0044

Pruszynski, J. A., Kurtzer, I., and Scott, S. H. (2008). Rapid motor responses are appropriately tuned to the metrics of a visuospatial task. *J. Neurophysiol.* 100, 224–238. doi: 10.1152/jn.90262.2008

Pruszynski, J. A., Kurtzer, I., and Scott, S. H. (2011). The long-latency reflex is composed of at least two functionally independent processes. *J. Neurophysiol.* 106, 449–459. doi: 10.1152/jn.01052.2010

Reig, R., and Silberberg, G. (2014). Multisensory integration in the mouse striatum. *Neuron* 83, 1200–1212. doi: 10.1016/j.neuron.2014.07.033

Reuschel, J., Drewing, K., Henriques, D. Y. P., Rösler, F., and Fiehler, K. (2010). Optimal integration of visual and proprioceptive movement information for the perception of trajectory geometry. *Exp. Brain Res.* 201, 853–862. doi: 10.1007/s00221-009-2099-4

Robbe, D. (2018). To move or to sense? Incorporating somatosensory representation into striatal functions. *Curr. Opin. Neurobiol.* 52, 123–130. doi: 10.1016/j.conb.2018.04.009

Scheidt, R. A., Conditt, M. A., Secco, E. L., and Mussa-Ivaldi, F. A. (2005). Interaction of visual and proprioceptive feedback during adaptation of human reaching movements. *J. Neurophysiol.* 93, 3200–3213. doi: 10.1152/jn.00947.2004

Seilheimer, R. L., Rosenberg, A., and Angelaki, D. E. (2014). Models and processes of multisensory cue combination. *Curr. Opin. Neurobiol.* 25, 38–46. doi: 10.1016/j.conb.2013.11.008

Sober, S. J., and Sabes, P. N. (2003). Multisensory integration during motor planning. *J. Neurosci.* 23, 6982–6992. doi: 10.1523/JNEUROSCI.23-18-06982.2003

Soechting, J. F., and Flanders, M. (1989). Errors in pointing are due to approximations in sensorimotor transformations. *J. Neurophysiol.* 62, 595–608. doi: 10.1152/jn.1989.62.2.595

Strick, P. L. (1983). The influence of motor preparation on the response of cerebellar neurons to limb displacements. *J. Neurosci. Off. J. Soc. Neurosci.* 3, 2007–2020. doi: 10.1523/JNEUROSCI.03-10-02007.1983

Suminski, A. J., Rao, S. M., Mosier, K. M., and Scheidt, R. A. (2007a). Neural and electromyographic correlates of wrist posture control. *J. Neurophysiol.* 97, 1527–1545. doi: 10.1152/jn.01160.2006

Suminski, A. J., Zimbelman, J. L., and Scheidt, R. A. (2007b). Design and validation of a MR-compatible pneumatic manipulandum. *J. Neurosci. Methods* 163, 255–266. doi: 10.1016/j.jneumeth.2007.03.014

Thach, W. T. (1978). Correlation of neural discharge with pattern and force of muscular activity, joint position, and direction of intended next movement in motor cortex and cerebellum. *J. Neurophysiol.* 41, 654–676. doi: 10.1152/jn.1978.41.3.654

Tillery, S. I., Flanders, M., and Soechting, J. F. A. (1991). coordinate system for the synthesis of visual and kinesthetic information. *J. Neurosci.* 11, 770–778. doi: 10.1523/JNEUROSCI.11-03-00770.1991

Vaillancourt, D. E. (2003). Neural basis for the processes that underlie visually guided and internally guided force control in humans. *J. Neurophysiol.* 90, 3330–3340. doi: 10.1152/jn.00394.2003

Vaillancourt, D. E., Mayka, M. A., and Corcos, D. M. (2006). Intermittent visuomotor processing in the human cerebellum, parietal cortex, and premotor cortex. *J. Neurophysiol.* 95, 922–931. doi: 10.1152/jn.00718.2005

van Beers, R. J., Wolpert, D. M., and Haggard, P. (2002). When feeling is more important than seeing in sensorimotor adaptation. *Curr. Biol. CB* 12, 834–837. doi: 10.1016/s0960-9822(02)00836-9

Van Essen, D. C., Drury, H. A., Dickson, J., Harwell, J., Hanlon, D., and Anderson, C. H. (2001). An integrated software suite for surface-based analyses of cerebral cortex. *J. Am. Med. Inform. Assoc. JAMIA* 8, 443–459. doi: 10.1136/jamia.2001.0080443

Wilson, C. J. (2014). The sensory striatum. *Neuron* 83, 999–1001. doi: 10.1016/j.neuron.2014.08.025

Author Disclaimer: The opinions, findings, and conclusions, or recommendations expressed are those of the author(s) and do not necessarily reflect the views of the National Science Foundation.

Conflict of Interest: The authors declare that the research was conducted in the absence of any commercial or financial relationships that could be construed as a potential conflict of interest.

frontiers | Frontiers in Neural Circuits

ORIGINAL RESEARCH
published: 22 June 2022
doi: 10.3389/fncir.2022.836121

Contribution of Phase Resetting to Statistical Persistence in Stride Intervals: A Modeling Study

Kota Okamoto[1], *Ippei Obayashi*[2], *Hiroshi Kokubu*[3], *Kei Senda*[1], *Kazuo Tsuchiya*[1] *and Shinya Aoi*[4]*

[1] Department of Aeronautics and Astronautics, Graduate School of Engineering, Kyoto University, Kyoto Daigaku-Katsura, Kyoto, Japan, [2] Cyber-Physical Engineering Information Research Core (Cypher), Okayama University, Okayama, Japan, [3] Department of Mathematics, Graduate School of Science, Kyoto University, Kyoto, Japan, [4] Department of Mechanical Science and Bioengineering, Graduate School of Engineering Science, Osaka University, Osaka, Japan

Stride intervals in human walking fluctuate from one stride to the next, exhibiting statistical persistence. This statistical property is changed by aging, neural disorders, and experimental interventions. It has been hypothesized that the central nervous system is responsible for the statistical persistence. Human walking is a complex phenomenon generated through the dynamic interactions between the central nervous system and the biomechanical system. It has also been hypothesized that the statistical persistence emerges through the dynamic interactions during walking. In particular, a previous study integrated a biomechanical model composed of seven rigid links with a central pattern generator (CPG) model, which incorporated a phase resetting mechanism as sensory feedback as well as feedforward, trajectory tracking, and intermittent feedback controllers, and suggested that phase resetting contributes to the statistical persistence in stride intervals. However, the essential mechanisms remain largely unclear due to the complexity of the neuromechanical model. In this study, we reproduced the statistical persistence in stride intervals using a simplified neuromechanical model composed of a simple compass-type biomechanical model and a simple CPG model that incorporates only phase resetting and a feedforward controller. A lack of phase resetting induced a loss of statistical persistence, as observed for aging, neural disorders, and experimental interventions. These mechanisms were clarified based on the phase response characteristics of our model. These findings provide useful insight into the mechanisms responsible for the statistical persistence of stride intervals in human walking.

Keywords: human walking, stride interval fluctuation, neuromechanical model, central pattern generator, phase resetting, statistical persistence

Edited by:
Monica A. Daley,
University of California, Irvine,
United States

Reviewed by:
Auke Ijspeert,
Swiss Federal Institute of Technology
Lausanne, Switzerland
Taishin Nomura,
Osaka University, Japan
Jonathan B. Dingwell,
The Pennsylvania State University
(PSU), United States

Correspondence:
Shinya Aoi
aoi.shinya.es@osaka-u.ac.jp

Received: *15 December 2021*
Accepted: *19 May 2022*
Published: *22 June 2022*

Citation:
Okamoto K, Obayashi I, Kokubu H, Senda K, Tsuchiya K and Aoi S (2022) Contribution of Phase Resetting to Statistical Persistence in Stride Intervals: A Modeling Study. Front. Neural Circuits 16:836121. doi: 10.3389/fncir.2022.836121

1. INTRODUCTION

Human walking is not perfectly periodic. The stride interval fluctuates from one stride to the next, exhibiting statistical persistence (Hausdorff et al., 1995; West and Griffin, 1998, 1999; Dingwell and Cusumano, 2010), which indicates that deviations in a time series are statistically more likely to be followed by subsequent deviations in the same direction. Although the stride interval fluctuations change depending on the gait speed and during development from childhood to adulthood, the statistical persistence remains unchanged (Hausdorff et al., 1996, 1999). However, the stride interval fluctuations for elderly subjects (Hausdorff et al., 1997) and patients with Huntington's disease (Hausdorff et al., 1997) or Parkinson's disease (Frenkel-Toledo et al., 2005) become uncorrelated. Experimental interventions for walking, such as the use of a metronome, also make the stride interval fluctuations uncorrelated (Hausdorff et al., 1996). It is largely unclear why statistical persistence appears in stride intervals in human walking and why this statistical property is changed by aging, neural disorders, and experimental interventions.

It has been hypothesized that the central nervous system has an underlying persistence and is responsible for the statistical persistence in stride intervals. This is supported by the finding that statistical persistence remains in patients with significant peripheral nerve degeneration (Gates and Dingwell, 2007). Various neural system models have been developed to reproduce the statistical persistence and investigate the associated mechanisms. Hausdorff et al. (1995) developed a model of the central pattern generators (CPGs) in the spinal cord and introduced "memory" into the CPG model by allowing transitions from frequency to frequency. Ashkenazy et al. (2002) extended this model by introducing a random walk for the signal transmission of neural circuits. West and Scafetta (2003) developed a "Super CPG" model that introduces external interventions *via* a forced van der Pol oscillator.

Human walking is a complex phenomenon generated through dynamic interactions between the central nervous system and the biomechanical system. It has also been hypothesized that the statistical persistence in stride intervals emerges through complex interactions during walking. Fu et al. (2020) integrated a biomechanical model composed of seven rigid links with a CPG model, which incorporated a phase resetting mechanism as sensory feedback as well as feedforward, trajectory tracking, and intermittent feedback controllers, to reproduce statistical persistence. They showed that a lack of phase resetting induces a loss of statistical persistence. However, it is difficult to fully understand the essential mechanisms responsible for generating and changing this statistical property because of the complexity of the neural and biomechanical models.

In human walking, the stance leg, which is almost straight, rotates around the foot contact point like an inverted pendulum. To investigate the essential mechanisms responsible for generating human walking from a dynamic viewpoint, simple compass-type mechanical models have been used (Kuo, 2001; Donelan et al., 2002; Kuo et al., 2005; Bruijn et al., 2011; Okamoto et al., 2020). Gates et al. (2007) and Ahn and Hogan (2013) reproduced the statistical persistence in stride intervals using simple compass-type models with sensory feedback controllers. However, they did not investigate the contribution of the feedback controllers to changes in the statistical persistence; thus, the essential mechanisms remain unclear.

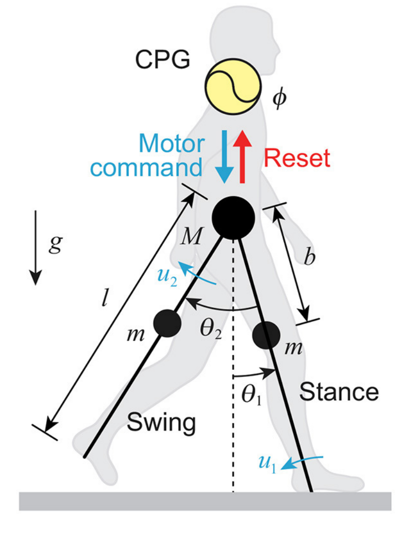

FIGURE 1 | Neuromechanical model of human walking composed of CPG model with phase resetting and compass-type biomechanical model.

The aim of this study is to clarify the contribution of phase resetting to the generation and change in the statistical persistence using a simple model. Specifically, we used a simplified neuromechanical model composed of a simple compass-type biomechanical model and a simple CPG model that incorporates phase resetting and a feedforward controller. Our model reproduced the statistical persistence in stride intervals. A lack of phase resetting induced a loss of statistical persistence, as observed in Fu et al. (2020). Furthermore, we clarified the mechanisms responsible for changes in this statistical property caused by phase resetting based on the phase response characteristics. Our findings provide important insights into the mechanisms underlying the generation and change of the statistical persistence in the stride intervals in human walking.

2. METHODS

2.1. Mechanical Model

We used a simple compass-type model (**Figure 1**). This model has two legs (swing and stance legs), the lengths of which are both l, connected by a frictionless hip joint. The masses are located at the hip and on the legs at a distance b from the hip joint; M is the hip mass and m is the leg mass. θ_1 is the angle of the stance leg with respect to the vertical, and θ_2 is the relative angle between the stance and swing legs. The tip of the stance leg, which corresponds to the ankle, is fixed on the ground. The stance leg rotates freely without friction. This model walks on level ground *via* joint torques u_1 (at the ankle) and u_2 (at the hip). g is the acceleration due to gravity. We used the following model parameters based on Winter (2004): $M = 50$ kg, $m = 11$ kg, $l = 1$ m, $b = 0.4$ m, and $g = 9.8$ m/s^2.

When the tip of the swing leg is in the air, the equations of motion for our model are

$$\begin{bmatrix} Ml^2 + m\{l^2 + (l-b)^2\} - 2mlb\cos\theta_2 + mb^2 & mlb\cos\theta_2 - mb^2 \\ mlb\cos\theta_2 - mb^2 & mb^2 \end{bmatrix} \begin{bmatrix} \ddot{\theta}_1 \\ \ddot{\theta}_2 \end{bmatrix} + \begin{bmatrix} -mlb(\dot{\theta}_2 - 2\dot{\theta}_1)\dot{\theta}_2 \sin\theta_2 \\ -mlb\dot{\theta}_1^2 \sin\theta_2 \end{bmatrix} + \begin{bmatrix} -\{gm(2l-b) + gMl\}\sin\theta_1 - gmb\sin(\theta_2 - \theta_1) \\ gmb\sin(\theta_2 - \theta_1) \end{bmatrix} = \begin{bmatrix} u_1 \\ u_2 \end{bmatrix} \quad (1)$$

The tip of the swing leg touches the ground (touchdown) when the following conditions are satisfied:

$$2\theta_1 - \theta_2 = 0 \quad (2)$$

$$\theta_1 < 0 \quad (3)$$

$$2\dot{\theta}_1 - \dot{\theta}_2 < 0 \quad (4)$$

We used condition (3) so that touchdown occurs only in front of the model to move forward, and condition (4) to ignore the scuffing of the leg tip on the ground when the swing leg is swung forward. We assumed that touchdown is a fully inelastic collision (no slip, no bounce) and that the stance leg lifts off the ground just after touchdown. Because the roles of the swing and stance legs are reversed just after touchdown, we obtain

$$\theta_1^+ = -\theta_1^- \quad (5)$$

$$\theta_2^+ = -\theta_2^- \quad (6)$$

where $*^-$ and $*^+$ are the state $*$ just before and after touchdown, respectively. Due to this collision, the angular velocities discontinuously change. We assumed that when the stance leg leaves the ground, it does not interact with the ground and the work of the joint torques can be neglected. These assumptions yield

$$\begin{bmatrix} \dot{\theta}_1^+ \\ \dot{\theta}_2^+ \end{bmatrix} = \{Q^+(\theta_1^-)\}^{-1} Q^-(\theta_1^-) \begin{bmatrix} \dot{\theta}_1^- \\ \dot{\theta}_2^- \end{bmatrix} \quad (7)$$

where

$$Q^+(\theta_1^-) = \begin{bmatrix} -Ml^2 - 2m(l-b)^2 - 2mlb(1 - \cos 2\theta_1^-) & mb(b - l\cos 2\theta_1^-) \\ -ml(b - l\cos 2\theta_1^-) & mlb \end{bmatrix}$$

$$Q^-(\theta_1^-) = \begin{bmatrix} 2m(l-b)(b - l\cos 2\theta_1^-) - Ml^2\cos 2\theta_1^- & -m(l-b)b \\ ml(l-b) & 0 \end{bmatrix}$$

2.2. CPG Model

The CPGs in the spinal cord are largely responsible for rhythmic leg movements, such as during locomotion (Grillner, 1975; Shik and Orlovsky, 1976; Orlovsky et al., 1999). They can produce oscillatory behavior even in the absence of rhythmic input and sensory feedback. However, sensory feedback is crucial for producing adaptive locomotor behavior. To investigate the contribution of CPGs to adaptive locomotion in humans, various oscillator models, such as the van der Pol oscillator (Dutra et al., 2003; West and Scafetta, 2003), Matsuoka oscillator (Matsuoka, 1987; Taga et al., 1991; Taga, 1995a,b; Ogihara and Yamazaki, 2001; Hase et al., 2003; Kim et al., 2011), and phase oscillator (Yamasaki et al., 2003; Aoi et al., 2010, 2019; Dzeladini et al., 2014; Aoi and Funato, 2016; Fu et al., 2020; Tamura et al., 2020; Owaki et al., 2021), have been developed.

In this study, we used a phase oscillator, whose phase is ϕ ($0 \leq \phi < 2\pi$), to generate the motor commands for our model. The oscillator phase follows the dynamics expressed by

$$\dot{\phi} = \omega \quad (8)$$

where ω is the basic frequency. We determined the joint torques u_1 and u_2 as

$$u_1 = A_1 \cos\phi + \sigma_1 \quad (9)$$

$$u_2 = A_2 \cos(\phi + \Delta) + \sigma_2 \quad (10)$$

where A_1 and A_2 are the amplitudes, σ_1 and σ_2 are noise terms, and Δ is the phase difference between u_1 and u_2.

It has been reported that locomotion rhythm and phase are regulated by the production of a phase shift and rhythm resetting (phase resetting) for periodic motor commands in response to sensory feedback (Lafreniere-Roula and McCrea, 2005; Rybak et al., 2006). Cutaneous feedback has been observed to contribute to phase shift and rhythm resetting behavior (Duysens, 1977; Schomburg et al., 1998). Phase resetting has thus been modeled so that the oscillator phase is reset based on foot contact information (Yamasaki et al., 2003; Aoi et al., 2010; Aoi and Funato, 2016; Fu et al., 2020; Tamura et al., 2020). In this study, we used the following relationship at touchdown:

$$\phi^+ = \phi_0 \quad (11)$$

where ϕ_0 is a constant. When phase resetting is not applied, ϕ is not regulated at touchdown. However, because the roles of the swing and stance legs are reversed just after touchdown so that $\theta_i^+ = -\theta_i^-$ ($i = 1, 2$), we used the following relationship at touchdown:

$$\phi^+ = \phi^- - \pi \quad (12)$$

so that $u_i^+ = -u_i^-$ ($i = 1, 2$) when the noise terms σ_1 and σ_2 are neglected. We designated ϕ_0 as the value to which ϕ^+ converged during steady walking (limit cycle) for the model without phase resetting and noise. Therefore, steady walking is identical between the models with and without phase resetting in the absence of noise. This allows us to clearly investigate the difference in the response to torque noise between cases with and without phase resetting.

This CPG model has four parameters, namely ω, A_1, A_2, and Δ. We used $\omega = 4.8$ rad/s based on Hausdorff et al. (1996). Without noise ($\sigma_1 = \sigma_2 = 0$), we first investigated the dependence of gait speed during steady walking on A_1, A_2, and Δ, and then calculated the energy cost $\varepsilon = \int (u_1^2 + u_2^2)dt$ for one step cycle for A_1, A_2, and Δ. We determined the parameter set (A_1, A_2, Δ) required to minimize ε for each gait speed. When phase resetting was used, we determined ϕ_0 for each gait speed using the obtained parameter set.

2.3. Torque Noise

To simulate the stochastic fluctuation of the gait, we used two independent series of white Gaussian noise for torque noise terms σ_1 and σ_2 in (9) and (10), respectively, as follows:

$$\sigma_i = \xi U_i \qquad i = 1, 2 \tag{13}$$

where ξ is the amplitude of the noise, and U_1 and U_2 are independent white Gaussian noise with standard deviation 1. This torque noise never induces consecutive touchdowns at extremely short intervals because of discontinuous and large changes in the state variables (5)–(7) at touchdown. We numerically solved the governing equations using the Euler-Maruyama method (Higham, 2001) with a time step of 10^{-5} s.

To be consistent with previous experiments on humans (Hausdorff et al., 1995, 1996, 1997), a stride was defined as two consecutive steps. Stride intervals were calculated based on the time difference between every other touchdown (strides did not overlap). Each simulation trial required the model to walk 1300 steps (650 strides). The first 150 strides were omitted from the analysis to remove transient behavior due to initial conditions.

2.4. Detrended Fluctuation Analysis

We used detrended fluctuation analysis (DFA) to determine the statistical persistence in the time series of stride intervals for each trial of the computer simulation. This method decreases the effect of noise and removes local trends, making it less affected by non-stationarities. The details of the method can be found elsewhere (e.g., Peng et al., 1993, 1994a,b; Hausdorff et al., 1995; Hardstone et al., 2012; Ihlen, 2012). Briefly, the feature amount $F(n)$ constructed from segments of length n of the time series exhibits a power-law relationship, indicating the presence of scaling as $F(n) \sim n^{\alpha}$. We investigate the scaling exponent α to determine the statistical persistence for the time series data.

In this study, we first formed the following accumulated sum using the sequence of stride intervals $x(i)$ for $i = 1, 2, \ldots, N$, where N is the total number of strides ($N = 500$):

$$y(i) = \sum_{k=1}^{i} [x(k) - \bar{x}] \qquad i = 1, 2, \ldots, N \tag{14}$$

where $\bar{x}$ is the mean stride interval from $x(1)$ to $x(N)$. We then divided the integrated series $y(i)$ into segments of length n ($n < N$), $y_j(s)$ ($j = 1, 2, \ldots, N/n, s = 1, 2, \ldots, n$), so that each segment is equal in length and non-overlapping. We next detrended each segment $y_j(s)$ by subtracting a least squares linear regression line $\hat{y}_j(s)$ fit to $y_j(s)$, and averaged the squares of the detrended data (i.e., the residuals). We thus obtained the standard deviation $F(n)$ as

$$F(n) = \sqrt{\frac{1}{n} \sum_{s=1}^{n} \left[y_j(s) - \hat{y}_j(s) \right]^2} \tag{15}$$

We used a set of n distributed equally on a logarithmic scale between 4 and $N/4$ (Jordan et al., 2006), specifically, $n = 4, 5, 6, \ldots, 87, 104$, and 125 (sample size is 20).

In general, $F(n)$ increases with increasing n and a graph of $\log F(n)$ vs. $\log n$ exhibits a power-law relationship, indicating the presence of scaling as $F(n) \sim n^{\alpha}$. We fit $\log F(n)$ vs. $\log n$ plots with a linear function using a standard least squares regression approach, and obtained the scaling exponent α from the slope of this line. In particular, $\alpha = 0.5$ indicates that the stride intervals are completely uncorrelated (i.e., white noise). That is, DFA will still produce $\alpha = 0.5$ even if the time series is rearranged in any manner (through surrogate data analysis). In contrast, $\alpha < 0.5$ indicates statistical anti-persistence in stride intervals and $0.5 < \alpha \leq 1.0$ indicates statistical persistence. When $\alpha > 1.0$, the time series is brown noise (i.e., integrated white noise) (Hausdorff et al., 1995).

3. RESULTS

3.1. Determination of Parameters for Each Gait Speed

Without noise ($\xi = 0$), our model achieved stable walking with a gait speed v of 0.25 to 0.6 m/s depending on the parameters A_1, A_2, and Δ. **Figure 2A** shows the contour of the evaluation criterion ε for A_1, A_2, and Δ, which generated $v = 0.3$, 0.4, and 0.5 m/s. **Figure 2B** shows the parameter sets (A_1, A_2, Δ), each of which minimized ε for a given gait speed v. The use of phase resetting did not affect these results. We use the parameter set $A_1 = A_1(v), A_2 = A_2(v)$, and $\Delta = \Delta(v)$ in the following sections.

3.2. Stride Interval Fluctuations

Figure 3 compares the simulation results between the models with and without phase resetting at a walking speed of 0.4 m/s ($A_1 = 4.9$, $A_2 = 10$, $\Delta = 0.47$) using the noise amplitude $\xi = 1$. **Figures 3A,B** show the angles θ_1 and θ_2 and the stride intervals, respectively, during 500 strides. Although ξ is identical between the models, the model without phase resetting has larger stride interval fluctuations than those for the model with phase resetting. **Figure 3C** shows a plot of $\log F(n)$ for $\log n$ and the scaling exponent α obtained from the slope of the fitted line. The model with phase resetting exhibits statistical persistence in stride intervals ($0.5 < \alpha \leq 1.0$), which is consistent with observations of healthy adults (Hausdorff et al., 1995). Furthermore, the standard deviation of stride interval fluctuations of the model with phase resetting is 0.03, which is also consistent with observations of healthy adults (Hausdorff et al., 1995). In contrast, the model without phase resetting exhibits statistical anti-persistence in stride intervals ($\alpha < 0.5$). **Figure 4** shows the dependence of α on ξ. The models with and without phase resetting, both of which kept walking when $\xi \leq 1$,

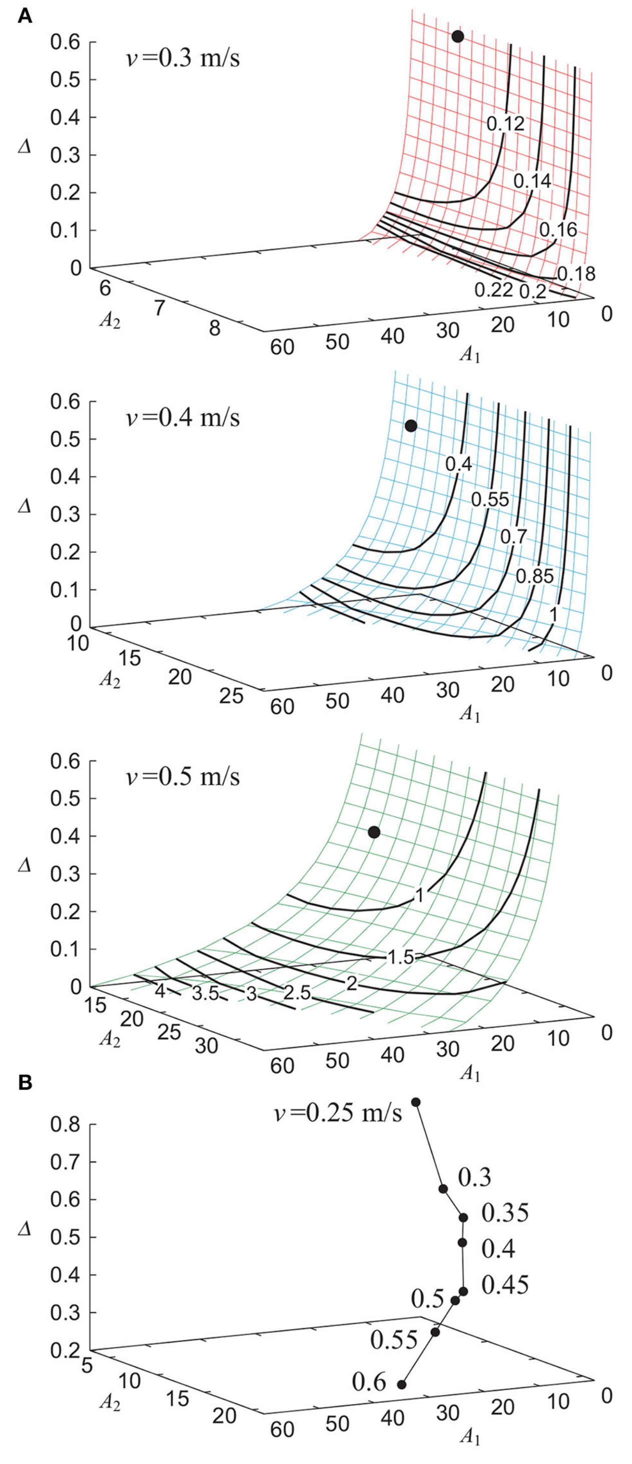

FIGURE 2 | Dependence of gait performance on parameters A_1, A_2, and Δ without noise. **(A)** Contour of evaluation criterion ε for parameters that generate gait speed $v = 0.3$, 0.4, and 0.5 m/s. Data point indicates the parameter set that minimizes ε. **(B)** Parameter sets that minimize ε for each gait speed v.

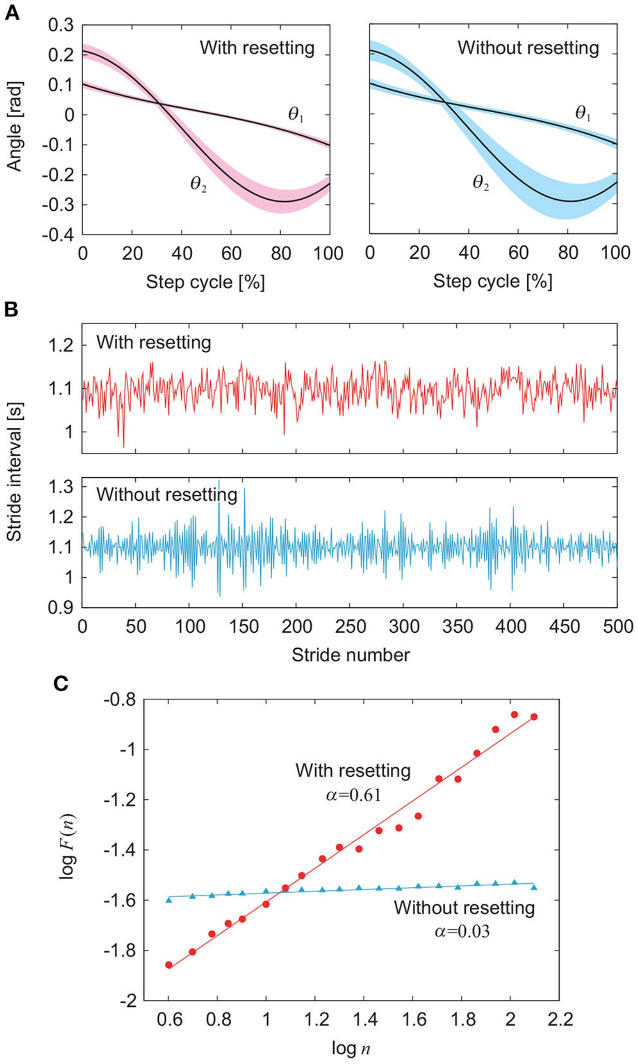

FIGURE 3 | Comparison of gait fluctuations between models with and without phase resetting at gait speed $v = 0.4$ m/s using noise amplitude $\xi = 1$ (see **Supplementary Movie**). **(A)** Angles θ_1 and θ_2. Black lines and colored areas indicate the average and standard deviation, respectively. **(B)** Stride intervals. **(C)** Plot of $\log F(n)$ for $\log n$ and scaling exponent α obtained from slope of fitted line.

exhibited statistical persistence and anti-persistence, respectively, regardless of ξ.

Figure 5 compares the simulation results for the models with and without phase resetting for various values of gait speed v using $\xi = 10^{-2}$. **Figures 5A,B** show the stride intervals and $\log F(n)$ plot, respectively, for $v = 0.3$ m/s ($A_1 = 1.3$, $A_2 = 6.1$, $\Delta = 0.57$), 0.4 m/s ($A_1 = 4.9$, $A_2 = 10$, $\Delta = 0.47$), and 0.5 m/s ($A_1 = 14$, $A_2 = 15$, $\Delta = 0.37$). **Figure 5C** shows the dependence of α on v. The model with phase resetting exhibits statistical persistence regardless of v, which is consistent

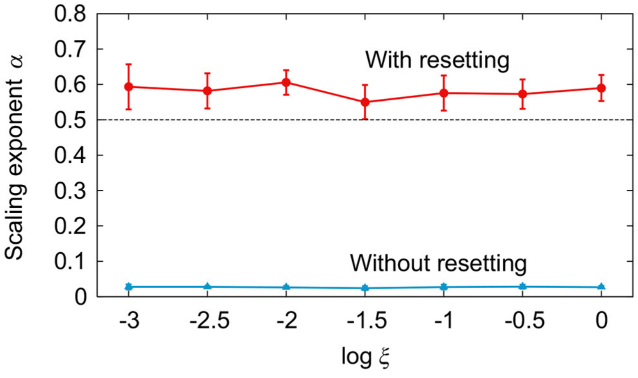

FIGURE 4 | Comparison of scaling exponent α for noise amplitude ξ between models with and without phase resetting at gait speed $v = 0.4$ m/s. Data points and error bars correspond to the means and standard deviations, respectively, of the results of 10 simulations.

with observations of healthy adults (Hausdorff et al., 1996). In contrast, the model without phase resetting exhibits statistical anti-persistence regardless of v.

4. DISCUSSION

4.1. Mechanisms for Statistical Persistence and Anti-persistence of Stride Intervals

In this study, the model with phase resetting exhibited statistical persistence in stride intervals ($0.5 < \alpha \leq 1.0$), whereas the model without phase resetting exhibited statistical anti-persistence ($\alpha < 0.5$) (**Figure 3**), as observed in a previous modeling study (Fu et al., 2020). Statistical anti-persistence is characterized by the alternation of large and small values. Fu et al. (2020) performed a linearized stability analysis on a model without phase resetting and noise, and showed that the dominant mode (least stable mode) characterized by Floquet multipliers was a pair of complex conjugates whose amplitude was less than but close to unity and whose argument was greater than $\pi/2$. This suggests that the fluctuation ξ_n of the stride number n can be approximately written as $\xi_n = (-r)^n \xi_1$, where $r \sim 1$ ($r < 1$) and ξ_1 is an initial deviation, corresponding to a slowly damped period-2 oscillation. They explained that this period-2 oscillation induced the alternation of long and short stride intervals and statistical anti-persistence. Although we performed the same stability analysis for our model, the dominant mode of our model without phase resetting and noise was positive real, whose amplitude is less than 1, indicating that the initial deviation monotonically decreases. In addition, our model with phase resetting had almost the same dominant mode as that for our model without phase resetting and it is difficult to conclude that these stability characteristics explain the difference in the statistical properties in stride intervals between the models with and without phase resetting. Furthermore, the amplitude of our dominant mode was 0.65 and the damping was relatively fast.

Next, we directly consider the difference in the response of the stride interval to disturbances. Specifically, we focus on the phase response curve in phase reduction theory (Winfree, 1980; Kuramoto, 1984), which explains how the phase of a limit cycle oscillator shifts by a perturbation at an arbitrary phase (**Figure 6**). The model with phase resetting shows a shift of the locomotion phase after the recovery due to phase resetting in (11) at foot contact, whereas the model without phase resetting shows no phase shift (Tamura et al., 2020). Furthermore, the phase shift for the model with phase resetting varies depending on the timing of the disturbance. Therefore, the accumulated sum y of stride intervals in (14) tends to move to the cumulative sum of the amount of phase shifts induced by input noise in the model with phase resetting, which results in a relatively smooth signal with large low-frequency components, as shown in **Figure 7**. In contrast, y tends to converge to 0 in the model without phase resetting, which results in a rough signal with large high-frequency components. Because the scaling exponent α increases with the degree of smoothness (Eke et al., 2000), this difference induces the difference in the scaling exponent α and statistical properties between the models with and without phase resetting.

4.2. Biological Relevance of Our Findings

The scaling exponent α greatly decreases during walking to a metronome in humans (Hausdorff et al., 1996), where the stride interval is constrained by an external cadence (i.e., metronome). This corresponds to the walking of the model without phase resetting, where the stride interval is constrained by the frequency ω in (8) of the phase oscillator. Therefore, the locomotion phase remains almost unchanged during walking to a metronome, and α decreases as in the model without phase resetting (**Figure 3**), as discussed in Section 4.1. It has been reported that α also greatly decreases for the stride interval fluctuations of elderly subjects (Hausdorff et al., 1997) and patients with Huntington's disease (Hausdorff et al., 1997) or Parkinson's disease (Frenkel-Toledo et al., 2005). Although the phase response characteristics have been clarified during walking for healthy adults (Yamasaki et al., 2003; Funato et al., 2016; Nessler et al., 2016), those during walking for elderly subjects and patients with neural disorders remain unclear. Investigating them would help clarify the mechanisms responsible for changes in the statistical persistence caused by aging and neural disorders.

Although stride interval fluctuations change depending on gait speed in humans, the statistical persistence remains unchanged (Hausdorff et al., 1996). Our model with phase resetting also exhibited statistical persistence regardless of the gait speed (**Figure 5**). The constraint on gait rhythm seems more crucial for the statistical persistence than the constraint on gait speed, as observed for walking to a metronome (Hausdorff et al., 1996).

The standard deviation of stride interval fluctuations is about 0.04 s in human walking, which is 3% of the mean stride interval (Hausdorff et al., 1995). It was difficult for previous studies (Gates et al., 2007; Fu et al., 2020) using biomechanical models to reproduce a magnitude of stride interval fluctuations similar to that for humans. Although Gates et al. (2007) reproduced statistical persistence in stride intervals ($0.5 < \alpha \leq 1.0$) using a simple biomechanical model as in this study, their model was not robust and the noise amplitude was limited.

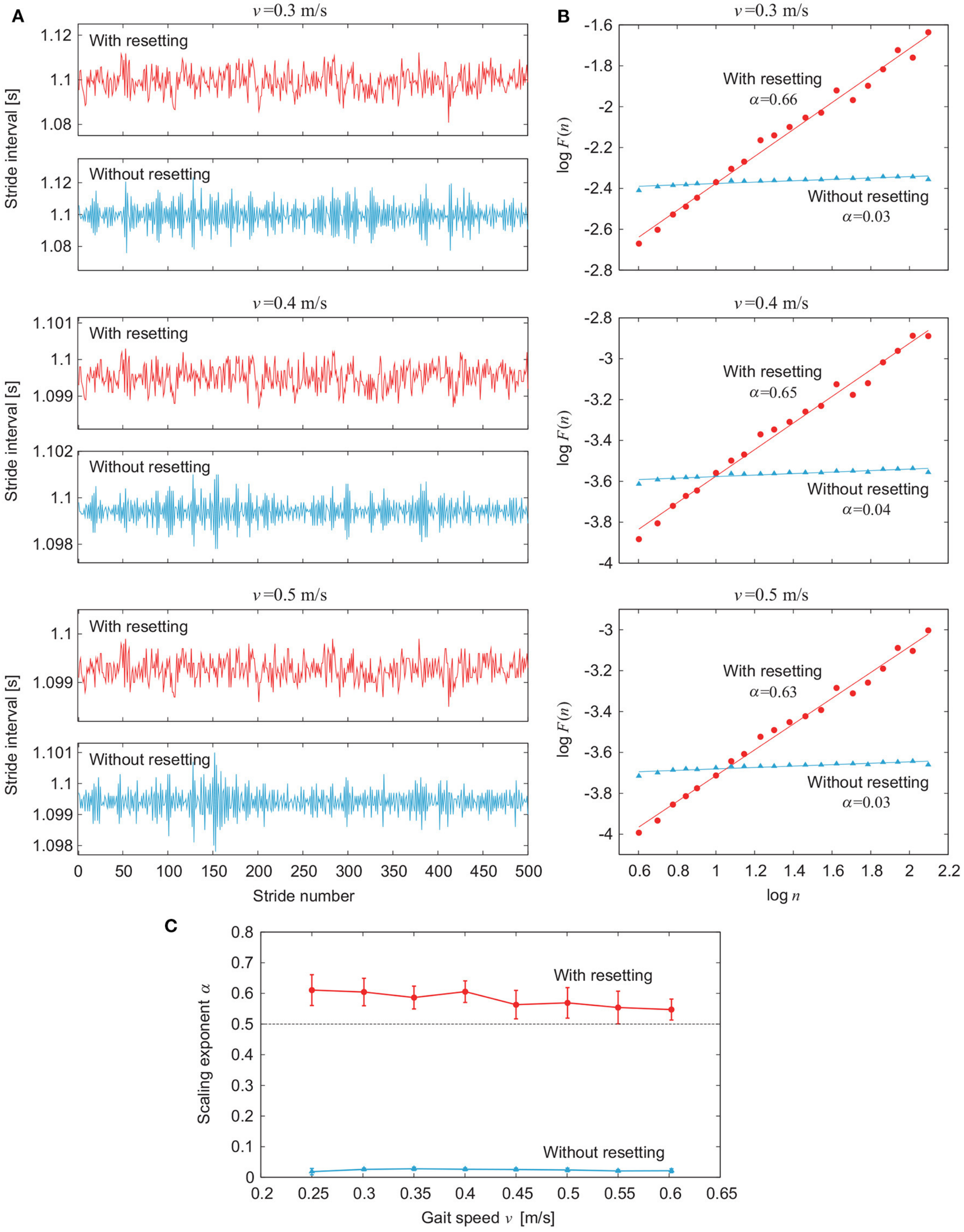

FIGURE 5 | Comparison of stride interval fluctuations for various values of gait speed v between models with and without phase resetting using noise amplitude $\xi = 10^{-2}$. **(A)** Stride intervals and **(B)** plot of $\log F(n)$ for $\log n$ for gait speed $v = 0.3$, 0.4, and 0.5 m/s. **(C)** Scaling exponent α vs. gait speed v. Data points and error bars correspond to the means and standard deviations, respectively, of the results of 10 simulations.

Therefore, their stride interval fluctuations were much smaller than those in humans. Furthermore, the scaling exponent α was sensitive to the noise amplitude, and the fluctuations exhibited brown noise at high noise levels ($\alpha > 1.0$). In contrast, phase resetting made our model robust, which allowed a magnitude of stride interval fluctuations similar to that for healthy adults

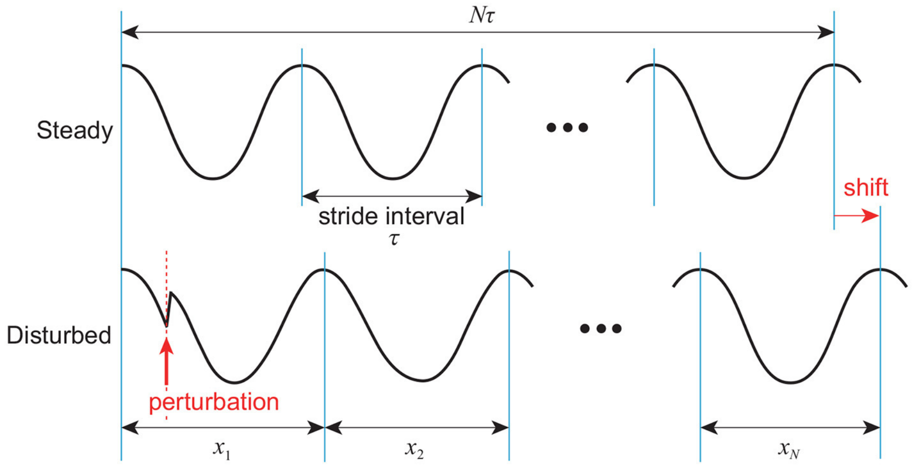

FIGURE 6 | Phase shift caused by disturbance to limit cycle of walking. After recovery, locomotion phase is shifted ($x_1 + \cdots + x_N > N\tau$).

(**Figure 3**). Furthermore, α was 0.5 to 1.0, which is consistent with observations of healthy adults, and was not sensitive to the noise amplitude (**Figure 4**), but sensitive to the controller (i.e., whether phase resetting was used).

Previous studies (Yamasaki et al., 2003; Aoi et al., 2010; Fujiki et al., 2018; Tamura et al., 2020) have shown that phase resetting contributes to adaptive walking. In this study, we found that it also contributes to the statistical persistence of gait. In addition to the fact that statistical persistence is impaired by aging (Hausdorff et al., 1997), central nervous system diseases, such as Parkinson's disease (Frenkel-Toledo et al., 2005) and Huntington's disease (Hausdorff et al., 1997), and experimental intervention for walking (Hausdorff et al., 1996), it has been suggested that statistical persistence is linked to important characteristics of gait. Bohnsack-McLagan et al. (2016) suggested that fluctuation persistence leads to redundancies in gait and helps predict and prevent fall risk. Ahn and Hogan (2013) and Fu et al. (2020) showed that fluctuation persistence appears in gait with low gait stability. Gates et al. (2007) showed that a decrease in the ability to perform finely controlled movements leads to an increase in motor output noise and impairs the persistence of fluctuations.

Many studies have reported long-range correlations in stride intervals in human walking based on the results of DFA (Hausdorff et al., 1995, 1996, 1997; Ashkenazy et al., 2002), which indicates that stride-to-stride correlations decay in a scale-free (fractal-like) power-law fashion and suggests that each stride depends explicitly on many previous strides. However, DFA is highly sensitive to yielding false positive results (Maraun et al., 2004; Höll and Kantz, 2015), and it is difficult to conclude the presence of long-range correlations from DFA alone. Instead, DFA provides a valid indicator of statistical persistence and anti-persistence in a time series (Maraun et al., 2004). In this study, we used statistical persistence instead of long-range correlations to interpret the results of DFA, as discussed in Dingwell and Cusumano (2010).

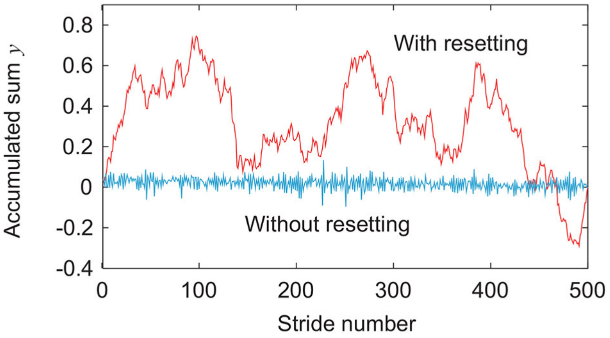

FIGURE 7 | Comparison of accumulated sum y of stride intervals between models with and without phase resetting at gait speed $v = 0.4$ m/s and using noise amplitude $\xi = 1$ in **Figure 3**.

4.3. Limitations of Our Model and Future Work

Based on the hypothesis that the statistical persistence in stride intervals emerge through dynamic interactions between the neural and biomechanical systems, we integrated a simple neural model and a simple biomechanical model to reproduce statistical persistence in stride intervals and change in this statistical property. However, our model is very simple and has limitations with regard to replicating many aspects of human walking. In particular, because the feedforward torques (9) and (10) were simply composed of a sinusoidal wave, the gait speeds of our model were slower than those of healthy adults (**Figure 2**). In addition, although statistical persistence could be associated with low gait stability (low convergence speed to the limit cycle) (Ahn and Hogan, 2013; Fu et al., 2020), our model had higher stability than that of complicated models due to its simplicity. The high stability of our model with phase resetting might have caused the scaling exponent α to be ~ 0.6, which is smaller than that (~ 1) in healthy adults (Hausdorff et al., 1995). Furthermore, stochastic noise is ubiquitous in the central nervous system and peripheral sensory-motor systems (Jones et al., 2002; van Beers et al., 2004; Churchland et al., 2006). However, our model used only torque noise, which may result in the difference between the statistical anti-persistence in the model without phase resetting and the white noise in walking to a metronome in humans (Hausdorff et al., 1996; Bohnsack-McLagan et al., 2016).

Based on the findings in this study, it is important to verify the essential mechanisms responsible for changes in the statistical persistence by using biologically detailed neuromusculoskeletal models. In a previous study (Tamura et al., 2020), we integrated a musculoskeletal model composed of seven rigid links and 18 muscles with a CPG model with a muscle synergy-based controller to investigate the contribution of phase resetting to the phase response characteristics during walking. In another previous study (Fujiki et al., 2019), we used a half-center type CPG model composed of a rhythm generator network, which was modeled using neuron populations of flexor and extensor centers based on Danner et al. (2016, 2017) and Rybak et al. (2006), to clarify the mechanisms responsible for the CPG responses to afferent stimulation using dynamic systems theory based on nullclines. We plan to incorporate these biologically detailed models to further investigate the mechanisms responsible for changes in the statistical persistence.

5. CONCLUSION

In this study, we clarified the contribution of phase resetting to the generation and change of statistical persistence using a simple neuromechanical model. Specifically, our model reproduced the statistical persistence in stride intervals. A lack of phase resetting induced a loss of statistical persistence. Furthermore, we clarified the mechanisms responsible for changes in statistical persistence caused by phase resetting based on the phase response characteristics. Our findings provide important insight into the mechanisms underlying the generation and change of the statistical persistence in the stride intervals in human walking.

DATA AVAILABILITY STATEMENT

The raw data supporting the conclusions of this article will be made available by the authors, without undue reservation.

AUTHOR CONTRIBUTIONS

SA developed the study design. KO performed simulation experiments and analyzed the data in consultation with SA, IO, HK, KS, and KT. KO and SA wrote the manuscript. All authors reviewed and approved it.

FUNDING

This study was supported in part by JSPS KAKENHI Grant Numbers JP21J23164 and JP20H00229; and JST FOREST Program Grant Number JPMJFR2021.

SUPPLEMENTARY MATERIAL

The Supplementary Material for this article can be found online at: https://www.frontiersin.org/articles/10.3389/fncir.2022.836121/full#supplementary-material

REFERENCES

Ahn, J., and Hogan, N. (2013). Long-range correlations in stride intervals may emerge from non-chaotic walking dynamics. *PLoS ONE* 8, e73239. doi: 10.1371/journal.pone.0073239

Aoi, S., and Funato, T. (2016). Neuromusculoskeletal models based on the muscle synergy hypothesis for the investigation of adaptive motor control in locomotion via sensory-motor coordination. *Neurosci. Res.* 104, 88–95. doi: 10.1016/j.neures.2015.11.005

Aoi, S., Ogihara, N., Funato, T., Sugimoto, Y., and Tsuchiya, K. (2010). Evaluating functional roles of phase resetting in generation of adaptive human bipedal walking with a physiologically based model of the spinal pattern generator. *Biol. Cybern.* 102, 373–387. doi: 10.1007/s00422-010-0373-y

Aoi, S., Ohashi, T., Bamba, R., Fujiki, S., Tamura, D., Funato, T., et al. (2019). Neuromusculoskeletal model that walks and runs across a speed range with a few motor control parameter changes based on the muscle synergy hypothesis. *Sci. Rep.* 9, 369. doi: 10.1038/s41598-018-37460-3

Ashkenazy, Y., Hausdorff, J. M., Ivanov, P. C., and Stanley, H. E. (2002). A stochastic model of human gait dynamics. *Phys. A* 316, 662–670. doi: 10.1016/S0378-4371(02)01453-X

Bohnsack-McLagan, N. K., Cusumano, J. P., and Dingwell, J. B. (2016). Adaptability of stride-to-stride control of stepping movements in human walking. *J. Biomech.* 49, 229–237. doi: 10.1016/j.jbiomech.2015.12.010

Bruijn, S. M., Bregman, D. J., Meijer, O. G., Beek, P. J., and van Dieën, J. H. (2011). The validity of stability measures: a modelling approach. *J. Biomech.* 44, 2401–2408. doi: 10.1016/j.jbiomech.2011.06.031

Churchland, M. M., Afshar, A., and Shenoy, K. V. (2006). A central source of movement variability. *Neuron* 52, 1085–1096. doi: 10.1016/j.neuron.2006.10.034

Danner, S. M., Shevtsova, N. A., Frigon, A., and Rybak, I. A. (2017). Computational modeling of spinal circuits controlling limb coordination and gaits in quadrupeds. *eLife* 6, e31050. doi: 10.7554/eLife.31050

Danner, S. M., Wilshin, S. D., Shevtsova, N. A., and Rybak, I. A. (2016). Central control of interlimb coordination and speed-dependent gait expression in quadrupeds. *J. Physiol.* 594, 6947–6967. doi: 10.1113/JP272787

Dingwell, J. B., and Cusumano, J. P. (2010). Re-interpreting detrended fluctuation analyses of stride-to-stride variability in human walking. *Gait Post.* 32, 348–353. doi: 10.1016/j.gaitpost.2010.06.004

Donelan, J. M., Kram, R., and Kuo, A. D. (2002). Mechanical work for step-to-step transitions is a major determinant of the metabolic cost of human walking. *J. Exp. Biol.* 205, 3717–3727. doi: 10.1242/jeb.205.23.3717

Dutra, M. S., de Pina Filho, A. C., and Romano, V. F. (2003). Modeling of a bipedal locomotor using coupled nonlinear oscillators of Van der Pol. *Biol. Cybern.* 88, 286–292. doi: 10.1007/s00422-002-0380-8

Duysens, J. (1977). Fluctuations in sensitivity to rhythm resetting effects during the cat's step cycle. *Brain Res.* 133, 190–195. doi: 10.1016/0006-8993(77)90063-4

Dzeladini, F., van den Kieboom, J., and Ijspeert, A. (2014). The contribution of a central pattern generator in a reflex-based neuromuscular model. *Front. Hum. Neurosci.* 8, 371. doi: 10.3389/fnhum.2014.00371

Eke, A., Hermán, P., Bassingthwaighte, J. B., Raymond, G. M., Percival, D. B., Cannon, M., et al. (2000). Physiological time series: distinguishing fractal noises from motions. *Pflügers Arch. Eur. J. Physiol.* 439, 403–415. doi: 10.1007/s004249900135

Frenkel-Toledo, S., Giladi, N., Peretz, C., Herman, T., Gruendlinger, L., and Hausdorff, J. M. (2005). Treadmill walking as an external pacemaker to improve gait rhythm and stability in Parkinson's disease. *Mov. Disord*. 20, 1109–1114. doi: 10.1002/mds.20507

Fu, C., Suzuki, Y., Morasso, P., and Nomura, T. (2020). Phase resetting and intermittent control at the edge of stability in a simple biped model generates 1/f-like gait cycle variability. *Biol. Cybern*. 114, 95–111. doi: 10.1007/s00422-020-00816-y

Fujiki, S., Aoi, S., Funato, T., Sato, Y., Tsuchiya, and Yanagihara, D. (2018). Adaptive hindlimb split-belt treadmill walking in rats by controlling basic muscle activation patterns via phase resetting. *Sci. Rep*. 8, 17341. doi: 10.1038/s41598-018-35714-8

Fujiki, S., Aoi, S., Tsuchiya, K., Danner, S. M., Rybak, I. A., and Yanagihara, D. (2019). Phase-dependent response to afferent stimulation during fictive locomotion: a computational modeling study. *Front. Neurosci*. 13, 1288. doi: 10.3389/fnins.2019.01288

Funato, T., Yamamoto, Y., Aoi, S., Imai, T., Aoyagi, T., Tomita, N., et al. (2016). Evaluation of the phase-dependent rhythm control of human walking using phase response curves. *PLoS Comput. Biol*. 12, e1004950. doi: 10.1371/journal.pcbi.1004950

Gates, D. H., and Dingwell, J. B. (2007). Peripheral neuropathy does not alter the fractal dynamics of stride intervals of gait. *J. Appl. Physiol*. 102, 965–971. doi: 10.1152/japplphysiol.00413.2006

Gates, D. H., Su, J. L., and Dingwell, J. B. (2007). Possible biomechanical origins of the long-range correlations in stride intervals of walking. *Phys. A* 380, 259–270. doi: 10.1016/j.physa.2007.02.061

Grillner, S. (1975). Locomotion in vertebrates: central mechanisms and reflex interaction. *Physiol. Rev*. 55, 247–304. doi: 10.1152/physrev.1975.55.2.247

Hardstone, R., Poil, S.-S., Schiavone, G., Jansen, R., Nikulin, V. V., Mansvelder, H. D., et al. (2012). Detrended fluctuation analysis: a scale-free view on neuronal oscillations. *Front. Physiol*. 3, 450. doi: 10.3389/fphys.2012.00450

Hase, K., Miyashita, K., Ok, S., and Arakawa, Y. (2003). Human gait simulation with a neuromusculoskeletal model and evolutionary computation. *J. Vis. Comput. Animat*. 14, 73–92. doi: 10.1002/vis.306

Hausdorff, J. M., Mitchell, S. L., Firtion, R., Peng, C. K., Cudkowicz, M. E., Wei, J. Y., et al. (1997). Altered fractal dynamics of gait: reduced stride-interval correlations with aging and Huntington's disease. *J. Appl. Physiol*. 82, 262–269. doi: 10.1152/jappl.1997.82.1.262

Hausdorff, J. M., Peng, C. K., Ladin, Z., Wei, J. Y., and Goldberger, A. L. (1995). Is walking a random walk? Evidence for long-range correlations in stride interval of human gait. *J. Appl. Physiol*. 78, 349–358. doi: 10.1152/jappl.1995.78.1.349

Hausdorff, J. M., Purdon, P. L., Peng, C. K., Ladin, Z., Wei, J. Y., and Goldberger, A. L. (1996). Fractal dynamics of human gait: stability of long-range correlations in stride interval fluctuations. *J. Appl. Physiol*. 80, 1448–1457. doi: 10.1152/jappl.1996.80.5.1448

Hausdorff, J. M., Zemany, L., Peng, C.-K., and Goldberger, A. L. (1999). Maturation of gait dynamics: stride-to-stride variability and its temporal organization in children. *J. Appl. Physiol*. 86, 1040–1047. doi: 10.1152/jappl.1999.86.3.1040

Higham, D. J. (2001). An algorithmic introduction to numerical simulation of stochastic differential equations. *SIAM Rev*. 43, 525–546. doi: 10.1137/S0036144500378302

Höll, M., and Kantz, H. (2015). The fluctuation function of the detrended fluctuation analysis - investigation on the AR(1) process. *Eur. Phys. J. B* 88, 126. doi: 10.1140/epjb/e2015-60143-1

Ihlen, E. A. F. (2012). Introduction to multifractal detrended fluctuation analysis in matlab. *Front. Physiol*. 3, 141. doi: 10.3389/fphys.2012.00141

Jones, K. E., Hamilton, A. F. C., and Wolpert, D. M. (2002). Sources of signal-dependent noise during isometric force production. *J. Neurophysiol*. 88, 1533–1544. doi: 10.1152/jn.2002.88.3.1533

Jordan, K., Challis, J. H., and Newell, K. M. (2006). Long range correlations in the stride interval of running. *Gait Post*. 24, 120–125. doi: 10.1016/j.gaitpost.2005.08.003

Kim, Y., Tagawa, Y., Obinata, G., and Hase, K. (2011). Robust control of CPG-based 3D neuromusculoskeletal walking model. *Biol. Cybern*. 105, 269–282. doi: 10.1007/s00422-011-0464-4

Kuo, A. D. (2001). A simple model of bipedal walking predicts the preferred speed-step length relationship. *J. Biomech. Eng*. 123, 264–269. doi: 10.1115/1.1372322

Kuo, A. D., Donelan, J. M., and Ruina, A. (2005). Energetic consequences of walking like an inverted pendulum: step-to-step transitions. *Exerc. Sport Sci. Rev*. 33, 88–97. doi: 10.1097/00003677-200504000-00006

Kuramoto, Y. (1984). *Chemical Oscillations, Waves, and Turbulence*. Berlin: Springer-Verlag. doi: 10.1007/978-3-642-69689-3

Lafreniere-Roula, M., and McCrea, D. A. (2005). Deletions of rhythmic motoneuron activity during fictive locomotion and scratch provide clues to the organization of the mammalian central pattern generator. *J. Neurophysiol*. 94, 1120–1132. doi: 10.1152/jn.00216.2005

Maraun, D., Rust, H. W., and Timmer, J. (2004). Tempting long-memory - on the interpretation of DFA results. Neuromechanical model. *Nonlinear Process. Geophys*. 11, 495–503. doi: 10.5194/npg-11-495-2004

Matsuoka, K. (1987). Mechanisms of frequency and pattern control in the neural rhythm generators. *Biol. Cybern*. 56, 345–353. doi: 10.1007/BF00319514

Nessler, J. A., Spargo, T., Craig-Jones, A., and Milton, J. G. (2016). Phase resetting behavior in human gait is influenced by treadmill walking speed. *Gait Post*. 43, 187–191. doi: 10.1016/j.gaitpost.2015.09.021

Ogihara, N., and Yamazaki, N. (2001). Generation of human bipedal locomotion by a bio-mimetic neuro-musculo-skeletal model. *Biol. Cybern*. 84, 1–11. doi: 10.1007/PL00007977

Okamoto, K., Aoi, S., Obayashi, I., Kokubu, H., Senda, K., and Tsuchiya, K. (2020). Fractal mechanism of basin of attraction in passive dynamic walking. *Bioinspir. Biomim*. 15, 055002. doi: 10.1088/1748-3190/ab9283

Orlovsky, G., Deliagina, T. G., and Grillner, S. (1999). *Neuronal Control of Locomotion from Mollusc to Man*. New York, NY: Oxford University Press. doi: 10.1093/acprof:oso/9780198524052.001.0001

Owaki, D., Horikiri, S., Nishii, J., and Ishiguro, A. (2021). Tegotae-based control produces adaptive inter- and intra-limb coordination in bipedal walking. *Front. Neurorobot*. 15, 629595. doi: 10.3389/fnbot.2021.629595

Peng, C.-K., Buldyrev, S. V., Goldberger, A. L., Havlin, S., Simons, M., and Stanley, H. E. (1993). Finite-size effects on long-range correlations: implications for analyzing DNA sequences. *Phys. Rev. E* 47, 3730–3733. doi: 10.1103/PhysRevE.47.3730

Peng, C.-K., Buldyrev, S. V., Hausdorff, J. M., Havlin, S., Mietus, J. E., Simons, M., et al. (1994a). Non-equilibrium dynamics as an indispensable characteristic of a healthy biological system. *Integr. Physiol. Behav. Sci*. 29, 283–293. doi: 10.1007/BF02691332

Peng, C.-K., Buldyrev, S. V., Havlin, S., Simons, M., Stanley, H. E., and Goldberger, A. L. (1994b). Mosaic organization of DNA nucleotides. *Phys. Rev. E* 49, 1685–1689. doi: 10.1103/PhysRevE.49.1685

Rybak, I. A., Shevtsova, N. A., Lafreniere-Roula, M., and McCrea, D. A. (2006). Modelling spinal circuitry involved in locomotor pattern generation: insights from deletions during fictive locomotion. *J. Physiol*. 577, 617–639. doi: 10.1113/jphysiol.2006.118703

Schomburg, E. D., Petersen, N., Barajon, I., and Hultborn, H. (1998). Flexor reflex afferents reset the step cycle during fictive locomotion in the cat. *Exp. Brain Res*. 122, 339–350. doi: 10.1007/s002210050522

Shik, M. L., and Orlovsky, G. N. (1976). Neurophysiology of locomotor automatism. *Physiol. Rev*. 56, 465–501. doi: 10.1152/physrev.1976.56.3.465

Taga, G. (1995a). A model of the neuro-musculo-skeletal system for human locomotion I. Emergence of basic gait. *Biol. Cybern*. 73, 97–111. doi: 10.1007/BF00204048

Taga, G. (1995b). A model of the neuro-musculo-skeletal system for human locomotion II. Real-time adaptability under various constraints. *Biol. Cybern*. 73, 113–121. doi: 10.1007/BF00204049

Taga, G., Yamaguchi, Y., and Shimizu, H. (1991). Self-organized control of bipedal locomotion by neural oscillators in unpredictable environment. *Biol. Cybern*. 65, 147–159. doi: 10.1007/BF00198086

Tamura, D., Aoi, S., Funato, T., Fujiki, S., Senda, K., and Tsuchiya, K. (2020). Contribution of phase resetting to adaptive rhythm control in human walking based on the phase response curves of a neuromusculoskeletal model. *Front. Neurosci*. 14, 17. doi: 10.3389/fnins.2020.00017

van Beers, R. J., Haggard, P., and Wolpert, D. M. (2004). The role of execution noise in movement variability. *J. Neurophysiol*. 91, 1050–1063. doi: 10.1152/jn.00652.2003

West, B. J., and Griffin, L. (1998). Allometric control of human gait. *Fractals* 6, 101–108. doi: 10.1142/S0218348X98000122

West, B. J., and Griffin, L. (1999). Allometric control, inverse power laws and human gait. *Chaos Soliton. Fract*. 10, 1519–1527. doi: 10.1016/S0960-0779(98)00149-0

West, B. J., and Scafetta, N. (2003). Nonlinear dynamical model of human gait. *Phys. Rev. E* 67, 051917. doi: 10.1103/PhysRevE.67.051917

Winfree, A. T. (1980). *The Geometry of Biological Time*. New York, NY: Springer-Verlag. doi: 10.1007/978-3-662-22492-2

Winter, D. A. (2004). *Biomechanics and Motor Control of Human Movement, 3rd Edn*. New York, NY: Wiley.

Yamasaki, T., Nomura, T., and Sato, S. (2003). Possible functional roles of phase resetting during walking. *Biol. Cybern*. 88, 468–496. doi: 10.1007/s00422-003-0402-1

Conflict of Interest: The authors declare that the research was conducted in the absence of any commercial or financial relationships that could be construed as a potential conflict of interest.

The reviewer TN declared a shared affiliation with the author SA to the handling editor at time of review.

Advantages of publishing in Frontiers

OPEN ACCESS
Articles are free to read
for greatest visibility
and readership

FAST PUBLICATION
Around 90 days
from submission
to decision

HIGH QUALITY PEER-REVIEW
Rigorous, collaborative,
and constructive
peer-review

TRANSPARENT PEER-REVIEW
Editors and reviewers
acknowledged by name
on published articles

Frontiers
Avenue du Tribunal-Fédéral 34
1005 Lausanne | Switzerland

Visit us: www.frontiersin.org
Contact us: frontiersin.org/about/contact

REPRODUCIBILITY OF RESEARCH
Support open data
and methods to enhance
research reproducibility

DIGITAL PUBLISHING
Articles designed
for optimal readership
across devices

FOLLOW US
@frontiersin

IMPACT METRICS
Advanced article metrics
track visibility across
digital media

EXTENSIVE PROMOTION
Marketing
and promotion
of impactful research

LOOP RESEARCH NETWORK
Our network
increases your
article's readership